Preparation and Characterization of Tungsten Carbide Micro/Nano Composites

A

Thesis

Submitted for the award of

The degree of

DOCTOR OF PHILOSOPHY

By

Akshay Kumar

Under the supervision of

Dr. O. P. Pandey **Dr. Kulvir Singh**

SCHOOL OF PHYSICS AND MATERIALS SCIENCE

THAPAR UNIVERSITY PATIALA-147004, INDIA

April - 2011

Dedicated to my family

Wife (Rajni) and Son (Arnav)

"Anyone who has never made a mistake has never tried anything new."

Albert Einstein (1879-1955)

THAPAR
UNIVERSITY
(Declared as Deemed-to-be-University u/s 3 of the UGC Act, 1956)
Thapar Technology Campus, Post Box No. 32
Patiala 147 004 Punjab India
Fax : +91-175-2364498, 2393005
URL : www.thapar.edu

CERTIFICATE

This is to certify that this thesis entitled **"Preparation and Characterization of Tungsten Carbide Micro/Nano Composites"** which is being submitted by Akshay Kumar in fulfillment of the requirements for the award of the degree of Doctor of Philosophy in the School of Physics and Materials Science, Thapar University, Patiala, Punjab, India is an exclusive record of candidate's own research work under our supervision. The thesis in part or in full has not been submitted in any other university or institute for the award of any degree. The thesis is fit to be considered for the award of degree of Doctor of Philosophy.

Dr. O.P. Pandey
Professor
School of Physics and Materials Science
Thapar University
Patiala-147 004 (INDIA)

Dr. Kulvir Singh
Associate Professor & Head
School of Physics and MaterialsScience
Thapar University
Patiala-147 004 (INDIA)

Index

Contents **Page No.**

ACKNOWLEDGEMENTS

At this momentous occasion of binding my thesis I would like to acknowledge the contribution of all those benevolent people who helped me during my PhD work. Knowledge is imparted through the developing relationship between the guru and the disciple. It is considered that this relationship, based on the genuineness of the guru, and the respect, commitment, devotion and obedience of the student, is the best way for subtle or advanced knowledge to be conveyed. I have been blessed to associate with. **Prof. Om Prakash Pandey** and **Dr. Kulvir Singh** (Associate. Prof). They provided me a chance to work under their guidance and supervision, assisting with all kind of support and inspiration, wide counsel, constant encouragement, sincere criticism, valuable suggestions, expertise and fruitful advice which they proffered throughout this investigation and preparation of the thesis.

I am profoundly obliged to **Distinguish Prof. K.K. Raina**, Deputy Director, Thapar University, Patiala for his constant encouragement and needful help during various stages of the work.

I am very thankful all **faculty of School of Physics and Materials Science.**

Dr Manoj Sharma, Dr Suneel Kumar, Dr Puneet Sharma, and Dr Rohit Dhir, are specially acknowledged for their whole hearted support.

My special thanks to **Dr. C. P. Khatter** (Prof. & Head Mechanical Engineering Department Mullana University) for his help and valuable suggestions at every stage of my work.

I am also thankful to **Dr. Bonamali Pal**, **Dr A.K. Lal** and **Dr. Manmohan Chhibber** for their whole hearted support.

My special thanks to **Mr. P.K. Singh** for his help and valuable suggestions for the characterization of materials.

Words are inadequate in expressing my sincere thanks to my friends **Dr. Anup Thakur, Dr Vishal Kumar, Mr. Arvind Kumar, Ms. Neeraj Sharma, Ms Kamalpreet Kaur, Mr Ranvir Singh, Mr Manjeet Kumar, Mr Gaurav Singla, Mr Suresh Kumar, Dr. Zinki Jindal, Dr. Sanjeev Kumar and Mr. Amit Awasthi** for their support in every moment of difficulty.

I am also indebted to **Dr Pankaj Kumar, Dr Anu Arora, Mr Manoj Kumar, Ms Jasmeet Grewal, Ms Bhupinder Kaur, Ms Gurvinder Kaur, Ms Shamita Thakur, Ms Chandini Khurana, Ms Samiksha Verma, Ms Mani Mahajan, Ms Shiwani Sharma, Ms Meenu, Mr Paramjot Jha, Mr Kapil Sood, Mr Harjinder Singh, Mr Praveen Jha and Mr Vipin Sharma** for their kind help and valuable suggestions.

I also thank **Mr Dinesh** and **Mr Ravi Sukhla** for their help and precious time which they devoted for my cause.

My special thanks to **Mr Vijay Kumar, Mr S. P. Yadav, Mrs Praveen, Mr. Indermani, Mr. Jant Singh and Mr Gurmeet Singh** for providing all kinds of help. All the staff of School of Physics and Materials Science is acknowledged who never turned me down whenever I approached for any help.

My family especially my wife **Mrs. Rajni Bala** deserve the special thanks and great appreciation for their patience, persistent moral support and capability to revitalize me during the course of the Ph.D. work at each step. Special thanks to my brother **Mr Sunil Kumar** who stood by me all the times.

Last but not least my father **Mr. Gian Chand** and my mother **Mrs. Pushpa Devi** are the two guiding pillars of my success. The constant motivation of my parents has been the sole source of inspiration and strength to carry out my work.

Above all, hidden force by **Almighty God** steered me in the right direction to achieve the goal.

Akshay Kumar

(Akshay Kumar)

List of Publications

Journals:

1) **Akshay Kumar**, K. Singh and O.P. Pandey, ***Synthesis of carbon nano tubes by thermo-chemical method and their structural investigation***, Ceramics International (under review) 2011.

2) **Akshay Kumar**, K. Singh and O.P. Pandey, ***Direct conversion of wolframite ore to Tungsten Carbide nano particles***, Int Journal of Refrectory Metals and Hard Materials, 29 (2011) 555-558. doi:10.1016/j.ijrmhm.2011.01.009

3) **Akshay Kumar**, K. Singh and O.P. Pandey, ***Sintering behavior of Nano structured WC-Co composite***, Ceramics International, 37 (2011) 1415-1422. doi:10.1016/j.ceramint.2011.01.001

4) **Akshay Kumar**, K. Singh and O.P. Pandey, ***Optimization of processing parameters for the synthesis of tungsten carbide (WC) nano particles through solvo thermal route***, Physica E- Low Dim Phys and Nano structures, 42 (2010) 2477–2483. doi:10.1016/j.physe.2010.06.002

5) **Akshay Kumar**, K. Singh and O.P. Pandey, ***Reduction of WO_3 to nano-WC by thermo-chemical reaction route***, Physica E- Low Dim Phys and Nano structures, 41 (2009) 677–684. doi:10.1016/j.physe.2008.11.016

6) **Akshay Kumar**, K. Singh and O.P. Pandey, ***Development Of Nanocomposite WC-Co Materials-An Overview***, Nano Science and Nano Technology-An Indian J 1(2), (2007) 59-69.

7) R. Kumar, R. Srivastava, **A. Kumar**, M. N. Kamalasanan, K. Singh, ***Green-light–emitting electroluminescent device based on a new cadmium complex***, Euro Physics Letters, 90 (2010) 57004. doi: 10.1209/0295-5075/90/57004

Presentations/Conference Papers:

1) **Akshay Kumar**, K. Singh, O.P. Pandey, ***Synthesis of Nano size WC-Co Composite by Carbothermic Reduction***, International Conference on Metals and Alloys: Past, Present & Future (METALLO 2007) **Third Prize.**

2) **Akshay Kumar**, K. Singh, O.P. Pandey, ***Synthesis and Characterization of Nanocomposite WC-Co Materials***, National Conference on Emerging Trends in Engineering materials, Feb 2007, Thapar Institute of Engineering & Technology, Patiala.

3) **Akshay Kumar**, K. Singh, O.P. Pandey, ***Synthesis of Tungsten Carbide nano crystals by thermo chemical route***, Punjab Science Congruence Feb. 2008 held at Thapar University Patiala.

4) **Akshay Kumar**, K. Singh and O.P. Pandey, ***Microstructural examination of sintered nano-structured WC-Co composite***, Materials research Society of India 22 meet, Feb 2011.

5) Raj Kumar, **Akshay Kumar** and O.P. Pandey, ***Synthesis of WC nano particles by reflux reaction***, Materials research Society of India 22 meet, Feb 2011.

List of Figures

Chapter 1 **Page No.**

Chapter 2

Chapter 3

Chapter 4

List of Tables

Chapter 1 **Page No.**

Chapter 2

Chapter 3

Chapter 4

Preface

Developing new methods of investigation and preparing materials with novel structural features by which progress has been made in the field of condensed matter physics, materials science is the basic theme of present work. Earlier it was known that solids deviating from perfectly ordered structure may exhibit attractive features. These deviations are divided in two categories; thermally disordering and disordered incorporating defects such as vacancies, dislocations, and grain or interphase boundaries. The basic idea of nanocrystalline materials is to generate a new class of disordered solids by introducing such a high density of defect cores. As the grain size is reduced, large fraction of atoms may lie at grain boundaries which may contribute to enhancement in different properties of the materials. Metallurgists are trying to use this advancement in the form of powder metallurgy (P/M). Among the materials synthesized by P/M process tungsten carbide (WC), discovered in 1898 is one of them. Tungsten carbide is used as a bearing material and finds its application in cutting tool industries. Exceptional hardness makes it suitable for these applications. Although it is hard but it is brittle also so it is always used in a ductile metal matrix as a binder and cobalt is one of the best suitable binder. Nano-grained WC/Co composites are the potential to become the new materials for tools, dies and wear parts. Considering these aspects there is an increasing interest to reduce the size of tungsten carbide (WC) grain for its applications in different engineering components to extract the advantages of higher hardness and toughness. The properties of nanostructured materials can be used to increase the strength of cutting tool based on

WC- Co materials. Benefits of nano-grained WC/Co approach include shorter sintering time, high purity, and precise control of composition. These materials have superior properties and more homogeneous microstructure than conventional WC/Co composites. Nano-grained WC/Co also allows optimization of specific properties without compromising others. Higher toughness and ductility can be achieved without reducing hardness and wear resistance. Considering these aspects the present work is undertaken.

The present work deals with the synthesis and characterization of WC nano material followed by compaction and sintering of WC-Co blend to get WC-Co composite. The entire work in this thesis is presented in **five chapters.**

In the **first chapter** general introduction to WC/ WC-Composites is given. The history of origin of tungsten carbide and its properties are described in first section of the chapter. Shifting from pure WC to sintered WC and then to WC Composites is described in the second section of the chapter. The last section deals with the work done to achieve nano WC composites.

Chapter 2 gives a detailed account of the literature survey in context of tungsten carbide composites. The various methods used to synthesize WC nano composites have been presented in this chapter. After reviewing all segment of literature the need to select solvo-thermal route for the synthesis of WC nano powder was felt and accordingly the reason for it is given. The last section of this chapter presents the gaps in the study so far with aims and objectives of the work of the thesis.

Chapter 3 describes about experimental procedure followed in the present work. On the basis of literature survey, nano particles of tungsten carbide were synthesized by thermo-chemical and mechano-chemical methods in a specially designed autoclave. The as prepared samples were characterized by different characterization techniques mentioned earlier. The details of synthesis techniques with characterization techniques are described in this chapter.

Chapter 4 deals with results and discussions on as prepared samples.

The chapter is divided in three sections; in the **first section** results obtained from thermo-chemical synthesis method are presented and discussed in details. The effect of variation of carbon source (methanol, ethanol and acetone), variation in reaction time (10, 12, 15 and 20 hours) along with variation of amount of selected carbon source is discussed. On the basis of results obtained from different experiments by taking different combination of tungsten source; carbon source and reducing agent one particular set has been optimized for maximum yield of WC nano particles. After investigating the product phases by XRD, DTA/TGA and TEM a possible mechanism for the conversion of tungsten oxide to tungsten carbide nano particles is proposed. The results of other experiments performed to confirm the proposed mechanism are also presented and discussed in this section.

In the **second section** the results obtained from mechano-chemical synthesis method obtained by varying milling time (10, 15, 20 hours) are presented and discussed. The role of different carbon sources (methanol, ethanol and acetone) are also discussed in this section.

The **third section** deals with the discussion on the results obtained from composites (5, 10, 15 and 20 wt% of Cobalt) synthesized using WC nano particles. The WC nano particles obtained from both the synthesis routes are used for the composite synthesis.

The sintering behavior of these composites at different time (1, 2, 3 and 4 hours) and temperatures (1250 ºC, 1300 ºC, 1350 ºC and 1400 ºC) in argon atmosphere is discussed in detail.

In **Chapter 5** the present work is summarized and concluded for the entire work done in the present investigation along with future scope. The present study shows that nano size WC can be synthesized using thermo chemical and mechano-chemical reaction route. During synthesis pressure generated due to temperature plays a major role for the conversion of WO_3 to WC. It seems that the particle size of WC decreases with the increased amount of carbon source upto certain level only. Reaction time of 20 hours and 36 ml (acetone) as carbon source gives a maximum yield of WC with the minimum amount of unreacted carbon in thermo-chemical reaction route. The liberation of hydrocarbon gases and hydrogen during course of synthesis leads to formation of carbon nano tube also. Thermal analysis indicates that the product contains more carbon if ethanol is used as carbon source as compared to acetone. The present synthesis route can be used to synthesize carbon nano tubes of $\approx$ 3-14 nm diameter by decomposition of acetone at 650 ºC. Nano WC in WC-Co composite after sintering grows to micron level because of higher sintering time and temperature. Low sintering time and temperature does not facilitate to get well sintered product.

Future scope of the work

The as synthesizd nano particles can be used in the electrical contact materials. The catalytical activity of the as synthesized particles can also be tested. In addition to this, the grain growth parameters of WC nano particles in composites should also be studied.

Chapter 1

INTRODUCTION

Overview

This chapter presents the origin and evolution of tungsten carbide. Crystal structure and tungsten–carbon phase diagram is discussed. Limitation of pure tungsten carbide, its use in the form of composites and the improved properties are discussed using W-C-Co phase diagram. Use of traditional composites and their limitations along with the reason to switch over to nano composites are presented. A brief idea of synthesis techniques of these nano composites is also presented here. The applications of these nano composites in military, sports, domestic and energy are discussed which itself explains the importance and the basic idea to take on this research project. Presentation of various chapters of the thesis is also given at the end.

1.1 Background

Developing new materials with novel structural features is one of the basic theme of materials science [1-2]. Earlier it was known that solids with fully ordered crystals structure have different properties than those have partially ordered or defect structure [3]. These deviations are mainly divided in two categories, thermal disordering and crystal disordering such as defects (vacancies, dislocations and grain boundaries) [4]. This basic idea to generate a new class of disordered solids by introducing a high density of defect cores has led to the discovery of nano crystalline materials [5]. Nano scale components have very high surface to volume ratio, making them ideal for use in composite materials, drug delivery systems, energy storage and reacting systems. Small grain size has a strong influence on the mechanical properties of materials. It results in, increased hardness, ductility, plasticity and enhancement in strength of materials [6-7]. These enhanced mechanical properties especially increased hardness can make a remarkable change in cutting tool industry which is a two billion-dollar industry worldwide. This industry form the backbone of manufacturing operations for metals, polymers and advanced materials such as intermetallics and composites which are used in many industries. Major portion (95%) of hard materials used in cutting tool industry is tungsten carbide- cobalt composite (WC-Co) [8]. These composites are aggregates of particles of tungsten carbide bonded with cobalt metal. The properties of these materials are derived from their constituents: the hard and brittle tungsten carbide and the ductile binder -cobalt. Nano particles of WC replacing the traditional WC particles in these composites may enhance the hardness as well as the life of the tool. In addition to this the nano particles of WC can also replace platinum catalyst in proton exchange membrane fuel cells. This is the basic idea to take this research project.

1.2 Tungsten carbide

1.2.1 Evolution of Tungsten carbide

Tungsten carbide was discovered in 1898 by P. Williams in his laboratory at the School of Pharmacy at the University of Paris [9]. Exceptional hardness and wear/erosion resistance showed that it can be a better option for metallurgical applications such as cutting tools and bearing materials. Tungsten carbide was initially used as wire-drawing dies. The cast pure WC was not found suitable for these applications because this stoichiometric compound WC, with 6.13 wt % carbon, does not melt congruently. The compound decomposed to a fragile mixture of W_2C, WC and graphite upon cooling. The lower carbon contents, resulted in mixture of WC and W_2C phases. This mixture product was very hard, but quite brittle also. Although it was brittle but usable in dies [9]. The materials scientists further tried to overcome the casting defects which are common in the molten product and produced first sintered tungsten carbide in year 1914, for use in drawing dies and rock drills. The increase in brittleness in this sintered product made it unsuccessful for industrial applications.

1.2.2 W-C Phase Diagram

The tungsten rich part of W-C phase diagram is shown in figure 1.1. Three W-C stoichiometries have been found. Namely: hexagonal W_2C, cubic sub-carbide WC_{1-x} and hexagonal WC. WC_{1-x} crystallizes in the NaCl type structure denoted by γ-phase, W_2C crystallizing in three modifications: the PbO_2, Fe_2N and CdI_2 types denoted by β, β’ and β” phases, respectively. While WC crystallizes in hexagonal and denoted by δ-phase. The allotropic transition of W_2C ($\beta \rightarrow \beta' \rightarrow \beta''$) occurs over a wide range of composition (25.5 to 34 wt.% C) at 2715 °C. This transition occurs through eutectoid reaction at 1250 °C ($\beta'' \rightarrow W + \delta WC$) which melts congruently with W solid solution at at 1715 ± 5 ºC and with γ-WC_{1-x} at approximately 2758 ºC.

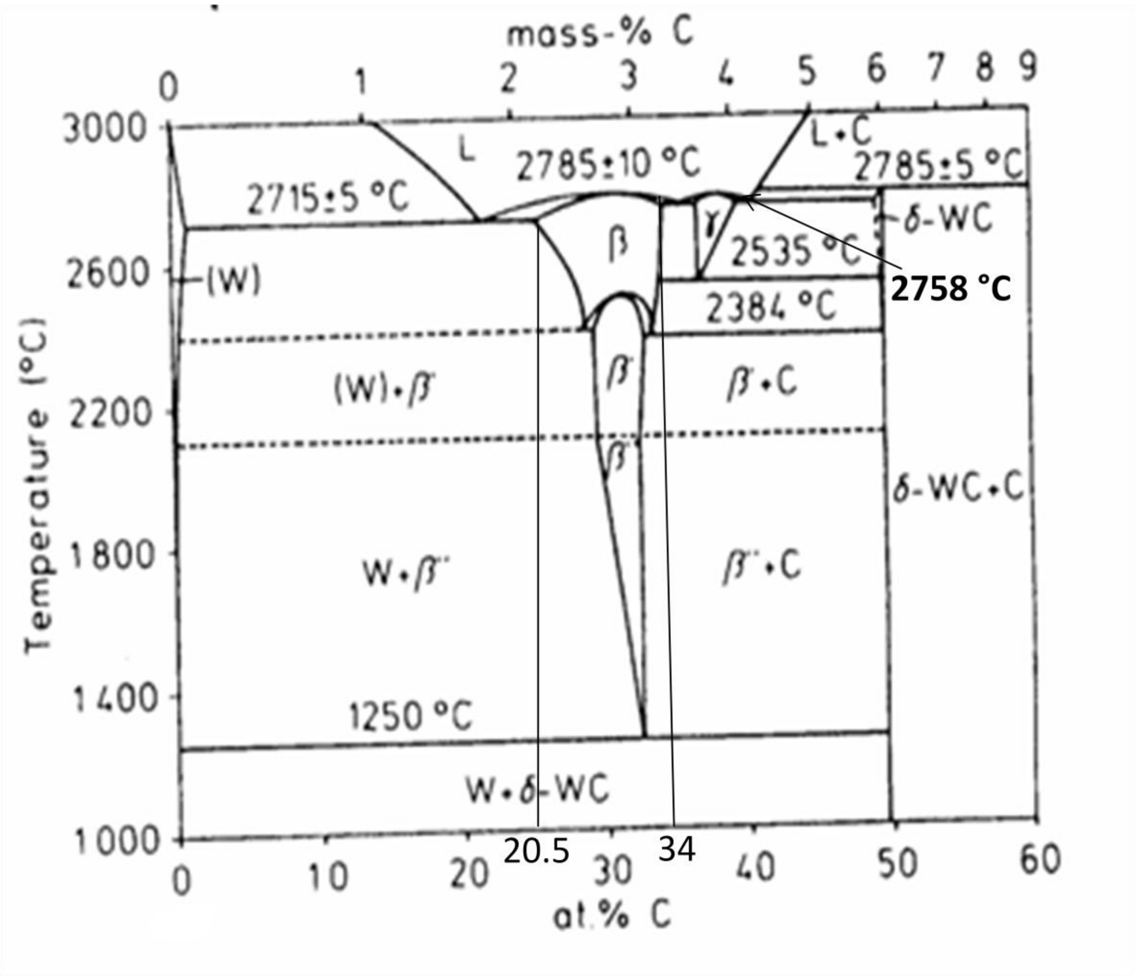

Figure 1.1: W-C Phase diagram [10].

Phases of W_2C stoichiometry are obtained as intermediate products during WC production. The γ-phase results from a eutectoidal reaction between β and δ at 2535 ºC and melts at 2785 ºC (approximately). It can be obtained at room temperature by extremely rapid cooling e.g., in plasma sprayed layers. The technically important δ-WC is the only binary phase stable at room temperature and has almost no solid solubility up to 2384 ºC but may become carbon deficient till melting [9,10].

1.2.3 Tungsten carbide crystal structure

The monocarbide, WC, has a simple hexagonal crystal structure (figure 1.2) with two atoms per unit cell and c/a ratio of 0.976 [11].

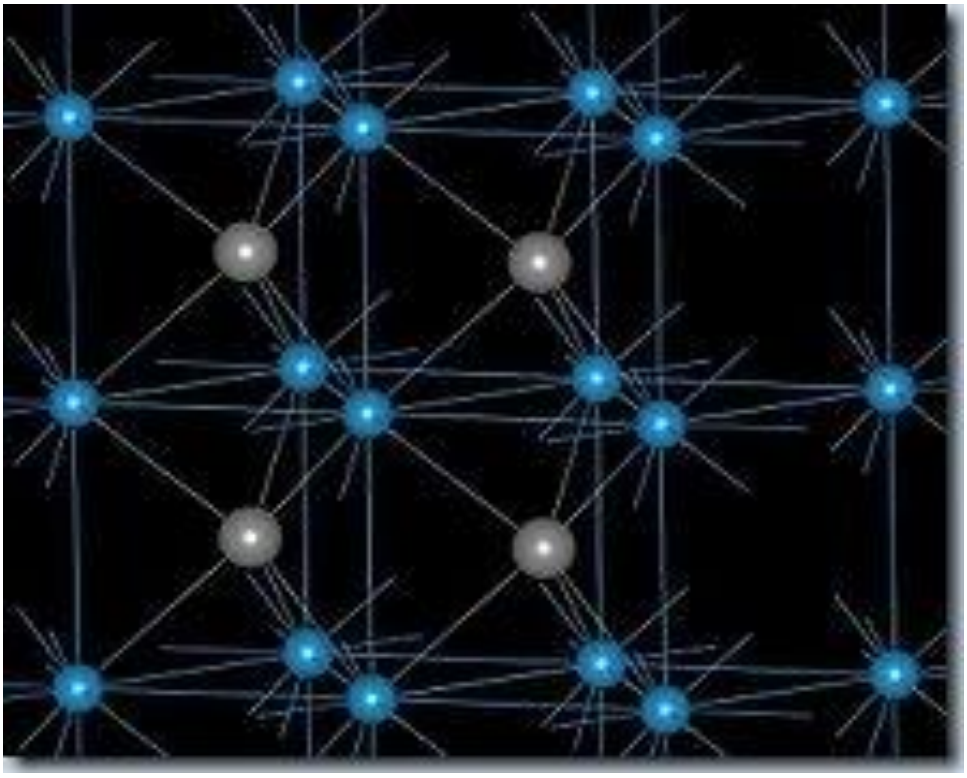

Figure 1.2: α-WC structure, carbon atoms are gray [12].

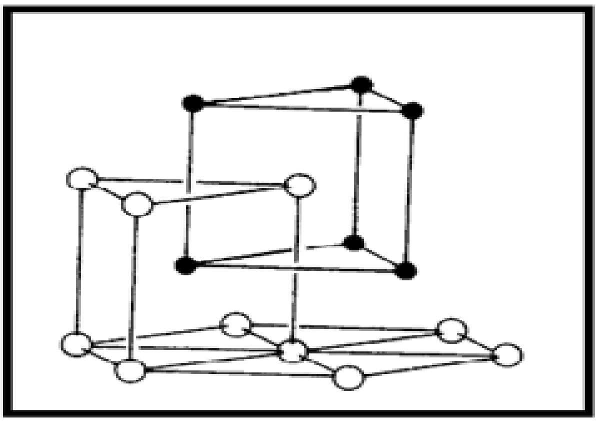

Figure 1.3: The structures of WC showing inter leaved trigonal prismatic cells [9].

The structure of WC showing interleaved trigonal prismatic cells is also shown in figure 1.3. In the primitive hexagonal lattice, half of the six-fold coordinated carbon positions are unoccupied. The structure unit of the hexagonal phase is thus the M_6C triangular prism with carbon in the center, or the C_6M with a six-fold coordinated metal atom. The advantage of this WC structure, relative to the NaCl-type, is to have lower energy for the electrons in the d-d orbital M-M bonding states [13].

1.3 Composites

Composite materials, often shortened to composites, are engineered or naturally occurring materials made from two or more constituent materials with significantly different physical or chemical properties which remain separate and distinct at the macroscopic or microscopic scale within the finished structure. One of the components is matrix, the monolithic material into which the reinforcement is embedded and is completely continuous. This means that there is a path through the matrix to any point in the material, unlike two materials sandwiched together. The other component(s) is reinforcement material, embedded into the matrix. The reinforcement does not always serve a purely structural task (reinforcing the compound), but is also used to change physical properties such as wear resistance, friction coefficient, or thermal conductivity. The reinforcement can be either continuous or discontinuous [14].

Composites are divided in the following categories:

- Polymer Matrix Composite
- Metal Matrix Composites
- Carbon Fiber Composites
- Ceramic Matrix Composites
- Multi-filamentary Superconducting Composites

Since this research work is in the category of Metal Matrix Composite, only this category is discussed in the following sections.

1.3.1. Metal Matrix Composite

Metal matrix composite consists of a metal or an alloy as the continuous matrix and a reinforcement that can be particles, short fiber or whisker, or continuous fiber. There are three kind of metal matrix composites (MMC’s):

- Particle reinforced MMC’s
- Short fiber or whisker reinforced MMC’s
- Continuous fiber or sheet reinforced MMC’s

1.3.2 Particle reinforced MMC's

These types of MMC's consist of particles of 1-25 μm length as reinforcement material. The aspect ratio (length to diameter of reinforcement particle) lies between 1- 4. SiC, WC or Al_2O_3 are some of the examples of particle reinforced MMC's.

1.3.3 Short fiber or whisker reinforced MMC's

In this type of MMC's short fiber or whisker are used as reinforcement materials with an aspect ratio of 10-1000. The diameter of the fiber used as reinforcement is between 0.1 to 25 μm. SiC, Al_2O_3, and C are some of the examples of short fiber or whisker reinforcement materials.

1.3.4 Continuous fiber MMC's

Continuous fibers or sheets are used as reinforcement materials in the matrix of copper, aluminum alloys, titanium alloys etc. The aspect ratio of the reinforcement in this case is >1000. The diameter of the fiber lies between 3-150 μm. SiC, Al_2O_3, C, B, W fiber or sheet can be used in these types of MMC's.

1.4.1 Cemented Carbide

Tungsten carbide powder, generally ranging in proportion between 70% - 97% of the total weight, is mixed with a binder metal, usually cobalt or nickel, compacted in a die and then sintered in a furnace. The term "cemented" refers to the tungsten carbide particles being captured in the metallic binder material and "cemented" together, forming a mechanical bond between the tungsten carbide particles and the binder (WC - Co), in the sintering process [15]. The cemented carbide industry commonly refers to these materials as simply "carbide", although the terms tungsten carbide and cemented carbide are used interchangeably. Moreover, in the absence of the metallic binder phase, tungsten carbide could be considered a ceramic material much the same as silicon carbide or aluminum oxide.

1.4.2 Cermet

A cermet is a composite material composed of ceramic (cer) and metallic (met) materials. It is the addition of the metallic binder, i.e. cobalt or nickel that makes the cemented carbide (WC - Co) a cermet and differentiates it from truly brittle materials, that is, the ceramic family of materials [9].

1.5 Cemented carbide development- Co as Metal matrix

In early 1920’s a German electrical bulb company, Osram, looked for alternatives to the expensive diamond drawing dies used in the production of tungsten wire, it was the beginning of research on cemented carbide. Systematic experiments were done from 1918 to1923 to bind powdered tungsten carbide with iron, nickel or cobalt. The first sintered cemented carbide dies were prepared in 1922. The wire-drawing tests showed cobalt to be the best additive. The invention of the cemented carbide tool materials was first disclosed in 1923 in Karl Schrter’s patent application [16]. These attempts led to the invention of cemented carbide. This carbide was soon produced and marketed by several companies for various applications where its high wear resistance was particularly important. In 1930’s first tungsten carbide-cobalt grades were successfully applied in the cutting and milling of cast iron. High temperature wear resistance, the hot hardness and the oxidation stability of hard metals have been considerably improved by the addition of titanium carbide and tantalum carbide.

1.5.1 Properties of Cemented carbide

Structure and final composition are responsible for the properties of sintered WC-Co composites [17]. Composite with optimum properties can be obtained if the carbon content is maintained within narrow limits. Carbon content deviated even slightly from the ideal may bring about the occurrence of either graphite or a ternary compound. Both of these phases are usually undesirable and results in degradation of mechanical properties.

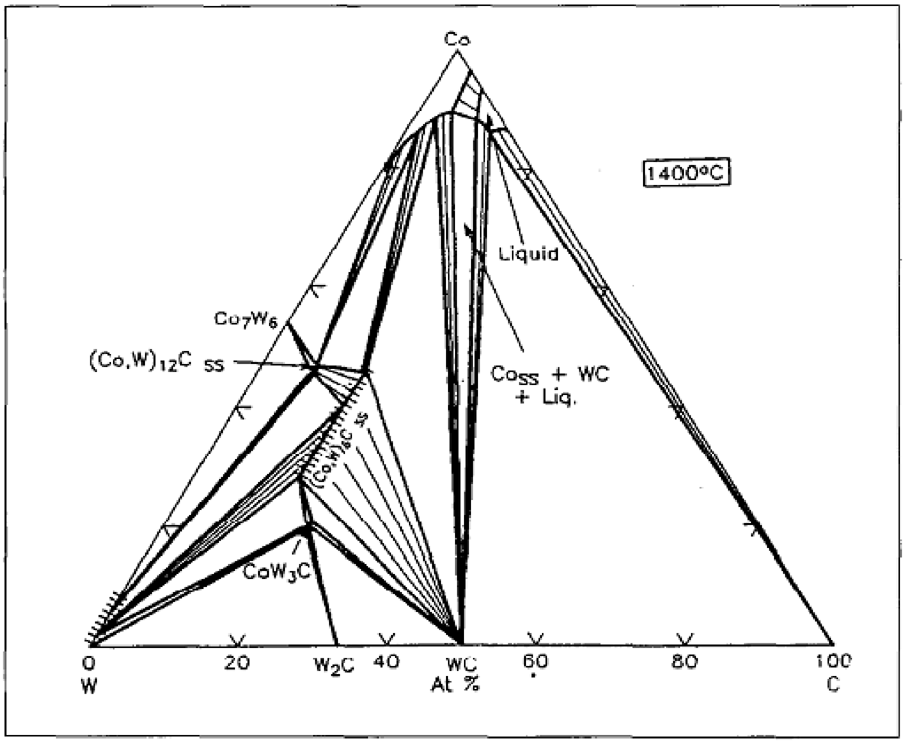

Figure 1.4: The isothermal section of WC-Co phase diagram at 1425 ºC [18].

It is well established fact that two types of η phase can be obtained – M_6C and $M_{12}C$. In M_6C the composition can vary within the range of $Co_{3.2}W_{2.8}C$ and Co_2W_4C, however, composition remains constant in $M_{12}C$ (Co_6W_6C) (figure 1.4). The M_6C type of η phase can nucleate and grow during the sintering process and is in equilibrium with the liquid phase. This phase reduces the effective contribution of WC to the strength of the composite and also embrittles the structure by replacing the binder with a brittle phase. The $M_{12}C$ type is formed in the solid state (during cooling) with small grains distributed throughout the matrix and is therefore effectively less embrittling [9]. WC-Co phase diagram in the sintering range of commercial WC-Co (isothermal section of the phase diagram at 1425 ºC) is shown in figure 1.4 [18]. Research shows that grain size and cobalt composition have great influence on mechanical properties of materials (table 1.1).

Table 1.1: Properties of representative cobalt-bonded cemented carbide grades [20].

Composition	**Grain size (in micron size)**	**Hardness (HRA)**	**Density (g/cm^3)**	**Transverse strength (MPa)**	**Compressive strength (MPa)**	**Modulus of elasticity (GPa)**
97WC-3Co	Medium	92.5-93.2	15.3	1590	5860	641
94WC-6Co	Fine	92.5-93.1	15.0	1790	5930	614
94WC-6Co	Medium	91.7-92.2	15.0	2000	5450	648
94WC-6Co	Coarse	90.5-91.5	15.0	2210	5170	641
90WC-10Co	Fine	90.7-91.3	14.6	3100	5170	620
90WC-10Co	Coarse	87.4-88.2	14.5	2760	4000	552

By means of this particle size reduction process, the fracture toughness and strength can be increased significantly. The most striking is the abrasion resistance, with finer grain composites (still in micron range) having much better abrasion resistance [19-20]. These results force metallurgists to move toward nano WC-Co composites.

1.6 Nano crystalline materials Research and Promise

These days nano scale particle research is the emerging section in the field of materials science [21]. Nano structured materials falls in the class of disordered materials. The deviation from the perfect crystal is induced by incorporating defects. For example, the atomic density in the core region of grain boundaries is reduced typically by reducing size to nano scale [3-4].

Nanotechnology can be defined as the study, design, creation, synthesis, manipulation and application of functional materials, devices and systems through control of matter at the nanometer scale (1-100 nm) and exploiting this novel phenomena and properties of matter at that scale to achieve better properties. Nanostructures can be engineered either by top-down or by bottom-up approach. In top down approach a bulk material is reduced in size to nano scale pattern while larger structures are built or grown atom by atom or molecule by molecule in bottom up approach [22].

1.6.1 Top-down Approach

The most common way to fabricate structures in the range of nanometers is the top-down approach. By using lithographic processes, small size elements are "cut" from larger pieces. The best known example is microelectronics devices. Using optical lithography semiconductor chips with critical dimensions down to 65 nm are being produced.

1.6.2 Bottom-up Approach

Bottom-up, or self-assembly, approaches to nanofabrication using chemical or physical forces operating at the nano scale to assemble basic units into larger structures. In nano fabrication bottom-up approach provides increasingly important complement top-down techniques. Inspiration for bottom-up approaches comes from biological systems where nature has harnessed chemical forces to create essentially all the structures needed in life. Researchers hope to replicate nature's ability to produce small clusters of specific atoms which can then self-assemble into more-elaborate structures.

The unique properties of nano scale particles and nano grain bulk materials can be attributed to two basic phenomena:

I. The first is that the number of atoms at the surface and/or grain boundaries in these materials are comparable to that of the atoms located in the crystal lattice, thus the chemical and physical properties are increasingly dominated by the atoms at these locations. As the grain size is reduced, large fraction of atoms may lie at grain boundaries which may contribute to enhancement in toughness of the materials.

II. The second phenomenon is the “quantum-size effect” or quantum confinement effect. When particles approach the nanometer size range, their electronic and photonic properties can be significantly modified as a result of the absence of a few atoms in the lattice and the resulting relaxation of the lattice structure.

1.7 Nanostructured WC/Co Composites

Over the past two decades, substantial research efforts have been directed towards the synthesis and sintering of nano sized tungsten carbide powders in order to manufacture cemented tungsten carbide materials with nano crystalline grain structure. The synthesis of WC nano particles is covered under these basic techniques.

- spray conversion
- mechanical alloying

- chemical vapor reaction

Modification in these techniques has also been done to overcome the limitations.

1.7.1 Spray conversion

McCandlish et al. [23] at Rutgers University developed and patented spray conversion processing to produce bulk quantities of nano structured tungsten carbide/cobalt powders (figure 1.5). Spray conversion processing allows the tungsten and cobalt to be mixed at the molecular level, which yields true nano structured material - tungsten carbide grains that are smaller than 50 nm.

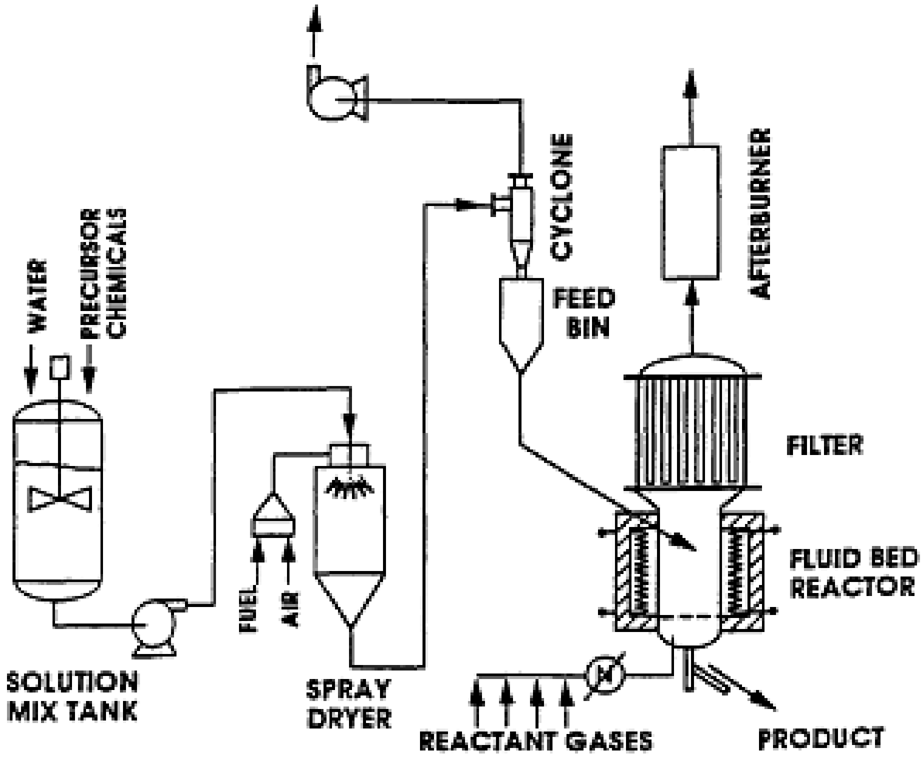

Figure 1.5: Schematic of spray conversion process [24].

The molecular mixing is accomplished by aqueous solution-phase reactions between suitable precursors, such as ammonium metatungstate $[(NH4)_6 (H_2W_{12}O_{40}).4H_2O]$ + cobalt chloride $[CoCl_2.nH_2O]$, or tris-ethylene diamine cobalt tungstate

[Co(en)$_3$WO$_4$+H$_2$WO$_4$]. The solution is spray-dried to give extremely fine mixtures of tungsten and cobalt salts. This precursor powder is reduced and carbonized in a fluidized-bed reactor to yield nano phase cobalt/tungsten carbide powder. The spray conversion process has been shown schematically, as in figure 1.5 [23-25].

1.7.2 Mechanical alloying

Mechanical alloying (MA) is a solid-state powder processing technique involving repeated welding, fracturing and re-welding of powder particles in a high-energy ball mill [26]. MA is capable of synthesizing a variety of equilibrium and non-equilibrium alloy phases starting from blended elemental or pre-alloyed powders. The non-equilibrium phases synthesized include supersaturated solid solutions, metastable crystalline, quasi-crystalline phases, nanostructures and amorphous alloys. Recent advances in these areas and also on disordering of ordered intermetallics and mechano-chemical synthesis of materials have been critically reviewed after discussing the process and process variables involved in MA. The often vexing problem of powder contamination has been analyzed and methods have been suggested to avoid/minimize it. The advantage of using MA for the synthesis of nano crystalline materials lies in its ability to produce bulk quantities of material in the solid state using simple equipment at room temperature. Nano structured material synthesis using MA was first reported by Thompson and Politis in 1987 [27], even though the specific mention of formation of “nanometer order crystalline structures produced by mechanical alloying” was by Shingu et al. [28]. Koch et al. [29] has summarized the results on the synthesis and structure of nano crystalline structures produced by mechanical attrition [30]. Grain sizes with nanometer dimensions have been observed in almost all mechanically alloyed pure metals, intermetallics and alloys (if they continue to be crystalline) (figure 1.6).

Thus, it appears to be a ubiquitous phenomenon. In spite of this, there have not been many investigations to explain why and how the nanometer- sized grains are obtained in these materials. Hellstern et al. [31] have described the mechanism of formation of nanostructures by MA/ Mechanical milling (MM).

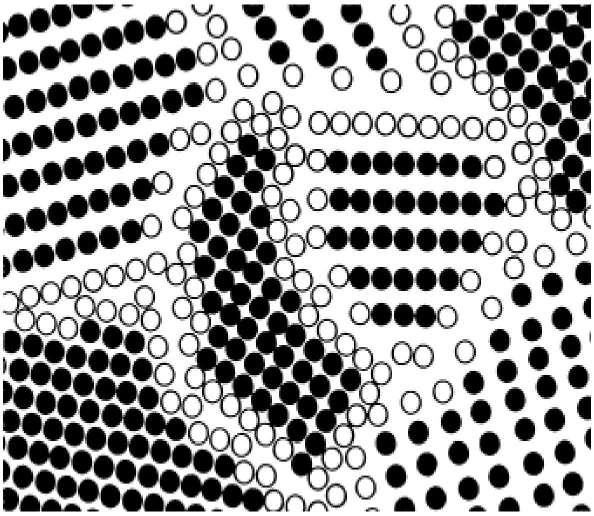

Figure 1.6: Schematic arrangement of atoms in an equiaxed nano crystalline metal.

From high-resolution TEM observations, these authors reported that at the early stages of MA, shear bands were observed due to the high deformation rates experienced during MA. These shear bands, which contain a high dislocation density, have a typical width of approximately 0.5±1.0 μm. With continued milling, the average atomic level strain increases due to the increasing dislocation density and at a certain dislocation density within these heavily strained regions, the crystal disintegrates into subgrains that are separated by low-angle grain boundaries. This results in a decrease of the lattice strain. On further processing, deformation occurs in shear bands located in previously unstrained parts of the material. The grain size decreases steadily and the shear bands coalesce. The small angle boundaries are replaced by higher angle grain boundaries, implying grain rotation, as reflected by the absence of texture in the electron diffraction patterns and random orientation of the grains observed from the lattice fringes in the high-resolution electron micrographs. Consequently, dislocation-free nanocrystalline grains are formed. Li et al. [32] have also proposed a model for the refinement of grain size during ball milling and noted that the grain size in the early stages of milling follows the relation:

$$d = Kt^{\frac{-2}{s}} \tag{1.1}$$

where d is the grain size, t is the time and K is a constant. The minimum grain size achievable by milling is determined by the competition between the plastic deformation via dislocation motion and the recovery and recrystallization behavior of the materials [33-34]. This balance gives a lower limit for the grain size (d_{min}) of pure metals and alloys. The d_{min} value obtained by MM was found to vary inversely with the melting point of Al, Ag, Cu and Ni (all having an fcc structure) [33] and directly with the stacking fault energy. However, when data from the bcc and hcp metals as well as several intermetallics are included, only fcc metals (with a relatively low melting point) showed this clear inverse dependence of minimum grain size on the melting point [29-30]. The d_{min} value was virtually independent of the melting point for the hcp, bcc and other fcc metals with high melting points, collectively it appears that d_{min} is in the order: fcc < bcc < hcp. Since, a number of process variables (method to estimate the grain size, milling intensity, milling temperature, alloying effects, contamination, etc.) can influence the minimum grain size achieved; systematic investigations are required before proper explanations can be offered for these variations. Several nano composites have also been synthesized by MA. Nano composites have also been obtained when the amorphous phases obtained by MA/MM are crystallized at relatively low temperatures

[35]. An important attribute of these nano composites is in preventing or minimizing grain growth till very high temperatures. Reinforcement of Cu and Mg with Al_2O_3 was reported to prevent grain growth up to the melting point of the metals [36]. Alloys in the nano crystalline form have also been shown to have much higher hydrogen sorption properties at low temperature than their polycrystalline coarse-grained counterparts. Also these materials are insensitive to air exposure [37].

1.7.3 Chemical vapor reaction

In general, the chemical vapor synthesis of WC–Co materials involves the reduction of a tungsten salt precursor with hydrogen and carburization with a hydrocarbon gas. If tungsten chloride is used as the precursor and the methane and hydrogen gases are used as the reducing agent and carbon source, the reaction equation is as follows:

$$WCl_6 + H_2 + CH_4 \rightarrow WC + 6HCl \qquad (1.2)$$

The free energy of the above reaction in the temperature range 800 – 1200 ºC is - 469 to - 630 kJ. In general, vapor phase reactions create a supersaturated vapor state which is thermodynamically less stable than the formation of the solid materials in nano powder form. It includes chemical super-saturation in which it is thermodynamically favorable for the vapor phase molecules to react chemically to form a condensed phase rather than stay in the vapor form. Vapor phase reactions offer the advantages of synthesizing high purity nano powders with good control over size, shape and crystal structure as well as easy control of reaction rate [38-39]. Several articles have been reported on the synthesis of nano sized tungsten carbide powder by vapor phase reactions which are discussed later.

1.8 Consolidation of Nano structured WC-Co composites

The traditional method of consolidating conventional WC-Co powders is by cold compaction, followed by liquid phase sintering at about 1400°C in vacuum, i.e. just above the WC-Co pseudo-binary eutectic temperature, 1320°C [23]. In general, sintering time measured in h are needed to achieve theoretical densities in high WC volume fraction alloys. Sintered conventional WC-Co materials must have greater than 99.9% relative density to have any prospects for industrial applications. The sintering temperature of a material decreases with the reduction of the particle sizes. This is especially true for nano sized powders including nano sized WC–Co powders. The experimental results showed that under similar condition of temperature and pressure different grain sizes leads to different percentage of densification. Grain sizes <0.3 µm, leads to 85% of densification, grain sizes < 0.7 µm leads to 70% of densification of WC–Co, which suggests that sintering is a function of the grain size [38]. Sintering of nano crystalline WC–Co leads to agglomeration of nano particles. True nano crystalline (<100 nm) WC–Co materials have not been consistently produced to date [39]. The need to fully densify the material and limit grain growth at the same time causes adverse considerations in process design. Many sintering techniques other than the traditional liquid phase sintering (LPS) have also been used as an attempt to get true nano crystalline WC-Co composites. These processes are discussed in details in chapter 2. Sintered grain sizes between 0.1 to 0.8 µm are currently manufactured commercially by using conventional ultrafine tungsten carbide powders.

1.9 Applications of WC-Co composites

Carbide cutting surfaces are often useful when machining through materials such as carbon steel or stainless steel. These are most suitable where other tools would wear away, such as in high-quantity production runs. Most of the time, carbide will leave a better finish on the part and allow faster machining. Most modern face mills use carbide inserts, as well as some lathe tools and end mills. To increase the life of carbide tools, they are sometimes coated. Four such coatings are TiN (titanium nitride), TiC (titanium carbide), Ti(C)N (titanium carbide-nitride) and TiAlN (titanium aluminum nitride). Most coatings generally increase the tool's hardness and/or lubricity. A coating allows the cutting edge of a tool to cleanly pass through the material without having the material stick to it. The coating also helps to decrease the temperature associated with the cutting process and increase the life of the tool.

1.9.1 Military

Tungsten carbide is often used in armor-piercing ammunition, especially where depleted uranium is not available or not politically acceptable. The first use of tungsten carbide projectiles occurred in Luftwaffe tank-hunter squadrons, which used 37 mm auto cannon equipped Ju-87G Stuka attack planes to destroy Soviet T-34 tanks. It is also used for making machine tools and small numbers of projectiles for the most elite combat pilots, like Hans Rudel. It is an effective penetrator due to its high hardness value combined with a very high density.

Tungsten carbide ammunition can be of the sabot type (a large arrow surrounded by a discarding push cylinder) or a subcaliber ammunition, where copper or other relatively soft material is used to encase the hard penetrating core, the two parts being separated only on impact as shown in figure 1.7. The latter is more common in small-caliber arms, while sabots are usually reserved for artillery use.

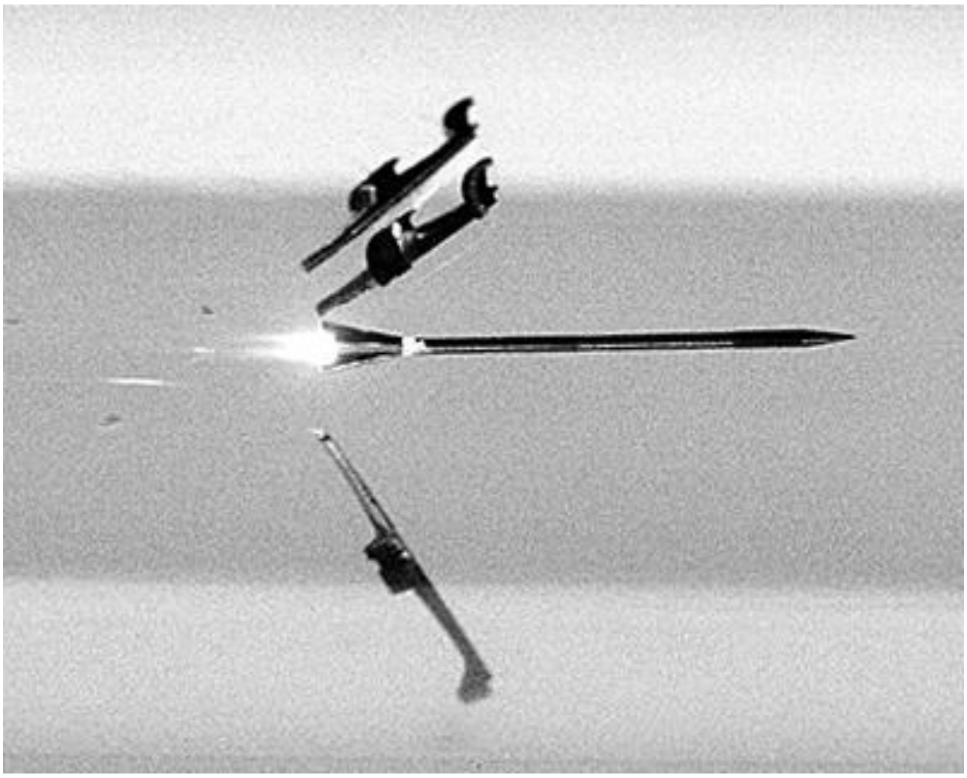

Figure 1.7: Sabot separating from missile.

Tungsten carbide is also an effective neutron reflector and as such was used during early investigations into nuclear chain reactions, particularly for weapons.

1.9.2 Sports

Hard carbides, especially tungsten carbide, are used by athletes, generally on poles which impact hard surfaces. Trekking poles, used by many hikers for balance and to reduce pressure on leg joints, generally use carbide tips in order to gain traction when placed on hard surfaces (like rock); such carbide tips last much longer than other types of tips. Sharpened carbide tipped spikes (known as studs) can be inserted into the drive tracks of snowmobiles. These studs enhance traction on icy surfaces. Some tire manufacturers, such as Nokian and Schwalbe, offer bicycle tires with tungsten carbide studs for better traction on ice. These are generally preferred over steel studs because of their wear resistance.

1.9.3 Domestic

Tungsten carbide is used as the rotating ball in the tips of ballpoint pens to disperse ink during writing. Tungsten carbide can now be found in the inventory of some jewelers, most notably as the primary material in men's wedding bands. When used in this application the bands appear with a lustrous dark hue often buffed to a mirror finish. The finish is highly resistant to scratches and scuffs, holding its mirror-like shine for years. Many manufacturers of this emerging jewelry materials state that the use of a cobalt binder may cause unwanted reactions between the cobalt and the natural oils on human skin. Skin oils cause the cobalt to leach from the material. This is said to cause possible irritation of the skin and permanent staining of the jewelry itself. Many manufacturers now advertise that their jewelry is "cobalt free". This is achieved by replacing the cobalt with nickel as a binder.

1.9.4 Energy

The polymer exchange membrane fuel cell (PEMFC) is one of the most promising fuel cell technologies. This type of fuel cell will probably end up powering cars, buses and may be even in houses. The PEMFC uses one of the simplest reactions of any fuel cell. There are four basic elements of a PEMFC: the anode, the negative post of the fuel cell, the cathode, the positive post of the fuel cell, the electrolyte (proton exchange membrane) and the catalyst (special material that facilitates the reaction of oxygen and hydrogen) (figure 1.8). Catalyst is usually made of platinum nano particles very thinly coated onto carbon paper or cloth.

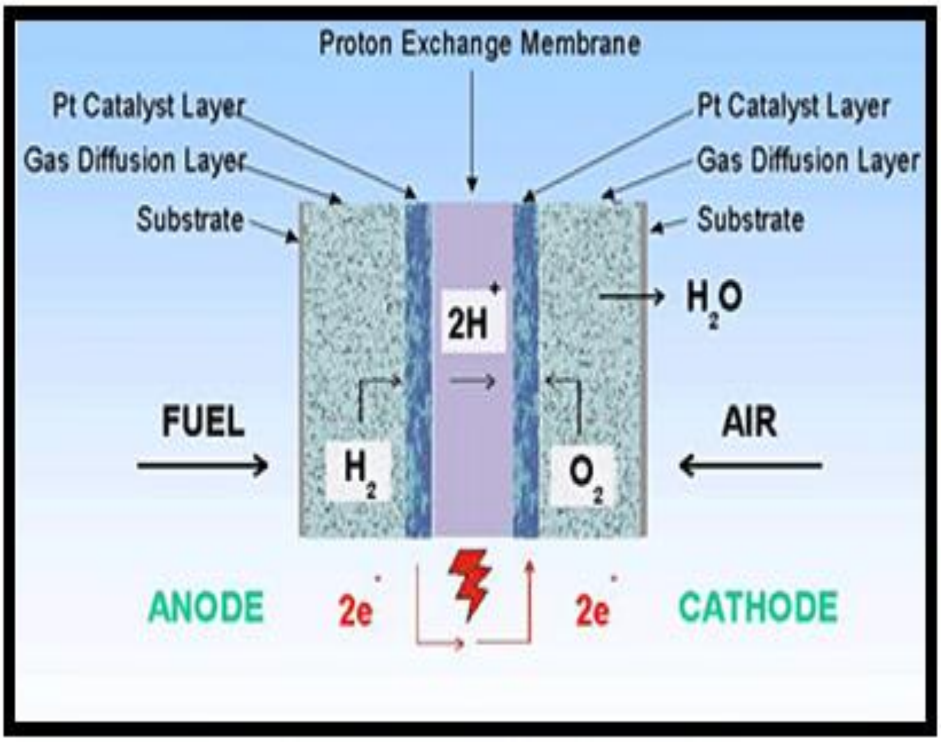

Figure 1.8: The parts of a PEM fuel cell [40].

The catalyst is rough and porous so that the maximum surface area of the platinum can be exposed to the hydrogen or oxygen. The platinum-coated side of the catalyst faces the PEM. Now a days WC nano particles are replacement of platinum nano particle because of its less cost and less catalytic poisoning.

References

[1] Y. Brechet, D. Bassetti, D. Landru and L. Salvo, Progress in Materials Science, 46 (2001) 407-428.

[2] Mike Finnis, Progress in Materials Science, 49 (2004) 1-18.

[3] S. Mahajan, Progress in Materials Science, 49 (2004) 487-509.

[4] Geoffrey E. Sprigges, Int. J. Refract. Met. Hard Mater, 13 (1995) 241-255.

[5] H. Gleiter, Progress in Materials Science, 33 (4) (1989) 223-315.

[6] K. Jia, T.E. Fischer and B. Gallois, Nanostruct. Mater, 10 (5) (1998) 875-891.

[7] C.S. Pande, K.P. Cooper, Progress in Materials Science, 54 (2009) 689-706.

[8] A. Upadhyaya, Metal Powder Report, 55(10) 2000 36-38.

[9] T.S. Sudarshan, Metal Powder Reports, 53 (2) (1998) 32-36.

[10] T. B. Massalski (Ed.), ASM Int., Materials Park, Ohio, Vol. (1-2) (1990).

[11] R. Telle, M. V. Swain (Ed.), Structure and Properties of Ceramics, Vol. 11, VCH, New York, (1994).

[12] Krawitz, D. Aaron, G. Reichel, Daniel, Hitterman, Richard, Journal of the American Ceramic Society, 72 (1989) 515-517.

[13] A. Cottrell, Chemical Bonding in Transition Metal Carbides, Institute of Materials, London, (1995).

[14] K.K. Chawla, Composite materials science and engineering, Springer (1998).

[15] J. Gurland and J. D. Knox, Tungsten Refract. Met. 3-1995, Proc. Int. Conf., 3rd 1995 (Pub. 1996), 219-228.

[16] K. Schrter, US Patent 1,549,615, 1925.

[17] A. E. McHale, Phase Equilibria Diagrams-Phase Diagrams for Ceramists, Vol. 10, American Ceramic Society, (Figure 8969), (1994).

[18] ASM, Engineered Materials Reference Book, ASM International, (1989) 182.

[19] H. J. Scussel, Friction and Wear of Cemented Carbides, ASM Handbook, 18, (1992) 796.

[20] Anisa Mnyusiwalla, Abdallah S Daar and Peter A Singer, Nanotechnology, 14 (2003) R9–R13.

[21] G. Cao, Nanostructures and nanomaterials, synthesis properties and applications, Imperical College Press, (2003).

[22] L.E. McCandllsh, B.H. Kear and B.K. Kim, Nanostructured Materials, 1 (1992) 119-124.

[23] B.H. Kear and L.E. McCandlish, Nanostructured Materials, 3 (1993) 19-30.

[24] L.E. McCandlish, B. H. Kear, J. Bhatia, U.S. patent no. 5,352,269 (1994).

[25] C. Suryanarayana, Progress in Materials Science, 46 (2001) 1-184.

[26] J.R. Thompson, C. Politis Europhys Lett, 3 (1987):199-205.

[27] P.H. Shingu, B. Huang, S.R. Nishitani, S. Nasu, Trans Japan Inst Metals 29 (1988) 3-10.

[28] C.C. Koch, Nanostructured Mater, 2 (1993) 109-129.

[29] C.C. Koch, Nanostructured Mater, 9 (1997) 13-22.

[30] E. Hellstern, H.J. Fecht, C. Garland, W.L. Johnson In: McCandlish LE, Polk DE, Siegel RW, Kear BH, editors. Multicomponent ultrafine microstructures, vol. 132. Pittsburgh, PA: Mater. Res Soc, (1989) 137-142.

[31] S. Li, K. Wang, L. Sun, Z. Wang, Scripta Metall Mater, 27 (1992) 437-442.

[32] J. Eckert, J.C. Holzer, C.E. Krill III, W.L. Johnson, J Mater Res, 7 (1992) 1751-1761.

[33] I. BoÈ rner, J. Eckert, Mater Sci Forum, 225-227 (1996) 377-382.

[34] C. Suryanarayana, F.H. Froes, Nanostructured Mater, 3 (1993) 147-153.

[35] J. Naser, W. Reinhemann, H. Ferkel, Mater Sci and Engg A, 234 (1997) 467-469.

[36] L. Zaluski, A. Zaluska, P. Tessier, J.O. StroÈ m-Olsen, R. Schulz, Mater Sci Forum, 225- 227 (1996) 853-858.

[37] Z. Zak Fang, Xu Wang, TaegongRyu, Kyu Sup Hwang, H.Y. Sohn, Int. Journal of Refractory Metals & Hard Materials, 27 (2009) 288–299.

[38] Kim BK, Ha GG, Woo Y. US patent 6511551; 2003.

[39] Gemma Crawley, Fuel Cell Today, (2006) 1-12.

Chapter 2

LITERATURE REVIEW

Overview

In this chapter the earlier reported work on nano tungsten carbide (WC) processing and properties is reviewed. The literature review is divided in three parts; the first part summarizes different methods of synthesis of nano sized powder including both monolithic WC and composite WC–Co powders. The second part deals with the sintering and consolidation of the nano sized powders. It emphasizes the challenges and the progress toward achieving nano scale grain sizes. Moreover, the limitations of the retention of nano size even in samples sintered at high temperature which is key criteria of present work is also described in the third part.

2 Synthesis of Tungsten Carbide nano particles

Since the discovery of Tungsten Carbide (WC) in 1898 [1] efforts have been made to exploit the exceptional hardness of this powder metallurgy product. Sintered carbide (1914) and cemented carbide (1923) were the major milestones of this journey. Two decades ago when nanotechnology was started, metallurgist tried to implement it to one of their oldest powder metallurgy product i.e. WC [2-3]. Numerous techniques have been developed to produce nano structured WC and WC–Co powders, only a few have been proven at the industrial level. Production challenges include powder properties and process- ability and economic considerations [4]. The synthesis techniques cover a diverse array of processes as is evident from the discussion below.

2.1 Spray Conversion process

This process was first introduced in the early 1990's. The success of the process is evident from the fact that it is used to produce the powders at an industrial level. It is a simple three-step process. It comprises of heating non-elemental tungsten containing material in a flowing atmosphere containing molecular hydrogen and molecular methane. Sufficient time is provided for complete conversion of the material to mono tungsten carbide. The dissolution of soluble salts of tungsten, cobalt and other additives allows uniform mixing at the molecular level. This phase uniformity is maintained in the spray drying process helps to get large, porous and flow able precursor powder [5-6]. **McCandlish et al**. [7] used trls (ethylenediamlne) cobalt tungstate, $Co(en)_3WO_4$, which after reduction and carburization yields WC-23 wt% Co. Other compositions (i.e. W/Co ratios) was also obtained from aqueous solution mixtures, such as $Co(en)_3WO_4$ + H_2WO_4 or AMT + $CoCl_2$ (where AMT-$(NH_4)_6(H_2W_{I2}O_{40}).4H_2O$). These solutions, upon atomization and rapid drying, precipitate as homogeneous powders with amorphous or microcrystalline structures, which were suitable precursors for subsequent thermo-chemical processing to the desired nano structured WC-Co powder. Spray dried powders had been used to produce WC-Co powders with from 3-30 wt% Co.

Wahlberg et al. [8] synthesized WC powders using three different routes depending on the starting materials used; (i) Direct polymerisation of sodium tungstate (Na_2WO4), (ii) Polymerization of an ammonium tungstate solution ($(NH_4)_2WO_4$ (aq)) prepared by converting a sodium tungstate solution (Na_2WO_4 (aq)) by ion exchange and (iii) Partial de-polymerisation of ammonium metatungstate ($(NH_4)_6[H_2W_{12}O_{40}]$). The complex was synthesized by the reaction of the tungstate salt and Co^{2+} at a pH around neutral and a temperature of 90-100 °C. The ammonium salt, $(NH_4)_8[H_2Co_2W_{11}O_{40}] \bullet xH_2O$, was obtained after the addition of ammonium acetate (NH4Ac). The powder obtained using route (i), contained appreciable amounts of sodium, also after re-crystallization. In Routes (ii) and (iii), an insoluble cobalt tungstate powder (pink/grey in color) was formed as a second product. Samples from routes (i) and (iii) were reduced under H_2 at 750 °C and carburized under H_2/CH_4 mixture at 1000 °C. Sintering tests were carried out at 1410 °C, after additions of 0.4% of VC. The powders after reduction and carburization have a particle size of 70-300 nm.

Gao et al. [9] have reported a direct gas phase process to produce nano grained WC from the tungsten precursor ammonium metatungstate. The kinetics of carburization and reduction reactions was controlled to permit simultaneous reduction and carburization. The kinetics was controlled by reacting a reduction carburization gas mixture, preferably hydrogen and carbon monoxide by slowly increasing the reaction temperature. This slow increase in temperature prevented the formation of undesirable W_2C which in turn interferes with the reaction efficiency. In this process the carbide formation is possible at low temperatures through a substitution of carbon for oxygen in the matrix. The authors also demonstrated a recycling process in which spent carbide tools of various compositions and grain sizes were recycled into nanostructured WC–Co composite powders. The scrap material is oxidized and acid leached to remove impurities and any binder material. This is then dissolved in a mixture of sodium hydroxide and spray dried to form precursor powder compound. Citric acid is used as carbon source; the powder formed after spray drying is calcined and carburized to form nano structured WC [10].

Kim et al. [11] modified the process by introducing mechanical milling. The milled powder was then converted to nano phase composite powder by gas phase reduction and carburization treatment of the spray dried powders that contain added carbon to assist in the carburization phase. The abnormal grain growth during sintering is controlled by adding water soluble salt of V, Ta or Cr which acted as grain growth inhibitors and helped in uniform distribution of the phases [12].

Zhang et al. [13] also varied the spray conversion process; it involved the co-precipitation of cobalt with salts of tungsten such as ammonium paratungstate. The hard metal constituents were mixed at the atomic level, followed by hydrogen reduction. An average particle size of 20–50 nm powders was prepared.

2.2 Ball milling and mechano-chemical synthesis

Nano crystalline materials have been synthesized by a number of techniques, but the advantage of using ball milling for the synthesis of nano crystalline materials lies in its ability to produce bulk quantities of material in the solid state using simple equipment and at room temperature. The first report of formation of a nano structured material synthesized by ball milling is by Thompson and Politis in 1987 [14]. This straight forward method was also used for producing nano sized WC powders/ WC-Co nano composites.

Xueming et al. [15] synthesized WC –Co composite using pure tungsten, graphite and cobalt powders with particle size smaller than 75 μm. The powder mixtures were milled for 10, 20, 50 and 100 hrs using WC balls (10 mm in diameter) and the ratio of ball-to-powder was 30:1. Fifty hrs milling transformed W particles to WC with average grain size of 14.2 nm. Further milling resulted in the reduction of particles size to 11.3 nm. Lower milling time only reduced the particle size of the reactant but the transformation was not observed.

Sherif El-Eskandarany et al. [16] synthesized nano crystalline WC powders by high energy ball milling of high purity elemental W and C elemental powders. After 82 hrs of milling, complete transformation of W to single phase hcp-WC was occurred. Increasing the milling time to 120 hrs leads to grain refinement and the end-product powder of this process consisted of nano crystalline grains of less than 5 nm in diameter.

Zhang et al. [17] used pure WC (99.8%) with mean particle size of 5.6 μm and Co (99%) with particle size of 1.0 μm as starting materials. Powder mixtures of WC– 10% wt. Co mixed with ethanol was sealed in WC–Co hard metal vial with WC–Co hard metal balls (8 and 12 mm in diameter and 50–50 in wt%, respectively) in a glove box containing inert atmosphere of Ar. The ball to powder weight ratio is controlled to be 15:1. After 10 hrs of milling, at 250 rpm, the grain size of WC is reduced to 11 nm, a severe internal strain is introduced and fcc-cobalt has transformed into hcp-cobalt by a mechanical induced allotropic transformation.

High energy milling has indeed been shown to be capable of producing nano scale WC and WC–Co nano composites. Various milling techniques can be used including attrition mills [18] and planetary mills [19].

Porat et al. [20] synthesized WC-Co composite powder by ball mill. The authors did a comparative study with the WC particles synthesized by spray conversion. The grain size of WC after milling for over 100 hrs can be as fine as 10–20 nm. The milled powder reaches full density at a temperature lower than the liquidus, while spray converted powder has to be sintered in the liquid phase to reach full density. The best combination of hardness and tensile rupture strength is achieved for spray converted powder. Mechanical milling techniques are versatile for forming nano structured materials but, long processing time leads contamination and high energy expenditures are the main disadvantages which forced to find other techniques or by optimizing the variables of the milling process [14-20].

Butler et al. [21] reported the production of WC–Co powders with 10-20 nm grain sizes from 0.8 μm sized powders in approximately 10 hrs milling time. Revolution of the mill canister generated an acceleration field that was nearly 60 times the force of gravity. This field was responsible for this unique high efficiency. Chemical reaction can also be induced using mechanical milling process, which is then termed as the mechano-chemical synthesis.

Tan et al. [22] modified the classical high energy milling process by using magnesium containing graphite mixtures. The graphite powder acted as the carbon source for carbide formation while the magnesium acted as reducing agent for reactive synthesis. Acid dissolution removed magnesium and the final powder contained 4-20 nm sized tungsten carbide.

Ban et al. [23] used other approach, termed integrated mechanical and thermal activation (IMTA) process. The starting materials for preparing the powder mixture were tungsten trioxide (WO_3) powder, graphite powder and cobalt oxide (CoO) powder. The powder mixture prepared contained WO_3, C and CoO with a molar ratio of 1.0:2.4:0.7. This powder mixture was high energy ball milled for different times in argon. The mechanically activated (high energy ball milled) powder was subsequently subjected to thermal activation. Thermal activation was carried out by heating the milled powder at 650 ºC for 2 hrs in a gas mixture of H_2 and Ar, followed by ramping to 1000 ºC and holding at this temperature for 2 h in pure argon in order to form a final product of nano structured WC + 18 wt% Co + 5.3 wt% C.

Kwon et al. [24] used activated tungsten powder and soot mixtures in a planetary mill with an acceleration of 60 ms^{-2} for 5–30 min. The balls to powder weight ratio was 30:1. After that the mixture was loaded into the vial which is then evacuated to a constant pressure of 10^{-2} Torr. After that the vial was filled with argon at a pressure of 2280 Torr. The activated mixture was taken out of the drum in an argon atmosphere. The mixture was annealed in vacuum at a pressure of 10^{-2} Torr at 650-820 °C for 0.5–2.0 h to get the final product.

Temuujin et al. [25] used wolframite ore, $FeWO_4$ (WO_3: 71.85, Fe_2O_3: 20.36, MnO_2: 5.46 and SiO_2: 1.1 wt%). The ore was ball milled prior to formulating the mixture in order to reduce the particle size to 10-mm regime. Active carbon with average particle size of 35 nm was used as carbon source. Powders were loaded in air in a planetary ball mill. The weight ratio of balls to powder was fixed at 50:1. Mixtures ground for 30 min or 2 hrs and the resultant powders were uniaxially compressed into pellets. The pellets were calcined in a tube furnace by heating at a constant rate, 20 ºC/min, up to 900 ºC or

1100 ºC under flowing Ar gas for 1 h. The well-crystallized WC contained only a small fraction of impurities, i.e., Fe_3W_3C, Fe_7W_6, W, Fe_3C and Fe. The results showed that milling for 2 hrs was sufficient for full conversion to WC at temperatures as low as 1100 ºC. The authors also studied the Mechano-chemical activation of mixtures of wolframite (FeWO4) with carbon, by ^{57}Fe Mossbauer spectroscopy [26]. The results showed that the mechano-chemically induced reactions are essentially independent of the nature of the carbon used as the starting material.

Qiao et al. [27] used mechanical alloying technique for the synthesis of WC based composite with Al and cobalt ($(W_{0.5}Al_{0.5})C_{0.8}$–Co). Elemental powders of tungsten, aluminum, cobalt and carbon were used as raw materials. The $(W_{0.5}Al_{0.5})C_{0.8}$–Co powders with different cobalt contents (8.7, 11.9 and 15.2 wt%) were prepared by mechanical alloying and solid state reaction. The $(W_{0.5}Al_{0.5})C_{0.8}$ powders were enclosed in graphite die under argon atmosphere and then were sintered in an inductive hot-pressing vacuum furnace from room temperature to sintering temperature (1350-1450 ºC). This new material has excellent thermal stability, superior mechanical properties.

Enayati et al. [28] used two routes; ball milling and mechanical alloying to synthesize nano structures WC. WC- 17 wt% Co powder was ball milled for different time duration (2,5,10 and 40 hrs). It was observed that nano crystalline WC phase can be obtained by ball milling of preformed WC-17 wt.% Co powder although an undesirable phase was formed upon subsequent annealing. Results of mechanical alloying of W–Co–C powder showed that, it was not possible to produce WC compound by mechanical alloying of W–Co–C powder mixture. However, during mechanical alloying of W–C powder mixture elemental tungsten and graphite reacted to form nano crystalline WC phase.

Zakeri et al. [29] synthesized WC based WC-Al composite by mechanical alloying. The experiment was performed in a planetary ball mill at 500 rpm. Pure Al, graphite and WO_3 powders were mixed to give the desired Al_2O_3(34)–WC(66) wt% composition. The mixture of the powders and the steel balls was charged into a steel vial (150 ml) in Ar atmosphere.

2.3. Chemical reaction synthesis

Chemical reaction synthesis of WC–Co materials involves the reduction of a tungsten salt precursor with hydrogen and carburization with a hydrocarbon gas. These types of reactions are vapor phase reactions in which a supersaturated vapor phase is formed which is thermodynamically less stable than the formation of the solid material in nano powder form. The chemical super saturation is thermodynamically favorable for the vapor phase molecules to react chemically to form a condensed phase rather than stay in the vapor form [4,30]. High purity nano powders can be synthesized using this technique with precise control of reaction rate.

Hojo et al. [31] synthesized WC phase by reduction of tungsten hexachloride (WCl_6) with hydrogen and carburization with methane. Temperature affected the size of the particles. For a relatively low temperature of 400 ºC the particle size was about 40–50 nm. As the temperature is increased to 1000 ºC the particles agglomerated causing an increased size of 80–110 nm. It was also concluded that for complete conversion of W to WC, temperature above 1400 ºC and excess amount of methane were required.

Fitzsimmons et al. [32] performed thermodynamic equilibrium calculations at a varying partial pressure of WCl_6-CH_4-H_2 and WF_6-CH_4-H_2. These calculations were then used to construct chemical vapor phase diagrams. The results indicated that for

WF_6 and WCl_6 systems the phase transformation from W to WC occurred at a lower partial pressure of CH_4 with decreasing total pressure. The partial pressure of CH_4 needed to produce WC is lower for WF_6 than WCl_6.

Wanner et al. [33] synthesized WC particles using WCl_6 as starting material through the intermediate tungsten complex W(2,2'-bipyridine)Cl_4 formation. The thermal decomposition under inert gas of the tungsten complex W(2,2'-bipyridine)Cl_4 and further activation under hydrogen gave tungsten carbide. The synthesis of the complexes was performed in very strict conditions under an inert atmosphere without even trace amounts of water or oxygen.

Medeiros et al. [34] also attempted to synthesize reduced sized WC particles. It was based on a gas–solid reaction between a W source and a C-containing gas. The gas phase was a mixture of H_2 and CH_4. Ammonium paratungstate and tungsten blue oxides were used as the tungsten source. The higher reactivity of the precursor material and the better contact between the gas–solid reactants explained the lower temperatures and higher reaction rates of this method compared to the conventional one. In this process very fine WC crystallites ($< 1\mu m$) can be produced but the particle size, shape and porosity depend on the precursor type and its particle size.

Zhang et al. [35] thermo-chemically decomposed cobalt doped ammonium paratungstate precursor to obtain nano structured WC particles. The precursor was prepared by co-precipitation from cobalt(II) hydroxide and ammonium paratungstate. Different decomposition behavior was observed when the calcination was carried out at medium temperature in flowing and non-flowing air. Nano structured powders with particle size of around 90 nm were obtained after calcination.

Kim et al. [36] synthesized nano sized tungsten carbide powder by the chemical vapor condensation process using tungsten hexacarbonyl ($W(CO)_6$) precursor. The precursor was decomposed into W and 6(CO) at 120 ºC. The loose agglomerated WC_{1-x} powders, which had a rounded cubic shape, were synthesized by carburization with carbon from the dissociation of CO gas in the temperature range of 600–800 ºC. Grain size was decreased from 53 to 28 nm with increasing reaction temperature. In vacuum, the grain size decreased drastically to 4 nm because of the reduced residence time of the vapor molecule in the reaction chamber.

Tang et al. [37] synthesized nano sized tungsten carbide powder by the vapor phase reaction of WCl_6–C_3H_8– H_2 mixtures in a tube reactor. Here C_3H_8 was used as carbon source and the operating temperature was above 1400 ºC to get fully carburized WC phase. It was also described that a post-treatment of produced powder by hydrogen, in which excess carbon of 9.2 wt.% in the product was fully removed after 1 h of treatment time at 1000 ºC.

Won et al. [38] also synthesized nano sized tungsten carbide powder by the vapor phase reaction of WCl_6–C_2H_2–H_2 mixtures in a horizontal tube reactor. The product in this case was a mixture of WC and W_2C. It was observed that the particle size of product increased with an increase in H_2 flow rate and the WCl_6 volatilizer temperature. The temperature had also affected the particle size. It increased with an increase in reaction temperature between 1000 and 1100 ºC but it decreased with temperature between 1100 and 1200 ºC. Particle obtained from this work varied from 100 nm to 1 μm in sizes.

Guo et al. [39] prepared tungsten carbide nano crystal by the simple reaction of WO_3, Mg and anhydrous CH_3CH_2OH in an autoclave at 600 ºC. In a typical experimental procedure, appropriate amounts of WO_3, Mg and anhydrous CH_3CH_2OH were put into a stainless steel autoclave. Then, the autoclave was sealed and put into an electronic furnace at 100 ºC, the temperature of the furnace was increased to 600 ºC in 50 min and maintained at 600 ºC for 15 hrs. Then, it was allowed to cool down to room temperature. The dark solid powders was collected and washed by diluted HCl to remove unreacted Mg powder. There were two types of tungsten carbide in the samples; one was pure WC and the other was wrapped by carbon. The diameters of WC nano crystals ranged from 100 to 200 nm.

Keller et al. [40] synthesized one-dimensional tungsten carbide-CNT nano structured material. The synthesis of the tungsten carbide was performed via two successive steps. First, deposition of tungsten, corresponding to 40 wt% of WO_3 relative to the CNT support, was performed by wet impregnation of the bare CNTs with an aqueous solution of ammonium paratungstatepentahydrate, $(NH_4)_{10}W_{12}O_{41}\cdot 5H_2O$. The CNTs were added to the precursor aqueous salt solution and stirred vigorously at 80 °C for 20 min, before the slow evaporation of the solvent at room temperature. The resulting material was further dried overnight at 120 °C and finally calcinated at 350 °C for 2 hrs. The carburization of WO_3 by the CNTs seemed to occur under dynamic vacuum at temperatures ranging between 1000 and 1300 °C to give one dimensional tungsten carbide in 7 to 30 hrs reaction durations.

Sohn et al. [41] used chemical vapor synthesis (CVS) process for the production of WC–Co nano composite powder. In this process tungsten hexachloride and cobalt chloride were used as the precursors. Hydrogen and methane were used as reducing and carburizing agents, respectively. The experimentation included a continuous feeding system to introduce the precursors into the reactor, which would be advantageous in an industrial application. It was observed that the formation of WC is highly dependent on the reaction temperature as well as methane concentration. When the reaction temperature or the methane concentration was not sufficiently high, W_2C or even W was formed instead of WC. When the concentration and temperature were appropriate, it was possible to prepare fine particles less than 30 nm. The limitation of the process was the difficulty in controlling excess carbon content in the produced powder which was then reduced by the post-treatment of produced powder using hydrogen.

Zheng et al. [42] synthesized nano-crystalline tungsten carbide thin films on pure flake Ni and foam Ni substrates by plasma enhanced chemical vapor deposition. WF_6, CH_4 and H_2 were used as precursors and Ar as carrier gas. The pure flake Ni and foam Ni substrates were cleaned in acetone by ultrasonic and then were dried in hot wind. Before deposition, the system was flushed with H_2 for 30 min at 800 ºC to remove the oxide on the surface of the substrates. After deposition, the films were annealed at N_2 atmosphere in deposition chamber. The components of the films were WC and W_2C. The film was composed of the rounded grains of about 10 nm in diameter. A vertical growth direction and columnar structure has been found.

Yoshinori et al. [43] synthesized WC and its precursors by reacting WO_3 with flowing NH_3, or H_2S or C_2H_5/H_2 or CH_4/H_2 mixtures. For preparation of WC, WO_3 powder was loaded into a quartz tube reactor of 3 × 50 cm in diameter and length respectively. The carburizing atmosphere consists of 20% CH_4 and 80% H_2. A total flow rate of 70 ml/min passed through the reactor, which was controlled by mass flow controllers. W_2N was obtained by temperature-programmed nitridation of WO_3 in flowing NH_3, which was converted to WC by carburization instead of WO_3 as described above. WS_2 was synthesized by reacting WO_3 with H_2S at 1023 K, which was followed by carburization in a way similar to that for W_2N. WP was also synthesized by similar procedure (figure 2.1).

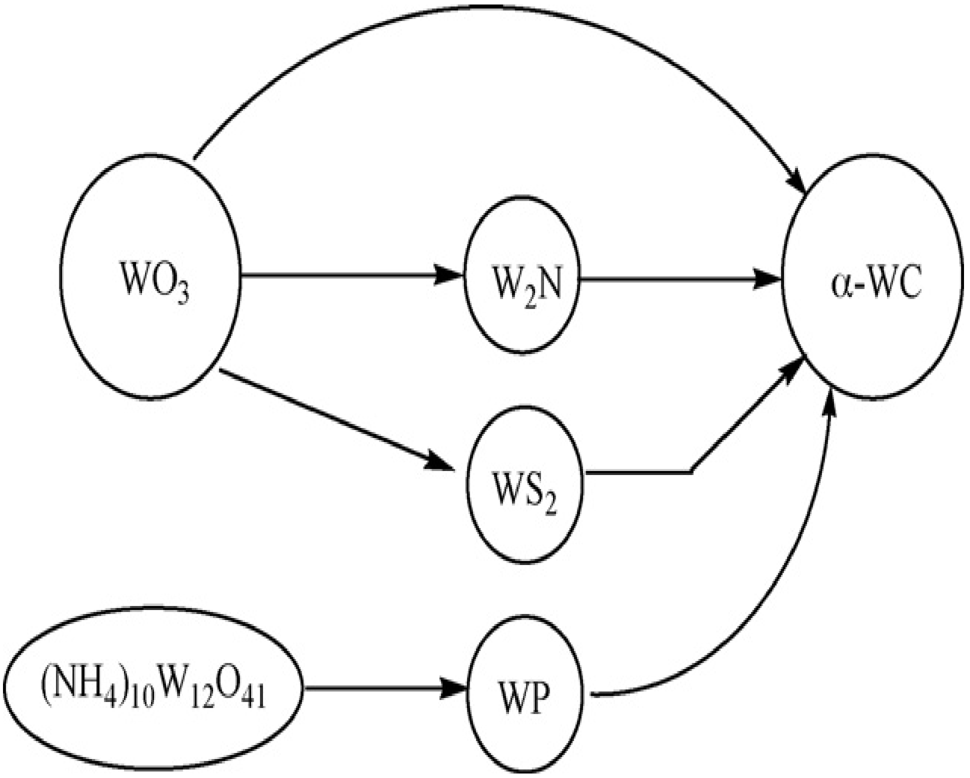

Figure 2.1: Conversion of WO_3 to α-WC.

Before exposure to the atmosphere, all samples were passivated in flowing 2 % air/N_2 (20 ml/min) for 1 h. The as prepared nano structured WC was also studied for its catalytic activities.

Ryu et al. [44-45] synthesized nano sized tungsten carbide powder by thermal plasma process using WCl_6 as the precursor. Various processing parameters were emphasized to optimize the process for the production of nano sized powder. Effect of experimental variables such as the molar ratio of reactant gases, plasma torch power, the flow rate of plasma gas and the addition of the secondary plasma gas (H_2) were investigated. The produced powder, which consisted mainly of WC_{1-x} phase, was subjected to heat treatment under hydrogen and the resulting product was analyzed for composition, grain size and carbon content. WC_{1-x} obtained by the thermal plasma process was less than about 20 nm and WC powder with grain size less than 40 nm was obtained after the hydrogen post-treatment of the produced WC_{1-x} powder.

Jang et al. [46] synthesized nano composites composed of WC and Pd nano particles. The synthesis was achieved by the sono-chemical decomposition of $W(CO)_6$ in the presence of a carbon support with Pd nano particles loaded on it. In this sono chemical process, the formed particles deposits preferentially on the Pd nano particles. Subsequent heat-treatment converted the deposit into WC nano particles in close contact with the Pd nano particles. The electrochemical data of this material indicated that WC enhanced the hydrogen oxidation (HOR) activity of Pd through the H^+ spillover.

Reddy et al. [47] synthesized nano structured WC and studied the influence of the precursor structure on nano structured W–C phase evolution during reduction and carburization of WO_3 under hydrogen environment. Nano structured WC was obtained from a chemically synthesized precursor consisting of hexagonal, monoclinic and partially amorphous WO_3 and amorphous C by heat treatment at 1000 ºC. The phase analysis of the heat treated product also revealed a small fraction of amorphous WC. No trace of W_2C, W or WC_{1-x} could be detected. Under identical heat treatment condition, a precursor comprising of commercial grade crystalline (monoclinic) WO_3 and graphite (crystalline C) led to pure W_2C while a precursor containing commercial grade crystalline (monoclinic) WO_3 and partially amorphous carbon (chemically synthesized) resulted to a blend of WC and W_2C phases. The W_2C phase, as obtained from the commercial grade WO_3, was orthorhombic. In contrast, the W_2C derived from the chemically synthesized precursor showed hexagonal structure. The mean crystallite size of pure WC was about 38 nm. The difference in the type of product phase(s) was attributed to the improved interface between the reacting species in case of chemically synthesized WO_3 and C.

Recently, **Shihong Zhang et al.** [48] used direct current magnetron sputtering technique for synthesis of nano composite of WC with Cu_3N. Films of Cu_3N–WC were synthesized on an arc ion plated TiNx interlayer by direct current magnetron sputtering. The Cu_3N–WC films, composed of columnar WC crystals 3–5 nm in size and amorphous Cu_3N phases, were grown using the layer-plus-island mode. Incorporation of the soft lubricant Cu_3N phase and the uniform distribution of WC hard phases resulted in significant improvements in friction coefficient and wear resistance.

2.4. Sintering and grain growth of nano crystalline WC–Co

High temperature sintering leads to the coarsening of the grains. Different techniques have been used to ensure retention of nano size in the sintered composites [49-108]. The techniques used are; hot isostatic pressing (HIP) [49], liquid phase sintering (LPS) [50-55], spark plasma sintering (SPS) [56-66], unconventional microwave sintering [67-68], rapid omni compaction (ROC) [69], high frequency induction-heated sintering (HFIHS) [70-72] and pulse plasma sintering (PPS) [73]. The smallest grain size measured till date in WC-Co composite where nano sized WC used as initial ingredient is 70 nm [74-75]. Considerable efforts are going on to achieve the goal of nano crystalline WC–Co composite to 100% density. The scientific community even today is devoting lot of time to study the densification and grain growth behavior during sintering of the nano sized WC-Co powders. In this part, understanding of the densification process, the growth behavior of nano sized WC–Co powders and the techniques for controlling gain growth during sintering are summarized.

2.4.1 Densification

In general, the reduced particle size leads to high surface area and decrease in sintering temperature of a material. This statement is also true for nano sized powders including nano sized WC–Co powders. **Peterson et al.** [76] investigated the early stage densification during sintering of a WC–Co material using image analysis to obtain pore size distributions of partially sintered samples. Sintering shrinkage is related to rearrangement of the WC particles. A bimodal pore size distribution developed during isothermal holding was obtained. This behavior was not monitored during heating. The isothermal holding after slow heating resulted in less densification than fast heating. It is suggested that isothermal holding yielded a more rigid compact when the equilibrium solubility is approached. The thermal expansion anisotropy of the WC–Co system played vital role during heating. Rearrangement was simulated with a discrete element method. The simulations also suggest that microstructure evolution retards significantly as isothermal conditions were established. Attempts of the author to introduce dissolution in the simulations failed to represent the expected increase in density.

Maheshwari et al. [77] did a comprehensive study on sintering of WC–10 Co powders with different initial particle sizes. The percent of densification for various initial particle sizes as a function of the continuous heating temperature is shown in figure 2.2.

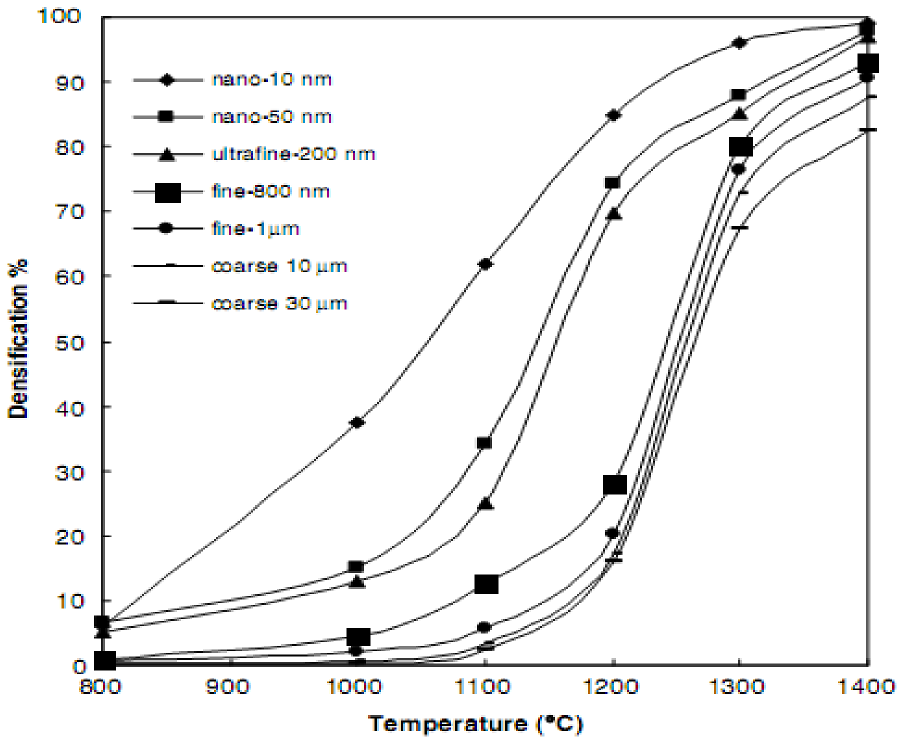

Figure 2.2: Densification of WC-Co as a function of temperature during heating for various initial particle sizes.

The graphical representation indicated that as the initial average particle size decreased from 30 µm to 10 nm, the entire temperature range of sintering decreased steadily. It is observed that approximately 90% of densification was accomplished in solid state sintering of the powder with 10 nm initial grain size. The author also confirmed the existence of two types of pores. These are, pores existing between agglomerates and the pores within agglomerates. The later are finer than the initial ones. The densification of individual agglomerates is relatively easy, while the elimination of the inter-agglomerate pores is more difficult.

2.4.2. Grain growth

Studies of the grain growth behavior showed that there is a more rapid grain growth during the early stages of sintering. **McCandlish et al.** [7] studied the effect of sintering time and concluded that dense structures in WC-10 wt% Co can be achieved in 30 seconds at 1400 °C, which gives WC grain size of about 200 nm. An additional 30 seconds sintering time increases the WC grain size to 2.0 microns. A small amount of uncombined C, or an addition of Cr, markedly inhibits grain growth during liquid phase sintering. On the other hand, ultra pure WC-Co powders can be consolidated by solid state sintering, where grain growth is much slower.

Fang et al. [52] studied the densification and grain size versus the liquid phase sintering time and temperature. It was found that densification of nano structured WC-Co powder could be completed in first 5 min. mainly, because of its fine grain size, nano structured powder densified more rapidly than the conventional samples. The addition of VC strongly hindered densification in the early stage of sintering. Grains grew extremely rapidly during first few minutes (< 5 min) of heating at different temperatures (approximately 1355, 1398, 1437 and 1477 °C). After the initial rapid stage, grain growth followed the linear relationship of coarsening.

Porat et al. [54] studied two types of WC-Co powders, nanometer and micron size particles by means of dilatometry. It was found that the sintering of the micron particle sized powder to full density is mainly done in the liquid phase sintering. The nano sized powder can be sintered in the solid phase, at a lower temperature. It was concluded that grain growth to a larger extent has already occurred at 1200 ºC while liquid phase was not expected to form until 1280 ºC.

Goren-Muginstein et al. [78] studied kinetics of densification during sintering the powder in a dilatometer up to 1450 ºC. It was concluded that three stages of sintering exists; (i) rearrangement of particles at low temperature (850 ºC) without grain or particle growth, (ii) neck formation between powder particles at l000- 1250 ºC and initial grain growth at 1200 ºC (iii) pore elimination accompanied by massive grain growth at 1300-1450 ºC. The nanometer WC grains start to grow at 1200 ºC in preferred crystallographic orientations.

Wang et al. [79] studied the grain growth of nano sized WC during the early stages of sintering as function of temperature and time. The effects of other influencing factors, such as the initial grain size, cobalt content and the grain growth inhibitor vanadium carbide (VC), were also investigated. The results showed that the grain growth process consists of an initial stage of rapid growth process which typically takes place during heat-up and the normal grain growth during isothermal holding. The initial rapid grain growth is at least partially attributed to the process of coalescence of grains via elimination of common grain boundary. The preferred orientation between WC grains within the aggregates is considered to be a favorable condition for coalescence of grains, hence rapid grain growth. The solution re-precipitation process was considered a mechanism of coalescence. Figure 2.3 shows that the original 10 nm grain size has increased almost 90-fold to 900 nm at 1400 ºC during heating. Similar behavior has also been reported for sintering of other nano crystalline metallic as well as ceramic powders [80-86]. The findings indicated that there must exist a critical temperature above which the grain growth accelerates dramatically as a function of temperature. The results also showed that there is a need to understand the fundamentals of the mechanisms of grain growth during sintering of nano scaled powders.

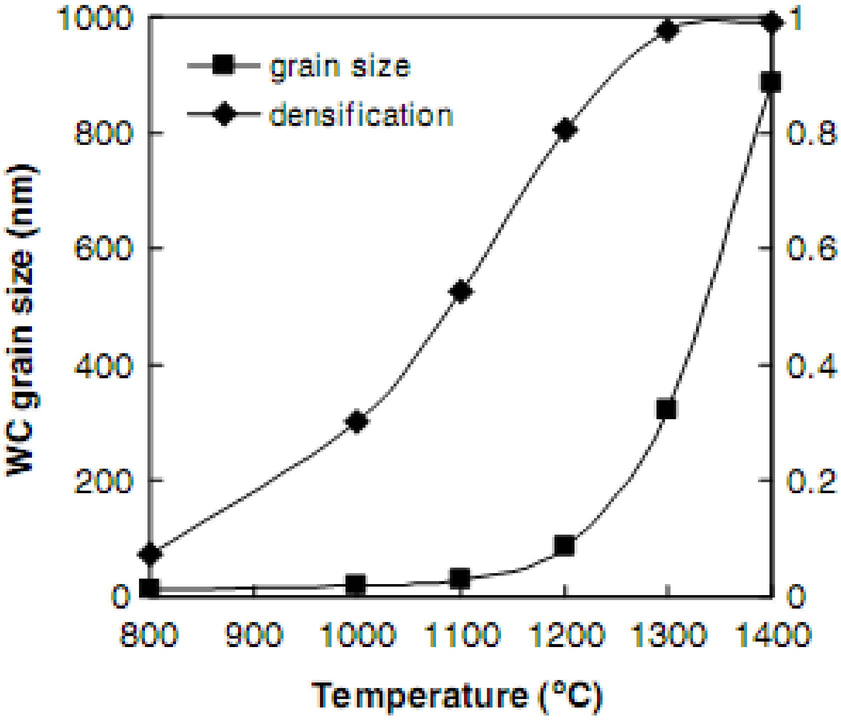

Figure 2.3: Grain growth versus densification relationship of WC-10wt%Co powder during heat-up.

Some new mechanisms were also proposed for the sintering of these composites. It was proposed that the rapid grain growth occurs by coalescence of grains. Coalescence is a unique way of grain growth in which mass transport mechanisms takes place. The mechanisms proposed for coalescence included various diffusion process and grain rotations.

Wang et al. [79,87] studied nano WC grain growth during heat-up. It was found that the growth of nano sized tungsten carbide occurred via coalescence of preferred-oriented-attached and faceted particles within aggregates. **Kumar et al.** [88] suggested that with a high degree of crystallographic anisotropy, the lattice shift along low-energy coincidence site. Lattice grain boundaries is a viable mechanism.

2.5 Different techniques controlling grain growth

2.5.1 Grain growth inhibitors

The presence of an unusually high surface and interface area provides a strong driving force for grain growth. This force leads to the inability to retain a nano scale grain size in the fully sintered bulk alloys [89]. It is recognized that the promise of nano structured WC–Co cemented carbides will not be realized, unless the grain growth problem is overcome. To control the grain growth in nano structured WC–Co composites, one of the keys is the proper selection of the second-phase additives as grain growth inhibitors. It was found that via standard liquid phase sintering, with the addition of 1.5 wt.% VC grain sizes of 100–150 nm at full density could be obtained [52, 90]. Commonly used inhibitors are chromium carbide, tantalum carbide and vanadium carbide. The relative effectiveness is ranked in the order VC > Cr_3C_2 > NbC > TaC. The other factors such as corrosion resistance and hot hardness may also affect the choice of grain growth inhibitors. The mechanism of growth inhibition is discussed in many research reports [90–98].

Peng et al. [99] did a numerical simulation with the aim to understand quantitatively the kinetic processes in the sintering of WC–Co composite with a Co gradient via liquid-phase-sintering of bi-layered WC–Co composites. The authors studied the migration of Co from regions with higher Co content to other regions with lower Co content, thus causing the redistribution of Co within the WC– Co composite.

Sadangi et al. [97] studied the effects of VC addition on grain growth in WC–Co. The findings suggested that the higher solubility and diffusivity of VC or Cr_3C_2 in cobalt binder made them effective in inhibiting grain growth. The solution re-precipitation of tungsten carbide is the mechanism of grain growth during sintering of WC–Co materials. The dissolution of VC and Cr_3C_2 in the binder phase suppresses this re-precipitation and act as grain growth inhibitors in the solid solution of cobalt phase. Low melting point ternary liquids(s) at temperatures in the range of 1200 - 1250 ºC are formed by these solid solution grain growth inhibitors. Since these low melting point solid solutions are saturated with grain growth inhibiting elements, the dissolution of W and C in the binder phase are prevented and grain growth are minimized.

Hashe et al. [100] also studied the sintering of WC–VC–Co composite in nitrogen atmosphere. The results indicated that sintering in nitrogen decreased the solubility of V in the binder phase and restricted the formation of very large cubic carbonitride grains. This nitrogen sintered material contains a depletion region at the surface. The grain growth in the depletion inhibited, which is attributed to the presence of VC in the material and is the best rated WC grain growth inhibitor.

Lay et al. [91] did microstructural examinations of VC-doped or VC-Cr_3C_2-doped WC-Co alloy by using high resolution transmission electron microscopy. Their results showed that during early process of sintering a thin layer of (V,W)Cx phase was deposited on various WC crystal faces with an epitaxial relationship. The results showed that Cr affected the interfacial layers and contribute to the resistance to W diffusion across VC layers and acted as a better inhibitor of the grain growth.

Choi et al. [101] related the process with edge energy. The addition of VC increased edge energy of WC crystal, which increases the energy barrier for coarsening process of WC grains controlled by 2D nucleation and inhibit grain growth.

Wang et al. [79] also studied the effect of VC in solid state during the early stage of sintering of nano crystalline WC–Co powder. The results indicated that doped WC grains formed aggregates with multi-faceted characteristics of layered structure, while

WC without doping becomes large fully developed prism shaped grains. It can be concluded that VC had effectively delayed the aggregation of nano sized particles coalescence into single crystals to higher temperatures.

2.5.2 Pressure assisted sintering

Another approach for controlling grain growth is pressure assisted sintering. **Azcona et al.** [49] used Hot Isostatic Pressing (HIP) to consolidate WC-10 wt% Co powders mixtures. Fully dense specimens of this composition have been obtained by HIP at 1000 ºC, a temperature well below those usually required for reaching the closed porosity stage in the WC-Co system. The authors also studied conventional processing by vacuum to study the individual effects of high isostatic pressure and vanadium carbide additions on densification and WC grain growth control of these hard metals. The finest mean grain size of WC after sintering has been obtained for the combined action of applied isostatic pressure and vanadium carbide (VC) additions are of 200 and 600 nm.

Prummer et al. [102] demonstrated that nano scale grain sizes after sintering can be achieved with ultrahigh pressure processes such as explosive compaction.

Dubensky et al. [69] consolidated nano scaled WC–Co powders using rapid omni-directional compaction (ROC) method. In the study, WC–8Co (grain size 50 nm) was sintered at 1000 ºC for 10 seconds under 830 MPa pressure. After sintering the final grain size was 150 nm.

2.5.3 Field assisted sintering techniques (FAST)

These sintering techniques are characterized by low sintering temperature, less densification time, which is a result of coupling of external field and applied pressure such as spark plasma sintering (SPS), high frequency induction-heated sintering (HFIHS) etc. In SPS for example, the applied electric field (pulse electrical current) generate rapid and simultaneous heating within samples. This combination of rapid heating with pressure provide high potential to make nano crystalline WC–Co using these techniques, without the addition of grain growth inhibitors. The final sintered grain is reported to be between 50 and 800 nm [73,103].

Zhao et al. [104] consolidated WC powders with a grain size in the range 40–70 nm by the spark plasma sintering (SPS) method over the temperature range 1425–1800 ºC under a uniaxial pressure of 126 MPa. WC powders consolidated to near theoretical densities (99.1%) with a grain size of 305 nm when heated at a high rate up to 1750 ºC with no holding time. The sintered material, however, contained W_2C.

Xiaoli et al. [105] consolidated W–Co composite nano powder in the size range 20–30 nm by freeze-drying, thermal decomposition and reduction. The SPS sintered body approached its theoretical density and the crystal size was about 0.7 μm.

Deorsola et al. [106] used pressure assisted fast electric sintering (PAFES) technique to sinter ultrafine WC-12 wt% Co composite. Fully dense ultrafine WC– 12 wt% Co has been obtained as a final product.

Shon et al. [107] compared sintering behavior and mechanical properties of WC–10 wt% Co, WC–10 wt% Ni and WC–10 wt% Fe hard materials produced by high-frequency induction heated sintering (HFIHS) method. The advantage of this process allows very quick densification to near theoretical density and prohibition of grain growth in nano-structured materials. Highly dense WC–10 Co, WC–10 Ni and WC–10 Fe with a relative density of up to 99 % with grain size of about 450, 490 and 450 nm, respectively, were obtained.

Table 2.1: Result of various sintering techniques with respect to densification and particle size [4].

Consolidation process	**Heating Temperature (ºC)**	**Hold Time (min)**	**Heating rate (ºC/min)**	**Pressure (MPa)**	**Powder Composition**	**Initial Grain Size**	**Grain growth inhibitor**	**Relative density (%)**	**Sintered grain size (nm)**	**Ref. No.**
HIP	1000	60	N/A	150	WC-10C0	----	No	100	~400	[49]
HIP	1000	60	N/A	150	WC-10Co-0.4VC	----	0.4VC	100	~200	[49]
SPS	1100	10	150	60	WC-12Co	40-250	No	99.89	800	[59]
SPS	1100	10	150	60	WC-12Co	40-250	VC	95.94	470	[59]
SPS	1150	5	100	10	WC-8Co	33	No	-----	200	
SPS	1000	10	100	100	WC-10Co	100	No	-----	~350	[63]
SPS	1240	2	100	60	WC-10Co	50	No	----	280	[66]
SPS	1240	2	100	60	WC-10Co	50	0.9VC	----	170	[66]
SPS	1100	5	N/A	25	WC-11Co	80	No	100	780	[103]
SPS	1200	5	N/A	30	WC-10C0-0.8VC	11	0.8VC	95.1	<100	[108]
HP	1300	20	N/A	30	WC-Co-0.6VC	----	0.6VC	100	169	[98]
HP	1700	~716	N/A	1500	WC-14Co	7	No	100	95	[16]
HP	1300	90	N/A	25	WC-11Co	80	No	100	780	[103]
HFIHS	1200	~1	1400	60	WC-10Co	100	No	99.4	323	[72]
PPS	1100	5	1000-1200	60	WC-12Co	60	No	98	50	[73]
ROC	1000	~0.2	N/A	830	WC-8Co	nanocarb	No	14.6	150	[69]
HFIHS	1200	~0.67	2000	60	WC–10Co	----	No	98.2	450	[107]
SPS	1298	3.5	580	15-100	WC-12Co	40-80	No	98.4	1000	[106]
SPS	1325	2	750	15-100	Wc-12Co	40-80	No	100	1000	[106]
SPS	1100	5	N/A	30	WC-12Co	20–30	Cr_2O_3	95.88	Not Sintered	[105]
SPS	1200	5	N/A	30	WC-12Co	20–30	Cr_2O_3	98.72	700	[105]
SPS	1300	5	N/A	30	WC-12Co	20–30	Cr_2O_3	99.34	1000	[105]
SPS	1425-1800	0	1500	126	------	40-70	No	95.5-100	254-305	[104]

As a summary, table 2.1 summarizes the results of various sintering techniques with respect to densification and grain size. These published findings show that no true nano crystalline (<100 nm) WC–Co materials have been consistently produced to date. Experimental observations seem to suggest that low limit of grain size refinement for WC–Co materials is 100 nm by using the available technologies. The need to fully densify the material and limit grain growth at the same time causes opposing considerations in process design. Finally, it is noted that sintered grain sizes between 0.1 to 0.8 μm are currently manufactured commercially by using conventional ultrafine tungsten carbide powders.

References

[1] T.S. Sudarshan, Metal Powder Report, 53(2) (1996) 32-36.

[2] H. Gleiter, Prog in Mater Sci, 33 (1989) 223-315.

[3] S. Berger, R. Porat and R. Rosen, Prog in Mater Sci, 42 (1997) 311-320.

[4] Z. Zak Fang, Xu Wang, Taegong Ryu, Kyu Sup Hwang, H.Y. Sohn, Int J Refract Metal Hard Mater, 27 (2009) 288–299.

[5] L.E. Mcchandlish, B.H. Kear, S.J. Bhatia, US patent 5352269; 1994.

[6] G.E. Spriggs, Int J Refract Metal Hard Mater, 13(5) (1995) 241-255.

[7] L.E. McCandllsh, B.H. Kear and B.K. Kim, Nanostruct Mater, 1 (1992) 119-124.

[8] Sverker Wahlberg, lngmar Grenthe and Mamoun Muhammed, Nanostruct Mater, 9 (1997) 105-108.

[9] L. Gao, B.H. Kear, P. Seegopaul, US patent 5919428; 1999.

[10] P. Seegopaul, L. Gao, US patent 6524366; 2003.

[11] B.K. Kim, G.G. Ha, Y. Woo US patent 6511551; 2003.

[12] G. Lee, G.H. Ha, B.K. Kim, J Korean Inst Metal Mater, 37(10) (1999) 1233–1237.

[13] Z.Y. Zhang, S.Wahlberg, M.S. Wang, M. Muhammed, Nanostruct Mater, 12(1-4) (1999) 163–166.

[14] J.R. Thompson, C. Politis, Euro phys Lett. 3 (1987) 199-205.

[15] Ma Xueming, Z. Ling, J. Gang, Y.D. Dong, J Mater Sci Lett. 16(12) (1997) 968–970.

[16] M.S. El-Eskandarany, A.A. Mahday, H.A. Ahmed, A.H. Amer, J Alloys Compd, 312(1-2) (2000) 315-325.

[17] F.L. Zhang, C.Y. Wang, M. Zhu, Scripta Mater, 49(11) 2003 1123-1128.

[18] H.J. Fecht, Nanostruct Mater, 1(2) (1992) 125–130.

[19] H.J. Fecht, E. Hellstern, Z. Fu, W.L. Johnson, Metall Mater Trans A, 21(9) (1990) 2333–2337.

[20] R. Porat, S. Berger, A. Rosen, Mater Sci Forum, 225–227 (1996) 629–634.

[21] B.G. Butler, J. Lu, Z.G.Z. Fang, R.K. Rajamani, Int J Powder Metall, 43(1) (2007) 35–43.

[22] G.L. Tan, X.J. Wu, Powder Metall, 41(4) (1998) 300–402.

[23] Z.G. Ban, L.L. Shaw, J Mater Sci, 37(16) (2002) 3397–3403.

[24] Y.S. Kwon, V.M. Andreev, O.I. Lomovsky, B.B. Bokhonov, J Alloys Compd, 386 (2005) 115–118.

[25] Jadambaa Temuujin, Mamoru Senna, Tsedev Jadambaa and Dondog Byambasuren, J. Am. Ceram. Soc, 88 (4) (2005) 983–985.

[26] K.J.D. MacKenzie, J. Temuujin, C. McCammonc and M. Senna, J Euro Ceram Soc, 26 (2006) 2581–2585.

[27] ZhuhuiQiao, Xianfeng Ma, Wei Zhao, Huaguo Tang, Shuguang Cai and Bo Zhao, J Alloys Compd, 453(1-2) (2008) 382-385.

[28] M.H. Enayati, G.R. Aryanpour and A. Ebnonnasir, Int J Refract Metal Hard Mater, 27 (2009) 159–163.

[29] M. Zakeri, M.R. Rahimipour, S. Kh. Sadrnezhad and R. Yazdanni-rad, J Alloys Compd, 491 (2010) 203–208.

[30] M.T. Swihart, Curr Opin Colloid Interf Sci, 8(1) (2003) 127–133.

[31] J. Hojo, T. Oku, A. Kato, J Less-Common Metal, 59(1) (1978) 85–95.

[32] M. Fitzsimmons, V.K. Sarin, Surf Coat Tech, 76(1–3) (1995) 250–255.

[33] S. Wanner, L. Hilaire, P. Wehrer, J.P. Hindermann, G. Maire, Applied Catalysis A: General, 203 (2000) 55–70.

[34] F.F.P. Medeiros, S.A. De Oliveira, C.P. De Souza, A.G.P. Da Silva, U.U. Gomes, J.F. De Souza, Materials Science and Engineering A, 315 (2001) 58-62.

[35] Zongyin Zhang, Mamoun Muhammed, Thermochimica Acta, 400 (2003) 235-245.

[36] J.C. Kim, B.K. Kim, Scripta Materialia, 50 (2004) 969–972.

[37] X. Tang, R. Haubner, B. Lux, B. Kieffer, J Phys IV Colloq, 510 (1995) 13–20.

[38] C.W. Won, B.S. Chun, H.Y. Sohn, J Mater Res, 8(10) (1993) 2702–2708.

[39] ChunliGuo, Yi Liu, Xiaojian Ma, YitaiQian and Liqiang Xu, Chemistry Letters, 35(11) (2006) 1210-1211.

[40] Nicolas Keller, Barbara Pietruszka, Valérie Keller, Materials Letters, 60 (2006) 1774–1777

[41] H. Y. Sohn, T. Ryu, J.W. Choi, K.S. Hwang, G. Han, Y.J. et al. Jom-Us, 59(12) (2007) 44–49.

[42] Huajun Zheng, Jianguo Huang, Wei Wang, Chunan Ma, Electrochemistry Communications, 7 (2005) 1045–1049.

[43] Yoshinori Hara, Noriko Minami, Hiroaki Itagaki, Applied Catalysis A, 323 (2007) 86–93.

[44] TaegongRyu, H. Y. Sohn, Kyu Sup Hwang, Zhigang Z. Fang, J Mater Sci, 43 (2008) 5185–5192.

[45] Taegong Ryu, H.Y. Sohn, Kyu Sup Hwang, Zhigang Z. Fang, J Alloys Compd, 481 (2009) 274–277.

[46] Ji-Hoon Janga, Juyeong Kimb, Yang-Hee Leea, Chanho Pakc, Young-Uk Kwon, Electrochimica Acta, 55 (2009) 485–490.

[47] K. Madhav Reddy, T.N. Rao, K. Radha, J. Joardar, J Alloys Compd, 494 (2010) 404–409.

[48] Shihong Zhang, Yinsheng He, Mingxi Li, Yizhu He, Sikchol Kwon, Jaehong Yoon, Tongyul Cho, Thin Solid Films, 518(18) (2010) 5227-5232.

[49] I. Azcona, A. Ordonez, J.M. Sanchez, F.Castro, J Mater Sci, 37(19) (2002) 4189–95.

[50] L. Bartha, P. Atato, A.L. Toth, R. Porat, S. Berger, A. Rosen, J Adv Mater, 32(3) (2000) 23–26.

[51] D.F. Carroll. Int J Refract Metal Hard Mater, 17(1–3) (1999) 123–132.

[52] Z.Z. Fang, J.W. Eason. Int J Refract Metal Hard Mater, 13(5) (1995) 297–303.

[53] L.E. McCandlish, P. Seegopaul, R.K. Sadangi. Adv Powder Metall Particulate Mater, 3 (1995) 313–317.

[54] R. Porat, S. Berger, A. Rosen, Nanostruct Mater, 7(4) (1996) 429–36.

[55] L. Zhang, T.E. Madey. Nanostruct Mater, 2(5) (1993) 487–93.

[56] X.Q. Liu, T. Lin, Z.M. Guo, F.E. Cui, J. Luo, J Iron Steel Res Int, 14 (2007) 1482–1484.

[57] F. Zhang, J. Shen, J. Sun, J Alloys Compd, 385(1–2) (2004) 96–103.

[58] S.X. Zhao, X.Y. Song, J.X. Zhang, X.M. Liu. Mater Sci Eng A, 473(1–2) (2008) 323–329.

[59] D. Sivaprahasam, S.B. Chandrasekar, R. Sundaresan, Int J Refract Metal Hard Mater, 25(2) (2007) 144–152.

[60] H.F. Zhao, L.H. Zhu, Q.W. Huang, Rare Metal Mater Eng, 34(1) (2005) 82–85.

[61] G. Maizza, S. Grasso, Y. Sakka, T. Noda, O. Ohashi, Sci Technol Adv Mater, 8(7–8) (2007) 644–654.

[62] X.Q. Wang, Y.G. Xie, H.L. Guo, O. Van der Biest, J. Vleuge, Rare Metal, 25(3) (2006) 246–252.

[63] S.I. Cha, S.H. Hong, B.K. Kim, Mater Sci Eng A, 351(1–2) 2003 31–38.

[64] C.C. Jia, H. Tang, X.Z. Mei, F.Z. Yin, X.H. Qu, Mater Lett, 59(19–20) (2005) 2566–2569.

[65] L. Sun, C.C. Jia, C.G. Lin, R.J. Cao, J Iron Steel Res Int, 14 (2007) 1485–1489.

[66] S.G. Huang, L. Li, K. Vanmeensel, O. Van der Biest, J. Vleuges, Int J Refract Metal Hard Mater, 25(5–6) (2007) 417–422.

[67] D. Agrawal, J. Cheng, P. Seegopaul, L. Gao, Powder Metall, 43(1) (2000) 15–16.

[68] E. Breval, J.P. Cheng, D.K. Agrawal, P. Gigl, M. Dennis, R. Roy et al. Mater Sci Eng A, 391(1–2) (2005) 285–295.

[69] E. M. Dubensky, R.T. Nilsson, US patent 5773735; 1996.

[70] H.C. Kim, I.K. Jeong, I.J. Shon, I.Y. Ko, J.M..Doh, Int J Refract Metal Hard Mater, 25(4) (2007) 336–340.

[71] H.C. Kim, D.Y. Oh, I.J. Shon, Int J Refract Metal Hard Mater, 22(4–5) (2004) 197–203.

[72] H.C. Kim, I.J. Shon, I.K. Jeong, I.Y. Ko, J.K. Yoon, J. M. Doh, Metal Mater Int, 13(1) (2007) 39–45.

[73] A. Michalski, D. Siemiaszko, Int J Refract Metal Hard Mater, 25(2) (2007) 153–158.

[74] J.M. Densley, J.P. Hirth, Scripta Mater, 38(2) (1997) 239–244.

[75] K. Jia, T.E. Fischer, B. Gallois, Nanostruct Mater, 10(5) (1998) 875–891.

[76] A. Petersson, J. Agren, Acta Mater, 53(6) (2005) 1673–1683.

[77] P. Maheshwari, Z.G.Z. Fang, H.Y. Sohn. Int J Powder Metall, 43(2) (2007) 41–47.

[78] G.R. Goren-Muginstein, S. Berger, A. Rosen, Nanostruct Mater, 10(5) (1998) 795–804.

[79] X. Wang, Z.Z. Fang, H.Y. Sohn, Int J Refract Metal Hard Mater, 26(3) (2008) 232–241.

[80] F. Zhou, J. Lee, E.J. Lavernia, Scripta Mater, 44(8–9) (2001) 2013–2017.

[81] Z.J. Shen, H. Peng, J. Liu, M. Nygren, J Eur Ceram Soc, 24(12) (2004) 3447–3452.

[82] S. Okuda, M. Kobiyama, T. Inami, S. Takamura, Scripta Mater, 44(8–9) (2001) 2009–2012.

[83] R. Klemm, E. Thiele, C. Holste, J. Eckert, N. Schell, Scripta Mater, 46(9) (2002) 685–690.

[84] G. Hibbard, K.T. Aust, G. Palumbo, U. Erb, Scripta Mater, 44(3) (2001) 513-518.

[85] W. Dickenscheid, R. Birringer, H. Gleiter, O. Kanert, B. Michel, B. Gunther, Solid State Commun, 79(8) (1991) 683–686.

[86] D.J. Chen, M.J. Mayo, Nanostruct Mater, 2(5) (1993) 469-478.

[87] Z. Fang, P. Maheshwari, X. Wang, H.Y. Sohn, A. Griffo, R. Riley, Int J Refract Metal Hard Mater, 23(4-6) (2005) 249–257.

[88] V. Kumar, Z. Fang, S. Wright, M. Nowell, Metall Mater Trans A, 37(3) (2006) 599–607.

[89] B.H. Kear, J. Colaizzi, W.E. Mayo, S.C. Liao, Scripta Mater, 44 (2001) 2065–2068.

[90] G. Gille, B. Szesny, K. Dreyer, H. van den Berg, J. Schmidt, T. Gestrich, et al. Int J Refract Metal Hard Mater, 20(1) (2002) 3–22.

[91] S. Lay, J. Thibault, S. Hamar-Thibault, Philos Mag, 83(10) (2003) 1175–1190.

[92] A. Bock, W.D. Schubert, B. Lux, Powder Metall Int, 24(1) (1992) 20–26.

[93] A. Adorjan, W.D. Schubert, A. Schon, A. Bock, B. Zeiler, Int J Refract Metal Hard Mater, 24(5) (2006) 365–373.

[94] B.K. Kim, G.H. Ha, G.G. Lee, D.W. Lee, Nanostruct Mater, 9(1–8) (1997) 233–236.

[95] N. Li, Y.X. Qiu, W. Zhang, Y.H. Wen, Y. Zhang, Y.G. Zhou, Rare Metal Mater Eng, 36(10) (2007) 1763–1766.

[96] S.I. Cha, S.H. Hong, Z Metallkd, 96(2) (2005) 172–176.

[97] R.K. Sadangi, L.E. McCandlish, B. H Kear, P. Seegopaul, Int J Powder Metall, 35(1) (1999) 27–33.

[98] C.G. Lin, E. Kny, G.S. Yuan, B. Djuricic, J Alloys Compd, 383(1–2) (2004) 98–102.

[99] Peng Fan, Zhigang Zak Fang, Int J Refract Metal Hard Mater, 27 (2009) 37–42.

[100] N.G. Hashe, S. Norgre, H. O. Andre´n b, J.H. Neethling, P.R. Berndt, Int J Refract Metal Hard Mater, 27 (2009) 20–25

[101] H.R. Lee, D.J. Kim, N.M. Hwang, D.Y. Kim, J Am Ceram Soc, 86(1) (2003) 152–154.

[102] R. Prummer, P. Weimar, Ceram Inter, 46(6) (2002) 394–398.

[103] L. Sun, C.C. Ha, M. Xian, Int J Refract Metal Hard Mater, 25(2) (2007) 121–124.

[104] Jinfeng Zhao, Troy Holland, CosanUnuvar, Zuhair A. Munir, Int J Refract Metal Hard Mater, 27 (2009) 130–139.

[105] Xiaoli Xi, Xiong Pi, Zuoren Nie, Shunlin Song, Xiangyang Xu, Tieyong Zuo, Int J Refract Metal Hard Mater, 27 (2009) 101–104.

[106] F.A. Deorsola, D. Vallauri, G.A. Ortigoza Villalba, B. De Benedetti, Int J Refract Metal Hard Mater, 28 (2010) 254–259.

[107] In-Jin Shon, In-Kyoon Jeong, In-Yong Ko, Jung-Mann Doh, Kee-Do Woo, Ceram Inter, 35 (2009) 339–344.

[108] L.H. Zhu, Q.W. Huang, H.F. Zhao, Mater Sci Lett, 22(22) 2003 1631-1633.

Chapter 3

EXPERIMENTAL PROCEDURES

Overview

In this chapter, the procedure adopted to synthesize tungsten carbide (WC) nano particles from raw materials is described. The description of autoclave which is used to synthesize WC nano particles is also given. The preparation route followed to prepare WC-Cobalt composite using as synthesized WC nano powders is presented. Various techniques which are used to characterize the samples are also given. As prepared WC nano powder samples were characterized by X-ray diffraction (XRD), differential thermal analysis (DTA)/thermo-gravimetric analysis (TGA) and high resolution transmission electron microscope (HRTEM). The composites prepared were characterized by XRD, optical microscope, scanning electron microscope (SEM) and energy dispersive spectroscopy (EDS).

The present chapter describes in detail the experimental procedures for the entire study. The procedure adopted for the synthesis and characterization of materials are described. The details of these are presented below:

3.1 Raw Materials

The raw materials used for preparing the samples were Tungsten (VI) oxide (WO_3) (99.9%, Sigma Aldrich), Methanol (99%, Merck Germany), Ethanol, (99%, Merck Germany), Acetone, (99%, Merck Germany), Magnesium turnings (99%, S.D. fine chemicals) and wolframite concentrate (Wolfram Bergbau Austria). All these materials except wolframite concentrate were used without any further purification.

3.2 Design and development of an autoclave

For the synthesis of nano WC powder the procedure followed is solvo-thermal route which involves vapor phase reaction. Since this reaction occurs at high temperature and pressure so it requires a vessel which can sustain high pressure. Such type of vessel is not available in market. In order to manufacture it the key parameters which were considered is materials selection which can sustain such high pressure without undergoing any type of phase transition. Moreover, the coefficient of thermal expansion should also be low. After several trials we could finalize one steel which has shown optimum results. The steel which has shown better results is 304 stainless steel. It is austenite steel containing 18% chromium, 8% nickel, with maximum carbon content of 0.08%. It is also called chromium-nickel austenitic steel.

An autoclave without any pressure monitoring assembly was designed and fabricated. It finds application at elevated temperatures. The difference of this autoclave from the traditional autoclaves is that, it can withstand high temperature and pressure. The main problem in the experimentation was leakage of gases generated during the reaction which was overcome in a series of experiments as described below:

I. Metal-metal contact of the lid and the autoclave was tried several time with different design. Limitation of the process was that after every experiment the lid stick to the autoclave.

II. Aluminum gasket was used but aluminum gasket could not sustain pressure beyond 450 °C causing leakage of gas.

III. Brass gasket was also tried but under high temperature and high pressure it melted. Though it provided better results as compared to aluminum gasket but not so productive.

IV. At last copper gasket was tried (melting point 1084 °C). In this experiment there was no leakage and hence it was finalized for further experimentation.

We have also tried to measure the pressure by connecting the top lid with high pressure gauge but every time it leaked from welded spot. It was further decided to take up pressure measurement parameter for subsequent study as it requires testing of autoclave with different design. However, in the present design pressure -volume-temperature (P-V-T) was kept in mind to avoid any accidental problem. While considering the design parameters the decomposition temperature of acetone, methanol and ethanol (400-600 °C) used in present investigation was considered. [1-4]. In the reactions the rate of pressure build up caused by their decomposition in a constant volume piezometer is in between 0.7 to 1.0 MPa per hour [5].

Figure 3.1: Specially designed autoclave.

3.3 Synthesis of WC particles

For the synthesis of WC nano particle following procedures were adopted:

- Chemical synthesis route
- Mechano chemical synthesis route

3.3.1 Synthesis of WC particle using Chemical route

In this part of experimentation WC nano particles were synthesized using WO_3. Magnesium turnings were used as reducing agent along with a carbon source. As per reaction the required amount of WO_3, Mg turning and a selected carbon source were put in the autoclave. The proposed reaction which may occur in the autoclave can be written as:

$$2WO_3 + R - CO - R + Mg \rightarrow WC + nC + MgWO_4 + nH_2 + nCO_2 \qquad (3.1)$$

Here *R* is used for CH_3 group.

3.3.1.1 Selection of carbon source

Selection of an appropriate carbon source is very important for the synthesis of nano sized WC particles. Best suited carbon source will generate appropriate amount of hydrogen gas during course of reaction which is very important for the reduction of WO_3. Three hydrocarbons, methanol, ethanol and acetone with different volumetric ratios were tried for the synthesis. Based on trial results, the best suited carbon source with appropriate volumetric ratio was selected for further synthesis.

3.3.2 Synthesis of WC particles from WO_3

Appropriate amount of WO_3, Mg and carbon source were put into a specially designed stainless steel autoclave. The constituent details and other variables are given in chapter 4 (result and discussion). The sealed autoclave was kept into furnace. The temperature of the furnace was increased from room temperature to different temperatures with heating rate of 5 ºC/min. The autoclave was kept inside the furnace for different durations at different temperatures followed by furnace cooling of the autoclave. After cooling the autoclave, when the reaction is over, the dark solid powder was taken out from the autoclave and dissolved in HCl (1:1) to remove unreacted Mg and other soluble phases from the product. The acid treated samples were washed with distilled water first followed by ethanol to eliminate the water absorbed in the powders. The dried powders were characterized to investigate the formation of WC phase in the synthesized mass.

3.4 Synthesis of WC particles from wolframite ore

WC nano particles were also synthesized from wolframite ore. The chemical composition of the ore is given in table 3.1.

Table 3.1: Chemical composition of wolframite**.**

S. No.	**Compound**	**Wt%**
1	WO_3	50.7
2	Fe_2O_3	34.227
3	SiO_2	9.579
4	Al_2O_3	3.155
5	MnO	1.785
6	TiO_2	0.270
7	SnO_2	0.156
8	K_2O	0.128

As it is evident from table that majority of component is WO_3. However, it also contains other impurities. These impurities have to be eliminated or minimized to certain extent to get ore enriched in W content.

3.4.1 Enrichment of the ore

The wolframite powder (10 g) was dissolved in 100 ml of dilute HCl (1:3). The solution was stirred for 30 min. During this process the change in color was observed. The solution got separated in two colored layers. The upper layer was pale yellow due to formation of $FeCl_3$ while the lower layer was parrot green colored (probably WO_3). The top layer was decanted several times by adding water into it. The filtrate of the lower layer (filtered using whatman 44 filter paper) was again washed with 100 ml of dilute HCl (1:3). Again the solution was separated in two colored layers. The solution was heated till boiling. It was observed during heating the color of the upper layer darkened which showed that there exist some unreacted particles in the lower layered solution. After this experimentation it was concluded that dilute HCl (1:3) cannot remove impurities completely. The same experiment was also carried out with HCl (1:2) and similar results were obtained. Finally HCl (1:1) was tried; wolframite powder (10 g) was dissolved in 100 ml of HCl (1:1) and heated. The filtrate of the second layer was again dissolved in 100 ml of HCl (1:1) and heated, no pale yellow color was observed even after heating for 30 min. The solution was parrot green in color. All the impurities except silica present in the ore (table 3.1) react with HCl to form water soluble product which are leached out (supported by XRD discussed in chapter 4). Some drops of HF were also added in the solution, the solution was heated till boiling with continues stirring for 30 min. HF can remove silica content from the ore in the form of salicylic acid. Detailed discussion on the reaction of impurities with HCl is given in chapter 4. The filtrate after acid treatment was washed several times with distilled water to remove acid traces. The powder was then washed with ethanol and heated in vacuum at 50 °C for 1 h to remove water traces.

3.4.1.1 Mechanical activation of the ore

The enriched ore powder is then milled for different durations (10, 15 and 20 h) at 292 rpm with 1:50 charge to ball ratio to activate the ore mechanically in a tungsten jar using tungsten balls. The diameter of the ball was 8 mm. These millings increase the surface area of the materials and hence increase the surface activity.

3.4.2 Synthesis of WC particles from ore

Powder obtained from enriched and mechanically activated ore was used as initial ingredients. The autoclave was charged with activated ore along with reducing agent (Mg) and appropriate amount of carbon source to carry out the reaction as mentioned in equation (3.1). Rest of the synthesis procedure is same as adopted in chemical synthesis route for WO_3 powder.

3.5 Preparation of WC-Co Composite

The as synthesized WC nano particles which have been prepared from pure WO_3 and enriched wolframite ore were used for the preparation of WC-Co composites for its end applications. Cobalt (Co) which acts as a binder was used in present investigation. The amount of binder (Co) was varied from 5 to 20% in a step of 5 i.e the binder used is 5, 10, 15 and 20 wt%. For the preparation of composites WC and cobalt powders were mixed in a ball mill with 1:5 charge to ball ratio for 2 h in WC jars using WC balls of 8 mm diameter at 147 rpm. To this mixture 2 wt% of polyvinyl alcohol (10 mol %) was mixed and dried.

3.5.1 Pellets preparation

Known weight of dried powders was transferred in a die which was manufactured from hardened die steel. The die along with punch was kept below hydraulic press (Polyhedron, India; Model 5010) and a compaction pressure of 503 MPa was applied slowly. After waiting for 1 min, the pressure was released. Afterward the compacted mass was ejected out from the die.

The above procedure was followed for preparation of pellets of different Co content and also using WC particles synthesized from WO_3 and ore both.

3.5.2 Sintering

The pellets obtained after compaction were sintered at different temperatures for different time in argon atmosphere in a calibrated resistance heating furnace. The flow sheet of the experimental procedure adopted is given in figure 3.2.

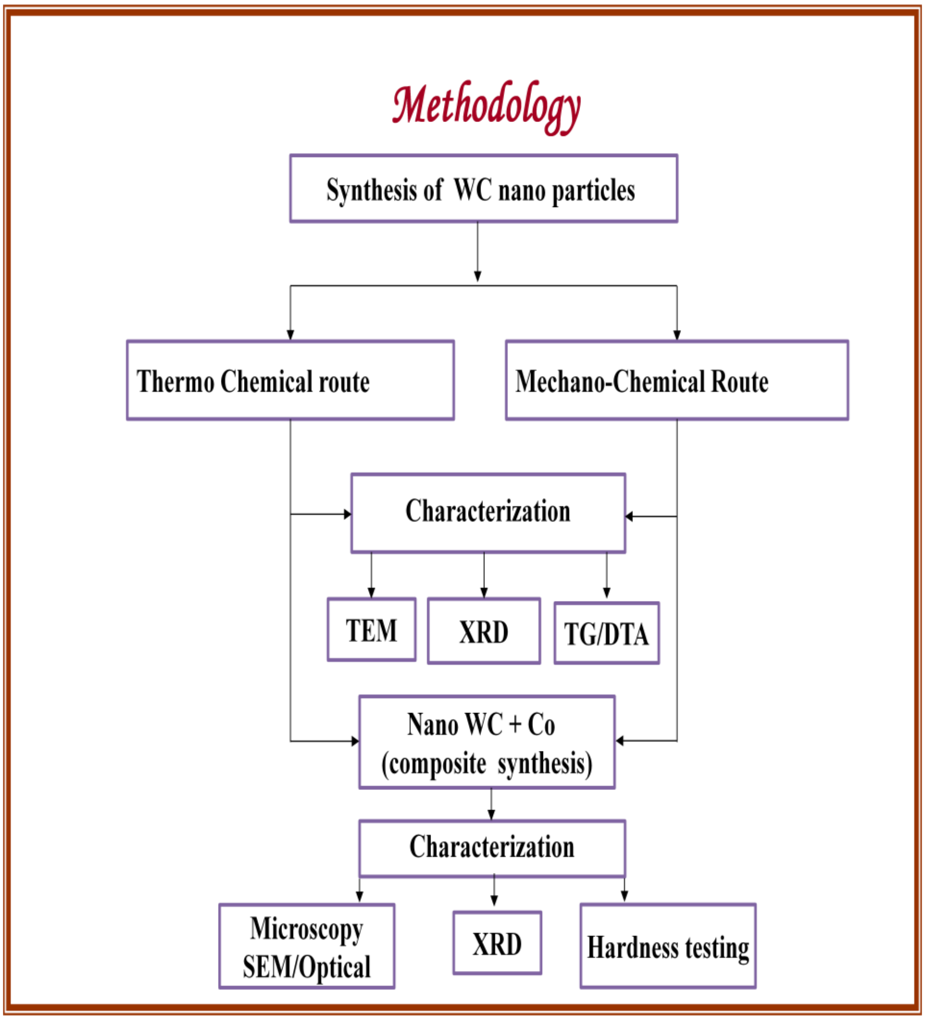

Figure 3.2: Flow chart of the experimental procedure.

3.6 Characterization of Materials

Characterization is an integral part of the study of any materials. As shown in flow chart (figure 3.2) WC nano particles are characterized using X-ray diffraction (XRD), thermal gravimetric/differential thermal analysis (TG/DTA), transmission electron microscopy (TEM) while the sintered WC-Co composites were characterized using optical microscopy, scanning electron microscopy (SEM), XRD and micro hardness tester. The details of these techniques are given below.

3.6.1 X-Ray Diffraction

X-ray diffraction is a versatile, non-destructive technique used to obtain crystallographic information about a sample. X-ray diffraction technique was used to identify various phases and their volume fraction in the samples (figure 3.3). The texture coefficient of different planes and the particle size was also analyzed by this technique. X-ray powder diffractrogram was recorded at room temperature by X-ray diffractrogram (Model Geiger flex D max IIIc and Xpert pro PAN alytical) using monochromatic CuK$_\alpha$ radiation (λ = 1.5418 Å) at a scan speed of 5 ^{o}/min (figure 3.3). The XRD patterns are taken in the range of 10° ≤ 2θ ≤ 80° for most of the samples. Lattice parameters were calculated with the help of the diffractogram obtained for each sample using Bragg’s law as describe below:

$$n\lambda = 2d\sin(\theta) \tag{3.2}$$

here d = inter-planar spacing, λ = wavelength of incident X-ray, θ = diffraction angle, n is an integer [6].

6 

Figure 3.3: X-Ray diffractometer.

The data obtained from XRD is indexed by standard powder diffraction files provided by International Centre for Diffraction Data (ICDD).

3.6.1.1 Calculation of lattice parameters and texture coefficient

The lattice parameters (a, c) were calculated with the help of inter-planar spacing ‘d’ as follows:

$$\frac{1}{d^2} = \frac{4}{3}\left(\frac{h^2 + hk + k^2}{a^2}\right) + \frac{l^2}{c^2} \qquad \text{for hexagonal systems} \qquad (3.3)$$

A comparison of peak intensity with standard specimen can be obtained through Harris's analysis, to obtain a texture coefficient using the relationship as given below:

$$\mathrm{P(h_ik_il_i)} = \frac{I(h_ik_il_i)}{I_0(h_ik_il_i)}\left[\frac{1}{\mathrm{n}}\sum_{i=1}^{n}\frac{I(h_ik_il_{i)}}{I_0(h_ik_il_i)}\right]^{-1} \tag{3.4}$$

P (h k l) is the texture coefficient of the plane specified by Miller Indices (h k l); I(h k l) and I_0(h k l) are the specimen and standard intensities respectively for a given peak and n is the number of diffraction peaks [7].

3.6.1.2 Calculation of particle size

The particle size of the as prepared sample is also calculated using XRD pattern. The full width at half maximum (β) of the diffraction peaks can be expressed as a linear combination of the contributions from the strain (ε) and particle size (L). Therefore, particle size can be calculated from the following relation.

$$\frac{\beta Cos(\theta)}{\lambda} = \frac{1}{L} + \frac{\varepsilon Sin(\theta)}{\lambda} \tag{3.5}$$

The plots of (sin θ) versus (β cos θ) is used for the particle size calculation. The above equation is an equation of a straight line. The intercepts on the (β cos θ) axis equals to λ/L which gives the average particle size of as prepared sample [8-10].

3.6.2 Differential thermal/Thermo gravimetric analysis (DT/TGA)

Differential thermal analysis (DTA) is a thermo analytic technique that gives information about the phase transformation behavior of the sample (figure 3.4). In DTA, the thermal event of sample is observed with respect to the inert reference sample in heating or cooling cycle under identical conditions. This differential temperature is then plotted against time, or against temperature (DTA curve). Changes in the sample, either exothermic or endothermic, can be detected relative to the inert reference. Thus, a DTA curve provides data on the transformations that have occurred, such as phase transitions, crystallization and melting. In the present work, differential thermal analysis of the powdered samples was done by DTA, Perking Elmer (Diamond TG/DTA) in nitrogen and oxygen atmosphere (figure 3.4) using platinum crucibles at different heating rates from 50 ºC to 800 ºC. In the present investigations Al_2O_3 is taken as reference sample. The DTA sensitivity depends upon the heating rate. It is reduced with the slower rates because temperature for a particular event decreases with decreasing heating rate.

The thermal stability of the samples was investigated using thermo gravimetric analysis (TGA).

Figure 3.4: Thermo gravimetric/ Differential Thermal Analyzer (TG/DTA).

Thermo-gravimetric analysis or thermal gravimetric analysis (TGA) is a type of testing that is performed on samples to determine changes in weight in relation to change in temperature. Such analysis relies on a high degree of precision in three measurements: weight, temperature and temperature change. As many weight loss curves look similar, the weight loss curve may require transformation before results may be interpreted. A derivative weight loss curve can be used to tell the point at which weight loss is most apparent. The temperature and weight loss detection limit are ± 1 ºC and 0.001 mg, respectively during DTA/TGA measurements.

3.6.3 Scanning Electron Microscopy (SEM)

The scanning electron microscope (SEM) is a very useful tool to study the morphological features of the samples using a high-energy beam of electrons (figure 3.5). The electrons interact with the samples and produce signals that contain information about the sample's surface topography, composition and morphology of crystalline phases.

Figure 3.5: Scanning electron microscope with EDS.

The types of signals that are produced by the SEM include secondary electrons (SE), back scattered electrons (BSE), characteristic X-rays, light (cathodoluminescence), specimen current and transmitted electrons. The detection of these signals requires specialized detectors for their detection that are located at different places in the machine. Scanning electron micrographs of the selected samples were taken by using JSM-6510 LV (Jeol) scanning electron microscope (figure 3.5). Before SEM analysis, the samples were ground and polished. The polished samples were etched by freshly prepared Morakami reagent (100 ml distilled water, 10 g $K_3Fe(CN)_8$ and 10 g KOH). The purpose of etching is to enhance microstructural features such as grain boundary and phases present in the structure.

3.6.4 Energy-dispersive X-ray spectroscopy

Energy-dispersive X-ray spectroscopy (EDS or EDX) is an analytical technique used for the elemental analysis or chemical characterization of a sample. It is one of the variants of X-ray fluorescence spectroscopy which relies on the investigation of a sample through interactions between electromagnetic radiation and matter, analyzing X-rays emitted by the matter in response to being hit with charged particles. Its characterization capabilities are based on the fundamental principle that each element has a unique atomic structure allowing X-rays that are characteristic of an element's atomic structure to be identified uniquely from one another. The system is attached with the scanning electron microscope and this technique is used for the elemental analysis of the as prepared composite materials. For EDS analysis Oxford INCA model no. 51-ADD 0076 (Inca) spectrometer is used. The instrument is attached with the SEM (figure 3.5).

3.6.5 Raman Spectroscopy

Raman spectroscopy (named after C. V. Raman) is a spectroscopic technique used to study vibrational, rotational and other low-frequency modes in a system. It relies on inelastic scattering or Raman scattering of monochromatic light, usually from a laser in the visible, near infrared or near ultraviolet range. The laser light interacts with molecular vibrations, phonons or other excitations in the system, resulting in the energy of the laser photons being shifted up or down. The shift in energy gives information about the phonon modes in the system. During the synthesis WC nano particles carbon nano tubes (CNT) were observed. Raman spectrum analysis is done using Micro-Raman T64000 Jobin Yvon triple monochromator system. For recording the spectra samples were excited at a wavelength of 514.5 nm. To identify that the CNTs are single wall or multiwall, this technique was used.

3.6.6 High resolution transmission electron microscopy

High resolution transmission electron microscopy (HRTEM) is a microscopy technique in which a beam of electrons is transmitted through an ultra thin specimen, interacting with the specimen as it passes through. An image is formed from the interaction of the electrons transmitted through the specimen; the image is magnified and focused onto an imaging device, such as a fluorescent screen, on a layer of photographic film, or to be detected by a sensor such as a CCD camera. TEMs are capable of imaging at a significantly higher resolution than light microscopes, owing to the small de Broglie wavelength of electrons. This enables the instrument's user to examine fine detail even as small as a single column of atoms, which is tens of thousands times smaller than the smallest resolvable object in a light microscope. TEM forms a major analysis method in a range of scientific fields, in both physical and biological sciences. At smaller magnifications TEM image contrast is due to absorption of electrons in the materials, due to the thickness and composition of the materials. At higher magnifications complex wave interactions modulate the intensity of the image, requiring expert analysis of observed images. Alternate modes of use allow for the TEM to observe modulations in chemical identity, crystal orientation, electronic structure and sample induced electron phase shift as well as the regular absorption based imaging. The TEM examinations were performed using TEM Models, Hitachi H-7500 and TECNAI $20G^2$ F TWIN and at different magnifications. For TEM study the synthesized powder was suspended in ethanol. One drop of the suspension was dropped on SiO_2 or carbon coated copper grid and alcohol was allowed to evaporate.

3.6.7 Selected area electron diffraction pattern

By adjusting the magnetic lenses such that the back focal plane of the lens rather than the imaging plane is placed on the imaging apparatus in TEM, a diffraction pattern can be generated. For thin crystalline samples, this produces an image that consists of a pattern of dots in the case of a single crystal, or a series of rings in the case of a polycrystalline or amorphous solid materials. For the single crystal case the diffraction pattern is dependent upon the orientation of the specimen and the structure of the sample illuminated by the electron beam. This image provides the investigator with information about the space group symmetries in the crystal and the crystal's orientation to the beam path.

3.6.8 Micro hardness testing

Micro hardness testing of metals, ceramics and composites is useful for a variety of applications for which 'macro' hardness measurements are unsuitable: testing very thin materials like foils, measuring individual microstructures within a larger matrix, or measuring the hardness gradients of a part along the cross section. Micro hardness testing per ASTM E-384 gives an allowable range of loads for testing with a diamond indenter; the resulting indentation is measured and converted to a hardness value. The actual indenters used are Vickers (more common; a square base diamond pyramid with an apical angle of 136°) or Knoop (a narrow rhombus shaped indenter).

Figure 3.6: Micro hardness testing machine.

The result for either Vickers or Knoop micro hardness is reported in kg/cm^2 and is proportional to the load divided by the square of the diagonal of the indentation measured from the test. Vickers micro hardness tester (Mitutoyo, Japan) is used for measuring micro hardness of the composites.

References

[1] F. O. Rice and R. E. Vollrath, Proceddings of National Academy of Science America, 15 (1929) 702-705.

[2] J. Christopher Brown, Erdogan Gulari, Catalysis Communications 5 (2004) 431–436.

[3] Wen-Jie Shen Yasuyuki Matsumura, Phys. Chem. Chem. Phys. 2 (2000) 1519-1522.

[4] S. H. C. Liang and I. D. Gay, Langmuir 1(1985) 593-599.

[5] V. I. Dvoryanchikov, M. M. Zaripilova and G. A. Rabadanov, Russian Journal of Physical Chemistry A, 82 (4) (2008) 677–679.

[6] B. D. Cullity, Elements of x-ray diffraction. Addison-Wesley Publishing, London. 1977.

[7] C.S. Barret, T.B. Massalski, Structure Metals, Oxford, Pergamon, 1980.

[8] S.B. Qadri, E.F. Skelton, D. Hsu, A.D. Dinsmore, J. Yang, H.F. Gray et al. Phys Rev B, 60(13) (1999) 9191-9193

[9] N. S. Ramgir, Y. K. Hwang, I. S. Mulla, J.S. Chang, Solid State Sci, 8 (2006) 359-362.

[10] A. L. Patterson, Phys Rev, 56 (1939) 978-982.

Chapter 4

RESULTS AND DISCUSSION

Overview

This chapter is divided in **three sections**; in the **first section** results obtained from thermo-chemical synthesis method are presented and discussed in detail. On the basis of the results obtained by XRD, DTA/TGA and TEM a possible mechanism for the conversion of tungsten oxide to tungsten carbide nano particles is proposed. The results of other experiments performed to confirm the proposed mechanism are also presented and discussed in this section. In the **second section** the results obtained from mechano-chemical synthesis method are presented and discussed. The role of different carbon sources is also discussed. The **third section** deals with the discussion on the results obtained from WC-Co composites synthesized using WC nano particles obtained from both the synthesis routes.

4 WC nano particles by thermo-chemical route

There are three major constituents for the synthesis of WC nano particles: tungsten source, carbon source and reducing agent. Tungsten source react with the carbon source to form the desired product and reducing agent facilitate the reaction. It is very important to choose a proper reactant and reducing agent to get the desired product. In this study three hydrocarbon derivatives such as methanol, ethanol and acetone were used as carbon source. In addition to these, WO_3 was used as tungsten source in the presence of reducing agent magnesium. The basic idea to use derivates of hydrocarbon is that they decompose thermally to form CO and H_2 [1]. H_2 facilitate reduction of tungsten to WC also pressure generated by it is very helpful in the synthesis of WC nano particles [2].

4.1 Synthesis of the WC nano particles

The preparation of WC nano powders was carried out in a specially designed stainless steel autoclave. The initial ingredients of the chemicals, their weight and sample label along with carbon source are given in table 4.1.

Table 4.1: Initial ingredients with sample label.

Sample's Label	**WO_3 (g)**	**Mg (g)**	**Carbon Source (ml)**
A(M)	3	1	20 (Methanol)
A(E)	3	1	20 (Ethanol)
A(A)	3	1	30 (Acetone)

Samples A(M), A(E) and A(A) were synthesized using methanol, ethanol and acetone as carbon source respectively. Appropriate amount of WO_3, Mg and anhydrous methanol/ethanol/acetone were put into a specially designed stainless steel autoclave as given in table 4.1. The sealed autoclave was kept into a resistance heating furnace. The temperature of the furnace was increased from room temperature to 600 ºC with heating rate of 5 ºC/min. The autoclave was kept inside the furnace for 15 h followed by furnace cooling of the autoclave. After reaction, the dark solid powder was taken out from the autoclave and dissolved in HCl (1:1) to remove unreacted Mg and other soluble phases from the product. The acid treated samples were washed with distilled water followed by ethanol to eliminate the water absorbed in the powders. The dried powders were characterized to investigate the formation of WC phase in the synthesized mass.

4.1.1 XRD analysis: Methanol as carbon source

A typical XRD for A(M) is presented in figure 4.1. The XRD is indexed with WO_3 (ICDD card No 83-0949), carbon (ICDD card No 75-2078), WC(ICDD card No 25-1047) and $MgWO_4$ (ICDD card No 70190) phases. The presence of unreacted WO_3 and excess amount of carbon showed that the reaction has not started. The reaction variables needed to be modified to start the reaction. In order to get the desired combination, different ratios of WO_3 (1,2 and 4 g), activated magnesium turning (2,3, and 4g) and methanol (12,24 and 42 ml) were tried but WC phase was not formed in any of these experiment.

The possible reaction which may have occurred at 600 ºC.

$$WO_3 + 2CH_3OH + Mg \rightarrow 2C + MgWO_4 + H_2O + 3H_2 \tag{4.1}$$

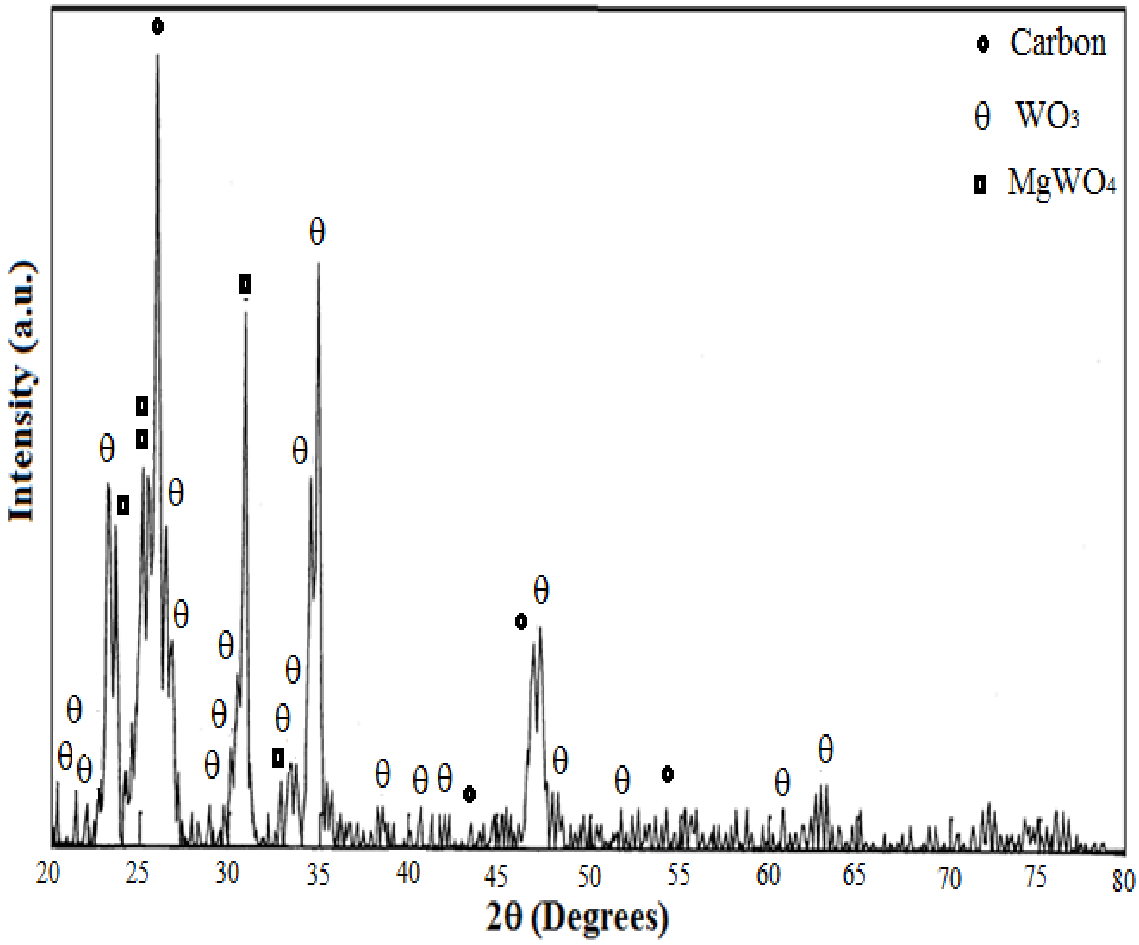

Figure 4.1: XRD pattern of product phases when methanol was used as carbon source.

As mentioned above the factors which facilitate the reaction is the combined effect of reducing agent and generated H_2. Apart from this, the amount of carbon present may also affect the reaction. As compared to reducing agent variation, the variation of carbon source was easy to handle so ethanol was used as carbon source to see the possibility of the formation of WC nano particles.

4.1.2 XRD analysis: Ethanol as carbon source

When ethanol is used as carbon source A(E) with a typical combination of reactants (table 4.1), WC nano particles are formed as indicated in figure 4.2(a,b). The XRD pattern of the as synthesized sample showed the presence of $MgWO_4$ and C phases along with WC, and WO_3 phases (figure 4.1 (a)). After acid treatment the sample exhibited WC, C and unreacted WO_3 phases. However, the XRD peaks of WC became broader after acid treatment (figure 4.2(b)), particularly WO_3 phase. This might be attributed to the fact that HCl also effect the WO_3 phase and leach out some portion of WO_3 phase.

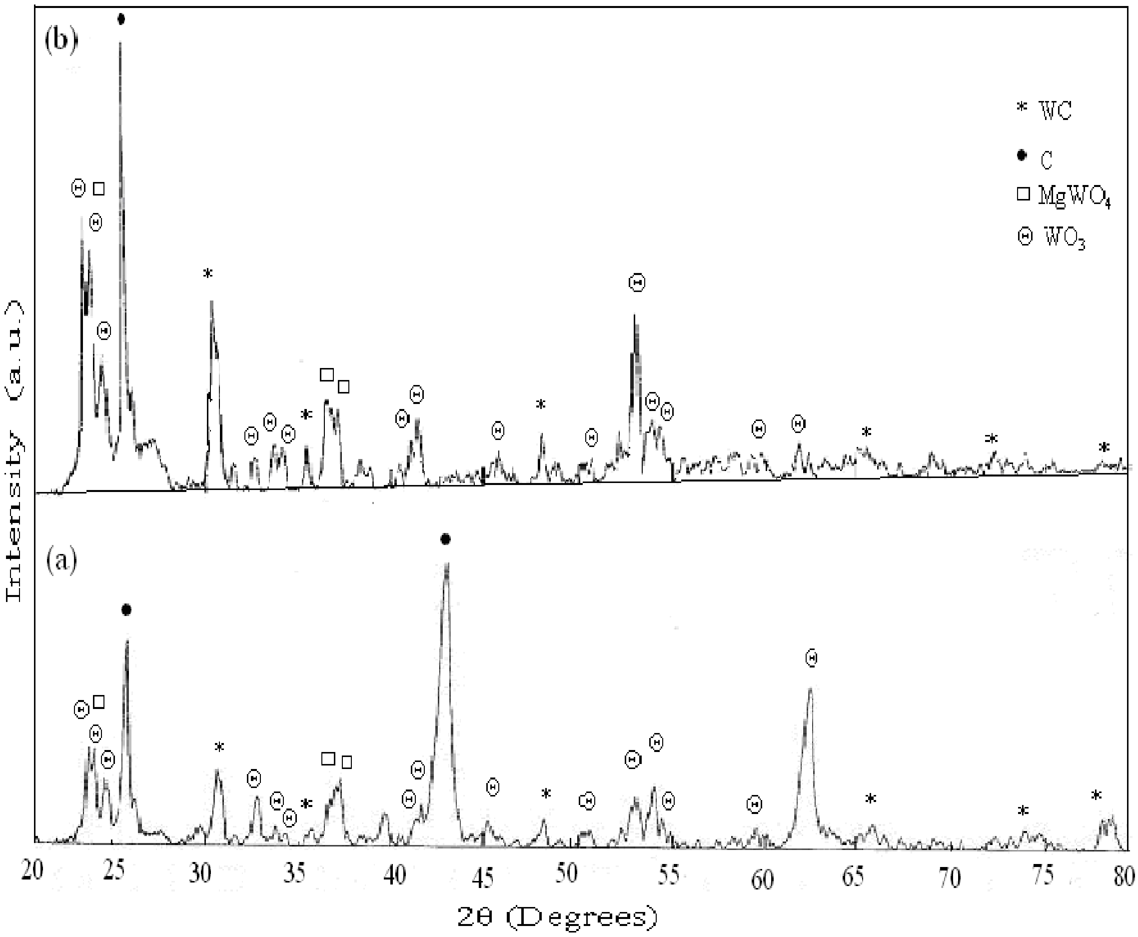

Figure: 4.2: XRD pattern of the product phases when ethanol was used as carbon source.

In addition to this, the peaks of WC and WO_3 are shifted to the lower angle as compared to standard WC (ICDD card No.25-1047), $MgWO_4$ (ICDD card No.27-0789) and WO_3 (ICDD card No.83-0949) peaks which clearly indicates that the disordering is increasing in this sample. The disordering might be due to high aspect ratio of WC nano particles as compared to the crystalline counterparts of WC. The possible reaction which may occur with ethanol:

$$2WO_3 + 2CH_3CH_2OH + Mg \rightarrow WC + C + MgWO_4 + 6H_2 + 2CO_2 \tag{4.2}$$

$$CH_3CH_2OH + Mg \rightarrow MgO + C_2H_6 \tag{4.3}$$

The lattice parameter was calculated using Bragg's law. Calculated lattice constant for WC phase are: a = 2.896 Å, c = 2.838 Å were very close to the reported value of hexagonal WC (a = 2.906 Å, c = 2.837 Å, ICDD card No.25-1047). In the sample the weak reflection is also observed at ~26.58° which could be attributed to (002) reflection of carbon (ICDD Card No. 26-1077).

Different combinations of reactants were unable to increase the yield of WC nano particles and unreacted WO_3 was always present along with excess amount of carbon. It forced to try another hydrocarbon derivative and acetone was selected for the same.

4.1.3 XRD analysis: Acetone as carbon source

XRD for a typical combination of reactants A(E) (table 4.1) is presented here (figure 4.3(a,b). It also showed the presence of $MgWO_4$ and C phases along with WC, and WO_3 phases. The possible reaction for this combination is:

$$2WO_3 + 4CH_3COCH_3 + Mg \rightarrow WC + 8C + MgWO_4 + 12H_2 + 3CO_2 \tag{4.4}$$

In comparison, to the XRD pattern of sample synthesized using ethanol, this sample showed broader peaks of WO_3 phase. On the other hand the peak width of WC phase is less as compared to the ethanol based sample. The major striking difference of the XRD pattern in both the cases is that the intensities of carbon peaks decreases when acetone was used as a carbon source. The XRD patterns of both the samples were indexed with monoclinic form of WO_3 phase (ICDD card No.83-0951).

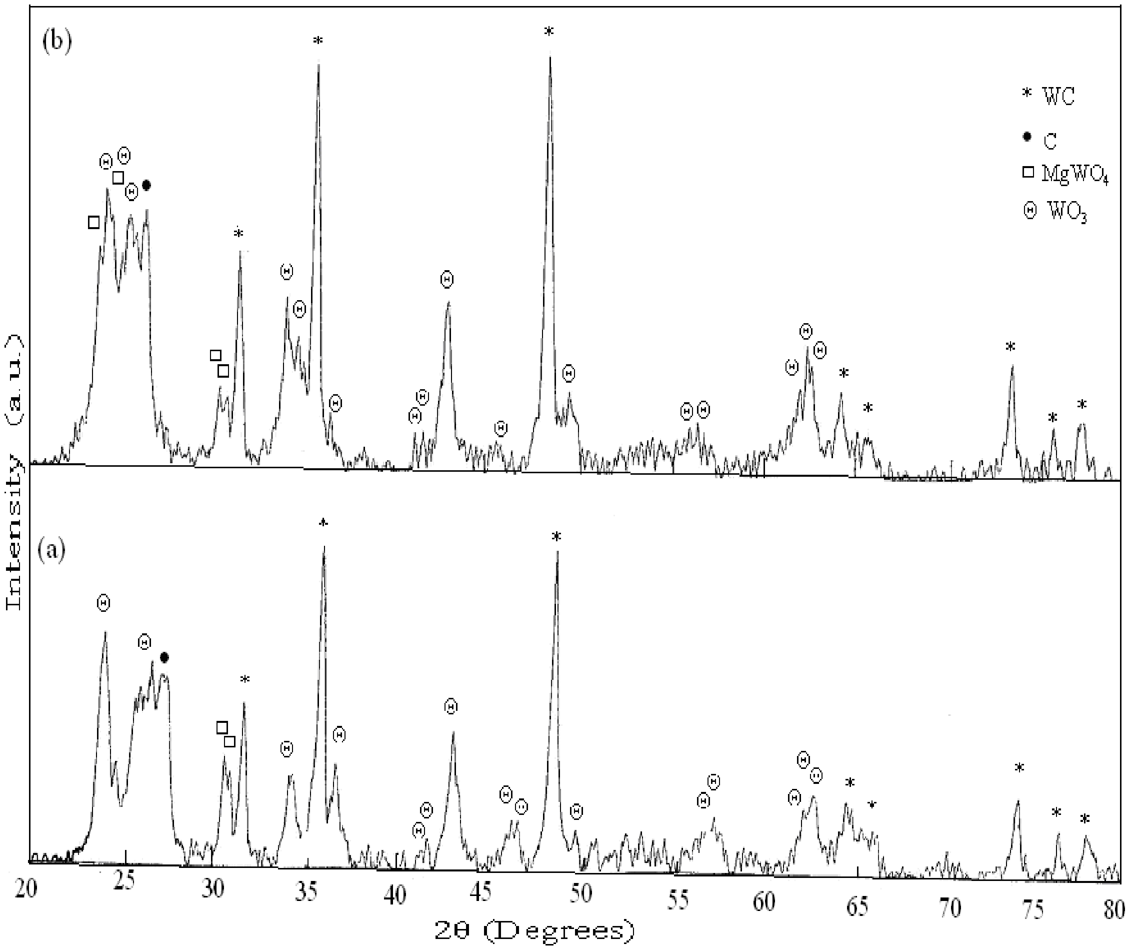

Figure 4.3: XRD pattern of product phases when acetone was used as carbon source.

Chunli Guo et al. [2] have reported the influence of the system pressure and reaction time and reaction temperature for the synthesis of WC. Since in our experiments the carbon source was different and the vapor pressure of acetone is more than the ethanol so, the carbon product is very less or negligible in case of acetone or else the carbon produced are consumed in the reduction process. In this case also the lattice parameter was calculated using Bragg's law for WC phase a = 2.901 Å, c = 2.832 Å which were in close proximation of the standard value. It seems from the XRD analysis of both carbon sources ethanol A(E) and acetone A(A) showed that acetone is most suitable for further synthesis but only XRD analysis is not enough so further comparative characterizations were also done.

4.2 DTA/TGA analysis of A(A) and A(E) samples

Samples prepared using acetone and ethanol were examined by DTA/TGA to check their stability and phase transitions. The DTA/TGA plots of both the samples are shown in figure 4.4 and 4.5. The A(A) sample showed one exothermic peaks at 640 °C. This broad peak at 640 °C may be attributed to the combustion of the carboneous matter. The DTA plot of A(E) sample showed a broad exothermic peak which was observed at 580°C as shown in figure 4.5. The TGA plot of sample A(A) exhibit 12% weight loss as compared to the sample A(E) which shows 90% weight loss (figure (4.5)). The weight loss of this particular sample clearly indicates that the carbon content in this sample A(E) is more as compared to A(A) sample. In a separate study Yu et al. [3] have reported the thermal decomposion of carbon nano tubes. In their results they have mentioned that oxidation of carbon nano tube begins from 530 ºC and combustion is completed at 678 ºC at the heating rate of 10 ºC/ min. Our findings also match with the study which indicated that the above mentioned carboneous matter may be carbon nano tubes (CNTs).

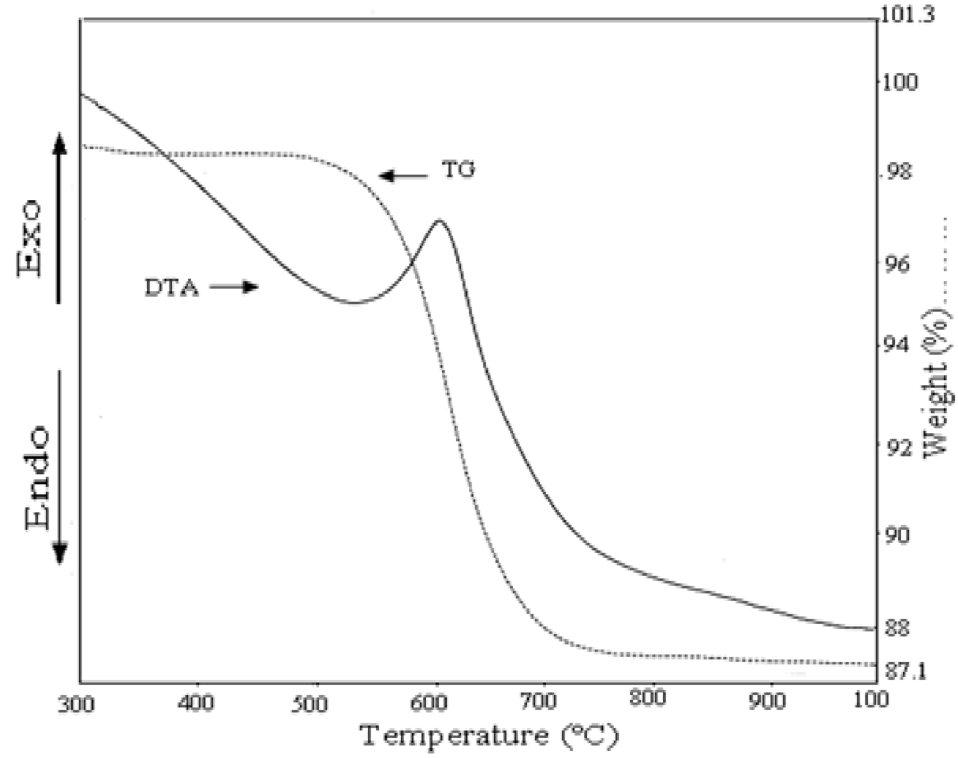

Figure 4.4: DTA/TGA graph of sample A(A).

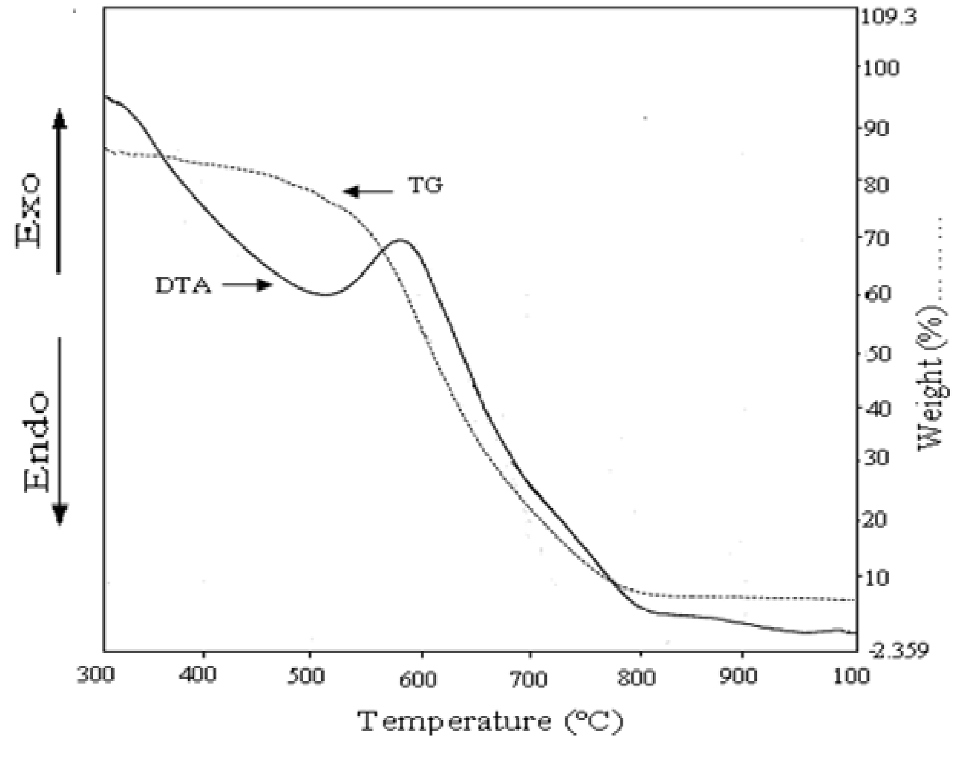

Figure 4.5: DTA/TGA graph of sample A(E).

To confirm the formation of CNTs another experiment was performed which is discussed in detailed in section 4.4 which also helped to propose a synthesis mechanism.

4.3. TEM analysis of A(A) and A(E) samples

TEM studies indicate that reduction of WO_3 takes place by adsorption of carbon at the surface of WO_3 first. These carbon particles engulf the WO_3 particle as can be seen in figure 4.6.

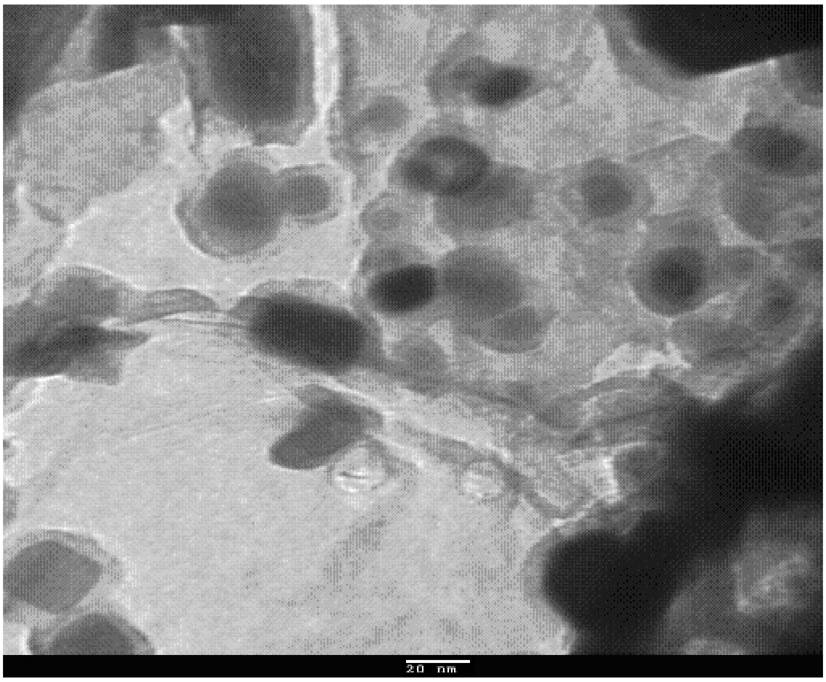

Figure 4.6: TEM image of sample A(A) showing engulfing nature of carbon.

The variation in contrast observed indicate that the transformation of WO_3 to WC is a multistage phenomenon. As the concentration of C increases at the surface, the WO_3 particles gets bind itself within the carbon layer (figure 4.7).

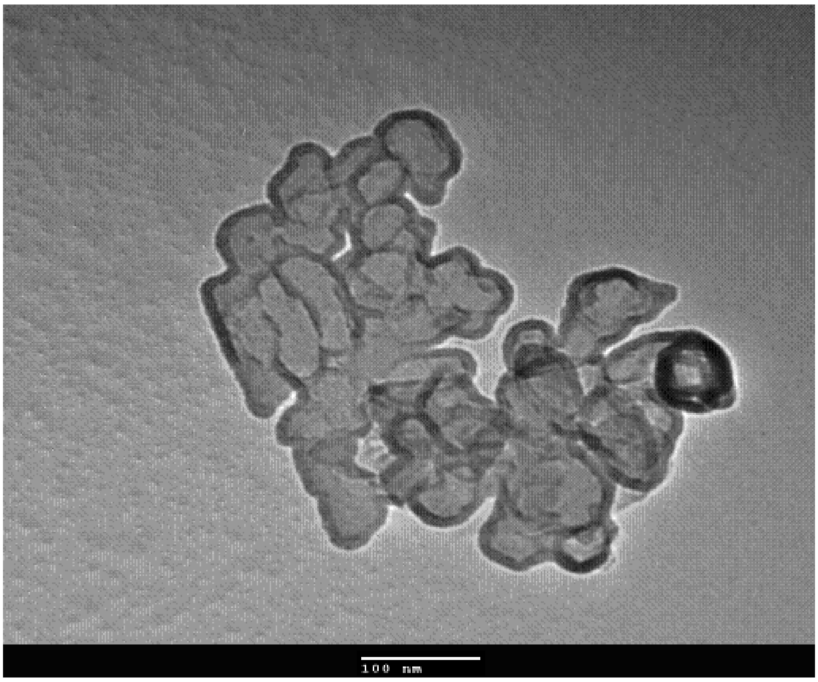

Figure 4.7: TEM image of sample A(A) showing individual WO_3 particle coated with carbon.

In a report Swift and Koc et al. [4] have reported the formation of WC from carbon coated WO_3 precursors. The TEM micrograph of carbon coated WO_3 precursors has similar resemblance to our micrograph (figure 4.7). As the concentration of carbon increases on the surface of WO_3 the process of transformation of WO_3 to WC starts as is evident from the faceted morphological feature (figure 4.8). The excess carbon existing on the surface tries to acquire the shape of carbon nano tube. The formation of the tube occurs through defect structures. The presence of amorphous carbon on the outer surface facilitates the process of reduction of WO_3 to WC. However, because of conducive atmosphere and also the formation of ethane and hydrogen during course of reaction leads to formation of such features.

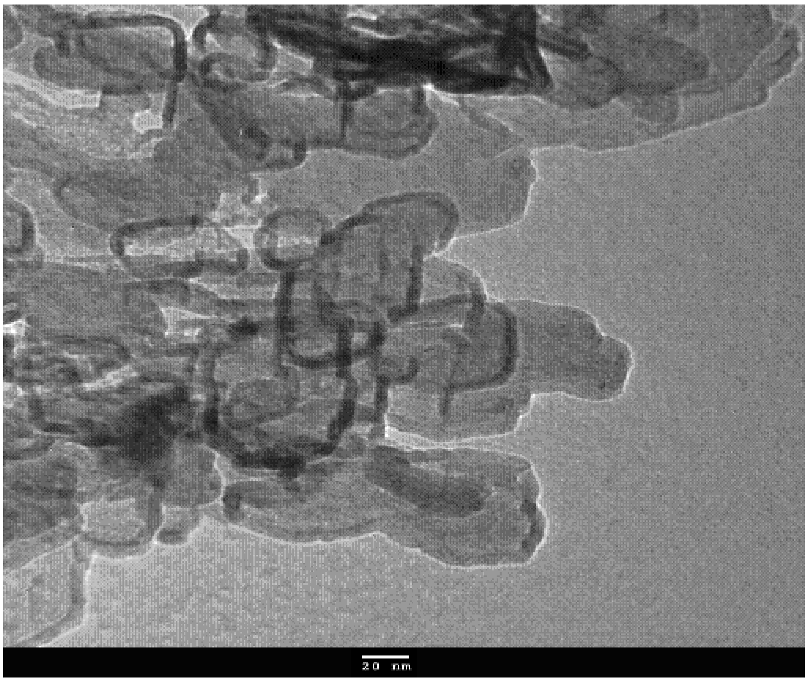

Figure 4.8: TEM image of sample A(A) showing formation of carbon nano tube.

The preparation route for the carbon nano tube from a mixture of ethane and hydrogen has been reported in several publications [5-6]. However, in most of these reports, apart from ethane and hydrogen, a catalyst is required for the synthesis of carbon nano tube [5-6]. In this present work either MgO or WO_3 is acting as surface catalyst. Moreover, the constituents present in autoclave cannot be ignored. The formation of mesoporous substance with controlled pore size, large pore volume and surface area which provide good electrochemical catalytic properties have been reported for WO_3 [7]. These mesoporous structure in WO_3 provide active site for hydrogen oxidations. The formation of the nano tube starts at different nodes (mesoporous) as can be seen in figure 4.9.

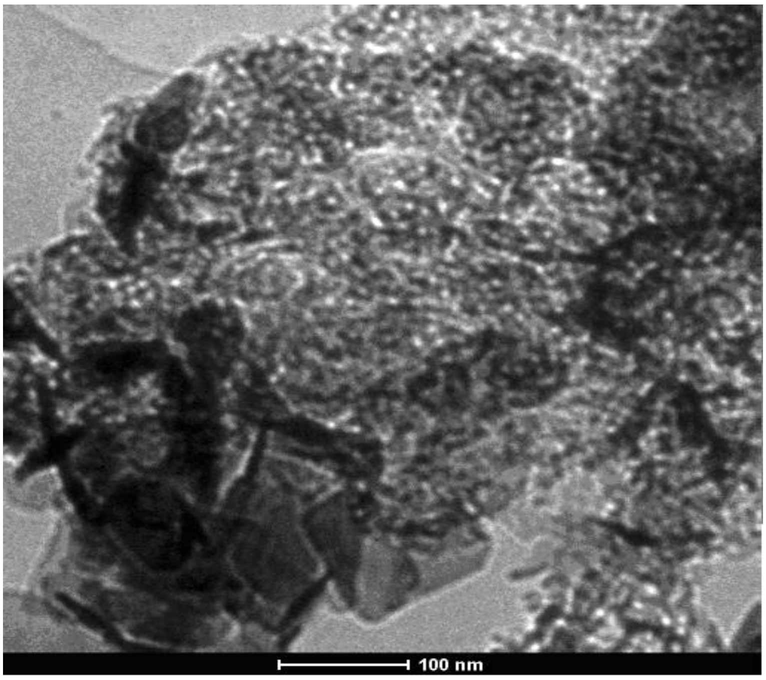

Figure 4.9: TEM image of sample A(E) showing porous nature and nucleation of carbon nano tube.

The surface gives the appearance of porous substance which has resemblance of mesoporous structure. The WO_3 particles are totally covered with porous amorphous carbon. The volume fraction of porous carbon increases during course of reaction. The pores existing at the surface provide nodal point for the diffusion of carbon. These nodal points provide active centre for reduction to occur. With variation in experimental conditions inside the autoclave the volume fraction of nano tube increases and after attaining critical condition these bursts (figure 4.10) leading to ejection of well formed crystals of WC (figure 4.11(a)) with respective SAED pattern in figure 4.11(b).

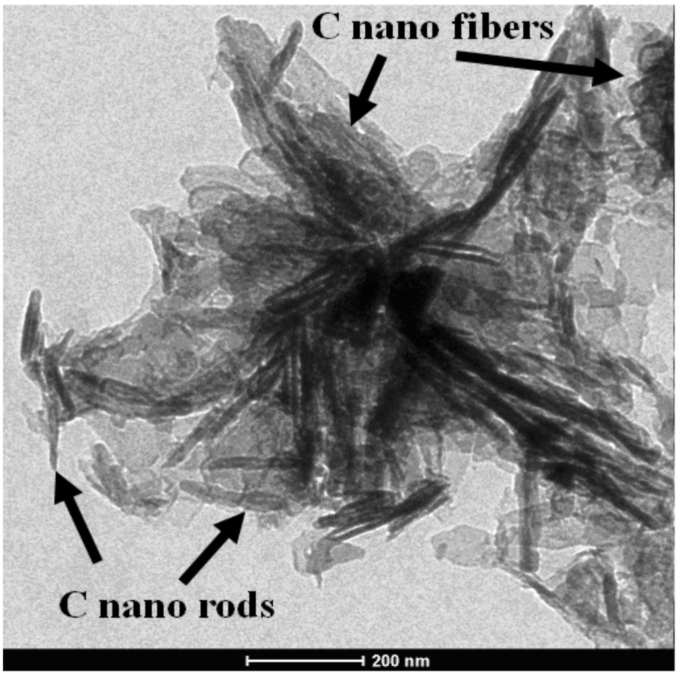

Figure 4.10: TEM image of sample A(E) showing bursting of carbon nano tube and formation of carbon nano fiber.

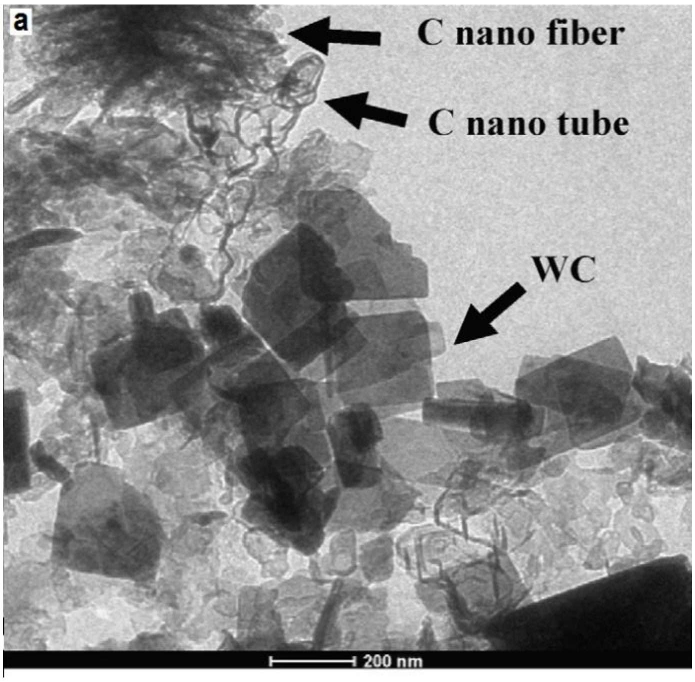

Figure 4.11(a): TEM image of sample A(E) showing faceted structure of WC particle.

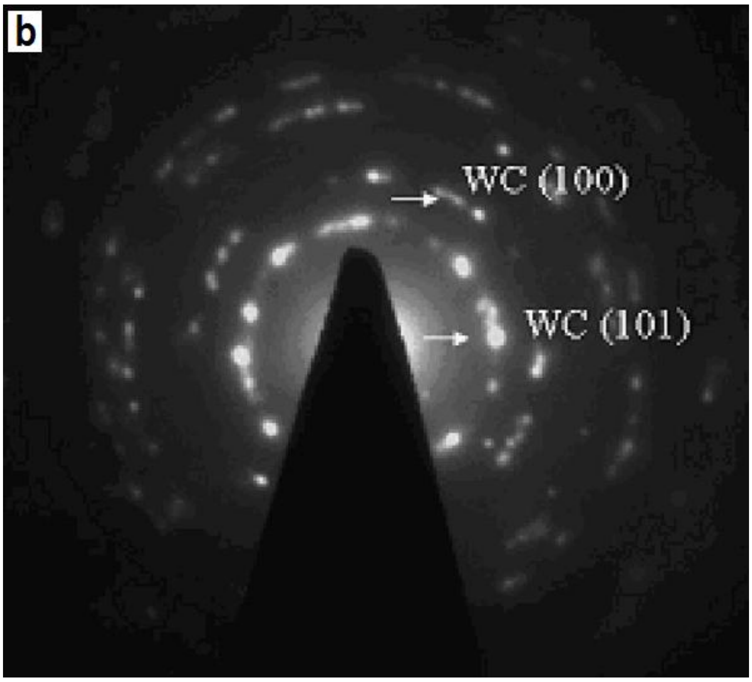

Figure 4.11(b): SAED pattern of WC particle of sample A(E).

In our experiment it was observed that unreacted WO_3 also exist. This is because of the fact that the carbon which is required for its reduction gets converted to carbon nano tube at the nodal points (pores) and because of this the active carbon required for reduction is not available at the surface. Based on the analysis of TEM structure observed in these experiments a possible mechanism for the formation of WC nano particles is illustrated in figure (4.12). Here the carbon which is responsible for reduction of WO_3 is amorphous carbon [4]. However, apart from amorphous carbon the structures observed give the formation of carbon nanotube and carbon nano fiber also. In order to confirm the nature of carbon, a separate experiment with carbon source alone was performed which is described in next section.

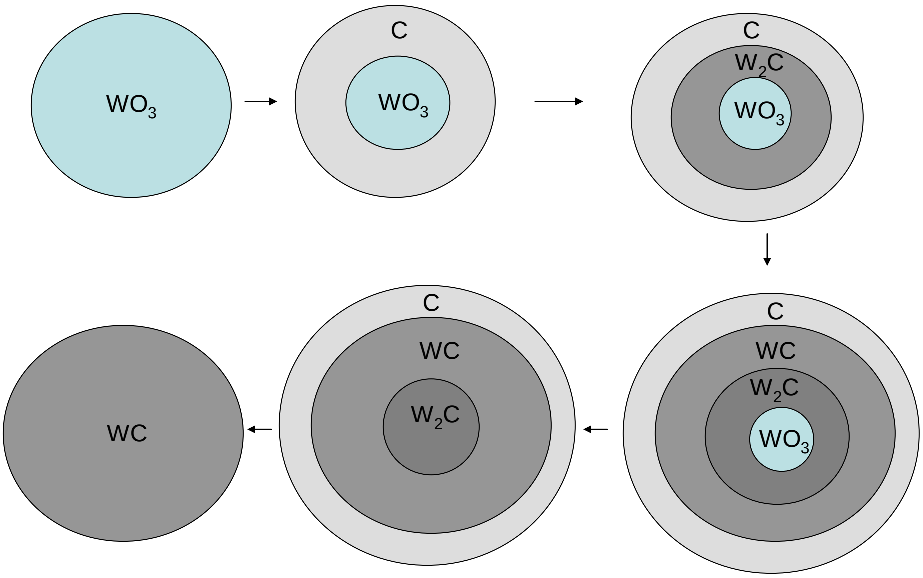

Figure 4.12: Mechanism for the formation of WC nano particles.

4.4 Synthesis of carbon nano tubes

In a separate experiment, autoclave was filled with acetone ensuring almost negligible oxygen present in the system. It was then sealed properly. This sealed autoclave was kept in a resistance heating furnace. The temperature of the furnace was increased from room temperature to 650 ºC with heating rate of 5 ºC/min. The heating of autoclave was done for 20 h at 650 ºC followed by furnace cooling. After completion of experiment, the dark solid powder was taken out from the autoclave.

4.4.1 XRD analysis of CNTs synthesized by thermo-chemical method

Acetone heated at 650 ºC for 20 h in the autoclave resulted a black mass indexed for carbon (ICDD card No. 41-1487) (figure 4.13(a)). The formation of carbon can be explained on the basis of following reaction:

$$CH_3COCH_3 \xrightarrow{\Delta} 3C + H_2O + 2H_2 \qquad (4.5)$$

During experiment acetone might have decomposed at 650 ºC due to high pressure which is created in autoclave. The lattice constants of the sample are calculated using following equation [8].

$$\frac{1}{d^2} = \frac{4}{3}\left(\frac{h^2 + hk + k^2}{a^2}\right) + \frac{l^2}{c^2} \qquad (4.6)$$

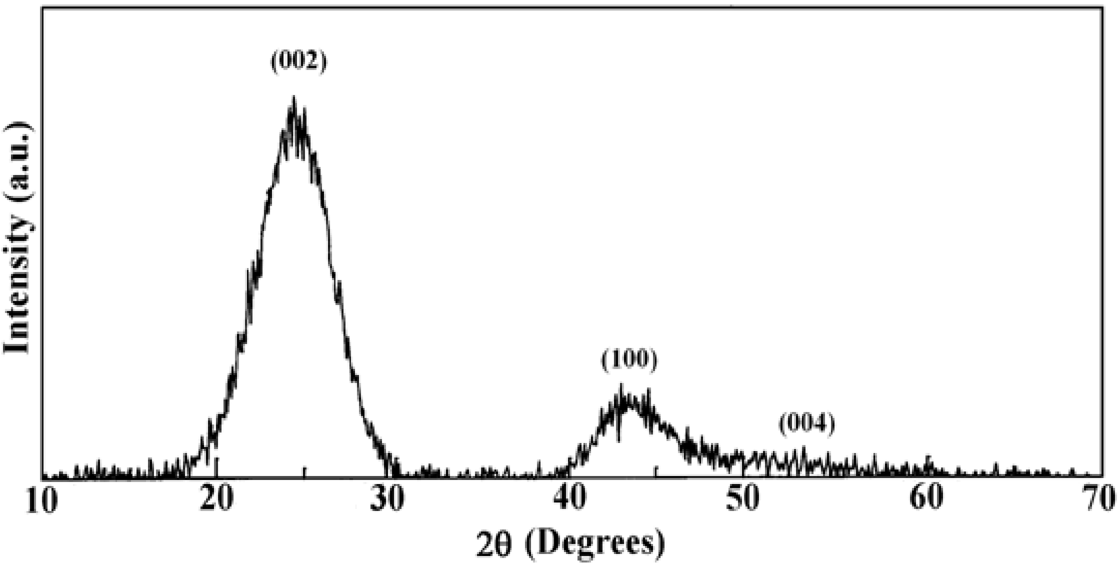

Figure 4.13(a): XRD pattern of carbon nano tube.

Where ‘a’ and ‘c’ are the lattice parameters, ‘h’, ‘k’ and ‘l’ are the miller indices and ‘d’ is the inter planer spacing. The calculated lattice constants a =2.38 Å, c =6.68 Å are very close to the reported value of carbon, a =2.470 Å, c =6.724 Å (ICDD card No. 41-1487). However, the diffraction peaks are shifted at higher 2θ values as compared to reported values which suggest the compressive strain in the lattice of present sample [9]. The broadening of XRD peaks indicates that the surface areas of particles are very large as compared to the standard graphite [5]. The particle size of the as prepared sample is calculated using XRD pattern. The full width at half maximum (β) of the diffraction peaks can be expressed as a linear combination of the contributions from the strain (ε) and particle size (L). Therefore, crystallite size can be calculated from the following relation [10].

$$\frac{\beta\cos\theta}{\lambda} = \frac{1}{L} + \frac{\varepsilon\sin\theta}{\lambda} \tag{4.7}$$

Figure 4.13(b) represents the plots of (sin θ) versus (β cosθ) for present sample which is a straight line.

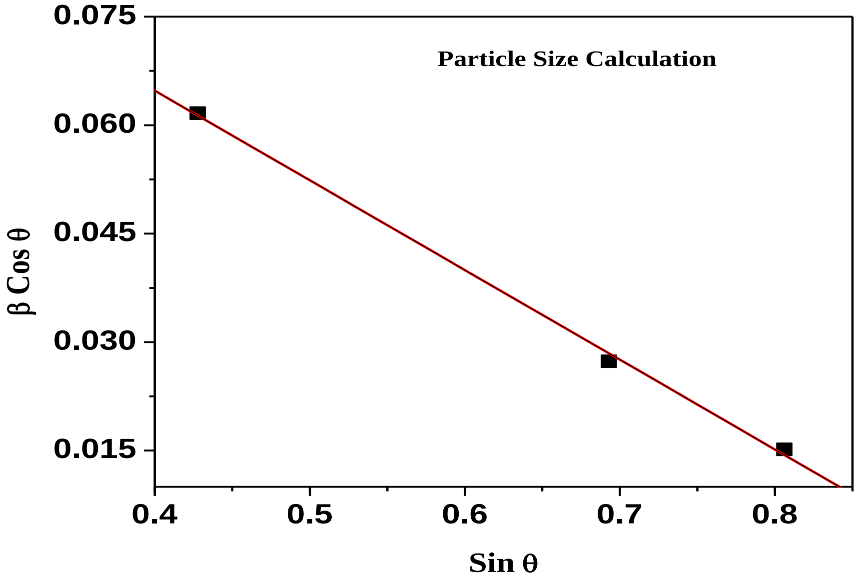

Figure 4.13(b): Graph between sin (θ) and β cos (θ)

The intercepts on the (β cosθ) axis equals to λ/L which gives the average particle size of as prepared sample. This comes out to be 3 nm. The strain rate is also calculated using the above equation which is equal to the slope of the plot as shown in figure 4.13(b) and it is -0.124. The negative slope indicates the presence of effective compressive strain in the crystal lattice which is also verified by the shifting of XRD peaks at higher diffraction angle. The higher magnitude of slope in the present sample suggests the enhancement in the strain with reduction of particle size [11]. Basically ‘β’ is inversely proportional to the diameter of particle which is very large corresponding to very small diameter of particle [12].

In the earlier reports, it is mentioned that the decomposition temperature and catalysts play very important role in synthesis of CNT. The diameter of CNT is function of catalyst and decomposition temperature. Higher decomposition temperature leads to formation of lower diameter of CNT [13]. In the present study, the diameter of the carbon particle which is CNT as described later is in the range of 3 to 14 nm. Moreover, no catalyst was used externally to decrease the decomposition temperature as reported earlier [14].

4.4.2 DTA/TGA analysis of CNTs

The DTA and TGA studies were done to find the decomposition temperature of carbon nanotubes. The DTA was done at different heating rates, 5 and 10 ºC/min which is shown in figure 4.14. The sharp exothermic peak observed at 615 ºC with small kink at 620 ºC in DTA curve corresponds to the presence of two types of carbon. The second peak in DTA curve was resolved after using higher heating rate during the experimentation i.e. 10 ºC/min. Figure 4.14 clearly indicates two exothermic peaks at 630 ºC and at 645 ºC. These two peaks clearly establish that the present sample exhibit two forms of CNT which may be SWCNTs and MWCNTs or it is also possible that these may be MWCNT with variation in diameters. The first peak observed is due to decomposition of thicker MWCNTs. On the other hand, the second peak in DTA curve might be due to the decomposition of thinner MWCNTs because thinner samples has higher stability as compared to thicker one [13].

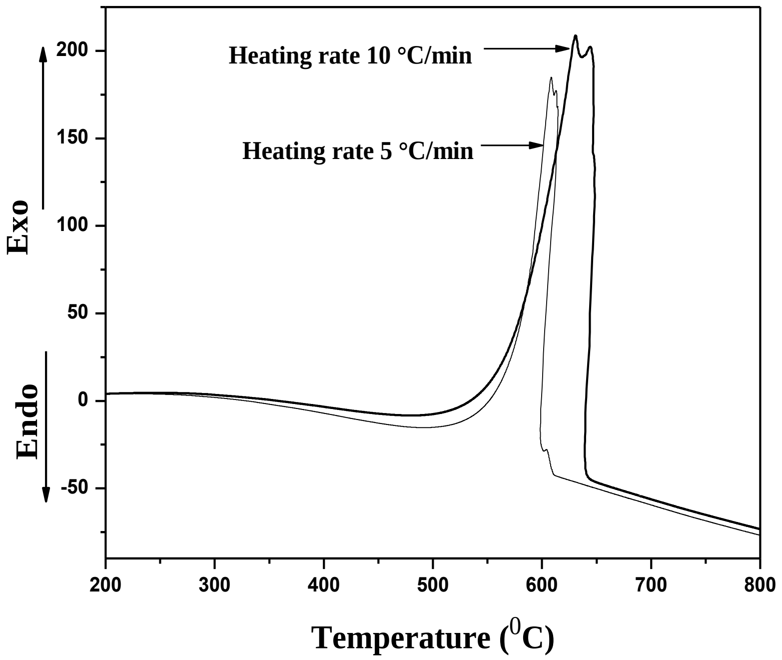

Figure 4.14: DTA Plot of CNTs at different heating rates showing exothermic peaks.

Some researchers have also reported the presence of two type of carbon. Obviously, thicker MWCNT decomposes at lower temperature as compared to SWCNT or thinner MWCNT due to the presence of higher defects in MWCNT. The splitting in peak corresponds to existence of these morphologies during combustion reaction [3]. The shifting of exothermic peak at high temperature with increasing heating rate is well established phenomenon which is observed due to delaying in decomposition of nanotubes. The peaks in DTA scan correspond to the temperature at which the rate of decomposition of CNT into CO_2 in presence of O_2 is maximum. Figure 4.15 shows TG curve with different heating rates. The weight loss observed is only 3% up to 500 ºC. Hou et al. [15] have reported that burning of impurities of amorphous carbon or carbon nano particles with more structural defects occur below 520 °C while CNTs burns at comparably high temperature. Thus we can conclude that the amount of amorphous carbon is very less in the present sample.

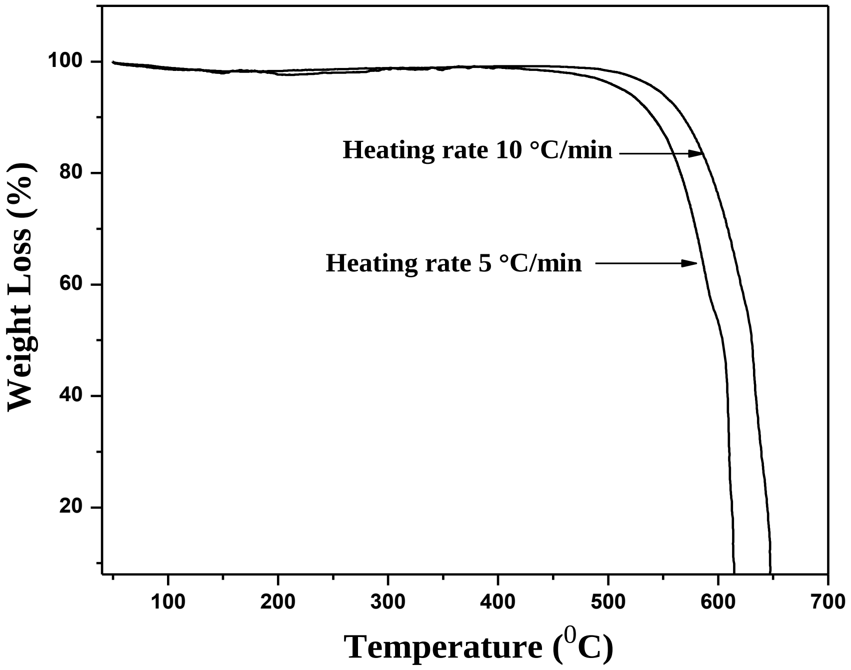

Figure 4.15: TGA Plot at two different heating rates showing loss of carbon.

4.4.3 Raman spectrum of CNTs

Raman spectrum shown in figure 4.16 is characterized by two main signals, corresponding to G-band and D-band. The G-band around 1581 cm^{-1} is due to the tangential phonon modes of graphitic sheets, and the D-band around 1350 cm^{-1} responses to the presence of defects or amorphous carbon [16-17]. The intensity of the G-band is stronger than that of the G-band. The I_G/I_D ratio of the as-grown MWCNT is 2.0, which indicates the existence of amorphous carbon impurities or lattice defects [18-20].

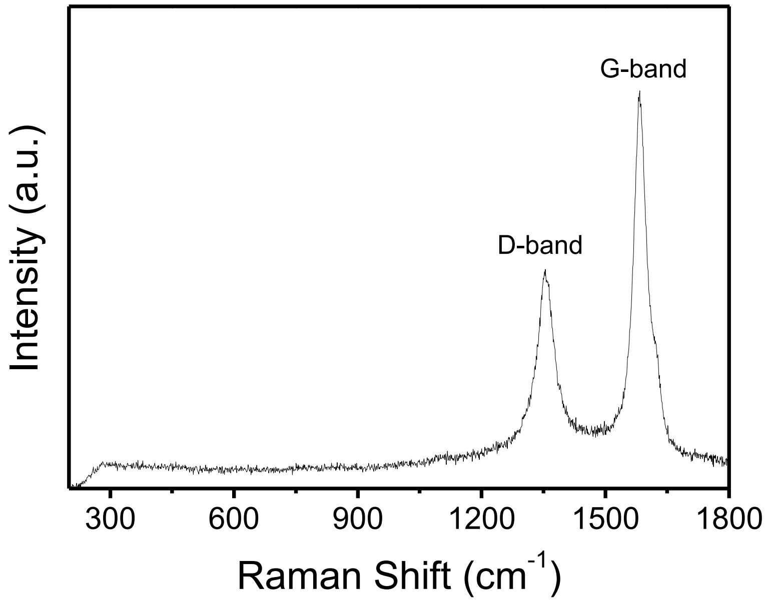

Figure 4.16: Raman spectrum of synthesized carbon nano tubes.

4.4.4 TEM studies of CNTs

Detailed TEM studies show that the size of the nano tube is in the range of 3 to 14 nm. The selected area electron diffraction pattern [SAED] of sample gives three rings corresponding to three different planes of carbon. However, presence of iron (Fe) is also observed in some of the samples and indexed in SAED pattern.

4.4.4.1 Growth Mechanism

At high temperature and pressure it is feasible that a turbulent situation in the autoclave may exist. Though autoclave is heated at constant temperature but possibility exists for temperature gradient in the system. Because of this there is continuous fluid flow from high temperature to low temperature within the autoclave. This may cause reflux action within the system. This refluxing may lead to formation of gelatinous substance. In due course of time this gelatinous substance gets converted into carbon-rich and carbon less zones as shown in figure 4.17.

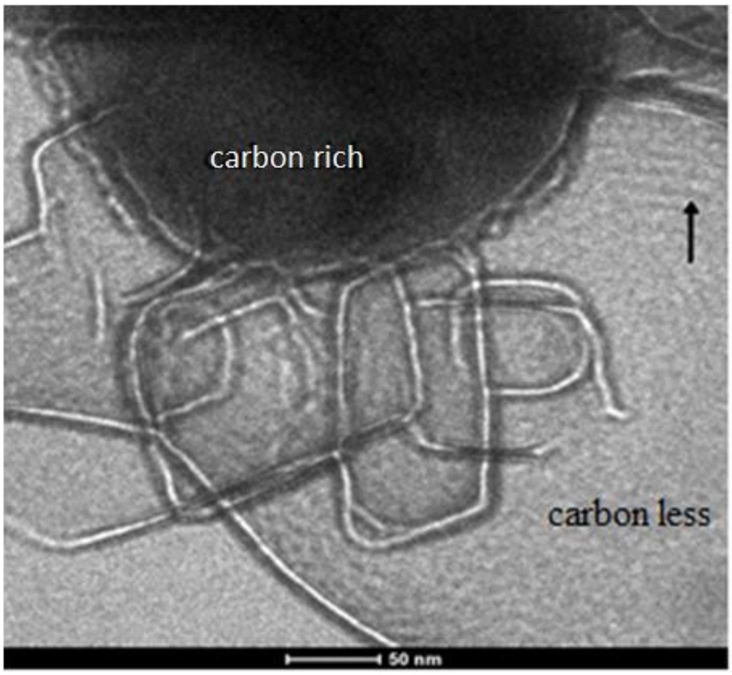

Figure 4.17: TEM showing growth of carbon nano tube from the interface.

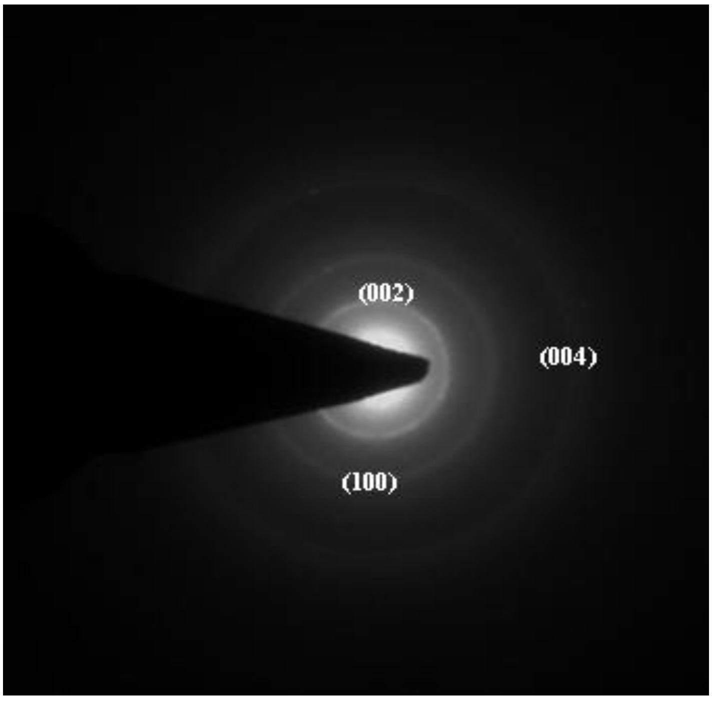

Figure 4.18: SAED pattern of carbon nano tube.

The black area is carbon rich (CR) and light one is carbon less zones (CL). The presence of wavy pattern near the interface indicates the turbulent type of situation also. Figure 4.18 is the corresponding SAED of carbon nano tube as shown in figure 4.17. The nucleation of carbon nano tube occurs from the interface of these zones (CR and CL) as is apparent in Figure 4.17. Growth of tube occurs in the low viscosity zone (CL). It is observed that some iron particles from the autoclave have diffused at elevated temperature which is trapped in CNTs (figure 4.19, 4.20). This iron may have transformed from the solid state into a quasi-liquid state despite of the fact that synthesis temperature was lower than the melting point of iron [11]. This iron particle may act as a nucleation site for the growth of carbon nanotube (a catalytic action also).

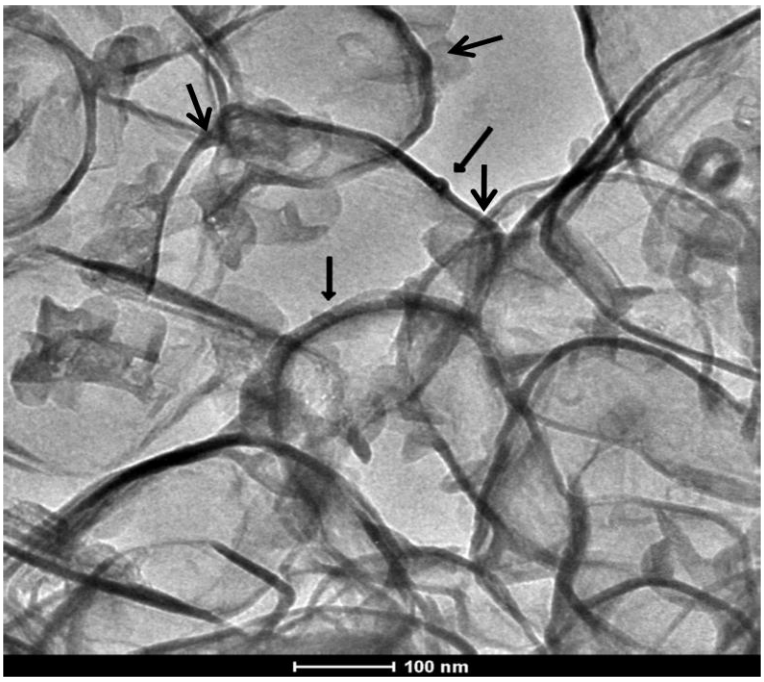

Figure 4.19: TEM of Sample showing presence of nano tube along with Fe particles.

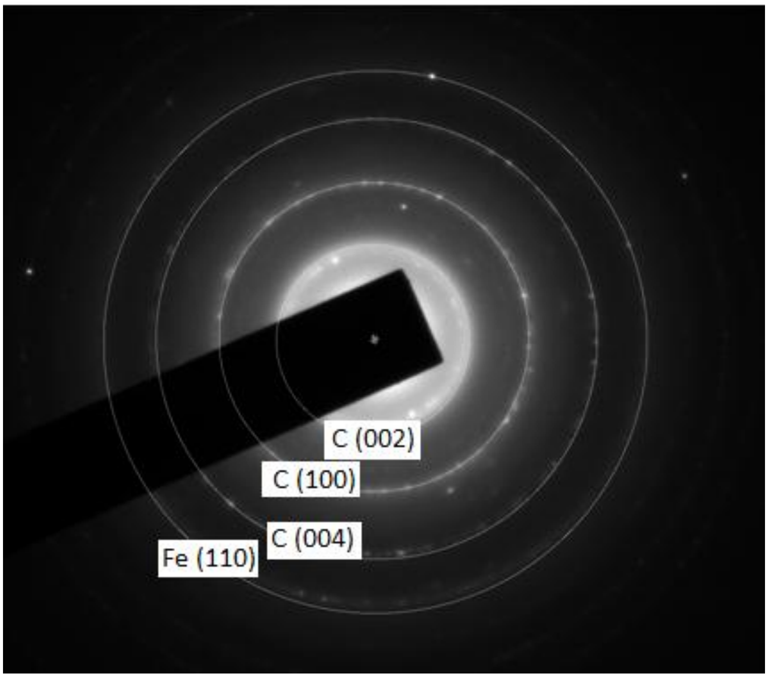

Figure 4.20: SAED pattern of nano tube along with Fe particles.

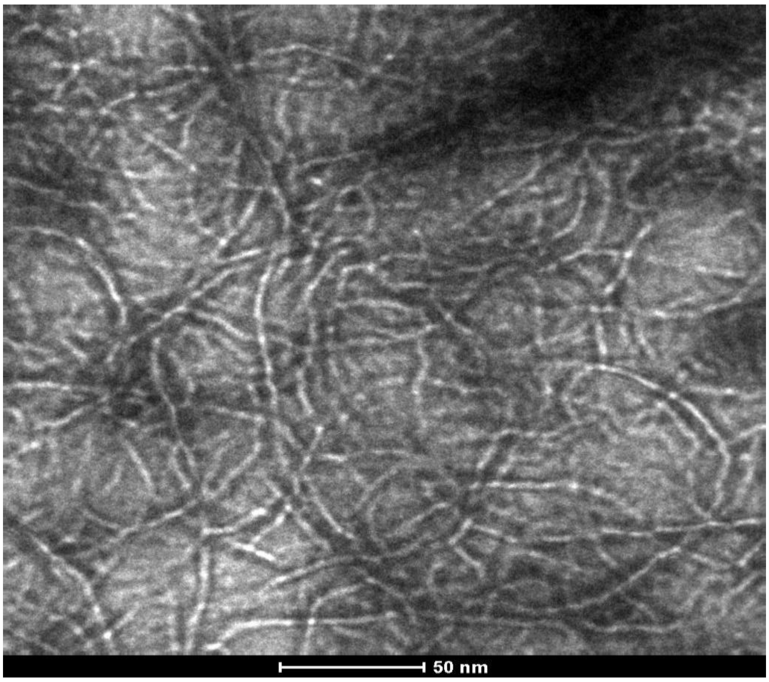

Figure 4.21: Fully grown Carbon nano tubes

A careful examination of the interface (figure 4.17) indicates that the growth methodology of the nanotube is faceted type (sharp bend rectangular mode) and the growth has occurred in the less viscous (CL) region. The preferred growth morphology of the nano tube is observed throughout the area (figure 4.21).

In same part banded type of morphology which is the case of initial nucleation and growth is also visible (marked as arrow in figure 4.17). As per Jackson model [21-22] which describes a relationship of relative change in surface free energy as a function of the fraction of sites which are occupied with variation in 'α' parameter. Where $\alpha = \frac{L_m}{KT_m}\xi$, the 'α' parameter depends on the latent heat (L_m), equilibrium temperature (T_m), boltzmann constant (k) and the crystallographic factor (ξ) which indicates the fraction of total binding energy which binds the atom in a layer parallel to the plane face to other atom in the layer. 'α' also depends upon the crystal face, the type of crystal and the phase from which the crystal is growing [21]. The sharp aligned growth of faceted type is only possible when 'α' lies in between 2 and 5. The small difference in the free energy between two faces of similar composition may result in the kinetically preferred intermediate metastable phase. However, the details of this are described in subsequent section (4.5.1). The variation in structure in large chain type morphology (figure 4.22 bottom sides) can lead to secure anisotropy in surface energy. This further leads to variation in growth morphology of phase [22]. Moreover, the system is under supercritical stage which is the area where little literature is available [18-20]. This influences the interface type of growth kinetics rather than phase separation leading to faceting tendency (phase separation has already occurred; carbon-rich zone and carbon less zone).

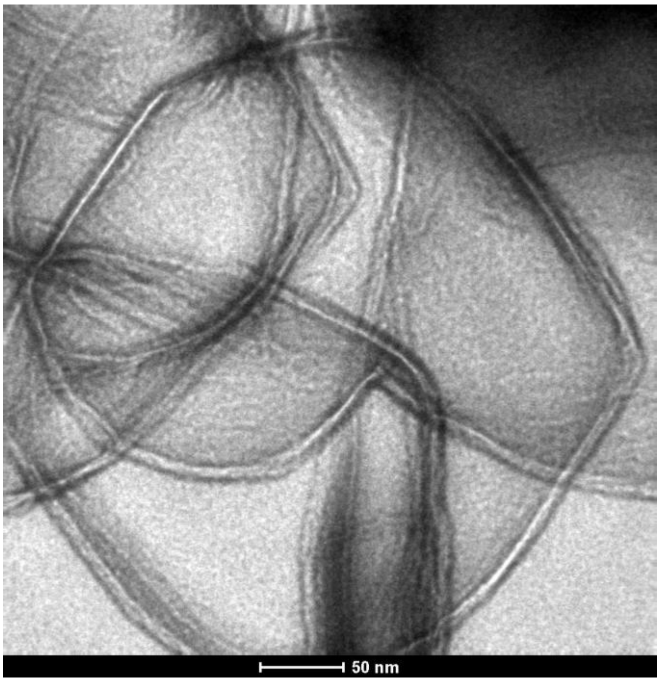

Figure 4.22: TEM of Sample showing sharp bending (a faceted growth feature).

As the growth of the nano tube proceeds in the gelatinous mass, the hindrance is observed for its further growth by the already grown nano tube. Moreover, the concentration of foreign particle (Fe) also increases due to solute rejection at the interface. These may get entrapped causing creation of nodes during growth which may also lead to change in growth direction as is evident in the micrograph in figure 4.19 marked as arrow.

As the concentration of nano tube increases this bending phenomenon increases. In the beginning the growth of single wall nano tube occurs and in due course of time these single wall nano tube is encapsulated by other growing tube with bonding at interface. The variation in thickness observed is for this reason.

The present studies revealed that simple thermo- chemical route can be used to synthesize the carbon nano tubes by decomposition of acetone at 650 ºC. This supports our proposed mechanism in section 4.3. Now it is required to optimize the processing conditions to convert WO_3 completely into WC nano particles with maximum yield and minimum impurities discussed in section 4.3.

4.5 Optimization of processing parameters for the synthesis of WC nano particles

During preparation of WC nano particles, it has been observed that acetone as carbon source has provided better yield as compared to other carbon sources. In this study the emphasis is to optimize the processing condition to enhance the yield of WC nano particles. For it the reaction time and the amount of carbon source (pressure) was varied which are described in subsequent sections.

4.5.1 Effect of reaction time

In order to study the role of reaction time same proportion of $WO_{3,}$ Mg and acetone (3g: 6g: 36ml) were taken in autoclave and heated for different duration at 800 ºC (Table 2, (S_1 to S_4).

Table 4.2: Details of reaction parameters

Reactant Sample	Reaction Time (H)	Amount of carbon source (ml)
S_1	10	36
S_2	12	36
S_3	15	36
S_4	20	36

In this case, the system will observe a constant pressure as volume of carbon source is constant and only reaction time may control the reaction product (WC).

4.5.1.1 XRD analysis: Reaction time variation

The X-ray diffractogram obtained for each set of experiment has been analyzed, which is shown in figure 4.23.

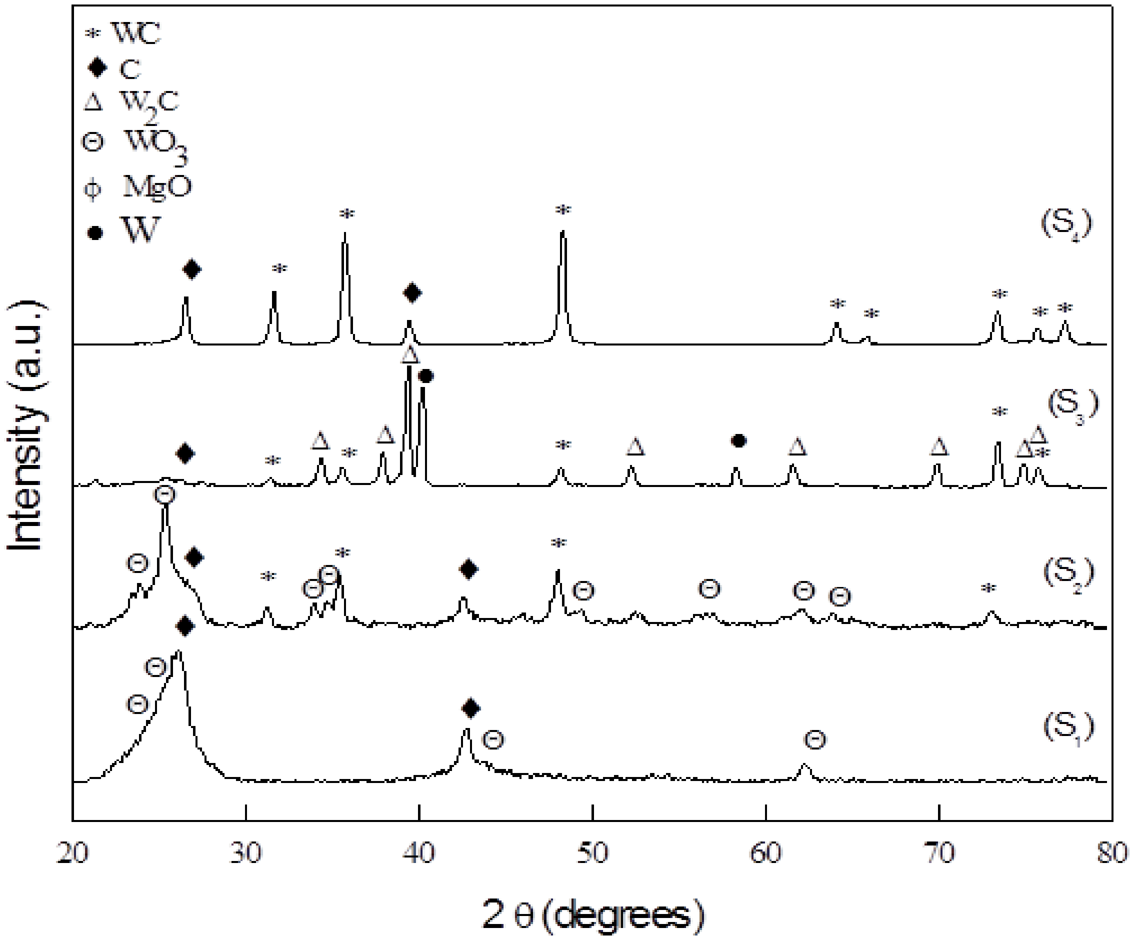

Figure 4.23: XRD pattern of samples S_1 to S_4 showing the presence of different phases.

The details of the XRD analysis have been given in tables 4.3 and 4.4. In Sample S_1 reaction time is very less (10 h). This does not provide sufficient time for diffusion to occur for the formation of WC particles. Only pyrolysis of acetone has occurred. In the sample S_2 where the reaction time has been increased to 12 h the formation of fine WC particles has started. However, the sample shows the peaks of WO_3, which indicate that the reaction time is not sufficient enough to convert the entire lot of WO_3 to WC. In case of sample S_3 where reaction time has been increased to 15 h indicates the presence of WC, W_2C, W and C peaks. This indicates that a reverse reaction has also occurred in which WC is converted into W, which reacts with other WC particles to form W_2C phase [23]. In the sample S_4, the reaction time is increased to 20 h. Here a saturation stage is reached where all WO_3 particles have been converted into ultra fine WC particles with excess carbon. It appears that the system is dynamic in nature where an optimum condition to achieve desired product phase is required. Optimum value of pressure and reaction time is observed for sample S_4. The reaction parameters also affect the particle size of WC; increased reaction time first increases the particle size and then decreases (table 4.3).

Table 4.3: Variation in particle diameter of WC in different samples

Sample	**WC Particle diameter (XRD) (nm)**
S_2	24.36
S_3	39.38
S_4	19.20

A comparison of peak intensity to obtain a texture coefficient with standard specimen can be obtained through Harris's analysis [24], using the relationship given below:

$$\mathrm{P(h_i k_i l_i)} = \frac{I(h_i k_i l_i)}{I_0(h_i k_i l_i)}\left[\frac{1}{\mathrm{n}}\sum_{i=1}^{n}\frac{I(h_i k_i l_{i)}}{I_0(h_i k_i l_i)}\right]^{-1} \tag{4.8}$$

P (h k l) is the texture coefficient of the plane specified by Miller Indices (h k l); I(h k l) and I_o(h k l) are the specimen and standard intensities respectively for a given peak and n is the number of diffraction peaks. The calculated texture coefficients of all the phases are tabulated in table 4.4. With the increase in reaction time the texture coefficient of the plane (100) increased from 0.94 to 1.79 (S_2 to S_4) while the texture coefficient of the plane (101) decreased from 1.03 to 0.97.

Table 4.4: Percentage of product phases and their texture coefficient.

Sample	**Phases Formed**				
	Phase	**Volume fraction**	**ICDD Card matched**	**Planes (hkl)**	**Texture coefficient**
S_1	WO_3	24	83-0949	020	0.49
				200	1.52
	C	76	75-1621	002	0.13
				100	1.88
S_2	WC	25	25-1047	100	0.94
				101	1.03
				001	0.99
	WO_3	21	83-0949	002	0.92
				020	1.14
				200	0.95
	C	54	75-1621	002	0.22
				100	1.79
S_3	WC	17	25-1047	100	0.99
				101	0.99
				001	1.02
	W_2C	44	20-1315	101	0.95
				100	0.84
				002	1.21
	W	36	04-0806	110	0.70
				200	0.90
				211	1.40
	C	3	26-1077	002	0.21
				100	1.88
S_4	WC	71	25-1047	100	1.79
				101	0.97
				001	0.99
	C	29	75-1621	002	0.14
				100	1.81

This shows that the microstructure is strongly textured in the plane (100) with the increase in reaction time while reaction time hinders the growth of the plane (101). The growth of (001) is almost constant with small variation in the sample S_3 which may be due to the growth of unwanted phase W_2C. This phase disappears at 20 h of reaction time and the texture coefficient goes to its original value. XRD analysis also shows that as the reaction time increases, volume fraction of WC increases (Table 4.4). In case of S_3 sample where it shows a decreasing trend, the decrease in % of WC phase may be because of the formation of W_2C phase and when the reaction time is further increased the yield is maximum.

4.5.1.2 DTA/ TGA analysis

The DTA curves of S_1 to S_4 samples are shown in figure 4.24. For S_1 sample, the DTA curve clearly indicates exothermic peaks which appear over a range of temperatures.

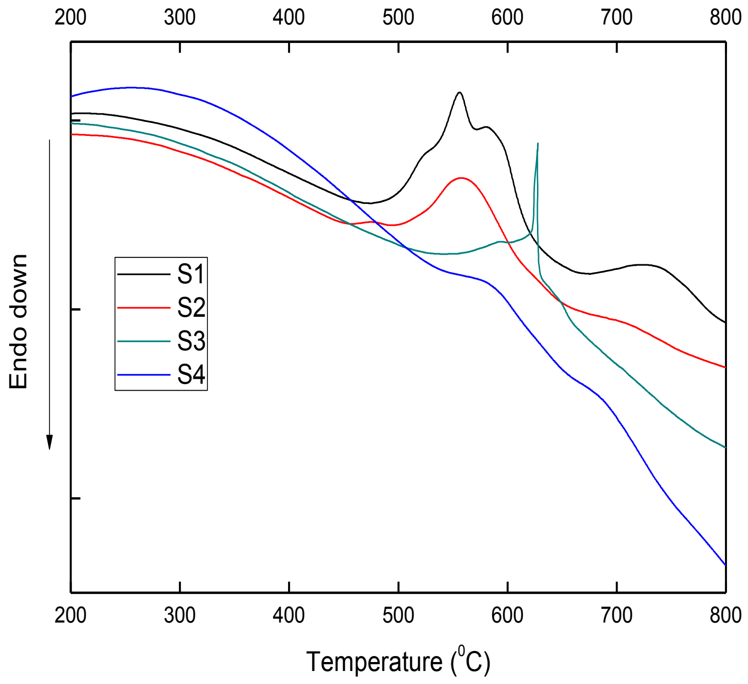

Figure 4.24: DTA of sample S_1 to S_4 at heating rate of 10°/min.

These peaks might be attributed due to different forms of the carbon. As the reaction time increases the three peaks get merged to each other and become sharpen, which is due to the presence of mono phase carbon [25]. Interestingly in S_4 sample, two weak peaks are observed at 578 ^{o}C and 675 ^{o}C. In earlier reports [3] these peaks have been designated for two different forms of carbon, which started decomposing on the above mentioned temperature. Similarly, the weight loss of the sample confirms that the reaction time decreases the yield of unreacted carbon, which becomes minimum in the sample S_4 (figure 4.25). The XRD results also supports the TGA data of present samples.

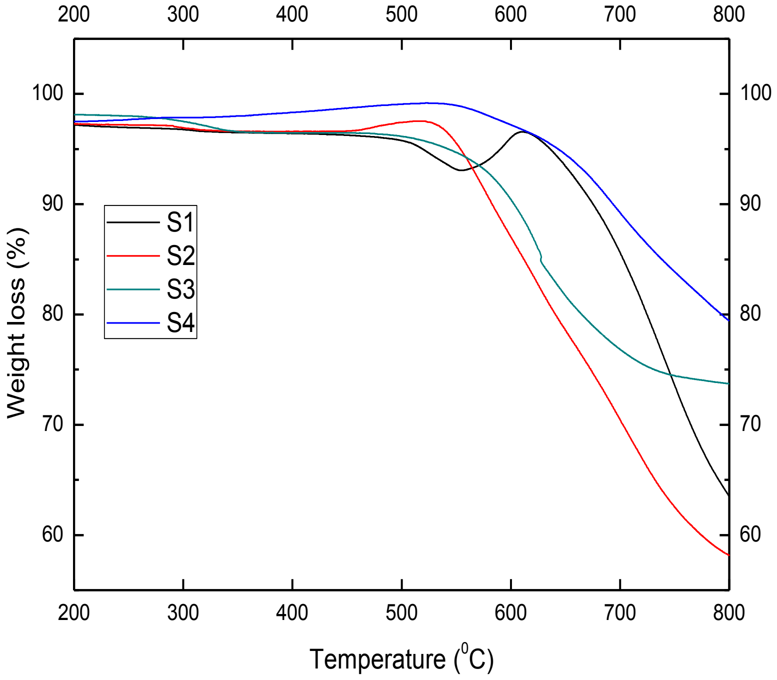

Figure 4.25: TGA of sample S_1 to S_4 at heating rate of 10°/min.

4.5.1.3 TEM analysis

TEM analysis was done for all the samples in which WC has formed. Sample S_2 indicates the presence of different phases, which have been marked with arrows (figure 4.26). TEM image of S_3 sample shows the similar features (figure 4.27). In the sample S_4, the WC particles are clearly visible with an average particle size of 23 nm (figure 4.28(a)) (table 4.5) indexed with (100) and (101) planes in SAED pattern (figure 4.28(b)). This particle size also matches with the particle size calculated by XRD technique (table 4.3).

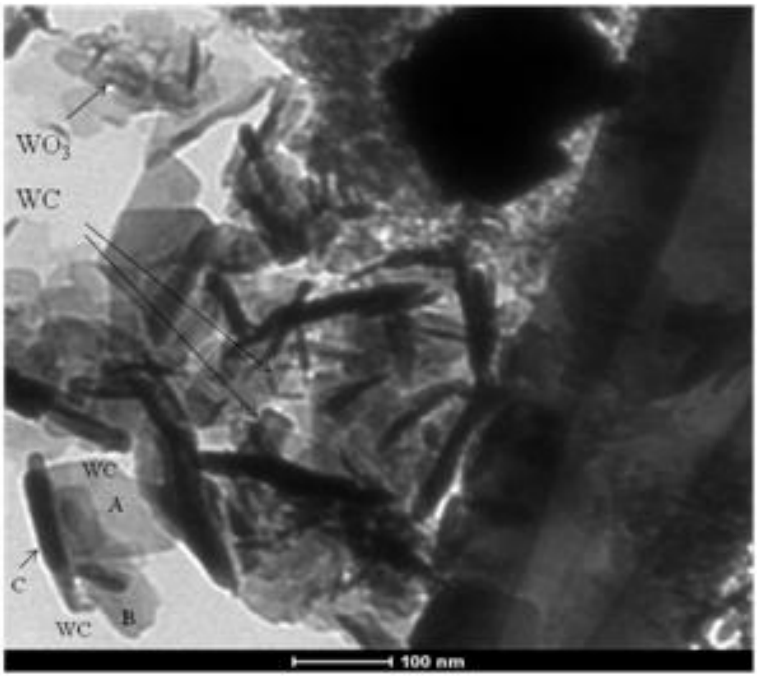

Figure 4.26: TEM micrograph of sample S_2 showing the presence of carbon nano fibers, WC and WO_3 phases.

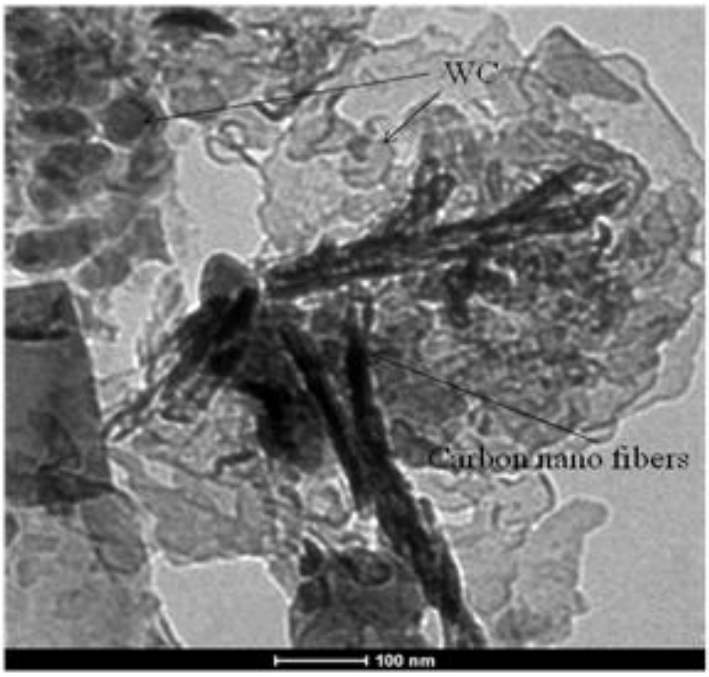

Figure 4.27: TEM micrograph of sample S_3 showing the presence of carbon nano fibers and WC phases.

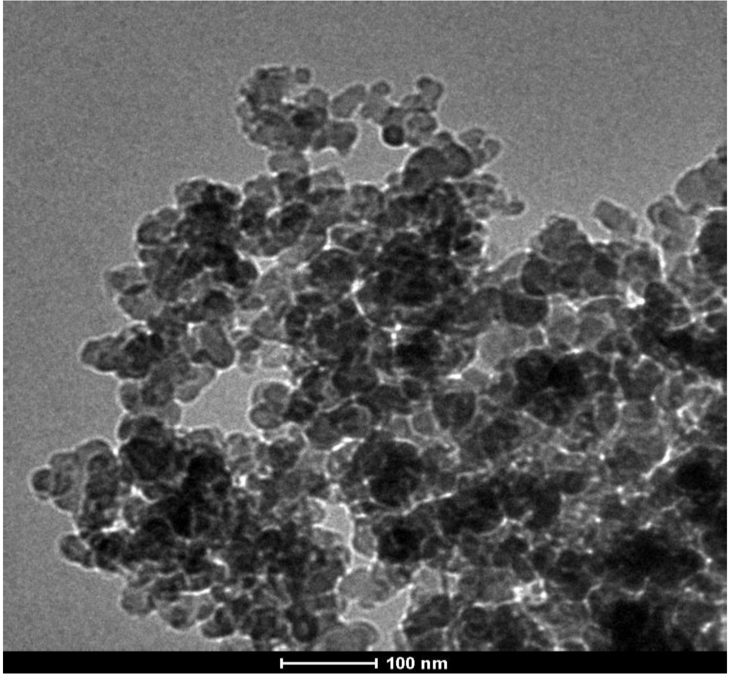

Figure 4.28(a): TEM micrograph sample S_4 showing the presence of WC phase.

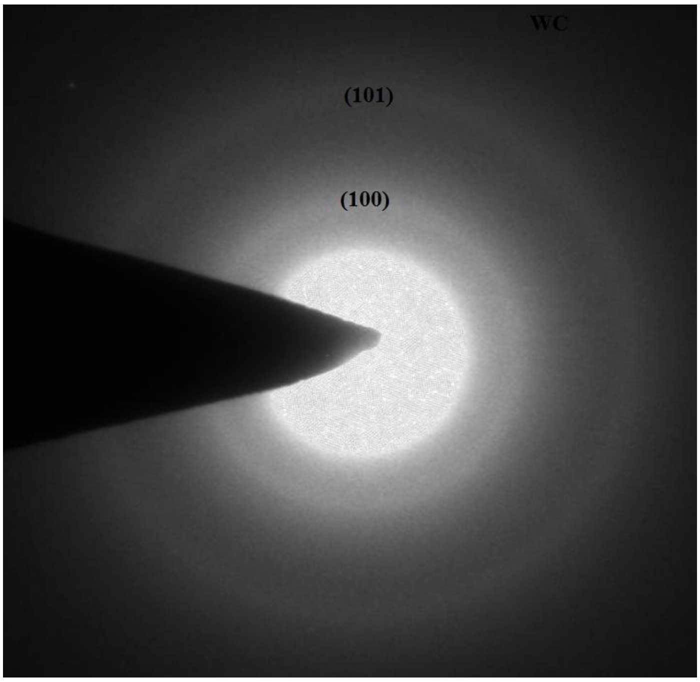

Figure 4.28(b): SAED pattern of sample S_4 showing the presence of WC phase.

Table 4.5: Variation in particle diameter of WC in different samples.

Sample no.	WC Particle diameter (TEM) (nm)
S_2	32
S_3	47
S_4	23

TEM analysis of all samples for the formation of WC phase indicates that in the entire reaction product free carbon exists. Only the amount of free carbon varies from one reaction product to another reaction product. In all these reactions Mg is added as reducing element, which picks up oxygen from the reactant phase and is converted to MgO. The reactant phase in the system is WO_3 and acetone. The amount of solid reactant (WO_3 and Mg) is same for entire reaction and only amount of acetone is varied. In case of optimized reaction (S_4) the product phase is WC and C only. TEM analysis revealed different features for each set of reaction, which is shown in figure 4.26-4.28. Figure 4.26 is for Sample S_2 where one can see the presence of faceted morphology of WC particle. In fact, carbon engulfs the WO_3 particle, and slowly it converts the WO_3 to WC. The faceted structure which is transparent and marked as ‘A’ and ‘B’ shows this transformation where WC particles ooze out and WO_3 (dark color) is inside the system. This is a slow transformation under high pressure. In case the carbon is sufficient enough the entire WO_3 is converted to WC leaving behind excess carbon as shown at C. Similar features were also observed for S_3 where excess of carbon can be seen. Since the nature of reaction is such that there is a variation of free energy with the fraction of the site which is occupied as the growth of WC occurs from the fluid source carbon which provides a smooth surface which can be explained by Jackson's model as given below [22, 26]:

$$\frac{\Delta F_s}{NkT_m} = \alpha * x(1-x) + x\ln(x) + (1-x)\ln(1-x) \tag{4.9}$$

Where ‘N’ is the number of possible sites available at the interface ‘k’ is Boltzmann constant ‘T_m’ is the equilibrium temperature and ‘x’ is the fraction of the site occupied. ΔF_s is the relative change in free energy. The fraction of the site occupied is:

$$\alpha = \frac{L_m}{kT_m}\xi \tag{4.10}$$

L_m is latent heat and ‘ξ’ is crystallographic factor.

The factor ‘α’ denotes the type of interface (smooth or rough) which ultimately controls the product phase through the reaction occurring at the interface. If ‘α’ factor is less than ‘2’ the surface free energy is lowest and the product phase is non faceted type but at $2 > \alpha < 3$ both faceted and non faceted features are possible. $\alpha > 3$ will lead to faceted features. In case of sample S_4, we get WC phase, which is also evident in micrograph

4.28 where 10 to 50 nm WC is obtained. On comparing the structural features of this reaction product, we find the structure is similar to that of the reported micrograph of another published work [27]. The unreacted carbon gets converted to carbon nano fibers as can be seen in figure 4.27. The process is dynamic in nature so one has to optimize every parameter. The WC phase is obtained in case of S_4, which gives optimized condition.

4.5.2 Effect of pressure

In order to see the role of pressure, the amount of carbon sources (acetone) was varied in different proportion with a constant proportion of WO_3 and Mg (3g and 6g respectively). The variation in the amount of acetone may lead to variation in the pressure generated due to decomposition of acetone in the autoclave which produces H_2 in the autoclave and may affect the particle size of the product WC phase. The different amount of acetone taken for the reaction is given in table 4.6 (S_4 to S_7). In this case reaction time (20 h) and reaction temperature (800 ºC) were kept constant.

Table 4.6: Details of reaction parameters.

Sample	**Reaction Time (h)**	**Amount of carbon source (ml)**
S_4	20	36
S_5	20	24
S_6	20	30
S_7	20	42

4.5.2.1 XRD analysis: pressure variation

The X-ray diffractogram obtained for each set of experiment has been analyzed, which is shown in figure 4.29.

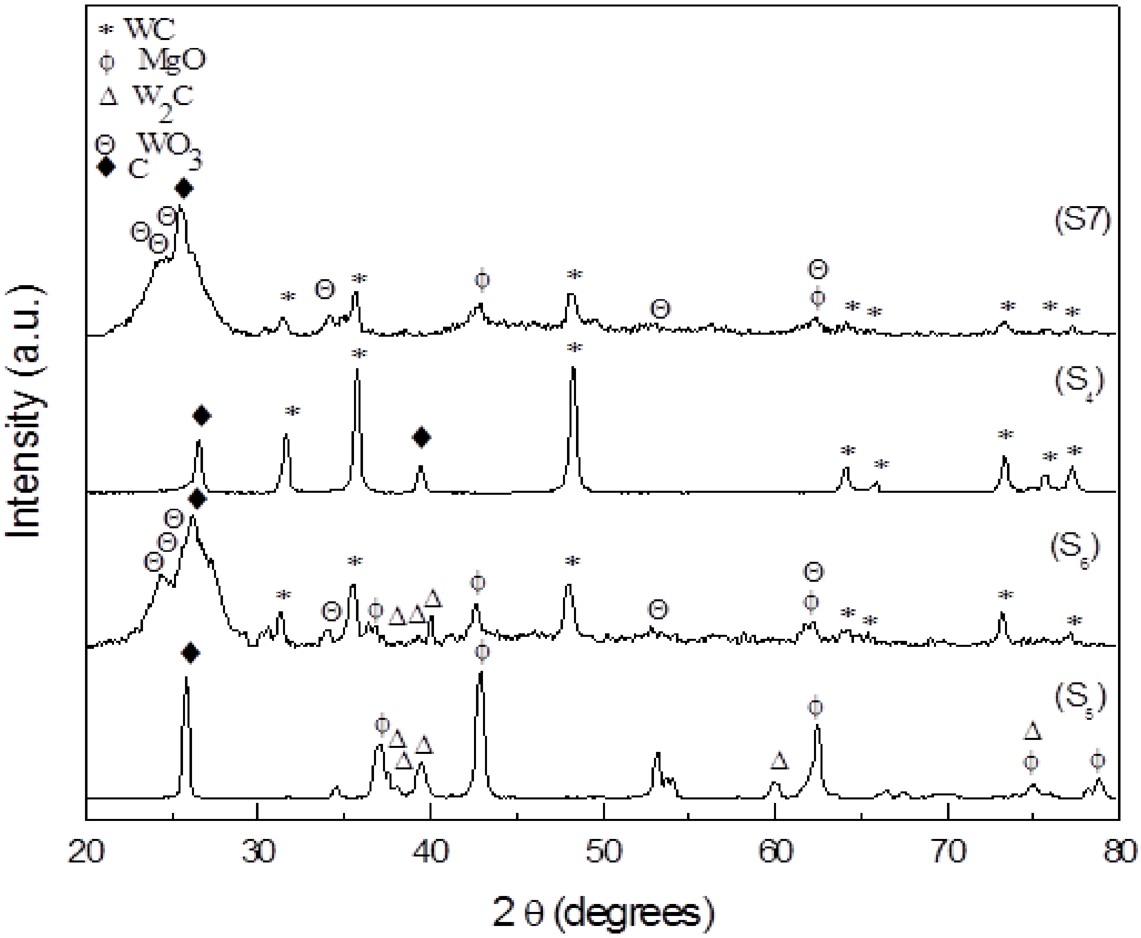

Figure 4.29: XRD pattern of samples S_4 to S_7 showing the presence of different phases.

The details of the XRD analysis have been given in table 4.7. In sample S_5 where the amount of acetone was reduced to 24 ml and reaction time was 20 h, the phases formed are W_2C, C and MgO. Here in this case pressure is not sufficient enough to convert W_2C phase to WC though the reaction time is the same but amount of carbon source is reduced. In the sample S_6 increased pressure resulted in the conversion of W_2C to ultra fine WC as the amount of acetone was increased from 24 ml to 30 ml. However, unreacted WO_3 is still present. In case of sample S_7 the amount of acetone was further increased to 42 ml where unreacted WO_3 is still present. The presence of peaks of WO_3 in XRD pattern of this sample indicates that complete conversion of WO_3 to WC has not occurred. It indicates that the refluxing action required for the conversion is not sufficient enough. From these observations, it appears that the system is dynamic in nature where an optimum condition to achieve desired product phase is required. However, an optimum value of pressure and reaction time is observed for sample S_4. The reaction parameters affect the particle size of WC. With an increase in the amount of carbon sources (pressure) the particle size decreases (Table 4.8). A comparison of peak intensity with standard specimen can be obtained through Harris's analysis [24], to obtain a texture coefficient using the relationship given in section 4.5.1.1.

The calculated texture coefficients of all the phases are tabulated in table 4.7. With the variation of the acetone amount (S_5 to S_7) initially (001) plane is the most textured plane. With an increase in the amount of acetone to 36 ml the microstructure is highly textured along (100) plane with 1.79 texture coefficient. As the amount of acetone is further increased to 42 ml the texture coefficient of (001) is highest. This plane grows at the cost of (100) plane. Processing parameter variation analysis shows that when the microstructure is highly textured along (100) plane the wt% of WC is highest.

Table 4.7: Percentage of product phases and their texture coefficient.

Sample No.	Phases Formed				
	Phase	**Volume fraction**	**ICDD Card matched**	**Planes (hkl)**	**Texture coefficient**
S_4	WC	71	25-1047	100	1.79
				101	0.97
				001	0.99
	C	29	75-1621	002	0.14
				100	1.81
S_5	W_2C	12	20-1315	101	0.74
				002	1.20
				100	1.06
	C	43	26-1077	002	0.21
				100	1.79
	MgO	45	40829	----	----
S_6	WC	18	25-1047	100	0.92
				101	0.92
				001	1.17
	W_2C	9	20-1315	101	0.94
				002	1.06
	WO_3	22	83-0949	002	0.60
				020	1.02
				200	1.38
	C	39	75-1621	002	0.17
				100	1.84
	MgO	12		-----	----
S_7	WC	17	25-1047	100	0.99
				101	0.97
				001	1.04
	WO_3	32	83-0949	002	0.78
				020	0.87
				200	1.35
	C	51	72-1621	002	0.21
				100	1.79

Table 4.8: Variation in particle diameter of WC in different samples.

Sample	**WC Particle diameter (XRD) (nm)**
S_4	19.20
S_6	68.44
S_7	21.00

XRD analysis also shows that as the amount of acetone is varied the wt% of WC shows an increasing trend at 36 ml acetone up to 71%. Further increase in acetone to 42 ml the wt% of WC falls from 71% to just 17%. This sharp decrease may be due to reverse reaction that may be taking place in the autoclave.

4.5.2.2 DTA/TG Analysis

The DTA/TG curves of S_4 to S_7 samples are shown in figure 4.30 and 4.31. As the reaction time is fixed in these samples (S_4 to S_7) and only the amount of acetone varied as shown in table 4.5, the amount of unreacted carbon obtained was different. As the amount of acetone increased to 30 ml, the unreacted carbon percentage increases. The unreacted carbon percentage suddenly decreases up to 20% in case of S_4 sample where carbon source content was 36 ml (figure 4.30 and 4.31). After increasing carbon sources content from 36 to 42 ml the unreacted carbon again showed increasing trend. The weight loss in TGA measurement is due to the decomposition of the carbon since all other formed phases are stable up to 800 °C. In all the samples, the TGA curve of S_4 sample shows minimum weight loss, which clearly indicates that S_4 (20 h, 36 ml) sample exhibit low unreacted carbon with higher yield of WC phase (figure 4.31). In other words, sample S_4 exhibits the optimized condition to achieve highest yield of WC nanaparticles. The XRD results also supports the TGA data of present samples.

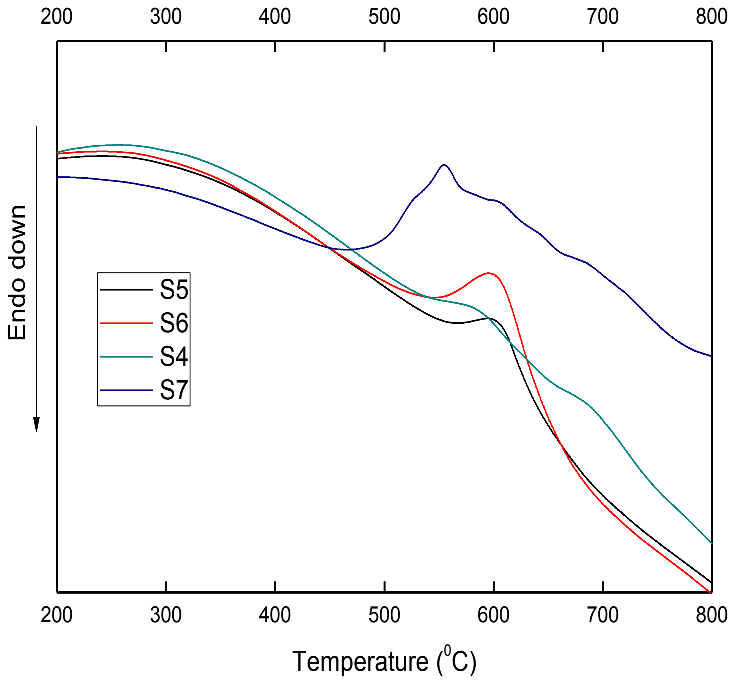

Figure 4.30: DTA of sample S_5 to S_7 at heating rate of 10°/min.

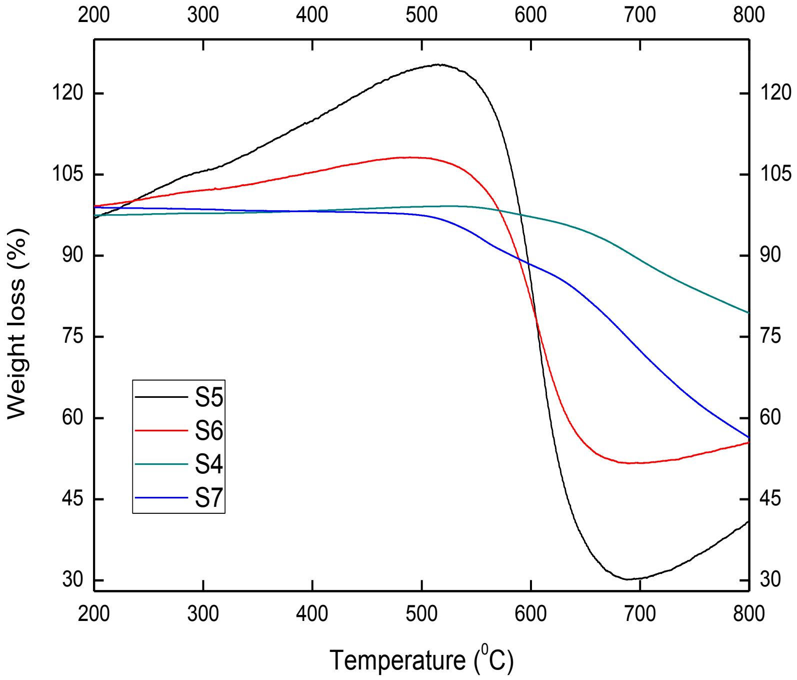

Figure 4.31: TGA of sample S_5 to S_7 at heating rate of 10°/min.

4.5.2.3 TEM Analysis

TEM analysis was done for all the samples in which WC has formed. TEM micrograph of sample S_4, clearly showed the WC particles with an average particle size of 23 nm (figure 4.28).

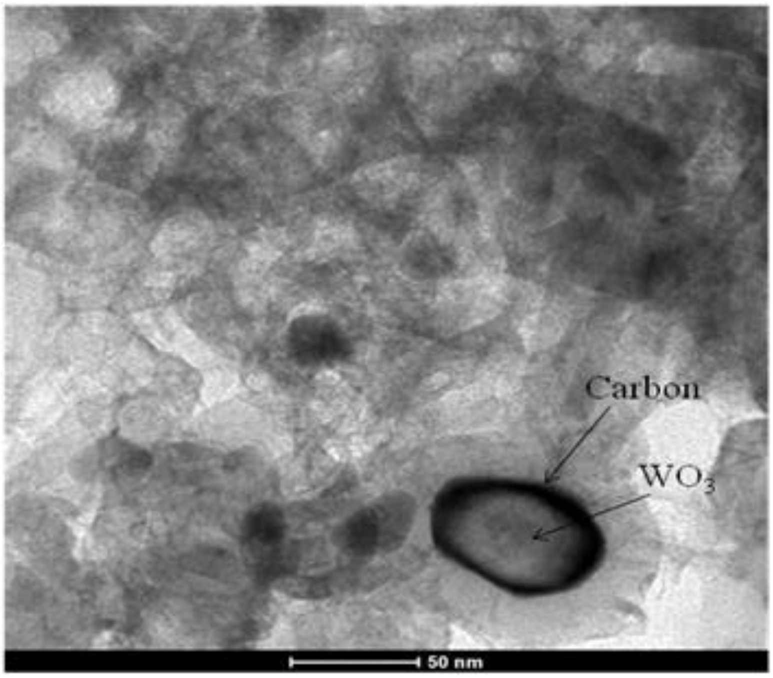

Figure 4.32: TEM micrograph of sample S_6 showing the interface of C and WO_3.

The WC particle size in case of sample S_6 is large, which is due to less pressure as the amount of carbon sources is less (figure 4.32). Further increase in the acetone amount does not help in complete conversion of WO_3 phase to WC (figure 4.33).

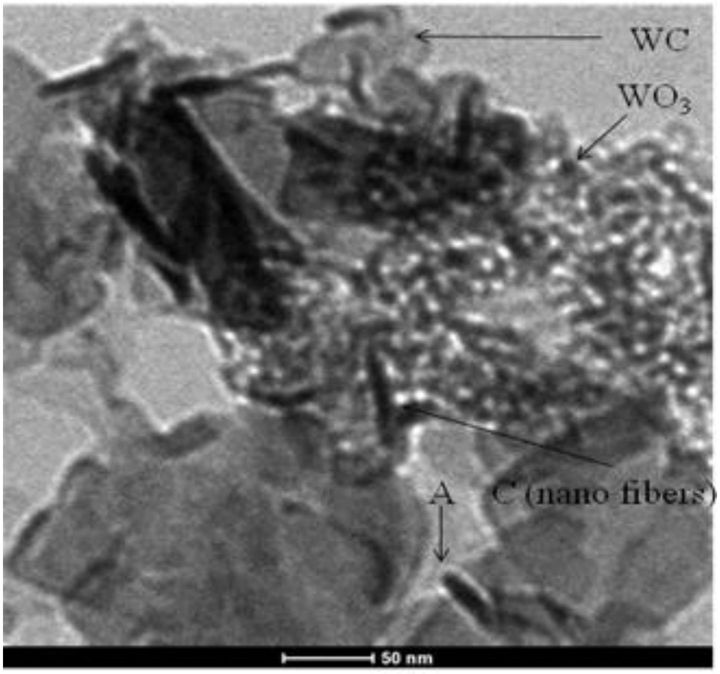

Figure 4.33: TEM micrograph of sample S_7 showing the presence of WC, WO_3 and carbon nano fibers.

The variation in particle size is given in table 4.9 also matches with the particle size calculated by XRD technique (table 4.8).

Table 4.9: Variation in particle diameter of WC in different samples.

Sample no.	**WC Particle diameter (TEM) (nm)**
S_4	23
S_6	72
S_7	26

TEM analysis of all samples for the formation of WC phase indicates that in the entire reaction product free carbon exists. Only the amount of free carbon varies from one reaction product to another reaction product. In all these reactions Mg is added as reducing element, which picks up oxygen from the reactant phase and is converted to MgO. The reactant phase in the system is WO_3 and acetone. The amount of solid reactant (WO_3 and Mg) is same for entire reaction and only acetone constant is varied. In case of optimized reaction (S_4) the product phase is WC and C only. Though the acid leaching of the entire product was done from same concentration of acid (1:1 diluted HCl) and also for the same period (2 h) for all the product phases (S_4 to S_7) which leads to leaching of MgO phase but in case of S_5 and S_6 the entire MgO is not leached out where acetone content is less (24 and 30 ml) as compared of 36 ml of the optimized reaction conditions where WC phase and C are present. Lesser acetone content could not build up sufficient pressure for reaction to occur. The only way to get the product phase MgO is through reaction (4.11) and (4.12) as described below.

$$3WO_3 + CH_3COCH_3 + 9Mg \rightarrow WC + W_2C + 9MgO + C + H_2O + 2H_2 \qquad (4.11)$$

$$CH_3COCH_3 + Mg \rightarrow MgO + C + C_2H_6 \qquad (4.12)$$

$$W_2C + C \rightarrow 2WC \qquad (4.13)$$

The formation of W_2C phase along with MgO and carbon are obtained for S_5. The entire amount of carbon produced is consumed for converting WO_3 to W_2C by following reaction.

$$2WO_3 + CH_3COCH_3 + 6Mg \rightarrow W_2C + 6MgO + 2C + H_2O + 2H_2 \qquad (4.14)$$

For Sample S_7 the possible mechanism is given in equations (4.15 and 4.16) below:

$$WO_3 + CH_3COCH_3 + 2Mg \rightarrow WC + 2MgO + 2C + 2H_2O + H_2 \qquad (4.15)$$

OR

$$WO_3 + CH_3COCH_3 + 3Mg \rightarrow WC + 3MgO + 2C + H_2O + 2H_2 \qquad (4.16)$$

In case of S_6 and S_7 unreacted WO_3 remains in the system.

TEM analysis revealed different features for each set of reaction, which is shown in figure 4.28, 4.32 and 4.33. At high temperature we get different volume fraction of product phases with variation in amount of carbon content and hence pressure is different. The optimized condition obtained is for S_4. This is because of the fact that the fluid available undergoes a supercritical stage which ultimately provides different pressure inside the autoclave for which the required condition is unexplored as pressure measuring device is not available. Moreover, such condition is not achieved for other cases (S_5 to S_7).

4.6. Synthesis by mechano-chemical routes: conversion of wolframite ore to WC particles

4.6.1 Enrichment of the ore

WC nano particles were also synthesized from wolframite which is an ore of tungsten. The chemical composition of wolframite which was supplied by Wolfram Bergbau, Austria, and used in present study is already given in table 3.1. The detail of its enrichment procedure followed is also described in the experimental section.

The ore was given leaching treatment by adding dilute hydrochloric acid (1:1). In this solution few drops of HF were added to break silica which gets converted to hexafluoro silicic acid and filtered easily. The possible reaction of wolframite during enrichment can be written as:

$$2FeWO_4 + 6HCl \rightarrow 2FeCl_3 + 2WO_3 + 2H_2O + H_2 \qquad (4.17)$$

The other compounds SiO_2, Al_2O_3, MnO, TiO_2, SnO_2 and K_2O also react with HCl/ HF to form water soluble chloride or fluorides which were then filtered out. The leached out products after the acid treatment provide high quality of tungsten oxides (WO_3, WO_2 and $W_{32}O_{84}$) with the possible reaction during leaching process which are listed below:

$$Fe_2O_3 + 6HCl \rightarrow 2FeCl_3 + 3H_2O \tag{4.18}$$

$$SiO_2 + 6HF \rightarrow H_2SiF_6 + 2H_2O \tag{4.19}$$

$$Al_2O_3 + 6HCl \rightarrow 2AlCl_3 + 3H_2O \tag{4.20}$$

The enriched wolframite was washed with distilled water several times to remove acid traces. The filtrate was again washed with ethanol to remove water traces. The powder is dried in vacuum heating furnace at 50 ºC for one hour. The dried powder was characterized by X-ray diffractrometer which is given in figure 4.34.

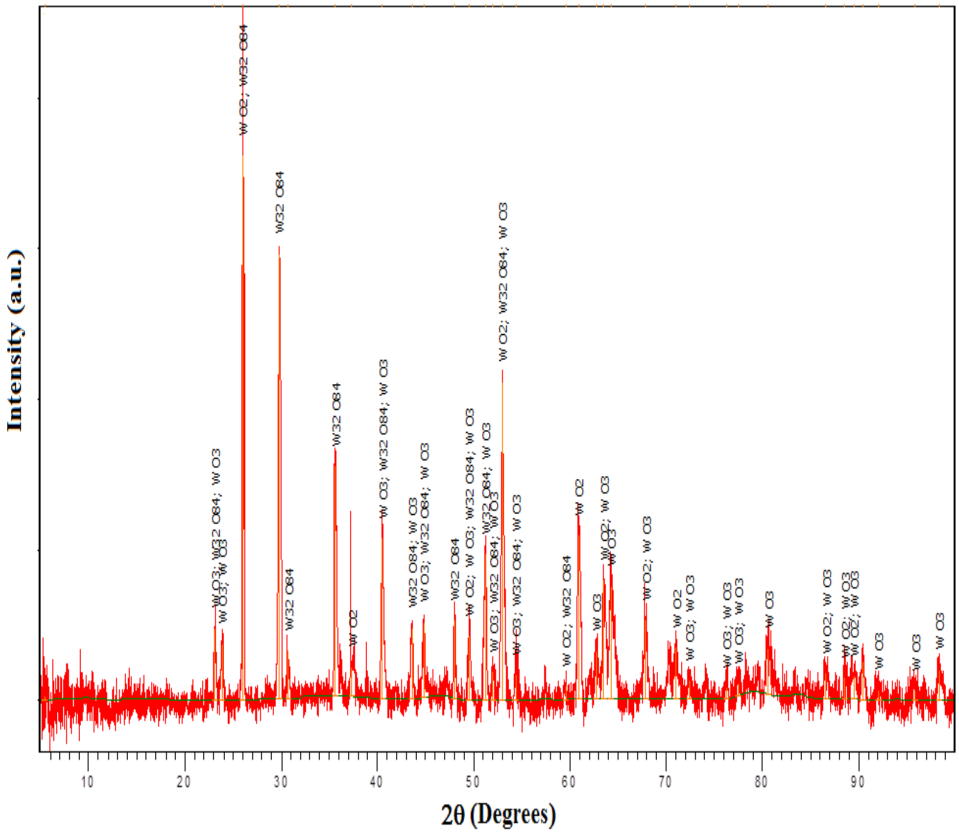

Figure 4.34: XRD of enriched wolframite ore.

All the peaks were matched and phases correspond to tungsten oxides ((WO_3, WO_2 and $W_{32}O_{84}$). The percentage of different phases is given in table 4.9. The powders (WE) obtained from processed ore is used for further experimentation.

Table 4.9: The composition of the enriched ore.

ICDD card No.	Compound Name	Chemical Formula	Phase (%)
01-074-6028	Tungsten Oxide	$W O_3$	3
01-071-0614	tungsten(IV) oxide	$W O_2$	24
01-089-4482	α-$W O_3$	$W O_3$	3
01-077-0810	Tungsten Oxide	$W_{32} O_{84}$	60
01-087-2383	α-$W O_3$	$W O_3$	10

4.6.2 Synthesis of WC nano particles

For the synthesis of WC nano particles three carbon sources; methanol, ethanol and acetone were used and the samples synthesized have been labeled as W_1 (methanol), W_2 (ethanol) and W_3 (acetone). Here activated magnesium turnings were used as reducing agent [2]. For all the experiments WE (3g), magnesium turning (6g) and 36 ml of carbon source were put in a specially designed stainless steel autoclave [28]. The autoclave was kept inside the furnace and heated upto 800 ºC at heating rate of 5°/min for 20 h followed by furnace cooling. After cooling the autoclave, the solid powder was taken out from it and dissolved in HCl (1:1) to remove unreacted Mg and other soluble phases from the product. The acid treated samples were washed with distilled water first followed by ethanol to eliminate the water absorbed in the powders. The dried powders were characterized by XRD to investigate the formation of WC phase in the synthesized mass.

4.6.3 XRD analysis of sample W_1 to W_3

XRD pattern of W_1 shows peaks of WO_3, C and W phases, sample W_2 shows peaks of W_2 (C,O), C and W phases while sample W_3 shows peaks of C and WC only (figure 4.35).

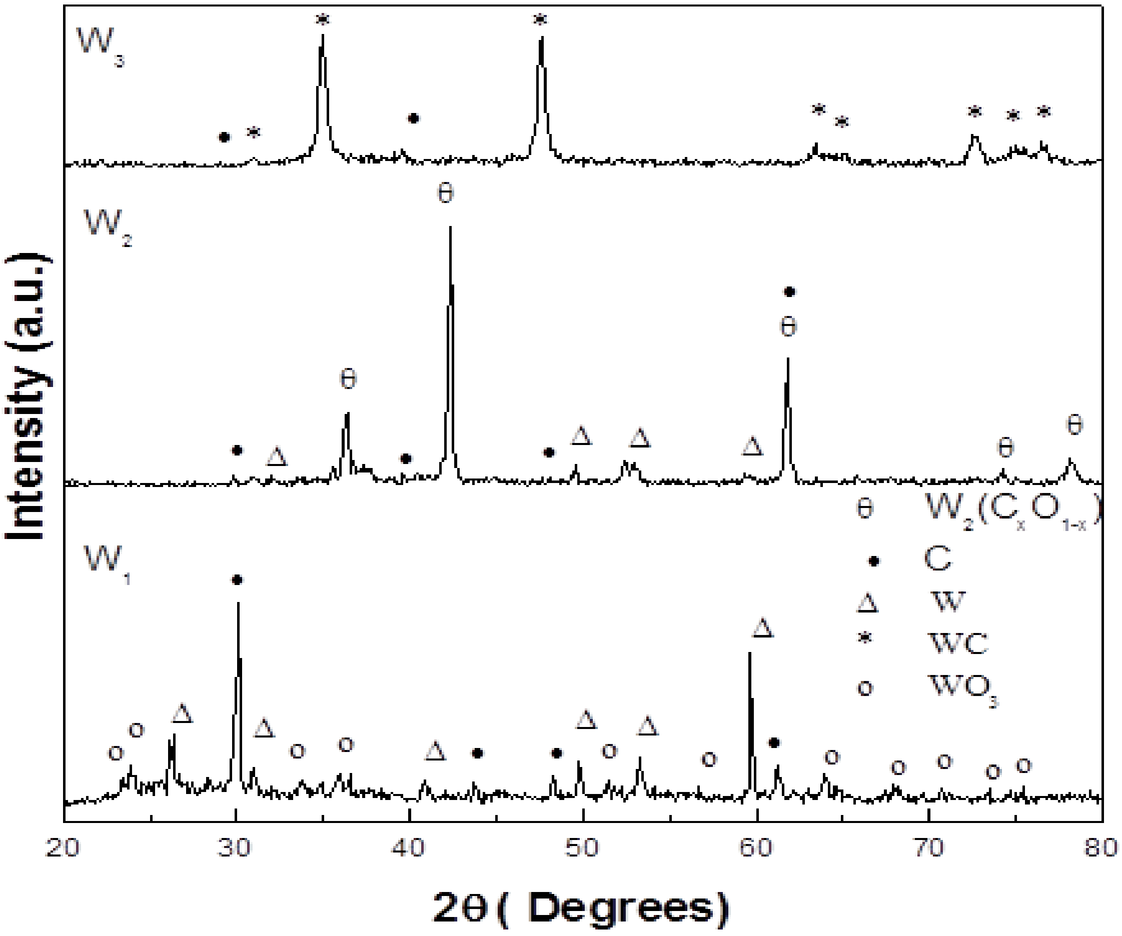

Figure 4.35: XRD pattern of sample W_1, W_2 and W_3.

The possible reaction which may occur with different carbon sources can be written as (here only WO_3 is discussed assuming that the other oxides WO_2 and $W_{32}O_{84}$ will behave in similar way):

$$WO_3 + CH_3OH + 2Mg \rightarrow W + C + 2MgO + 2H_2O \tag{4.21}$$

$$3WO_3 + C_2H_5OH + 7Mg \rightarrow W_2(C_xO_{1-x}) + W + C + 7MgO + 2H_2O + H_2 \tag{4.22}$$

$$WO_3 + 4CH_3COCH_3 + Mg \rightarrow WC + 9C + MgO + 12H_2 + 3CO_2 \tag{4.23}$$

When methanol is used as carbon source H_2 is not evolved which plays a vital role in the reduction of WO_3 to WC [28-29]. In this case only decomposition of WO_3 and methanol takes place. When ethanol is used as carbon source H_2 is generated but the yield is very low so it could not convert WO_3 to WC. However, the reduction has occurred. Acetone as carbon source acted as best carbon source which generated enough H_2 for the reduction. The pressure generated by hydrogen is also responsible for the synthesis of nano WC particles [25]. After these results next set of experiments were designed. Here the powders were mechanically activated.

4.6.4 Mechanical activation of enriched ore

WE was milled for 10, 15 and 20 h at 292 rpm with 1:50 charge to ball ratio in tungsten jar using tungsten balls (FRISCH Puloerisette) to activate the ore mechanically. This mechanically activated WE powder was used as tungsten source. Three separate experiments adopting similar condition were performed which were leveled as W_4, W_5 and W_6 (table 4.10).

Table 4.10: Mechanical activation time of samples S_3 to S_6.

Sample label	Milling time (h)
$W_{3,}$	0
W_4	10
W_5	15
W_6	20

The ingredients in these experiments were same i.e. WE (3g), magnesium turning (6g) and 36 ml acetone and the rest of synthesis process was same as described above.

4.6.5 XRD analysis of samples W_3 to W_6

XRD of W_3 to W_6 samples are shown in figure 4.36. As the milling time was increased from 0 to 20 h, the intensity of unreacted carbon is decreased. The peak width also increased with milling showing refinement in the size of synthesized WC particles.

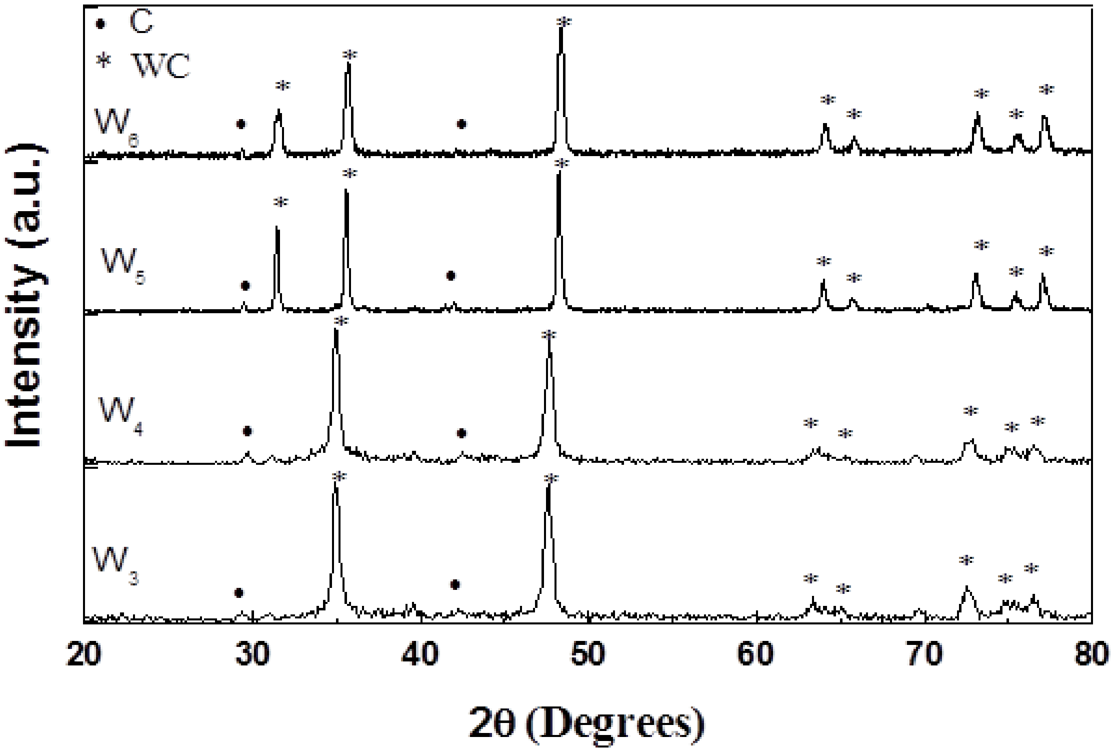

Figure 4.36: XRD pattern of sample $W_{3,}$ $W_{4,}$ W_5 and W_6 showing presence of C and WC Phases.

Table 4.11: Particle size (XRD) of samples S_3 to $S_{6.}$

Sample label	Particle size (nm) (XRD)
$W_{3,}$	13
W_4	15
W_5	17
W_6	13

Particle size of WC nano powder estimated from XRD is given in table 4.11. The particle size was calculated using scherrer's equation [10].

4.6.6 DTA/TG analysis of Samples W_3 to W_6

The samples W_3 to W_6 were examined by DTA/TGA to check their stability and phase transitions. The DTA/TGA plots of the samples are shown in figure 4.37 and 4.38.

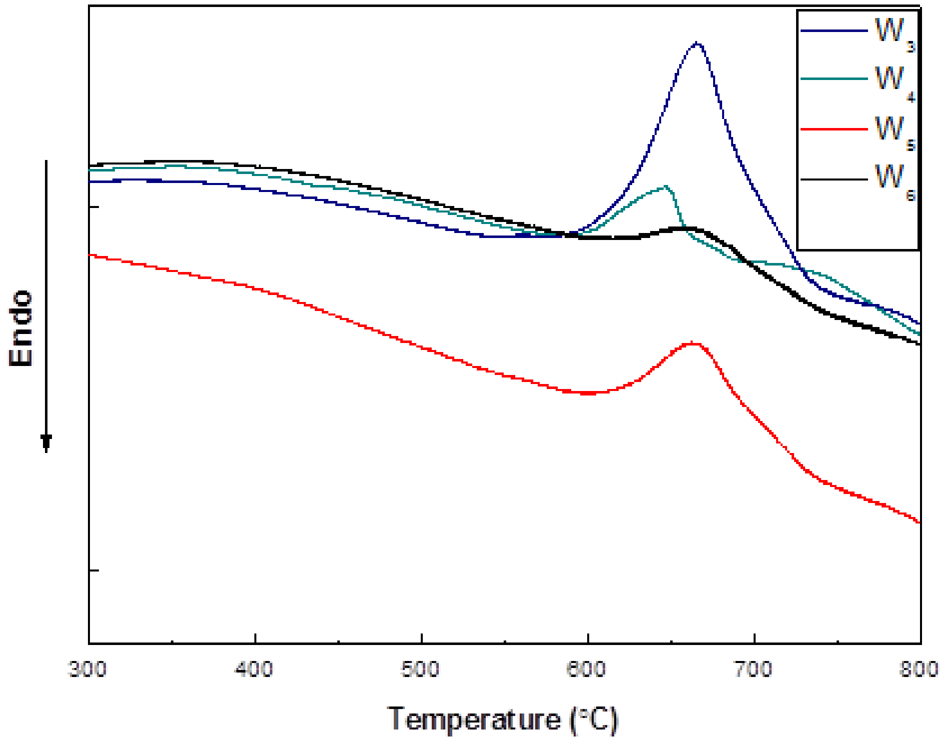

Figure 4.37: DTA plot of sample W_3,W_4,W_5,W_6 showing exothermic peaks.

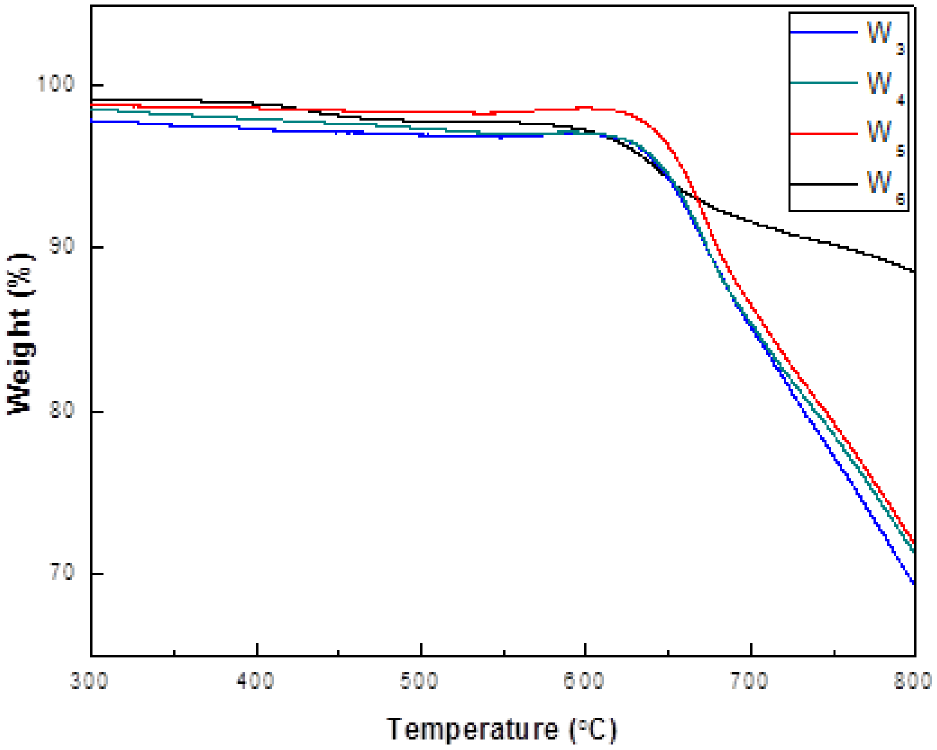

Figure 4.38: TGA plot of sample W_3,W_4,W_5,W_6 showing weight loss of samples.

The entire sample showed one exothermic peak in a region between 580 °C to 660 °C. This broad peak in this range may be attributed to the combustion of the carboneous matter which starts at 580 °C and depending upon the particle size and nature of the carboneous materials (amorphous, carbon nano tubes) the peak shifts to higher temperatures [3]. The TGA plot of the samples is shown in figure 4.38. W_3 exhibit 32% weight loss, W_4 exhibit 29% weight loss, W_5 exhibit 28% weight loss while W_6 exhibit only 11% weight loss. The decrease in weight loss with increased milling time showed that reactivity of finer particle (WO_3) increases which resulted in higher volume fraction of WC nano particle which is visible as carbon percentage decreases with increase in milling time. Moreover, carbon being lighter substance always remains at the surface while sampling for thermal analysis.

4.6.7 TEM analysis of samples W_3 to W_6

Structural characterization of tungsten carbide particles prepared from acetone as carbon source was done in detail by HRTEM. Figure 4.39 shows TEM micrograph of W_3 sample where uniform size of nano WC particles can be seen.

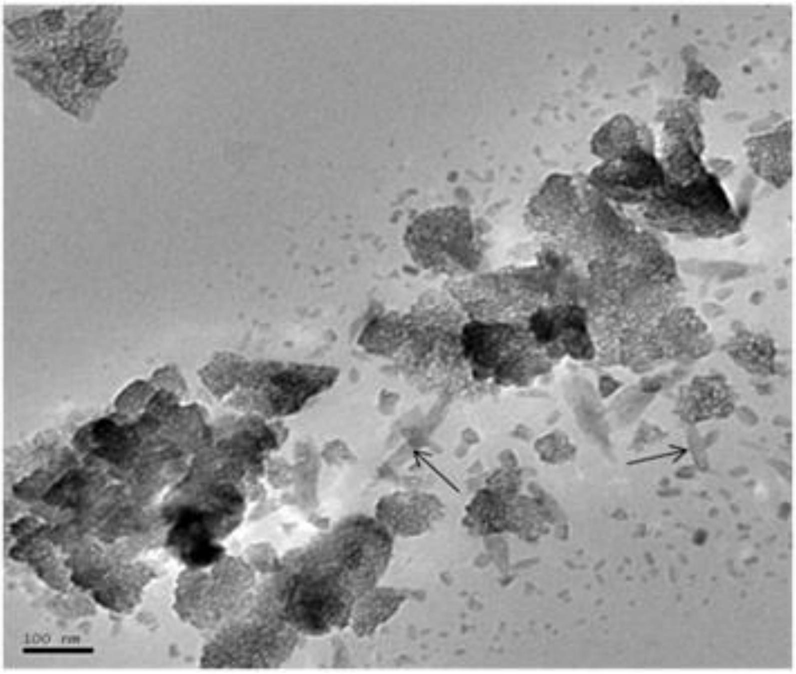

Figure 4.39: TEM of sample W_3 showing agglomerated WC particles.

The particles seems to be agglomerated and it appears that reduction reaction is not complete giving appearance of porous structure as also reported elsewhere [30]. The size of these clusters is in the range of 50 to 120 nm. It appears that nano particles are embedded into amorphous carbon matrix which is generated by decomposition of acetone. However, the sizes of these nano particles are around 10 nm. At some places nano rods of WC can also be seen in the microstructure, which is also reported by other workers [31]. Figure 4.40 represents the TEM micrograph of sample $W_{4.}$ In this case size ranges from 50 to 100 nm.

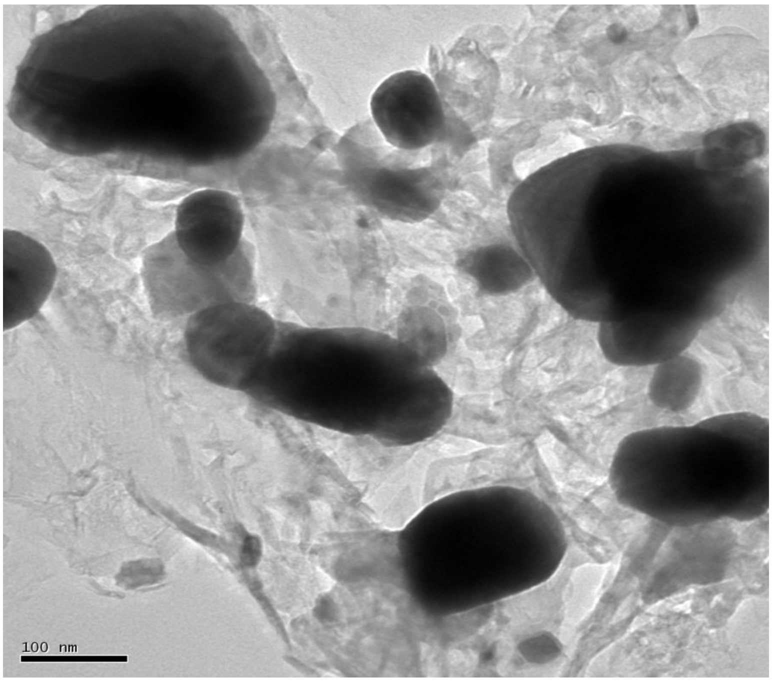

Figure 4.40: TEM of sample W_4 showing engulfing action.

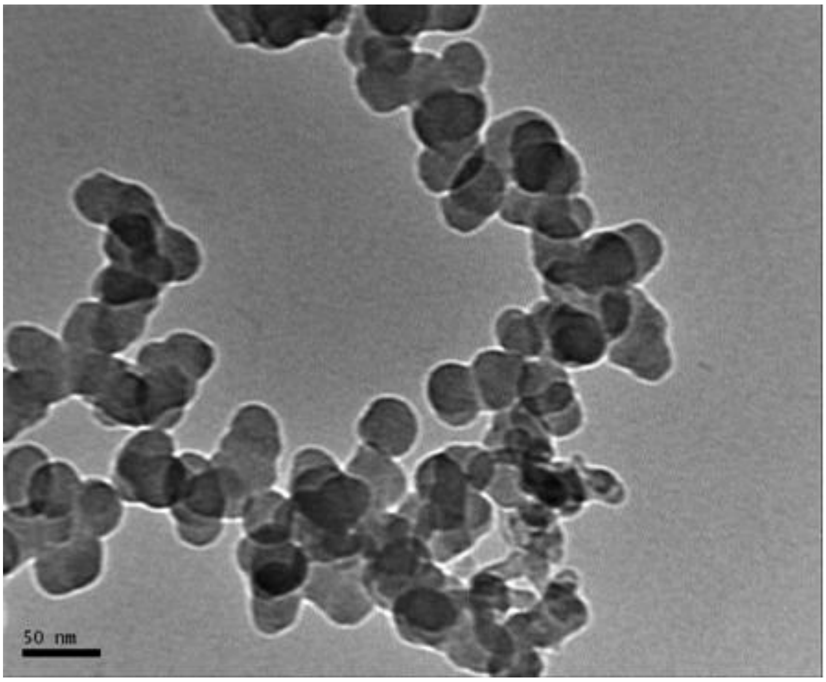

Figure 4.41: TEM of sample W_5 showing uniform nano size WC particles.

The variation in contrast observed indicate that the reduction of WO_3 starts from the surface and proceeds further when the WO_3 is encapsulated by geletaneous amorphous carbon as has been also reported [28-29]. However, when milling time was further increased the synthesized WC particles become uniform and smaller in size as can be seen in TEM micrograph of W_5 which is shown in figure 4.41. Here no trace of geletenous amorphous carbon is observed. Moreover, the particles are uniform and grown completely. The WC particles are nearly spherical and the size varies from 20 to 25 nm. The variation in size is minimum in this case. Figure 4.42 shows TEM micrograph of WC particles when milled for 20 h (W_6).

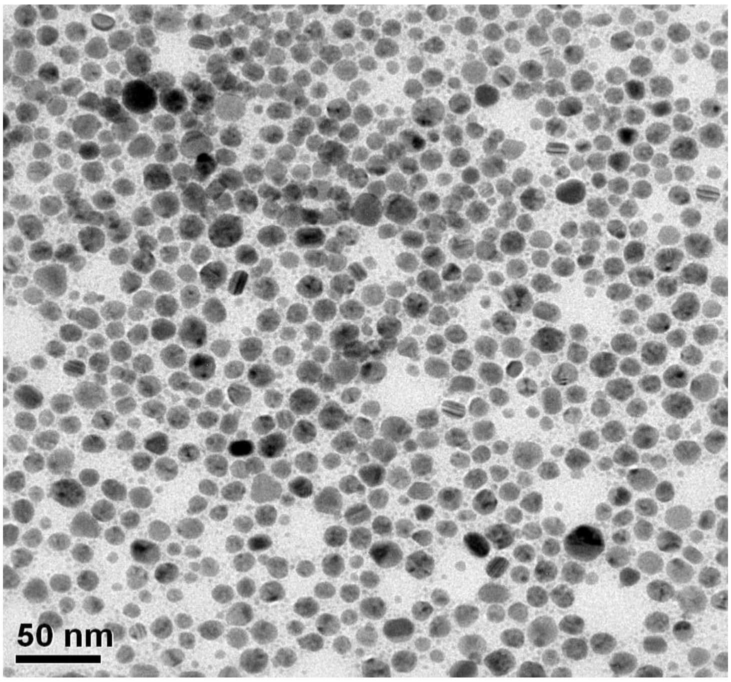

Figure 4.42: TEM of sample W_6 showing uniformly distributed nano WC particles.

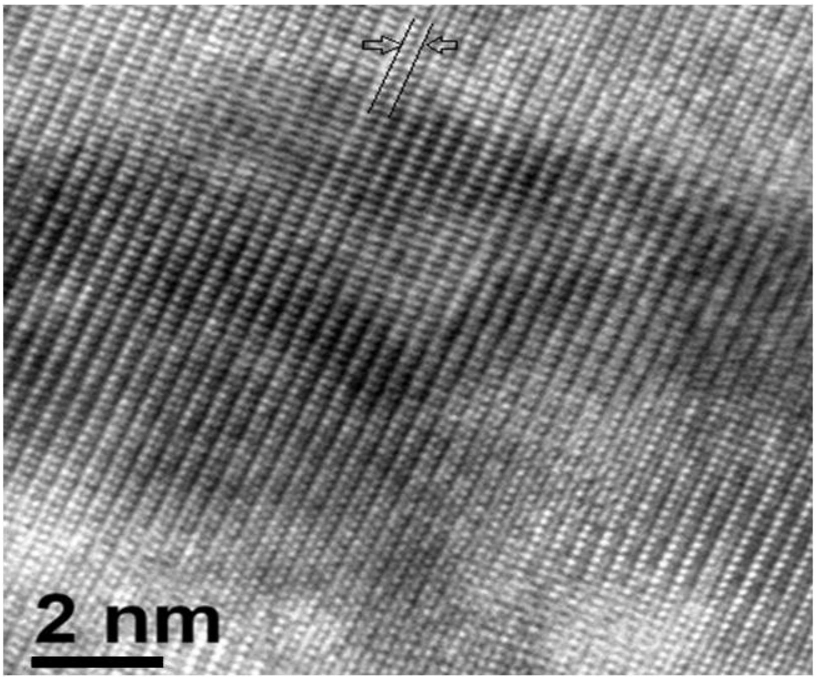

Figure 4.43: HRTEM of sample W_6 showing lattice fringing.

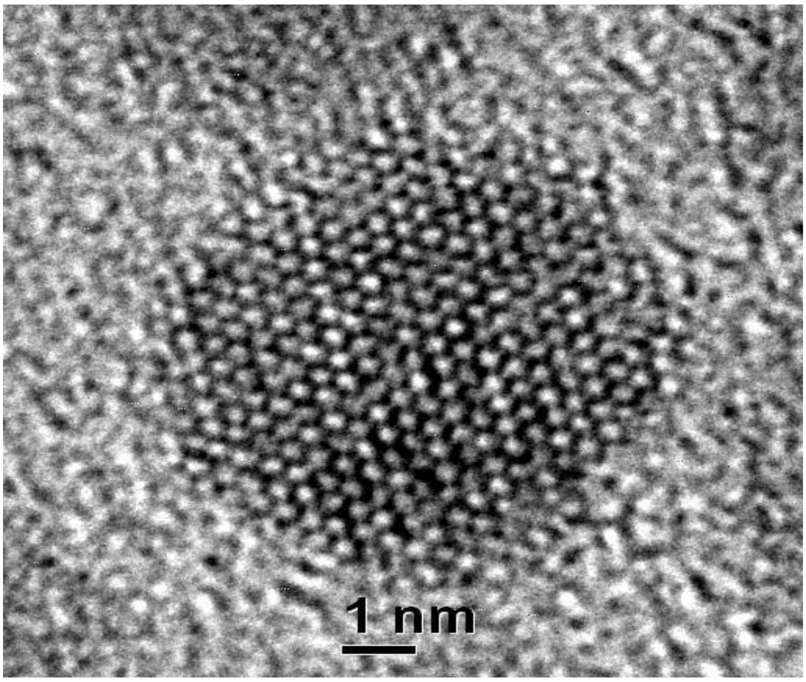

Figure 4.44: HRTEM of sample W_6 showing lattice fringing in single nano particle.

Here tungsten carbide nanocrystals of average 13 nm size can be seen. The observed particle size (13 nm) is in close proximity of that which was estimated using Scherrer's equation (13.4 nm). At some places nano rods are also visible. The inter-planer spacing 'd' calculated from HRTEM (figure 4.43 and 4.44) for this sample is 0.285 nm, which is very close to (001) plane of WC (0.28369 nm).

These HRTEM results also proved that tungsten carbide nano particles were well crystallized. The diffused ring selected area electron diffraction pattern (SAED) is also indexed for (101) and (100) planes of WC (figure 4.45).

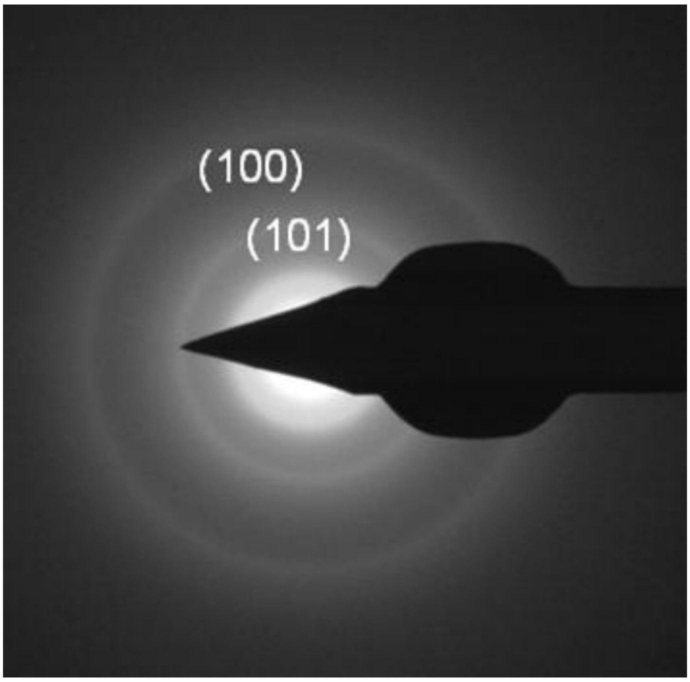

Figure 4.45: SAED pattern of sample W_6 showing ring pattern of different phases.

4.7. Sintering behavior of nano structured WC-Co composite

The synthesized WC nano particles of present work were further used for making WC-Co composites. Cobalt nano powders were obtained from Entraco metals Pvt Ltd and its purity is more than 99%.

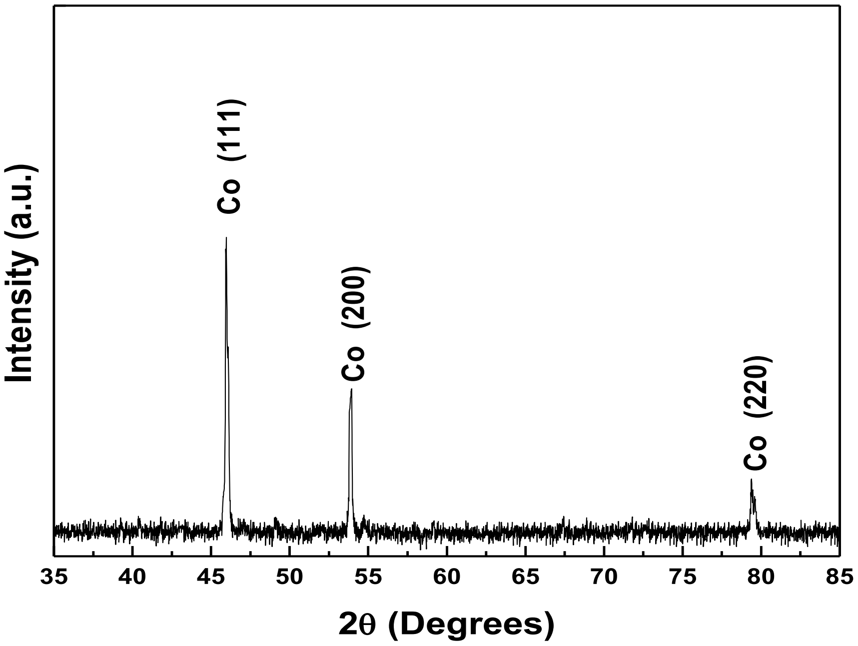

Figure 4.46: XRD pattern of cobalt nano powder.

The XRD analysis confirms that the powder is of single phase (figure 4.46). The calculated average particle size from XRD pattern using Scherrer's equation (as given in experimental details) is ≈ 58 nm. WC-Co composites have been prepared by mixing different weight percentage of cobalt nano particles in synthesized WC nano particles. The dried powders were ball milled for 4 h using tungsten balls in a tungsten jar at ≈ 300 rpm with 1:50 charge to ball ratio. In milled powder few drops of 10 mole % polyvinyl alcohol (PVA) was mixed. Known weight of dried powders was transferred in a die of 15 mm diameter for compaction using pressure of 503 MPa. The pellets obtained after compaction were sintered at different temperatures for different time duration in argon atmosphere in a calibrated resistance heating furnace. The details of experimental conditions followed for their sintering are given in table 4.12.

Table 4.12: Different samples with the sintering time, temperature and composition. (Y=done, N= not done)

Sample Labels	**Composition (WC/Co)**	**Heating temperature (°C) and time (h)**						
		1250	1300	1350				1400
		(1h)	(1h)	(1h)	(2h)	(3h)	(4h)	(1h)
WP_1	95/5	Y	Y	Y	Y	Y	Y	Y
WP_2	90/10	Y	Y	Y	Y	Y	Y	Y
WP_3	85/15	Y	Y	Y	Y	Y	Y	Y
WP_4	80/20	N	N	Y	N	N	N	N
WF_1	95/5	Y	Y	Y	Y	Y	Y	Y
WF_2	90/10	Y	Y	Y	Y	Y	Y	Y
WF_3	85/15	Y	Y	Y	Y	Y	Y	Y
WF_4	80/20	N	N	Y	N	N	N	N

As the WC nano particles were prepared using two different sources of tungsten (WO_3 and wolframite) as described in section 4.6, so two different sets of composites were synthesized, labeled WP_i for WO_3 as tungsten source and WF_i for wolframite as tungsten source. Here 'i' varies from 1 to 4 (table 4.12). Since the powders synthesized from ore may contain some impurities even at very low levels but may either facilitate or hinder the sintering process so a separate study for composites synthesized using these powders was essential which may be helpful for its commercial exploitation.

4.7.1 Sintering of WC-Co composite

4.7.1.1 Effect of temperature variation for 5 wt% cobalt binder in Composite

The sintering behavior of green composites pellets were investigated after different heat treatments. The temperature was varied from 1250 ºC to 1400 ºC with an interval of

50ºC. Sintering time (1 h) and binder composition (5 wt% cobalt) is kept constant (WP_1 and WF_1 series table 4.12).

4.7.1.1.1 XRD analysis

XRD patterns of the as synthesized composites showed that there is no reacted phase of WC and cobalt is present. WC and Cobalt remained unreacted as indexed with ICDD card No.25-1047 and 88-2325 respectively. The typical XRD patterns of sintered composites are shown in figure 4.47 and 4.48 for the composites synthesized by WC powders obtained from WO_3 and wolframite as tungsten source, respectively.

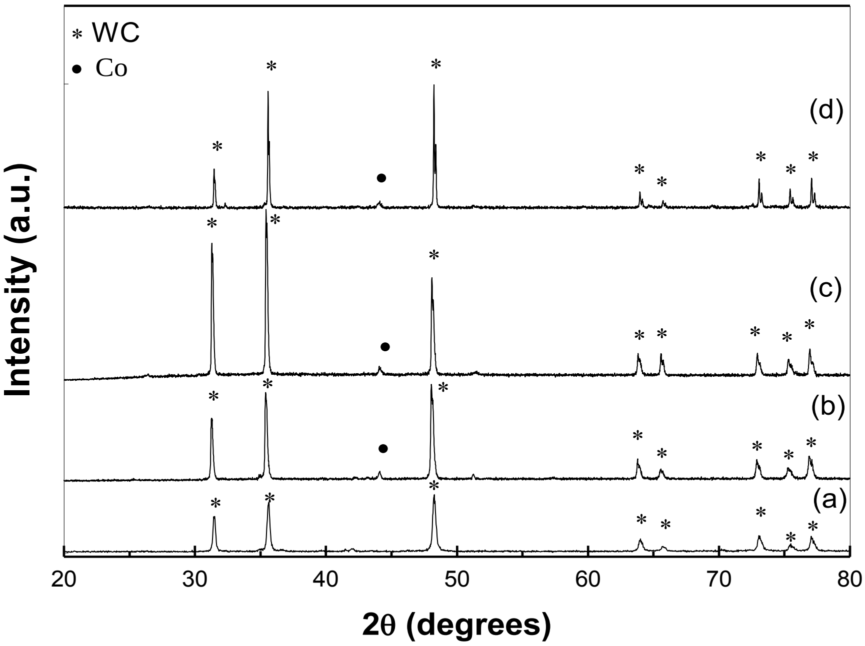

Figure 4.47 (a, b, c & d): XRD of samples of WP_1 series sintered at 1250, 1300, 1350 and 1400 ºC for 1 h respectively.

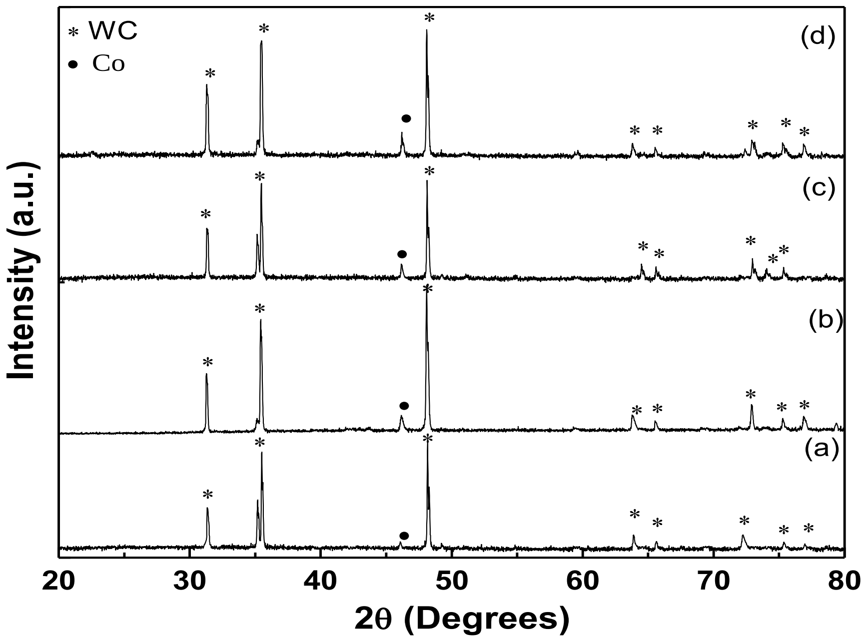

Figure 4.48 (a,b,c,d): XRD of samples of WF_1 series sintered at 1250, 1300, 1350 and 1400 °C for 1 h respectively.

It is well established fact that free carbon determines the presence of η phase as well as shape of WC particle in a WC–Co alloy [32]. In all the samples no free carbon is present and hence no trace of η phase is there. The broadening in the peaks is related with the size of particles [33]. The grain size, internal stress and density calculated in this case are given in table 4.13. In this case also the material is showing non uniform tensile strain. The density of composite is increasing with the increase in the sintering temperature.

Table 4.13: Particle size, micro strain and density as a function of sintering temperature for composites having 5% Co binder.

Temperature (ºC)	**Composite synthesized from WC obtained from WO_3**			**Composite synthesized from WC obtained from wolframite**		
	Particle size (nm)	**Micro strain ($*10^{-4}$)**	**Relative Density (%)**	**Particle size (nm)**	**Micro strain ($*10^{-4}$)**	**Relative Density (%)**
1250	40.41	3.20	69	37.63	4.76	71
1300	51.5	6.75	79	49.72	8.49	82
1350	66.94	1.54	90	65.75	6.67	89
1400	68.14	2.63	92	70.08	4.38	93

4.7.1.2 Microstructural examination

As reported above the sintering temperature was varied from 1250 ºC to 1400 ºC with an interval of 50 ºC where sintering time (1 h) and binder composition (5wt% cobalt) is kept constant. At 1250 ºC, particle size of the sintered product varied from 45 nm to 2 µm (figure 4.49 (a,b,c & d)).

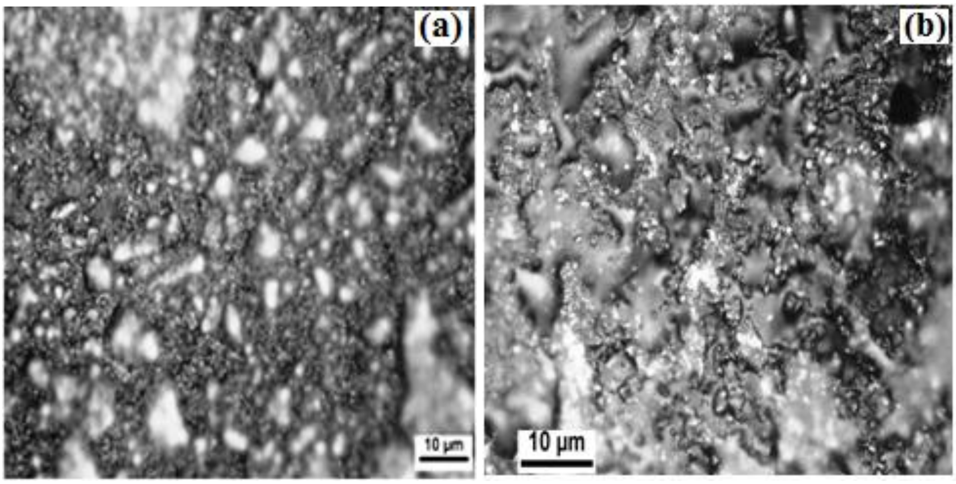

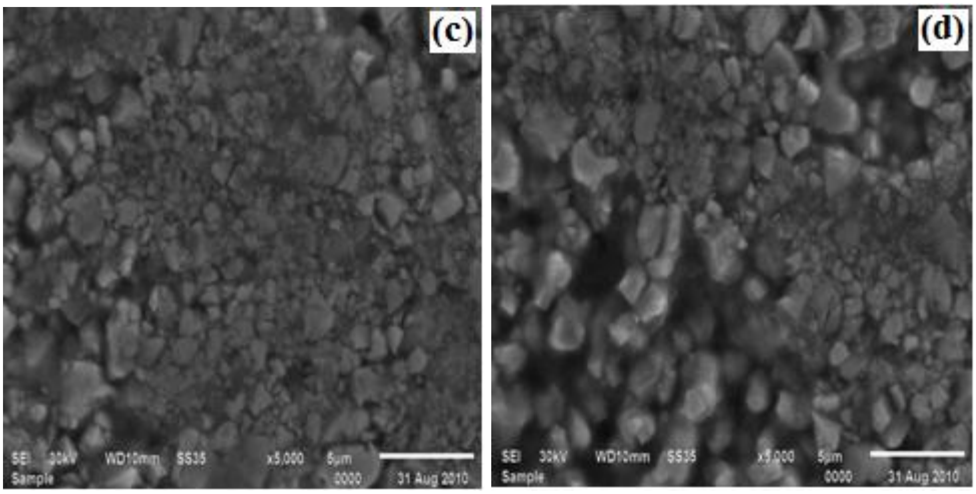

Figure 4.49 (a,b,c,d): Optical micrograph (a,b) SEM (c,d) of WC-Co(5%) composite (WP_1 series) sintered at 1250 ºC for 1 h.

The variation in particle size observed is non-uniform as can be seen in figure 4.49. The size at the central part is very small as compared to the other areas. During sintering the flow of heat start from edges and in the central part less amount of heat is available. However, particles binding occurred but grain growth is not observed.

Samples synthesized using ore and sintered under similar conditions have developed fine size WC grains as can be seen in figure 4.50 (a,b). The substance has gone under liquid phase sintering and have developed better microstructure as can be seen in figure 4.50 (c).

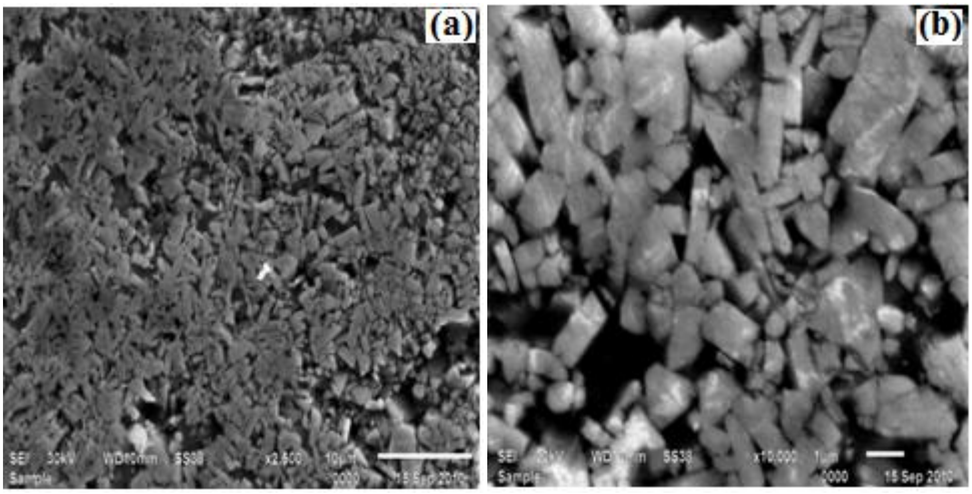

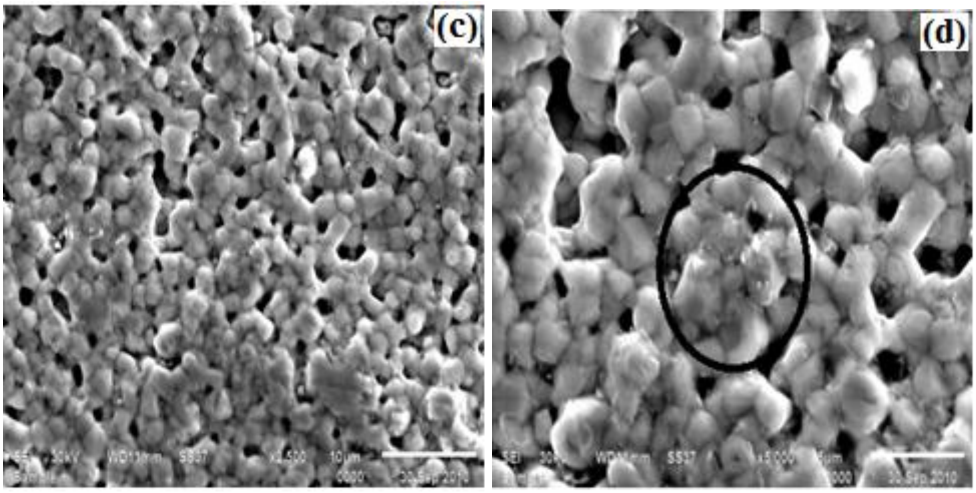

Figure 4.50(a,b,c,d): SEM of WC-Co(5%) composite (WF$_1$ series) sintered at 1250 ºC for 1 h.

The key factor observed is development of very fine size glassy phase figure 4.50 (c). These glassy phase helps in binding the grain as can be seen in figure 4.50 (d) where the area is encircled. The sample has developed better structure as compared to samples synthesized by pure chemicals.

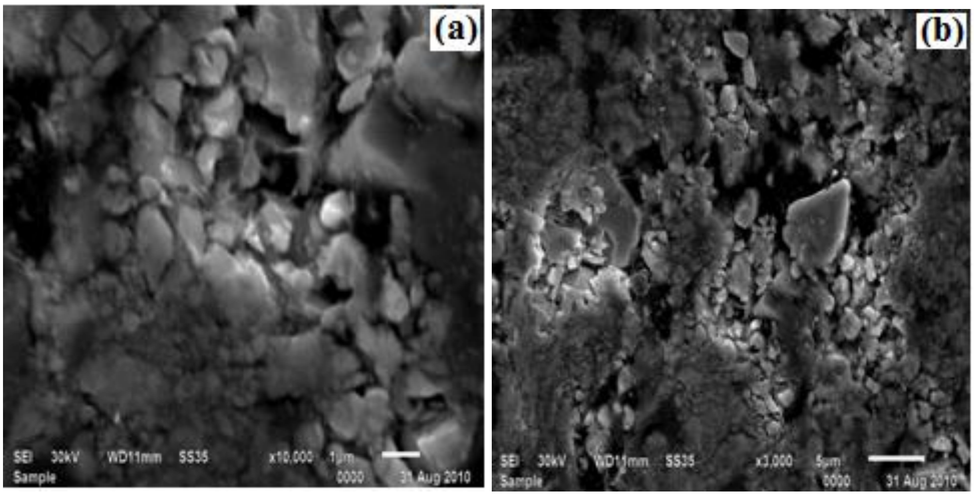

Figure 4.51(a,b): SEM of WC-Co(5%) composite (WP$_1$ series) sintered at 1300 ºC for 1 h.

The WC particles did not show any significant changes in grain shape until 1300 ºC. Only few isolated WC grains are present in the powder, mainly WC grains agglomerates are observed. The grains at certain places do not acquire prismatic shape. They are rather rounded, neither prismatic nor basal facets are observed at the surface of WC grains (figure. 4.51(a,b)). However, its formation is apparent at some places.

However, the micro-structural examination of samples synthesized from WC powder obtained from wolframite and sintered under similar conditions showed mixed morphology. Figure 4.52 depict such type of features. Moreover, the grain growth at certain places has started (figure 4.52(a)). Since, the sample could not attain uniform temperatures throughout the section, such features develops. This leads to growth of rod type of morphology by coalescence process in the cavity formed during liquid phase sintering (figure 4.52 (b) and continuously well defined grains do form (figure 4.52 (c,d)).

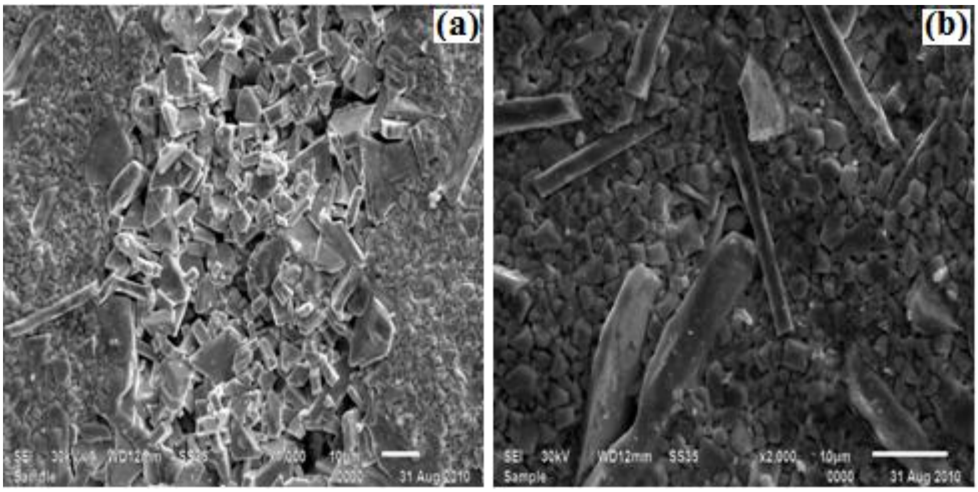

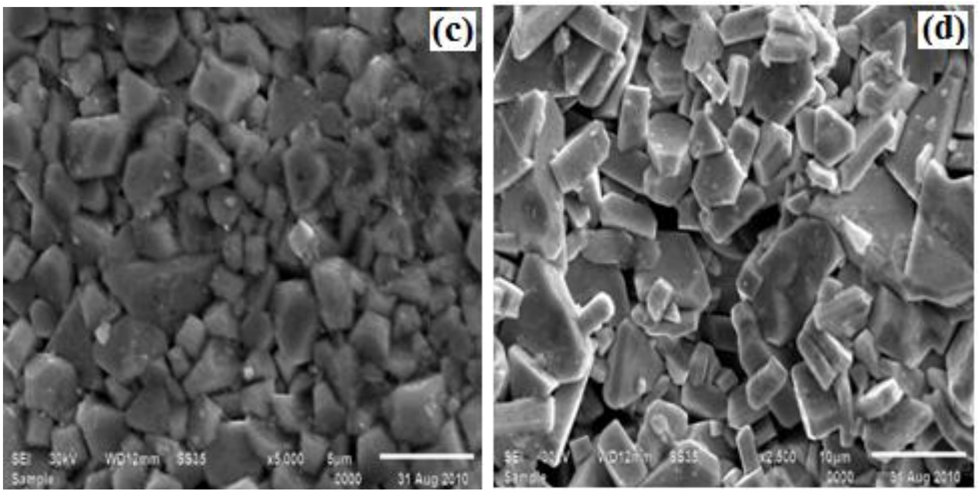

Figure 4.52(a,b,c&d): SEM of WC-Co(5%) Composite (WF$_1$ series) sintered at 1300 ºC for 1 h.

After the increase in sintering temperature at 1350 °C for 1 h a significant change in shape of WC grain has taken place. The grains start to grow with increase in temperature (figure 4.53(a). It consists of fine WC grain along with coarse WC. The growth of grain occurs by the process of coalescence (defocused area in figure 4.53 (a)). This is more clear in figure 4.53 (b) where growth occurs in the area of voids. The system is dynamic in nature as can be seen in the flow pattern of figure 4.53 (c,d).

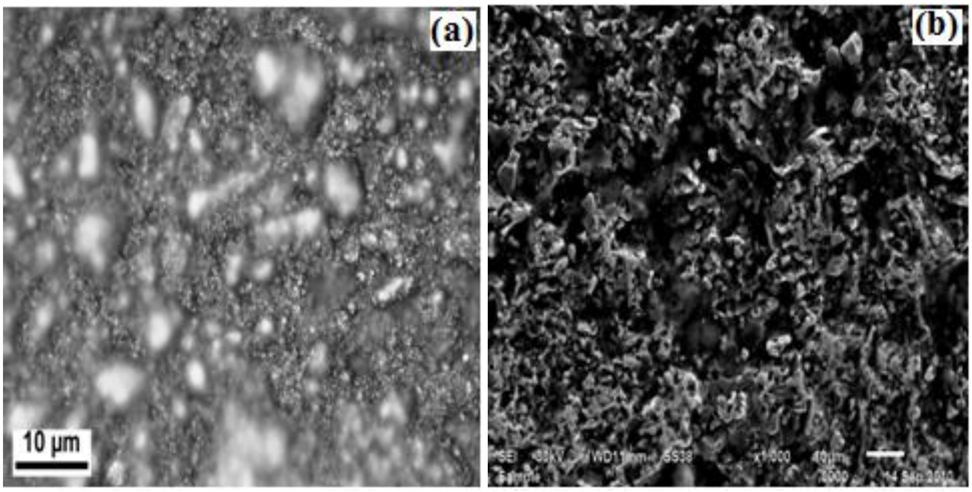

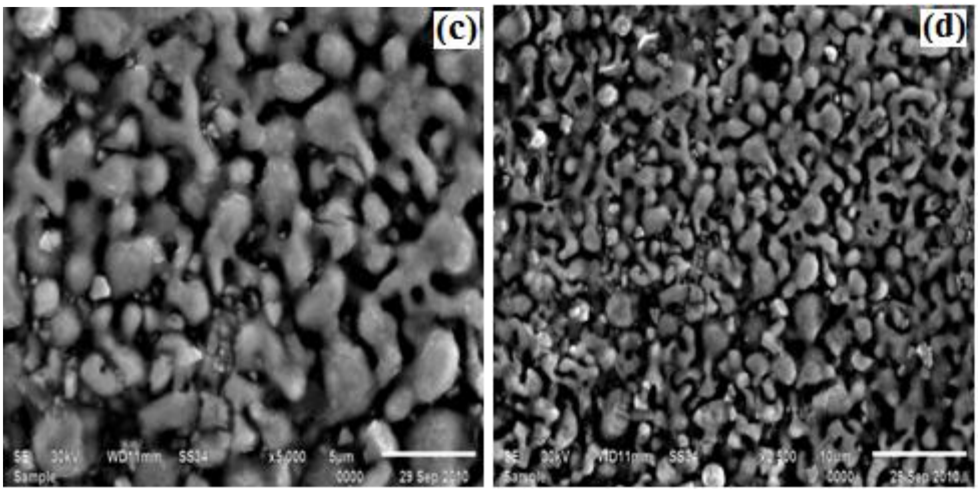

Figure 4.53(a,b,c,d): Optical micrograph (a) SEM (b,c,d) of WC-Co(5%) composite (WP_1 series) sintered at 1350 ºC for 1 h.

Composite synthesized from wolframite ore also showed similar structural features (figure 4.54(a)). The interesting feature observed here is that nano WC particles grow like rod (figure 4.54(b)). These rods thicken with time and ultimately acquire the faceted type morphology (figure 4.54(c)). Moreover, such types of features are only observed in samples which have been synthesized from powders obtained from wolframite ore.

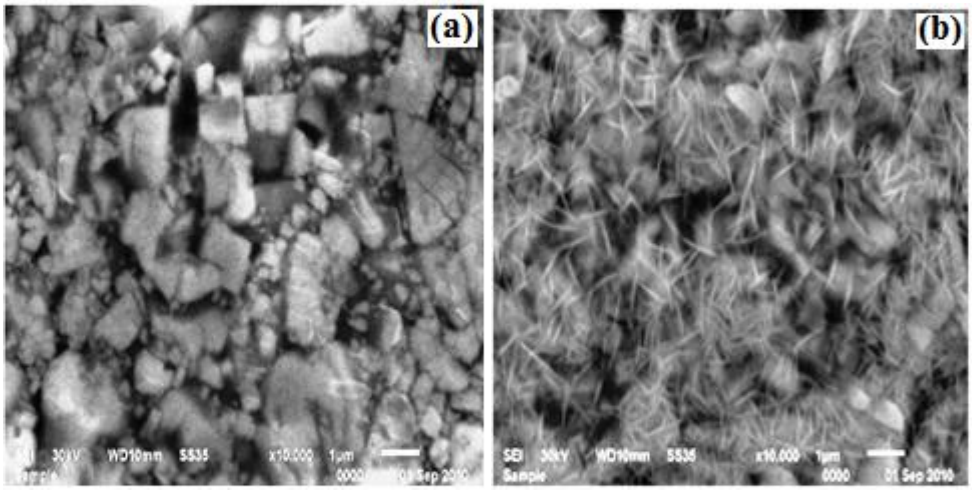

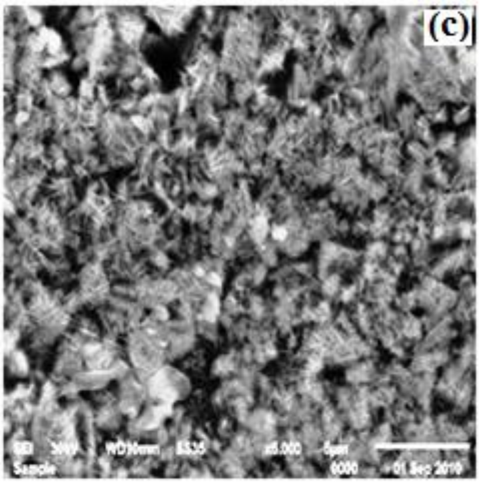

Figure 4.54 (a,b,c): SEM of WC-Co(5%) composite (WF$_1$ series) sintered at 1350ºC for 1 h.

Similarly at higher sintering temperature (1400 ºC) it generates the homogenous type of features containing fine size WC particles (bright one in figure 4.55 (a)). However, when analyzed under SEM it provides the structure of product which is under fluid flow condition. The growth of WC grain is rapid. Moreover, the diffusion is fast so voids generated are of large size (figure 4.55 (b)).

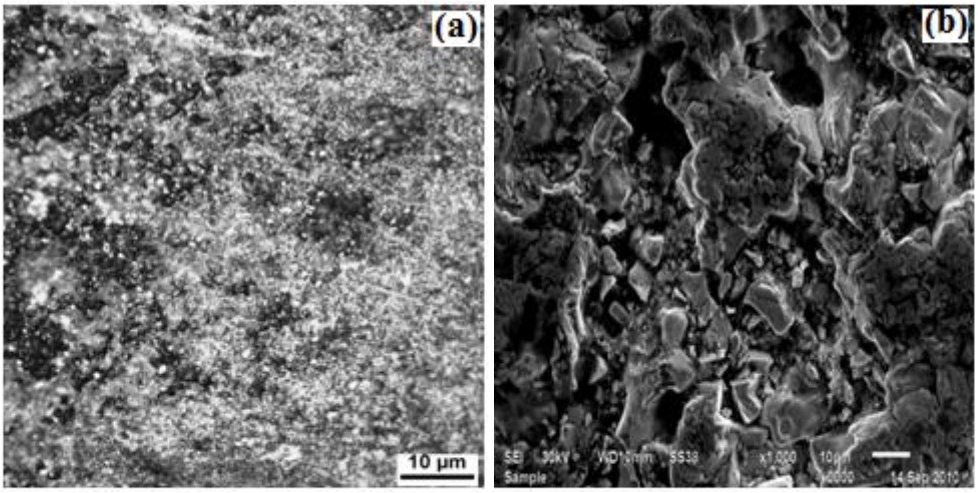

Figure 4.55(a,b) Optical micrograph(a), SEM (b) of WC-Co(5%) composite (WP$_1$ series) sintered at 1400 ºC for 1 h.

Composite synthesized from WC powder obtained from wolframite ore showed different type of structural features (figure 4.56 (a,b). Grains observed are fully grown with less voids. However, the WC particles are of larger size near void areas. This is because of fact that smaller size WC particles grow by coalescence causing a decrease in surface area and volume. The overall analysis of structure indicate that samples containing 5% Co have lot of porosity when sintered at 1250 °C and 1300 °C for 1 h ((figure 4.49 to figure 4.52).

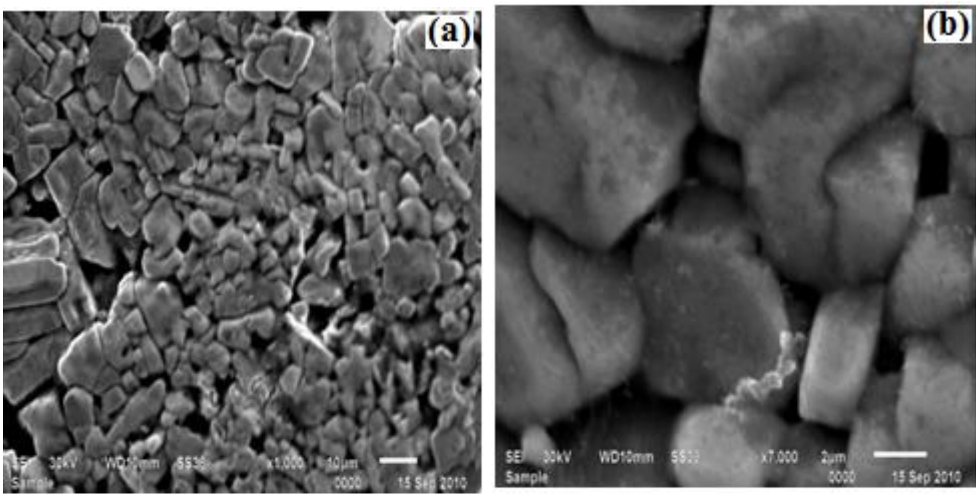

Figure 4.56(a,b): SEM of WC-Co(5%) Composite (WF$_1$ series) Sintered at 1400ºC for 1 h.

When the sintering temperature was increased to 1350 °C, homogeneous structure was obtained (figure 4.53 and figure 4.54). As the temperature was increased to 1400 °C, material starts flowing causing improper grain growth with porous structure (figure 4.55 and figure 4.56). Detailed micro structural examination showed that the grain growth occurred by process of coalescence. However, composite synthesized using WC particles derived from wolframite develops fine size of needle like structure which grows to faceted type with time.

4.7.2 Effect of temperature variation for 10 wt% cobalt binder in Composite

In order to study the effect of sintering temperature on pellets of the composites having 10% Co binder, the sintering temperature was varied from 1250 ºC to 1400 ºC with an increment of 50 ºC. Sintering time (1 h) and binder composition (10wt% cobalt) is kept constant (WP_2 and WF_2 series table 4.12).

4.7.2.1 XRD analysis

XRD patterns of the as synthesized composites showed the presence of WC and Co phases which are indexed with ICDD card No.25-1047 and 88-2325, respectively. The XRD patterns of sintered pellets are shown in figure 4.57 and 4.58 for the composites synthesized from WC obtained from WO_3 and wolframite as tungsten source, respectively. In all the samples no free carbon is present and hence no trace of η phase is there.

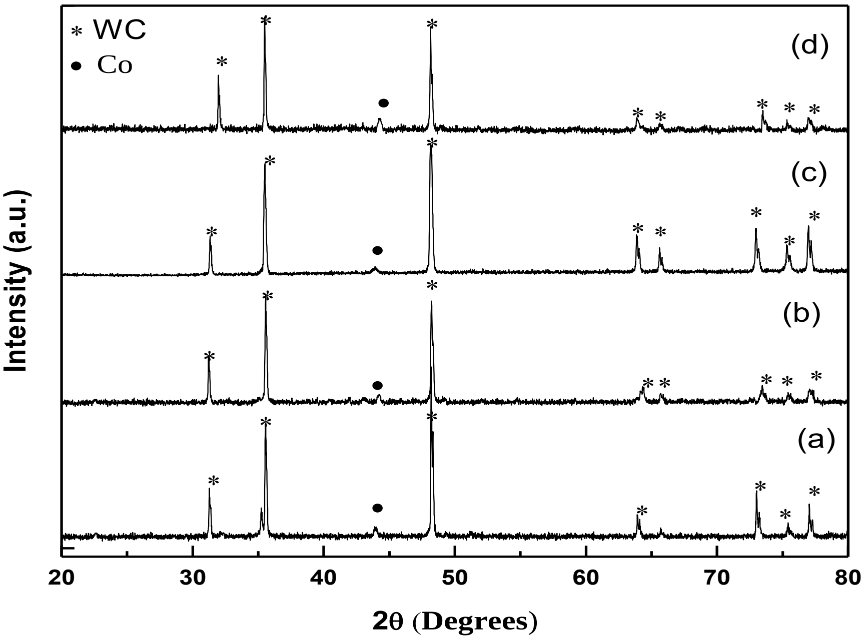

Figure 4.57 (a, b, c & d): XRD of WC-Co(10%) composite (WP$_2$ series, table 4.12) sintered at 1250, 1300, 1350 and 1400 °C for 1 h respectively.

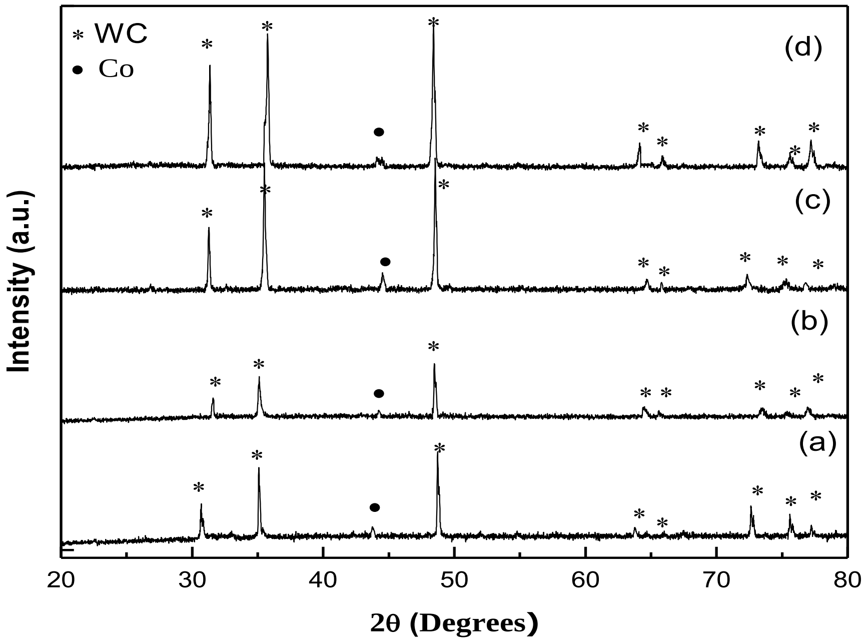

Figure 4.58 (a, b, c & d): XRD of WC-Co(10%) composite (WF$_2$ series, table 4.12 sintered at 1250, 1300, 1350 and 1400 °C for 1 h respectively.

The grain size, internal stress and density calculated in this case are given in table 4.14. In this case also the material is showing non uniform tensile strain. The increment in density is observed with increasing sintering temperature.

Table 4.14: Particle size, micro strain and density as a function of sintering temperature for composites having 10% Co binder.

Temperature (ºC)	**Composite synthesized from WC obtained from WO_3**			**Composite synthesized from WC obtained from wolframite**		
	Particle size (nm)	**Micro strain ($*10^{-4}$)**	**Relative Density (%)**	**Particle size (nm)**	**Micro strain ($*10^{-4}$)**	**Relative Density (%)**
1250	44.49	4.70	73	40.35	5.76	70
1300	53.52	5.35	81	46.45	6.58	79
1350	66.09	7.86	92	69.65	8.87	90
1400	70.12	4.49	93	73.36	3.35	94

4.7.2.2 Microstructural analysis

When the binder content (Co) was increased to 10% and sintered at 1250 ºC a continuous network structure was observed at some places (figure 4.59(a)). This network is of WC particles of finer size as can be seen in figure 4.59(b) (central part). Moreover, the flow pattern indicates the flow direction of heat which also make the particles aligned.

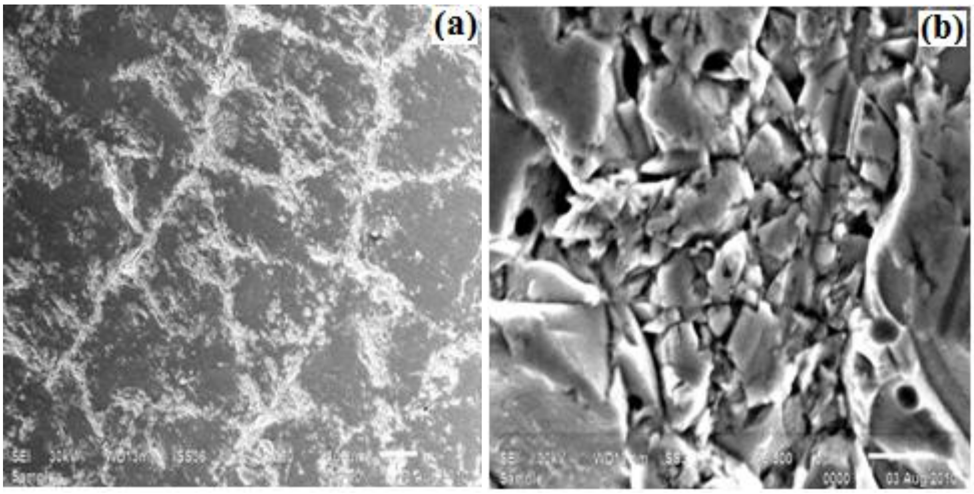

Figure 4.59 (a,b): SEM of WC-Co(10%) Composite (WP_2 series) Sintered at 1250 ºC for 1 h.

Composites made from WC particles derived from wolframite ore also exhibited the network pattern. The WC particles are very fine (figure 4.60(a)). Higher magnification micrographs indicate that growth of WC particles is taking place along the network structure (figure 4.60(b)).

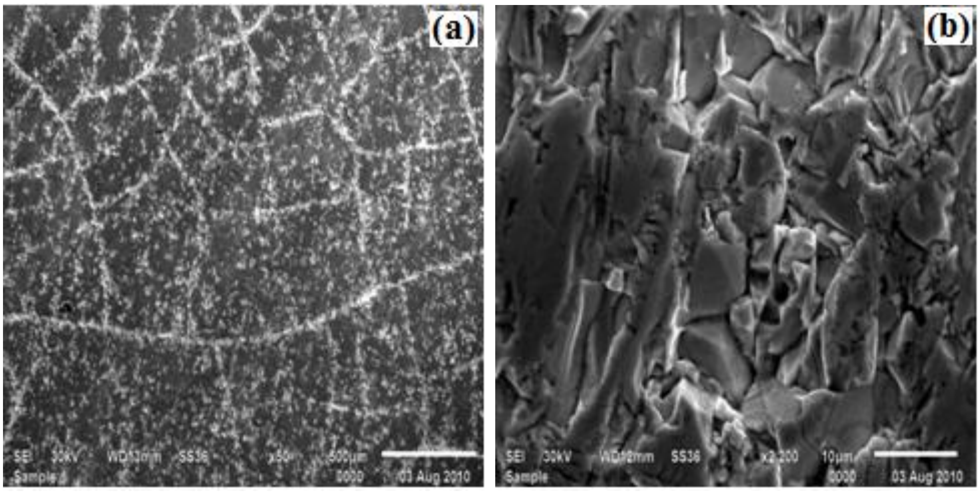

Figure 4.60(a,b): SEM of WC-Co(10%) Composite (WF_2 series) sintered at 1250 ºC for 1 h.

Composites made of WC obtained from pure chemicals using 10% binder and sintered at 1300 ºC have shown fully grown structures (figure 4.61(a)). However, the dissolution of network has not started yet (figure 4.61(b)) even at higher temperature.

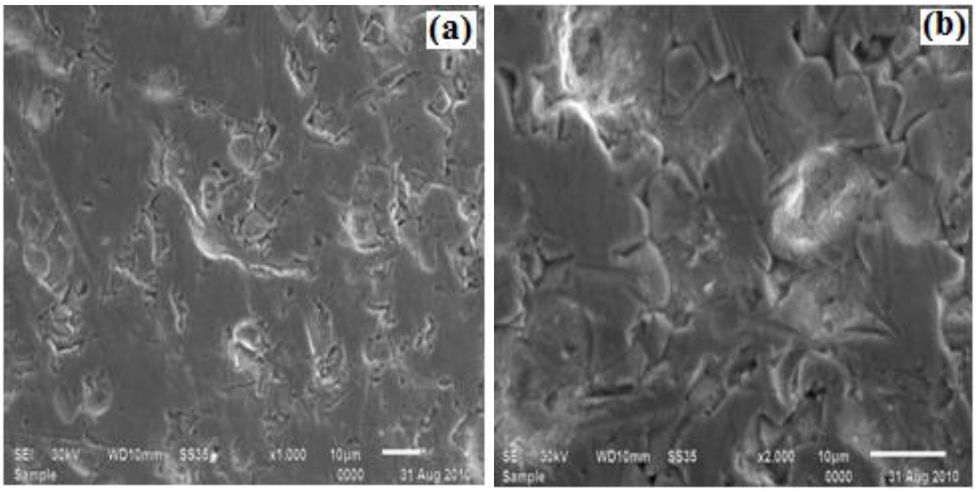

Figure 4.61(a,b): SEM of WC-Co(10%) composite (WP$_2$ series) sintered at 1300 ºC for 1 h.

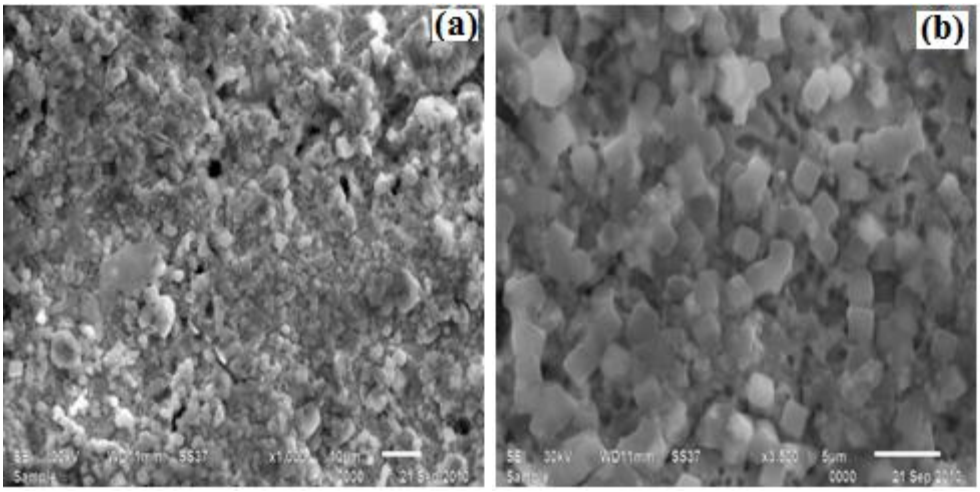

Figure 4.62(a,b): SEM of WC-Co(10%) composite (WF$_2$ series) sintered at 1300 ºC for 1 h.

Composite derived from WC powders obtained from wolframite ore also exhibited fully dense structure with finer to coarse type of morphology (figure 4.63(a)). However, it appears that the structure is fully dense product as can be seen the cuboid type of WC particles (figure 4.62(b)). At 1350 ºC sintering temperature we could observe the dissolution of WC particles followed by their growth (figure 4.63(a)). The grains are growing to rod type of features (figure 4.63(b)). The rod type of morphology is mostly observed in the area near the voids which is created by coalescence process.

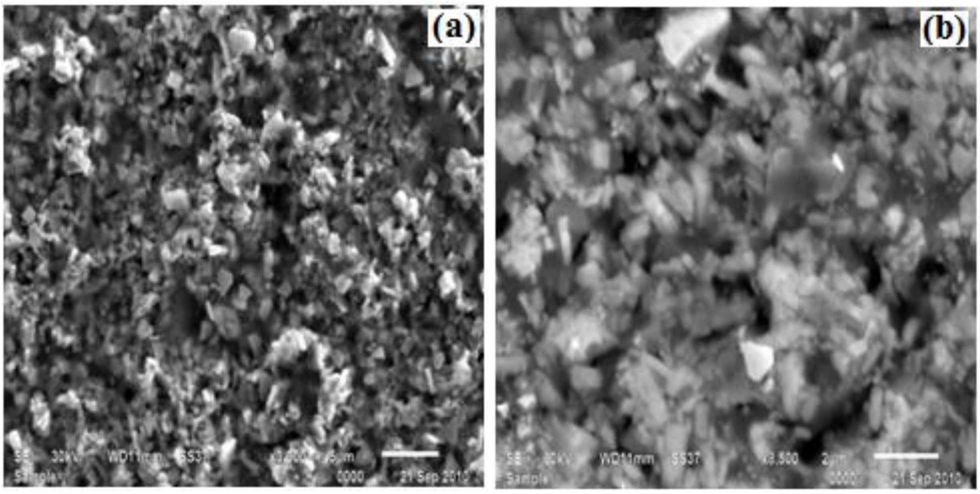

Figure 4.63(a,b): SEM of WC-Co(10%) composite (WP$_2$ series) sintered at 1350 ºC for 1 h.

Powders sintered at 1350 ºC for 1 h derived from WC synthesized using wolframite have exhibited very good structures as compared to previously reported samples. Low magnification micrographs give the appearance of uniform grain size throughout the structure. The flow pattern arising during grain growth can be easily seen (figure 4.64(a)). These grain growth may lead to development of faceted type of morphology as can be seen in the areas where crack type of morphology is observed as shown in figure 4.64(b,c). The subgrain structure seen in figure 4.64(d) which lead to development of faceted features.

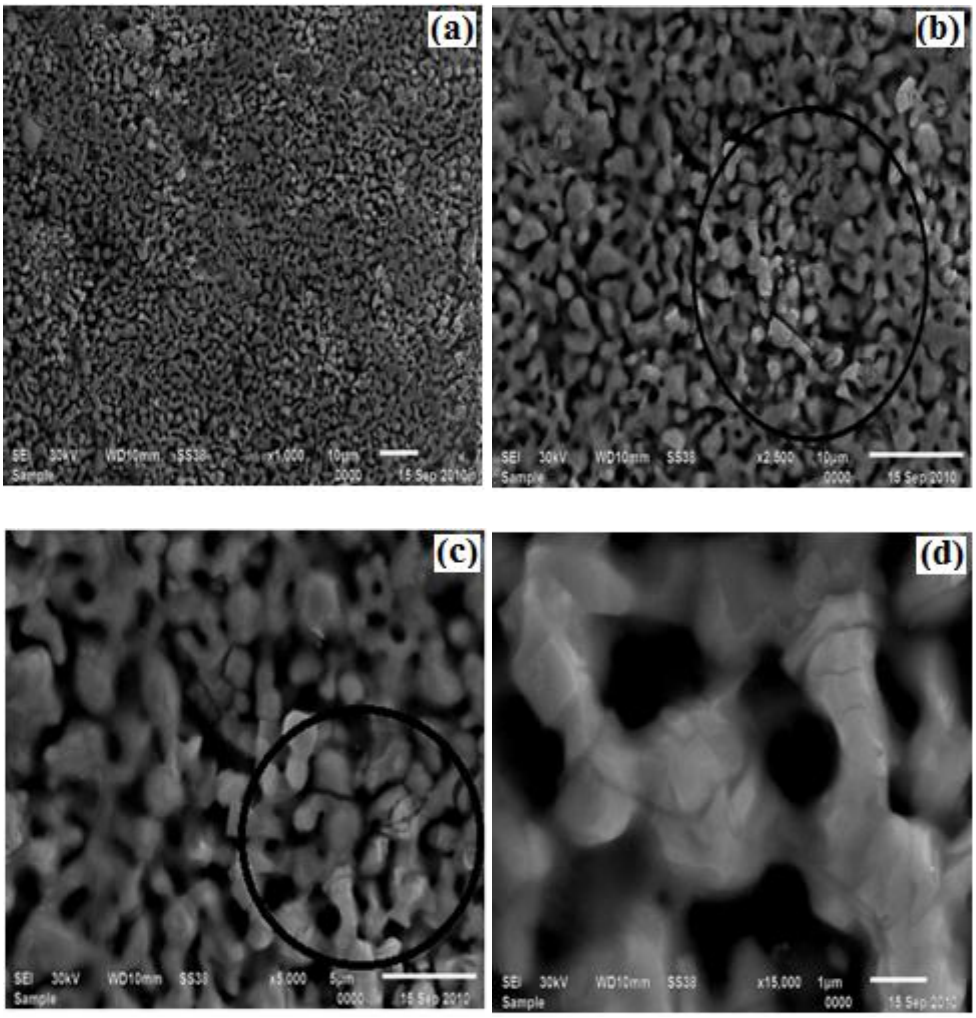

Figure 4.64(a,b,c,d): SEM of WC-Co(10%) composite (WF$_2$ series) sintered at 1350 ºC for 1 h.

In case of WC obtained from wolframite we could see mixed structure (faceted and non faceted) while in case of WC obtained from WO$_3$ only faceted morphology is present (figure 4.65(a,b)). The prismatic type of grains in case of WC (wolframite) indicates that the composite has undergone complete sintering (figure 4.66(a,b)).

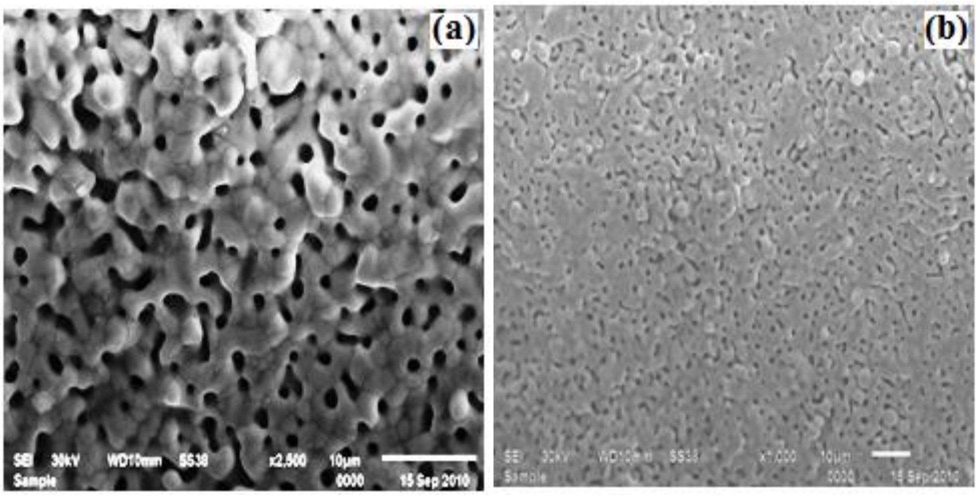

Figure 4.65(a,b): SEM of WC-Co(10%) composite (WP_2 series) sintered at 1400 ºC for 1 h.

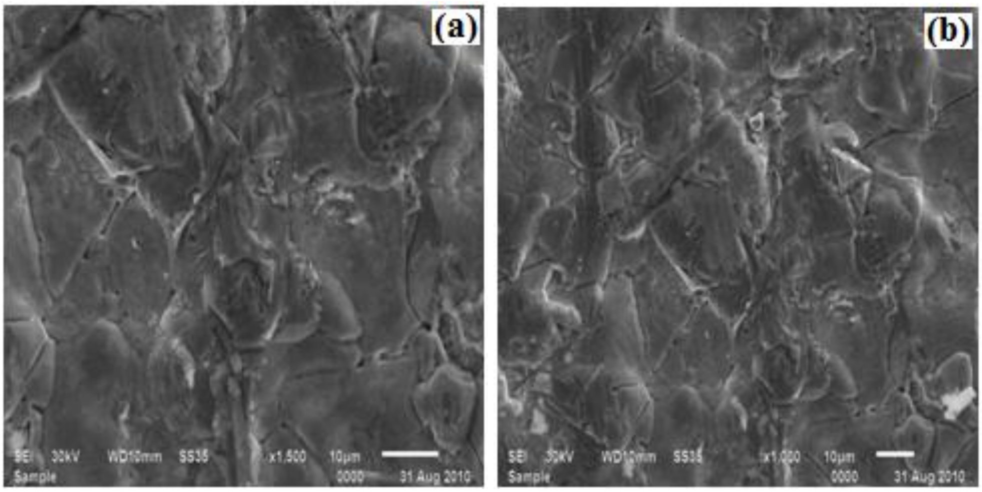

Figure 4.66(a,b): SEM of WC-Co(10%) composite (WP_2 series) sintered at 1400 ºC for 1 h.

4.7.3 Effect of temperature variation on 15wt% cobalt composite

Effect of sintering temperature on pellets of the composites having 15% Co binder, were studied. Sintering temperature was varied from 1250 ºC to 1400 ºC with an increment of 50 ºC with constant sintering time (1 h) and binder composition (15wt% cobalt). The details are also given in table 4.12 (WP_3 and WF_3 series).

4.7.3.1 XRD analysis

XRD patterns of the as synthesized composites indicated that no reacted phase of WC and cobalt is formed. WC and cobalt remained unreacted and indexed with ICDD card No.25-1047 and 88-2325, respectively. The typical XRD patterns of sintered composite are shown in figure 4.67 and 4.68 for the composites synthesized from WC powders obtained from WO_3 and wolframite as tungsten source respectively.

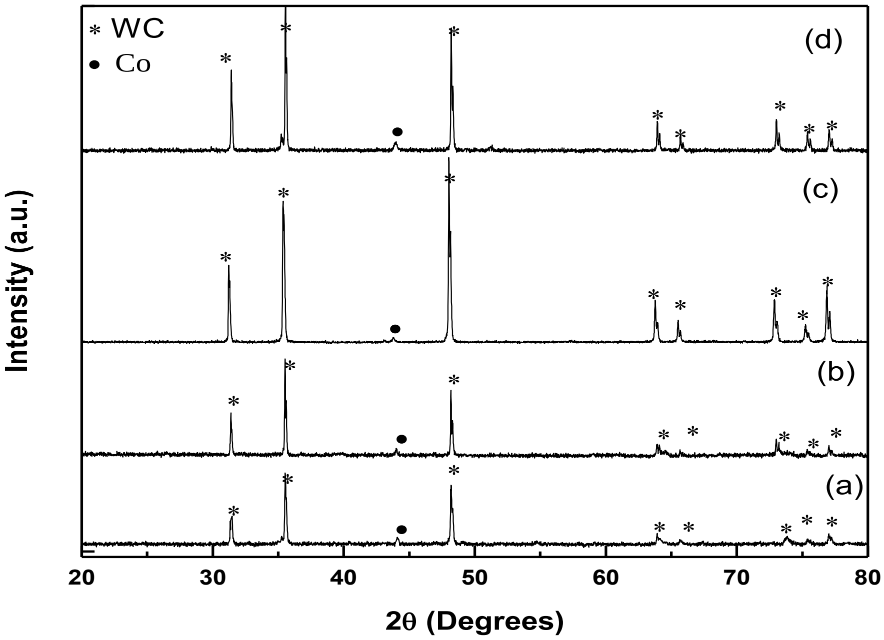

Figure 4.67 (a,b,c,d): XRD of WC-Co(15%) composite (WP_3 series, table 4.12)sintered at 1250, 1300, 1350 and 1400 °C for 1 h, respectively.

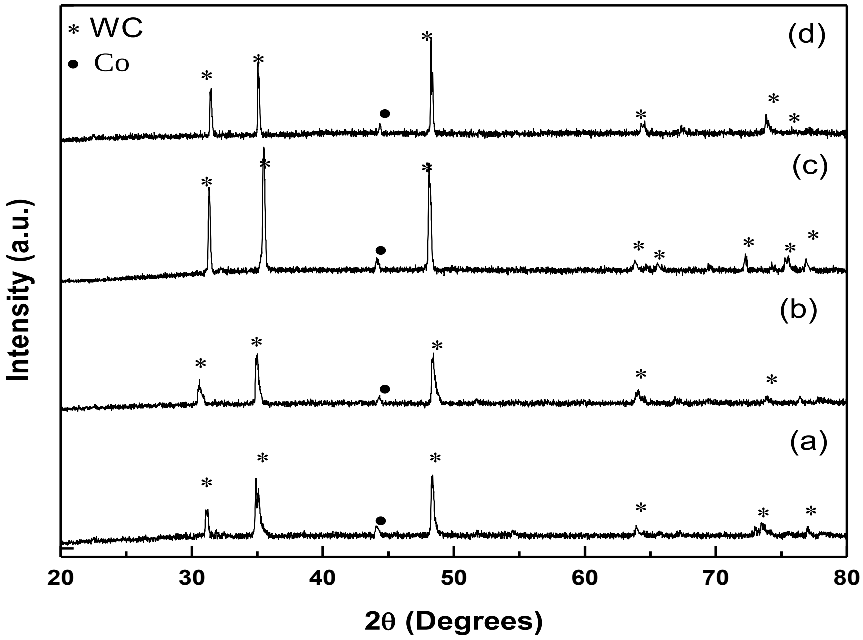

Figure 4.68 (a,b,c,d): XRD of WC-Co(15%) composite (WP_3 series, table 4.12) sintered at 1250, 1300, 1350 and 1400 ºC for 1 h respectively.

Table 4.15: Particle size, micro strain and density as a function of sintering temperature for 15% Co binder.

Temperature (ºC)	**Composite synthesized from WC obtained from WO_3**			**Composite synthesized from WC obtained from wolframite**		
	Particle size (nm)	**Micro strain ($*10^{-4}$)**	**Relative Density (%)**	**Particle size (nm)**	**Micro strain ($*10^{-4}$)**	**Relative Density (%)**
1250	43.58	3.55	79	42.78	6.46	78
1300	50.59	4. 47	88	48.37	3.45	87
1350	66.56	6.45	97	60.78	6.77	95
1400	73.77	5.89	99	76.38	5.85	99

The grain size, internal stress and density calculated in this case are given in table 4.15.

In this case also the materials are showing non uniform tensile strain. The density is observed to increase as the sintering temperature is increased.

4.7.3.2. Microstructural analysis

When the binder content was increased to 15%, the sintered products have developed fully grown faceted morphology (figure 4.69 (a)). The interconnected liquid phase is also visible in microstructure. The structural features observed at higher magnification indicated that growth is not complete at 1250 ºC as shown in figure 4.69(b).

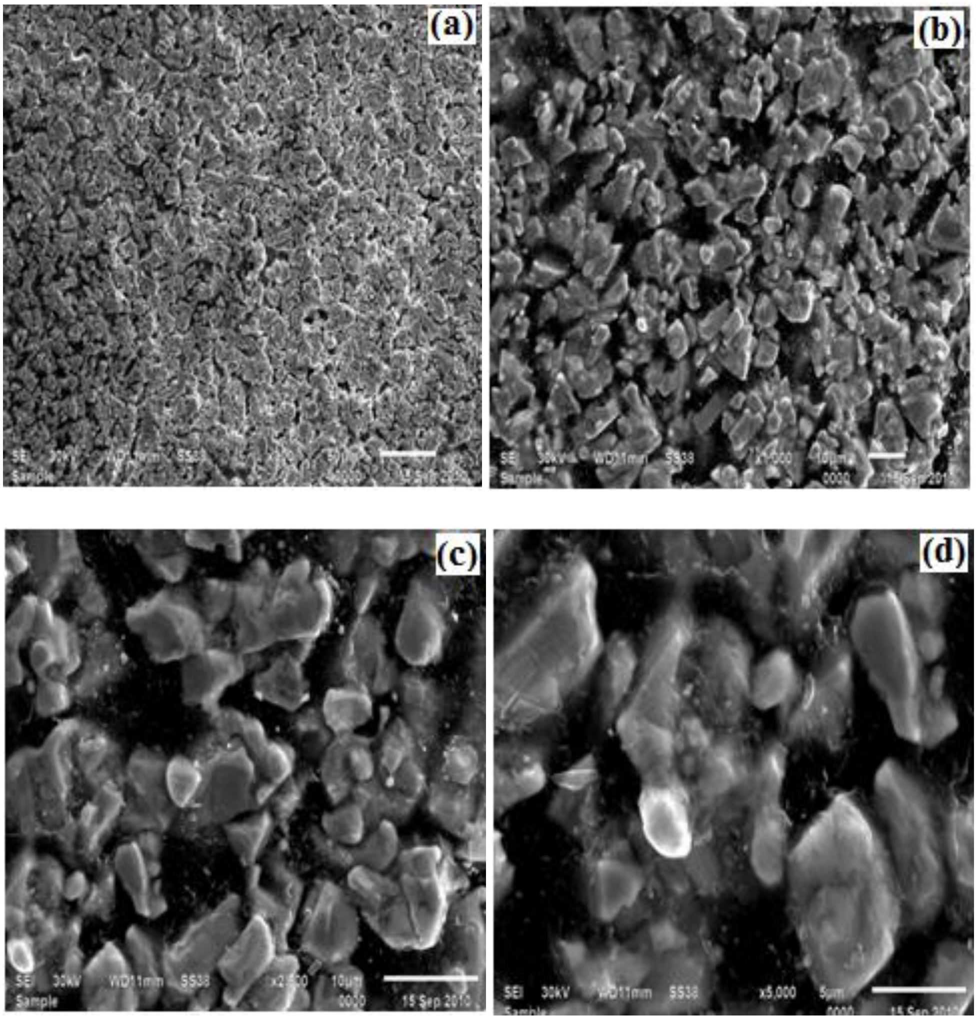

Figure 4.69(a,b,c,d): SEM of WC-Co(15%) composite (WP$_3$ series) sintered at 1250 ºC for 1 h.

Though faceting features are observed but fluid flow condition is also apparent (figure 4.69(c,d)). Composite made under similar condition using powder synthesized from wolframite indicate that grain growth has occurred along the network type of structure. This type of structure is developed during sintering (figure 4.70(a)). The coarse and finer WC particles (figure 4.70(b)) are clearly seen which is indicating incomplete process of final growth. Later stage of growth could lead to development of faceted structure as is apparent in figure 4.70(b).

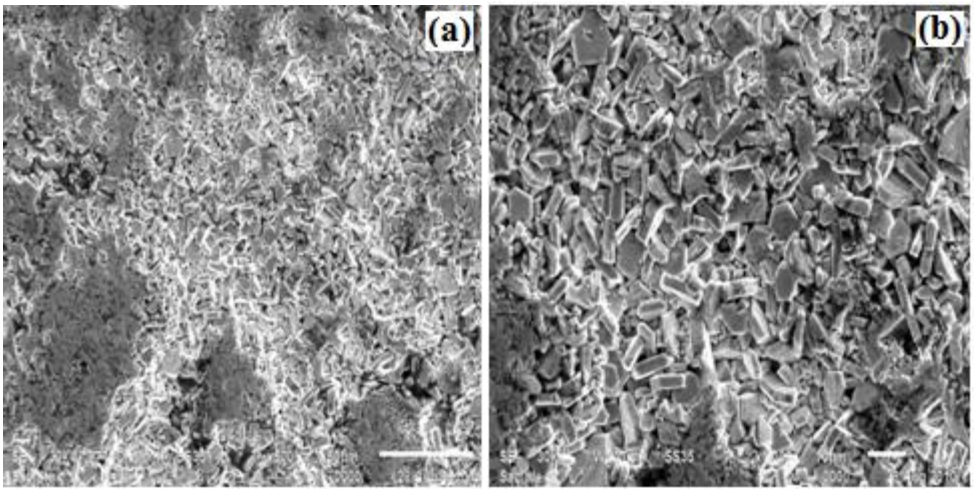

Figure 4.70(a,b): SEM of WC-Co(15%) composite (WF$_3$ series) sintered at 1250 ºC for 1 h.

When the sintering temperature was increased to 1300 ºC for 15% binder the structure observed was fully dense (figure 4.71(a)). However, the grain growth is not completed. It appeared in figure 4.71(b) the diffusion process is still occurring at this temperature. The presence of pores and small particles along these pores are evident for such type of phenomenon.

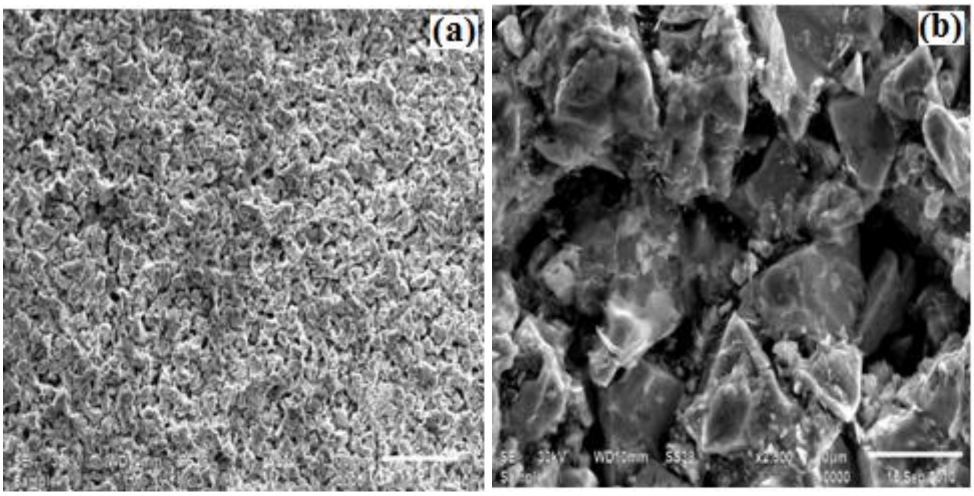

Figure 4.71(a,b): SEM of WC-Co(15%) composite (WP$_3$ series) sintered at 1300 ºC for 1 h.

Similar features are also observed for samples made of WC synthesized from wolframite ore. Figure 4.72(a) presents the view of same where one can see elongated faceted rod type of structure. Higher magnification view of the same is shown in figure 4.72(b).

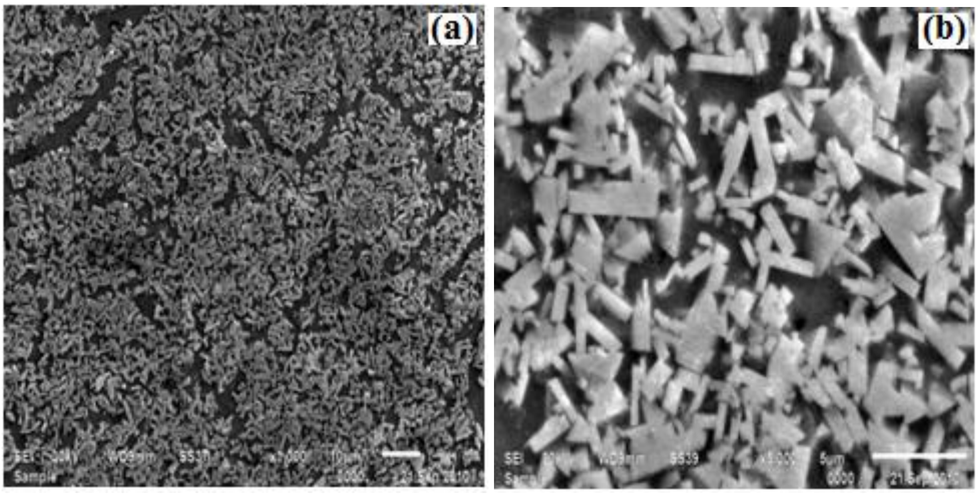

Figure 4.72(a,b): SEM of WC-Co(15%) Composite (WF$_3$ series) sintered at 1300 ºC for 1 h.

Samples sintered at 1350 ºC have exhibited uniform microstructures (figure 4.73(a)). The dull structure is evident for incomplete grain growth which is also evident in figure

4.73(b).

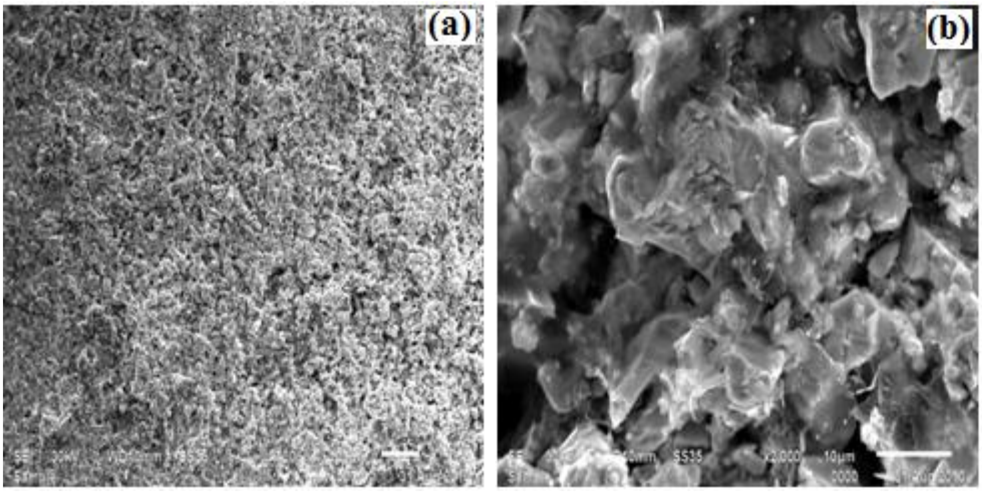

Figure 4.73(a,b): SEM of WC-Co(15%) composite (WP$_3$ series) sintered at 1350 ºC for 1h.

This observation is further supported in other micrograph (figure 4.74(a)) of composite synthesized from wolframite where elongated grain growth has occurred. The presence of subgrain structure in bigger particle (figure 4.74(b)) indicates that the process of diffusion and grain growth is not complete.

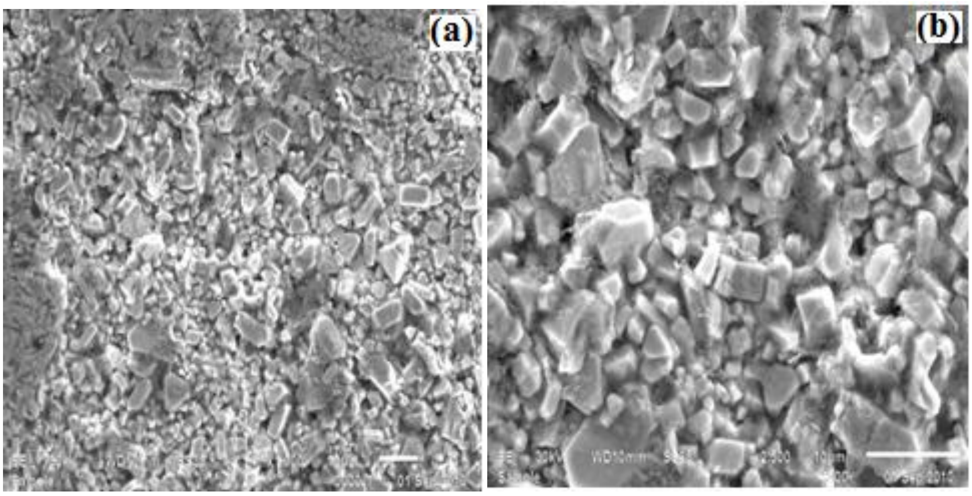

Figure 4.74(a,b,): SEM of WC-Co(15%) composite (WF$_3$ series) sintered at 1350 ºC for 1 h.

Composite sintered at 1400ºC have shown long elongated grains of WC (figure 4.75(a)). The composite seems to be fully sintered with little porosity (figure 4.75(b)). However, the flow pattern observed in composite of wolframite indicates that the sintering process is still going on as can be seen in figure 4.76(a,b).

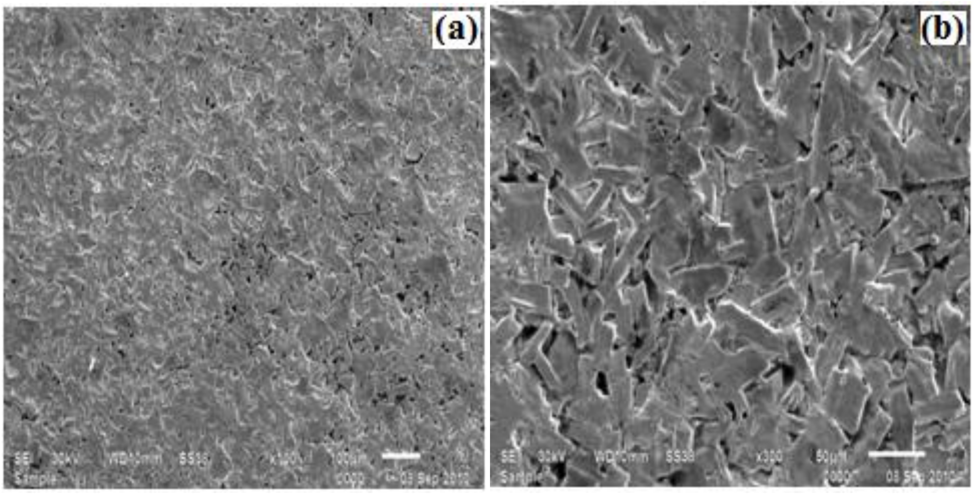

Figure 4.75(a,b): SEM of WC-Co(15%) composite (WP_3 series) sintered at 1400 ºC for 1 h.

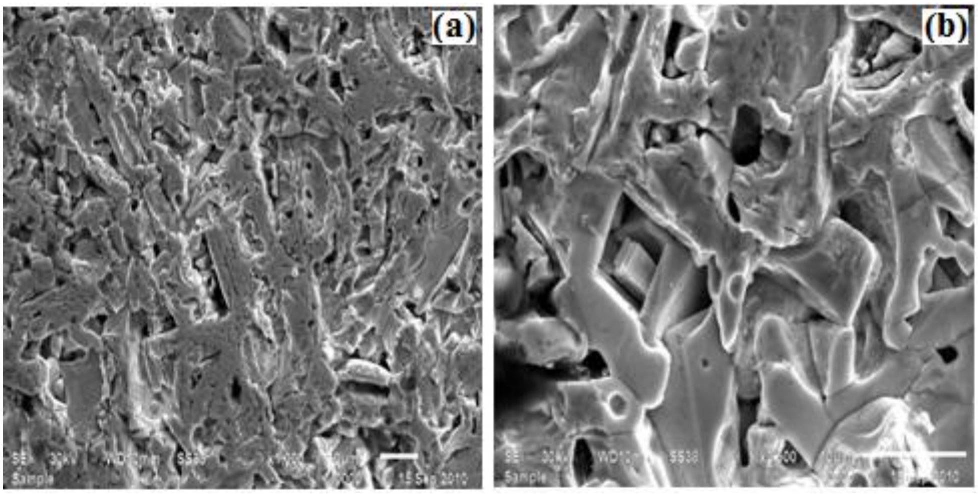

Figure 4.76(a,b): SEM of WC-Co(15%) composite (WF_3 series) sintered at 1400 ºC for 1 h.

4.7.4 Effect of sintering time variation on 5wt % WC-Co composite

In order to see the effect of sintering time the composites were sintered at 1350 °C for 1 to 4 h at an interval of 1 h. The binder composition (5wt% cobalt) is kept constant (WP_1 and WF_1 series table 4.12).

4.7.4.1 XRD analysis

XRD patterns of the as synthesized composites showed that in this case also there is no reacted phase formed. In other words, WC and cobalt have not reacted to form complex phases. WC and Cobalt remained unreacted as indexed with ICDD card No.25-1047 and 88-2325 respectively. The XRD patterns of sintered pellets are shown in figure 4.77 and 4.78 for the composites synthesized from WC obtained from WO_3 and wolframite as tungsten source, respectively.

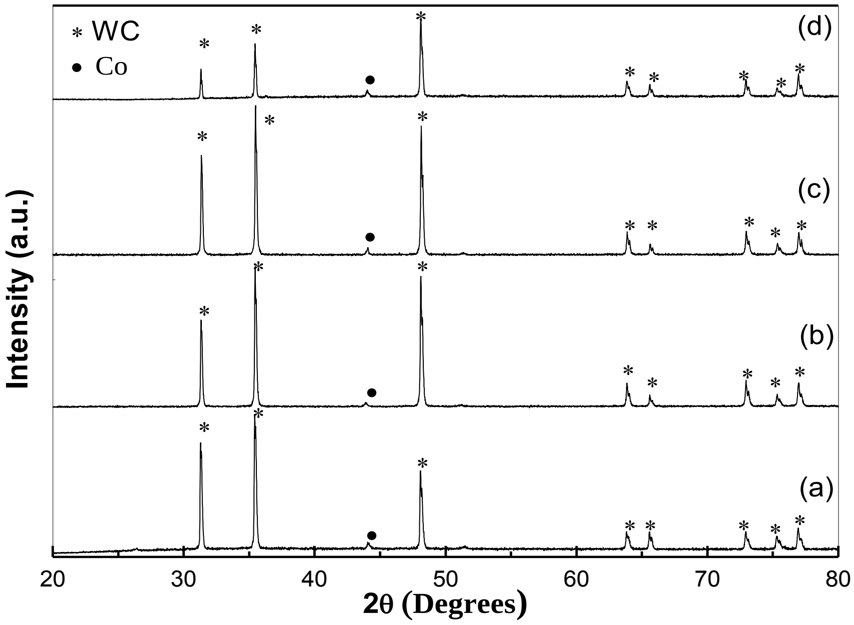

Figure 4.77 (a,b,c,d): XRD of WC-Co(5%) composite (WP_1 series table 4.12) sintered at 1350 ºC for 1,2,3 & 4 h, respectively.

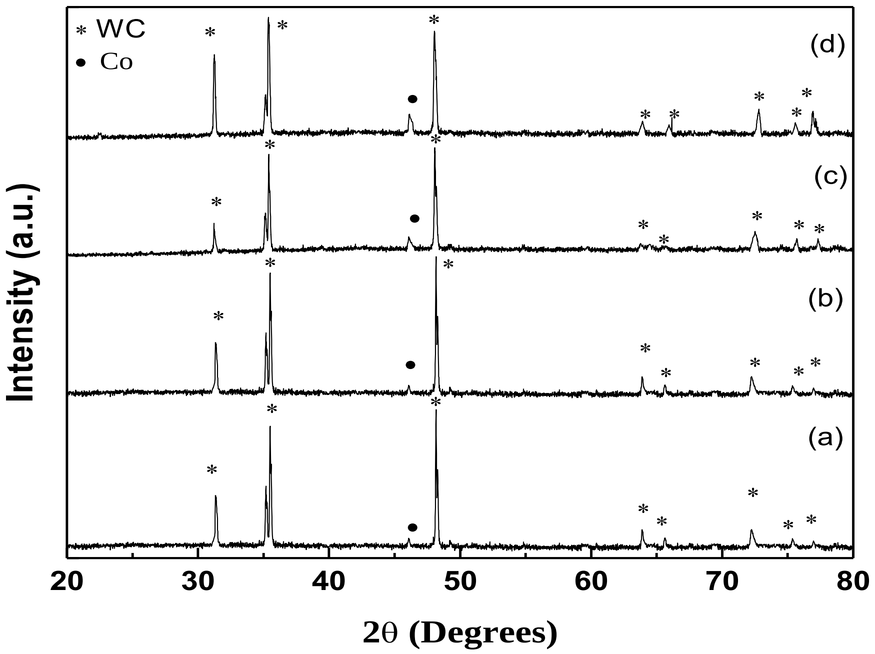

Figure 4.78 (a,b,c,d): XRD of WC-Co(5%) composite (WF_1 series table 4.12) sintered at 1350 °C for 1,2,3 & 4 h, respectively.

The grain size and lattice strain are derived from the intercept and the slope of the linear plot (table 4.16).

Table 4.16: Particle size, micro strain and density as a function of sintering time for 5% composite.

Time (h)	Composite synthesized from WO_3			Composite synthesized from wolframite		
	Particle size (nm)	Micro strain ($*10^{-4}$)	Relative Density (%)	Particle size (nm)	Micro strain ($*10^{-4}$)	Relative Density (%)
1	66.94	1.54	95	65.75	6.67	94
2	67.84	2.56	98	69.49	3.45	96
3	70.31	3.75	99	71.25	6.77	98
4	72.64	2.73	99	76.38	5.85	99

The positive slope of βcos(θ) versus sin(θ) indicates the presence of effective non uniform tensile strain in the crystal lattice which is also verified by the shifting of XRD peaks [34-35].

4.7.4.2 Microstructural analysis

The liquid phase sintering started at 1 h heat treatment as can be seen in the flow characteristics in the micrograph in section 4.7.1.2 (figure 4.53 (a,b,c & d) for WC obtained from WO_3 and figure 4.54 (a,b,c) for WC obtained from wolframite). The grain size was observed to vary between 0.5 to 4 µm as can be seen in the microstructure (figure 4.53(a,b,c & d)). The microstructure does not show clear grain boundaries between the layers. However, interconnected continuous flow pattern is observed (black zone). It is logical to reason that there are indeed grain boundaries between the layers because the size of crystallites measured by XRD (66.94 nm) is much smaller than it would be if all these aggregates are individual grains (table 4.16). This is a clear evidence of grain growth by coalescence. When the sintering time is increased to 2 h these crystallites starts collapsing and grain growth occurs as evident in figure 4.79 (a & b).

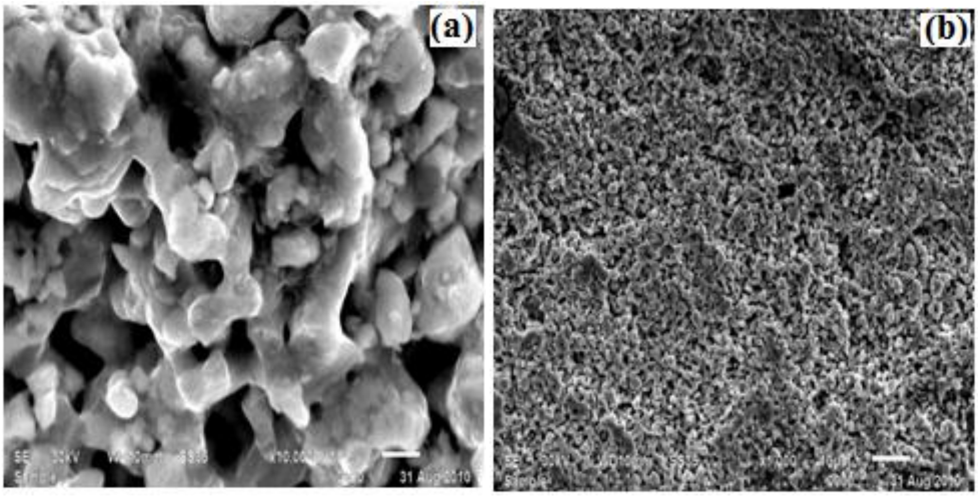

Figure 4.79(a,b): SEM of WC-Co(5%) composite (WP_1 series) sintered at 1350 °C for

2 h.

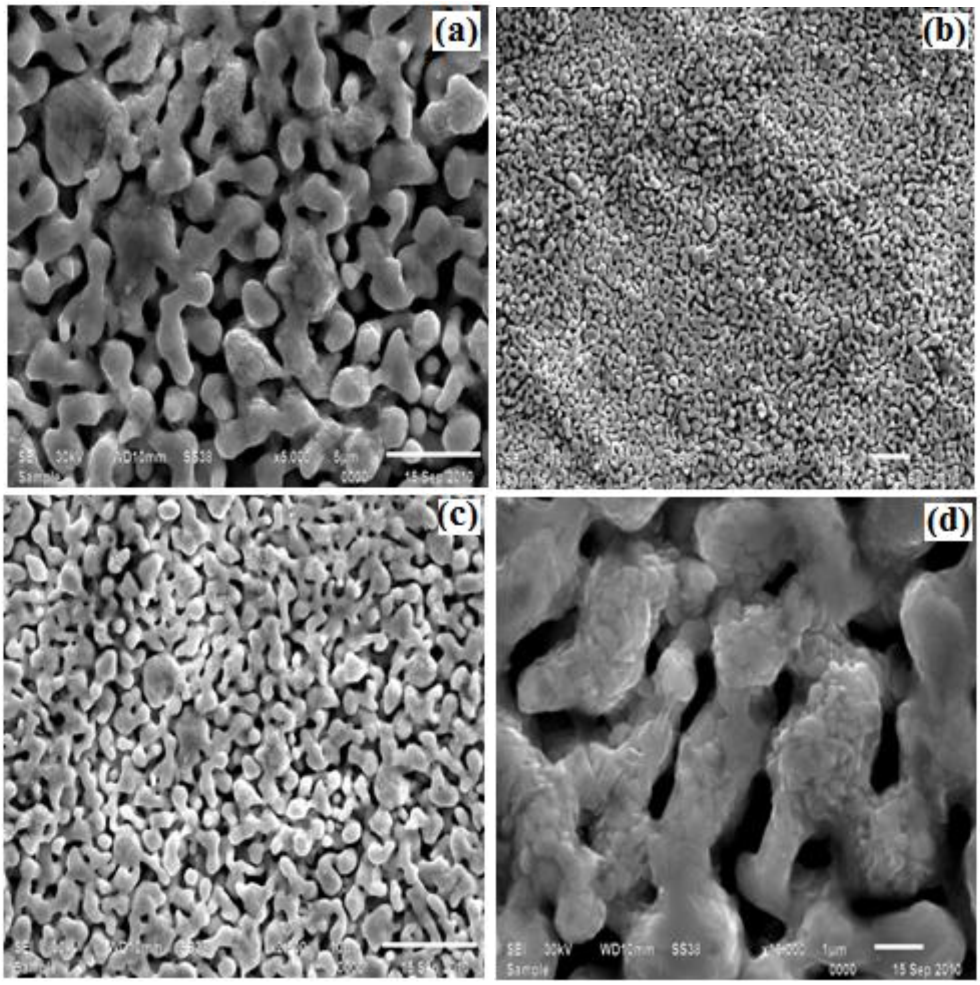

Figure 4.80(a,b,c,d): SEM of WC-Co(5%) composite (WF$_1$ series) sintered at 1350 ºC for 2 h.

However, a different pattern is observed for composite synthesized from wolframite - WC. Here complete sintering is observed but the process is still in dynamic state (figure 4.80 (a,b,c,d)). This may be because of higher volume fraction of WC and higher sintering time. As the heating time is increased further the formation of stable faceted WC particles increases as can be seen in the microstructure (figure 4.81 and figure 4.82)).

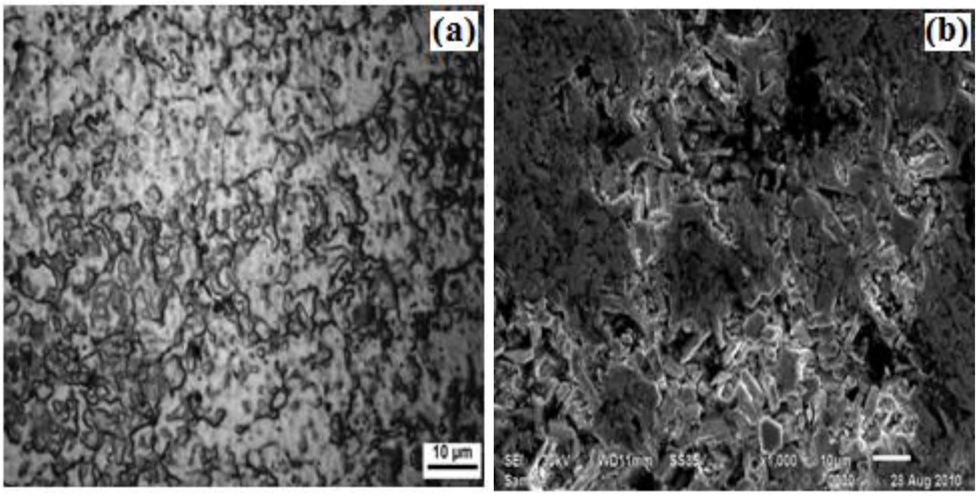

Figure 4.81 (a,b): Optical micrograph(a) SEM (b) of WC-Co(5%) composite (WP_1 series) sintered at 1350 ºC for 3 h.

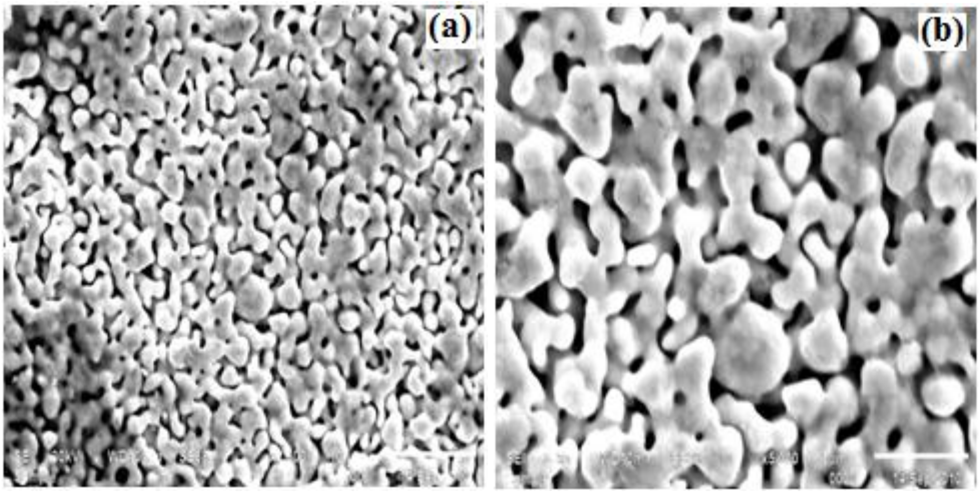

Figure 4.82(a,b): SEM of WC-Co(5%) composite (WF_1 series) sintered at 1350 ºC for 3 h.

Here the network breaks and large particles are formed (figure 4.81(a)). However, this does not lead to a stable one as porosity also exists in the structure (figure 4.81(b)). The overall study indicates that the nano WC particles grow with time.

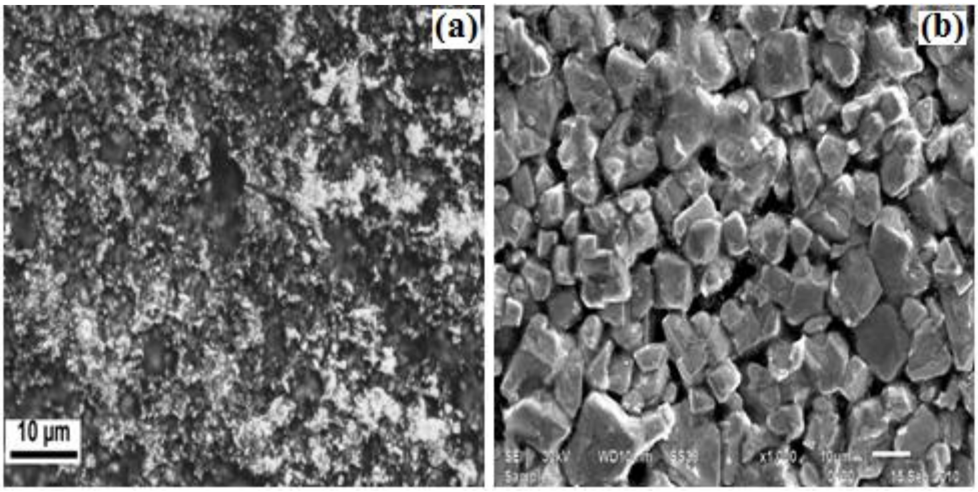

Figure 4.83 (a,b): Optical micrograph(left) SEM(right) of WC-Co(5%) composite (WP_1 series) sintered at 1350 ºC for 4 h.

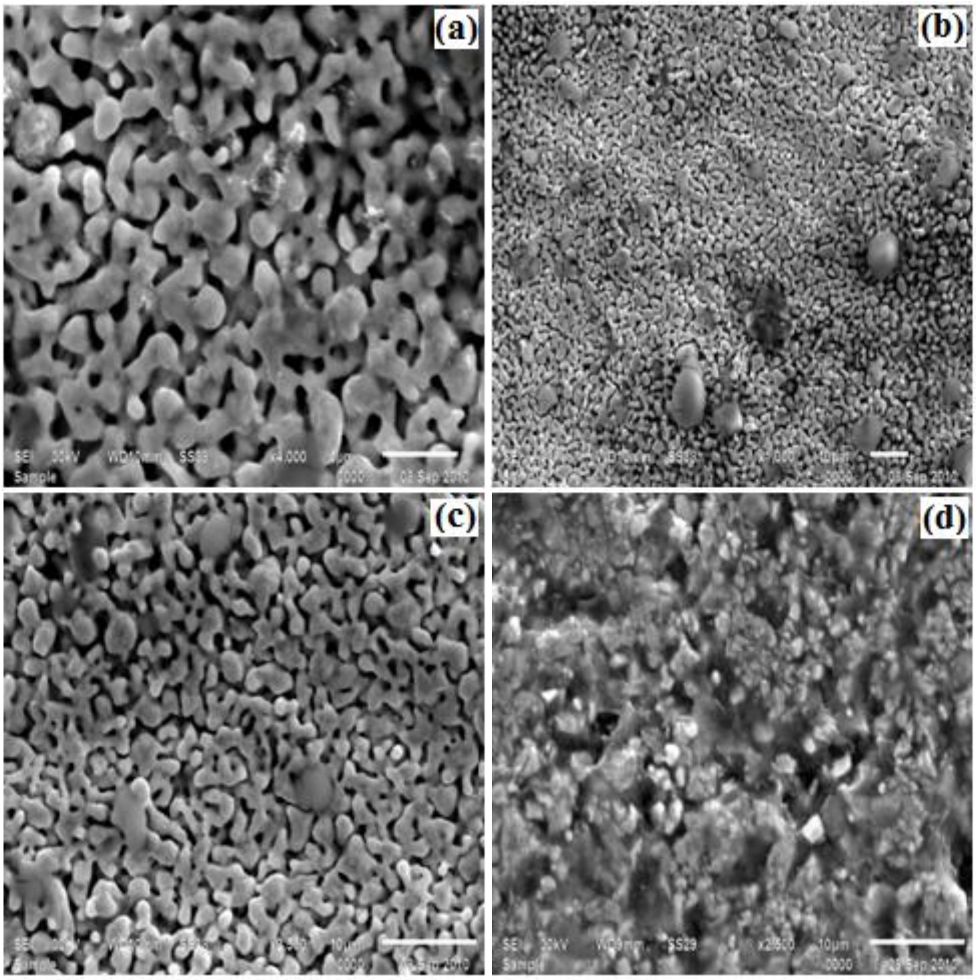

Figure 4.84(a,b,c,d): SEM of WC-Co(5%) composite (WF_1 series) sintered at 1350 ºC for 4 h.

These aggregates disappear further and are replaced by the angular shaped single crystal grains of larger size that are also like the result of the coalescence process (figure 4.79-4.84) [36]. The crystallite size showed an increasing trend with the increase in sintering time.

4.7.5 Effect of time variation on 10 wt % WC-Co composite

In order to see the effect of sintering time the composites were sintered at 1350 °C for 1 to 4 h at an interval of 1 h. The binder composition (10wt% cobalt) is kept constant (WP_1 and WP_2 series in table 4.12).

4.7.5.1 XRD analysis

WC and cobalt have not reacted to form complex phases, as evident from WC and Co remained unreacted and indexed with ICDD card No.25-1047 and 88-2325 respectively. The XRD patterns are also shown in figure 4.85 and 4.86 for the composites synthesized from WO_3 and wolframite as tungsten source.

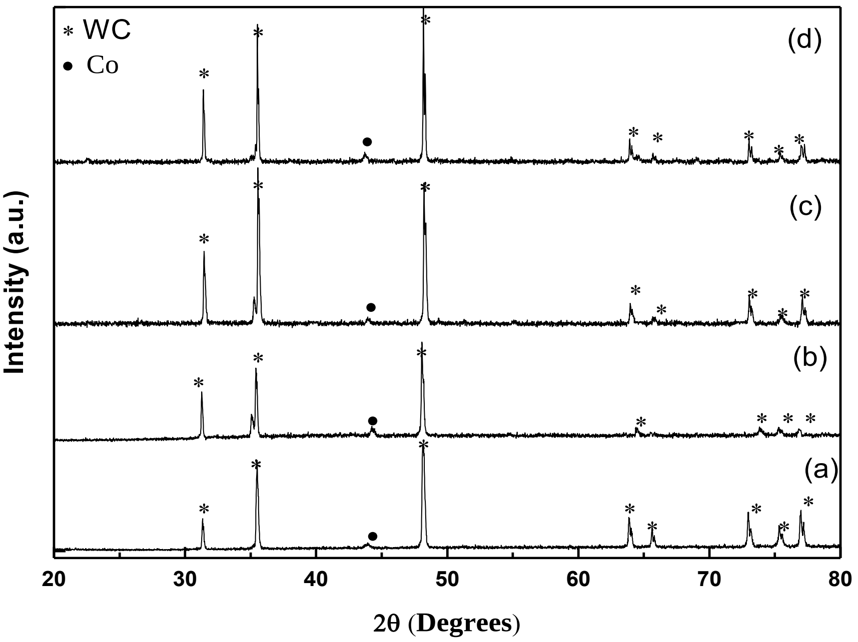

Figure 4.85 (a, b, c & d): XRD of WC-Co(10 wt%) composite (WP_2 series table 4.12) sintered at 1350 ºC for 1,2,3 & 4 h, respectively.

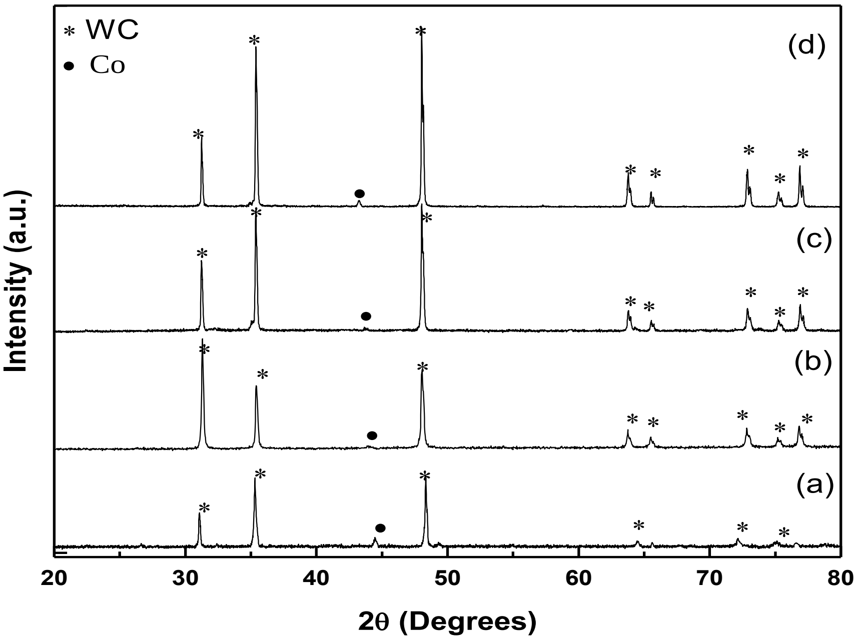

Figure 4.86 (a, b, c & d): XRD of WC-Co(10 wt%) composite (WP_2 series table 4.12) sintered at 1350 ºC for 1,2,3 & 4 h, respectively.

The grain size and lattice strain are derived from the intercept and the slope of the linear plot (table 4.16). The positive slope of βcos(θ) versus sin(θ) indicates the presence of effective non uniform tensile strain in the crystal lattice which is also verified by the shifting of XRD peaks [34-35]. The density is almost constant with increase in sintering time in both the cases.

Table 4.17: Particle size, micro strain and density as a function of sintering time for 10 % binder.

Time (h)	Composite synthesized from WC obtained from WO_3			Composite synthesized from WC obtained from wolframite		
	Particle size (nm)	**Micro strain ($*10^{-4}$)**	**Relative Density (%)**	**Particle size (nm)**	**Micro strain ($*10^{-4}$)**	**Relative Density (%)**
1	65.67	3.59	92	59.65	8.87	90
2	66.53	4.43	92	43.57	4.55	91
3	71.82	6.58	93	71.25	5.37	93
4	75.88	6.89	94	78.13	6.88	94

4.7.5.2 Microstructural Examination

Microstructural features of 10 wt% composite synthesized from powder obtained from WO_3 and wolframite and sintered for 1 h at 1350 °C is discussed under section 4.7.2.2 in figure 4.63 and figure 4.64. When the sintering time was increased to 2 h, the grain growth phenomenon was observed. Figure 4.87(a,b) presents low magnification micrographs showing fully sintered grain. However, in case of samples synthesized from WC powders derived from wolframite, there are non uniform grains (figure 4.88(a,b)). It may be because of non-uniform conditions prevailing at some places which leads to variation in size. Faceted grains having different morphology can be seen.

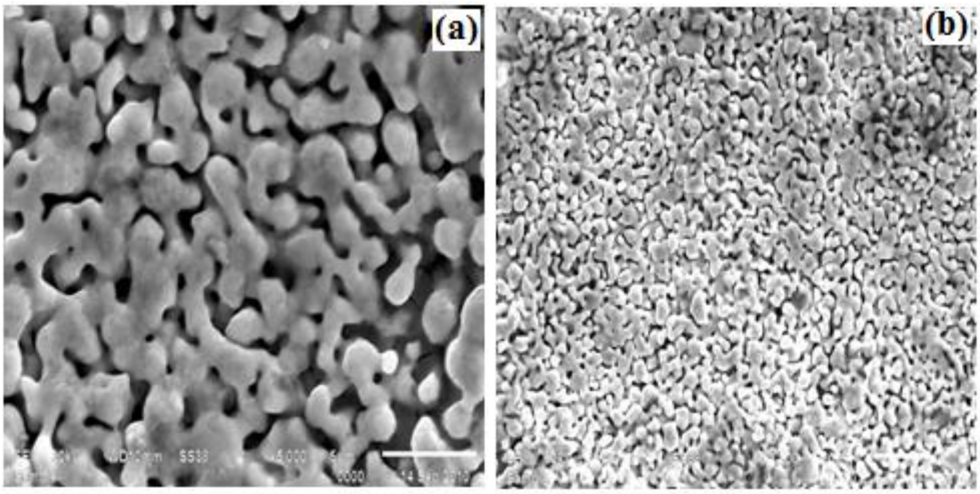

Figure 4.87(a,b): SEM of WC-Co(10%) composite (WP$_2$ series) sintered at 1350 ºC for 2 h.

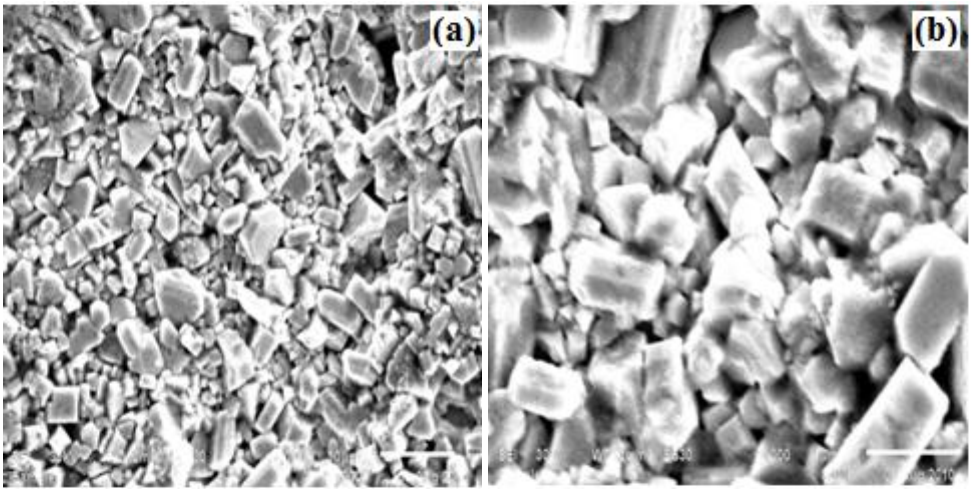

Figure 4.88(a,b): SEM of WC-Co(10%) composite (WF$_2$ series) sintered at 1350 ºC for 2 h.

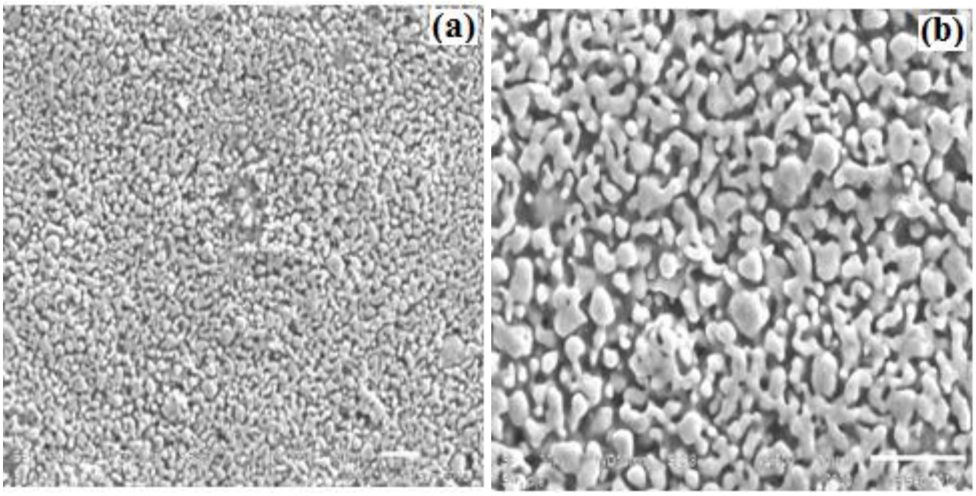

Figure 4.89: SEM of WC-Co(10%) composite (WP$_2$ series) sintered at 1350 ºC for 3 h.

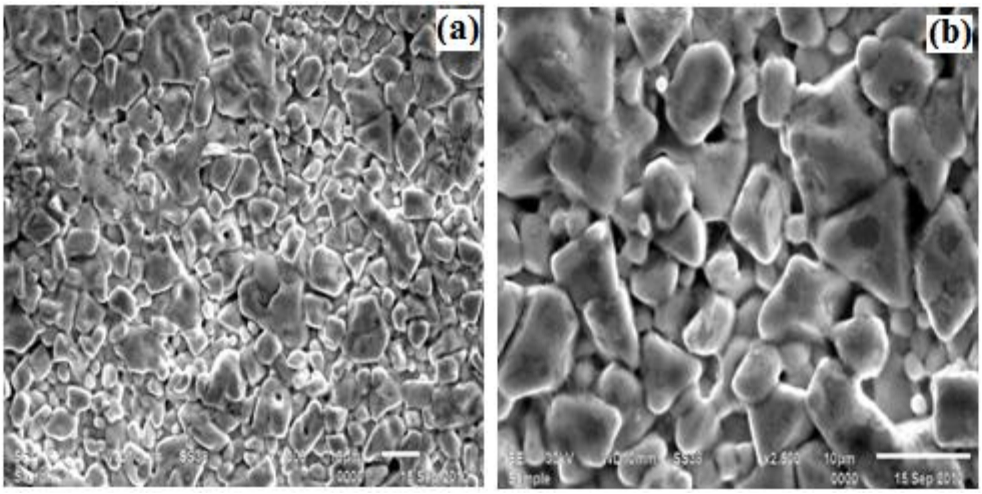

Figure 4.90(a,b): SEM of WC-Co(10%) composite (WF$_2$ series) sintered at 1350 ºC for 3 h.

As the time was increased to 3 h the grain growth process is more pronounced as can be seen in figure 4.89(a,b) for WP$_2$ series and figure 4.90(a,b) for WF$_2$ series. Smallar grains undergo coalescence process to achieve faceted structure. The morphology obtained at the surface of these grains further gives the appearance of flow patterns as can be seen. These indicate that further growth of grains is also possible.

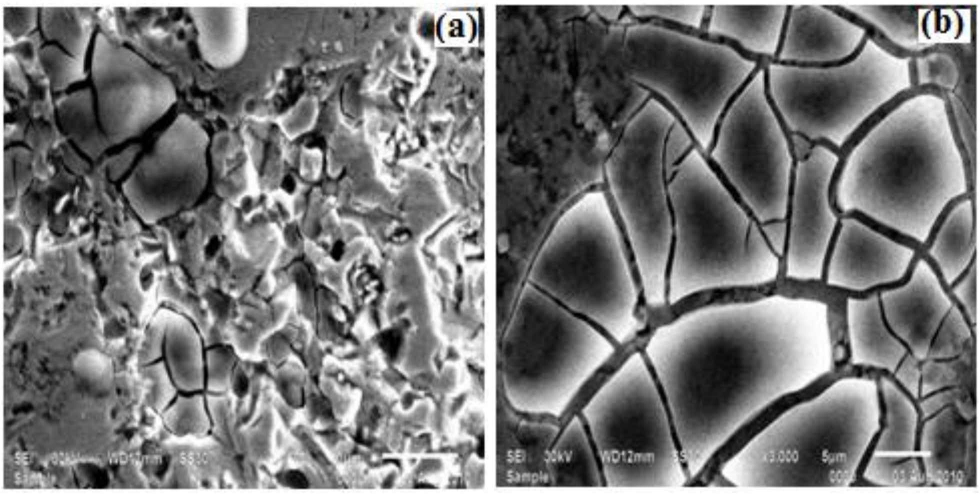

Figure 4.91(a,b): SEM of WC-Co(10%) composite (WP_2 series) sintered at 1350 ºC for 4 h.

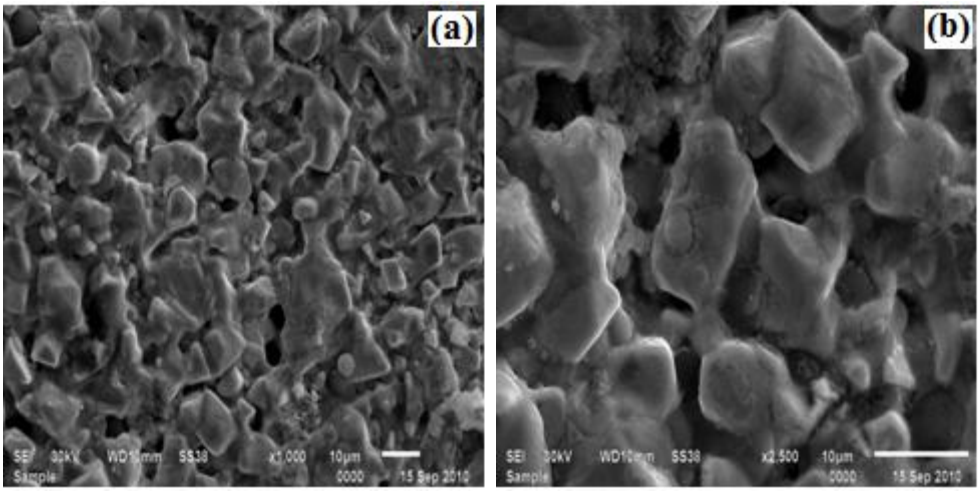

Figure 4.92(a,b): SEM of WC-Co(10%) composite (WF_2 series) sintered at 1350 ºC for 4 h.

As the sintering time was increased to 4 h cracks are visible (figure 4.91(a,b). These cracks are appearing because of non-uniform flow of binder. Binder (Co) comes at the surface and because of its connectivity with beneath grains it develops internal stresses causing cracking. Such type of features is not seen in case of wolframite derived composites. However, surfaces have also micro cracks as are visible in figure 4.92 (a,b).

4.7.6 Effect of time variation on 15 wt % WC-Co composite

4.7.6.1 XRD analysis

Typical XRD patterns are shown in figure 4.93 and 4.94 (a, b, c & d) for the composites synthesized from WO_3 and wolframite as tungsten source. The XRD pattern do not exhibit any reacted phase. The formed phases are indexed with WC (ICDD card No.25-1047) and Cobalt (ICDD card No.88-2325) phases, respectively.

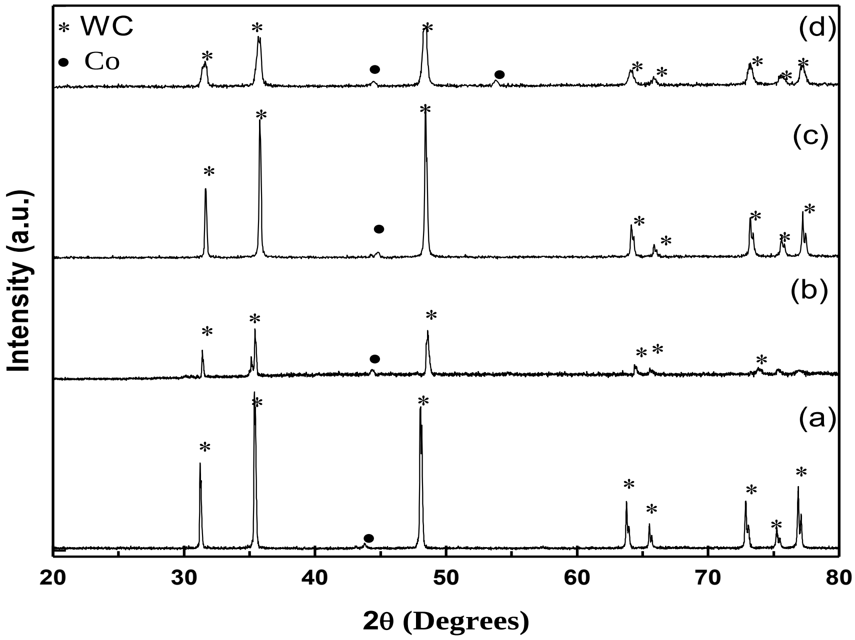

Figure 4.93 (a,b,c,d): XRD of WC-Co(15 wt%) omposite (WP_3 series, table 4.12) sintered at 1350 ℃ for 1,2,3 & 4 h, respectively.

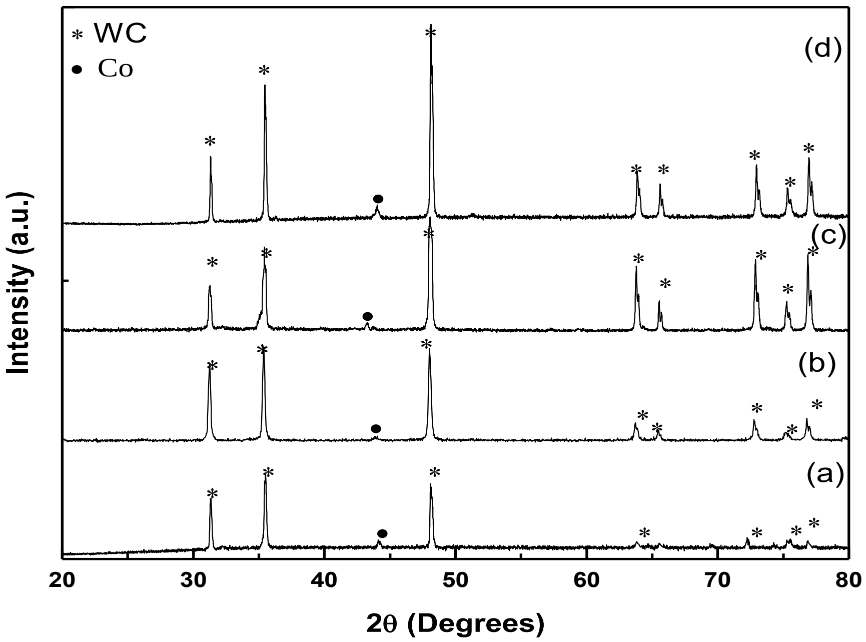

Figure 4.94 (a, b, c & d): XRD of WC-Co(15 wt%) composite (WF_3 series, table 4.12) sintered at 1350 ºC for 1,2,3 & 4 h, respectively.

The grain size and lattice strain are derived from the intercept and the slope of the linear plot and the values are summarized in table 4.18.

Table 4.18: Particle size, micro strain and density as a function of sintering time for 15 % binder.

Time (h)	**Composite synthesized from WC (WO_3)**			**Composite synthesized from WC (wolframite)**		
	Particle size (nm)	**Micro strain ($*10^{-4}$)**	**Relative Density (%)**	**Particle size (nm)**	**Micro strain ($*10^{-4}$)**	**Relative Density (%)**
1	66.56	6.45	92	60.78	6.77	90
2	66.58	6.45	92	64.77	5.64	93
3	73.85	5.89	93	72.88	6.47	93
4	76.89	7.69	94	78.13	5.45	94

The positive slope of βcos(θ) vs. sin(θ) indicates the presence of effective non uniform tensile strain in the crystal lattice which is also verified by the shifting of XRD peaks [34-35]. The density is almost constant with increase in sintering time in both the cases. Likely to early observations, the microstructure and density do not show any well defined trend with respect to sintering temperature.

4.7.6.2 Microstructural examination

Microstructure for WC-Co (15 wt%) composite sintered at 1350 ºC for 1 h is discussed in section 4.7.3.2 (figure 4.73 for WO_3 and figure 4.74 for wolframite). As the time is increased grain growth is observed. Initially it develops as cuboids type (figure 4.95 (a,b)).

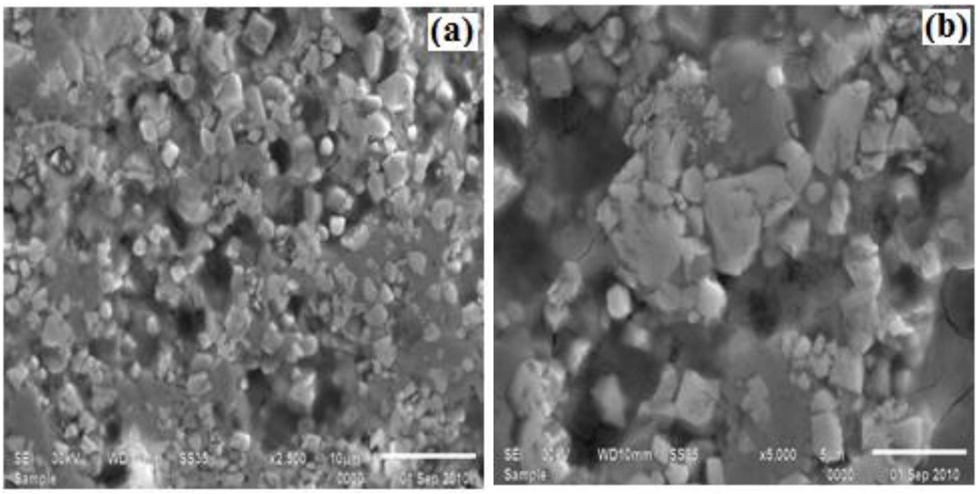

Figure 4.95(a,b): SEM of WC-Co(15%) composite (WP_3 series) sintered at 1350 ºC for 2 h.

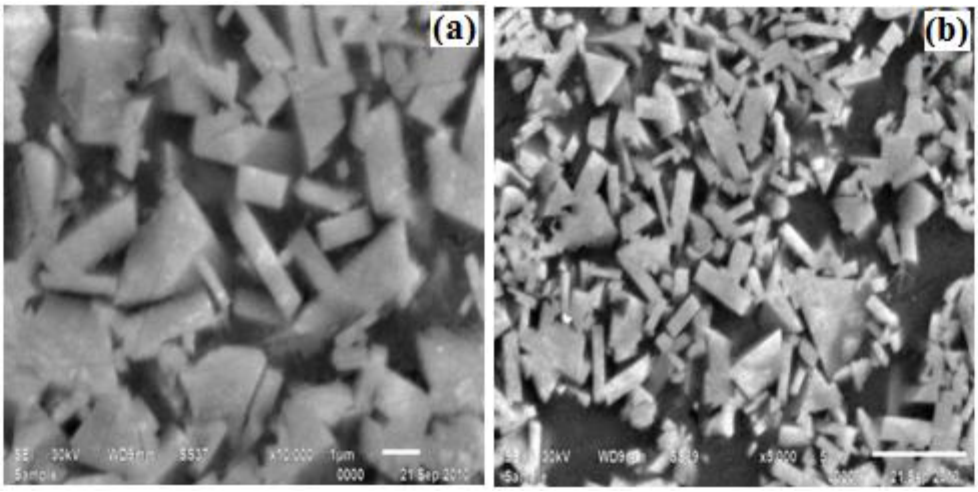

Figure 4.96(a,b): SEM of WC-Co(15%) composite (WF$_3$ series) sintered at 1350 ºC for 2 h.

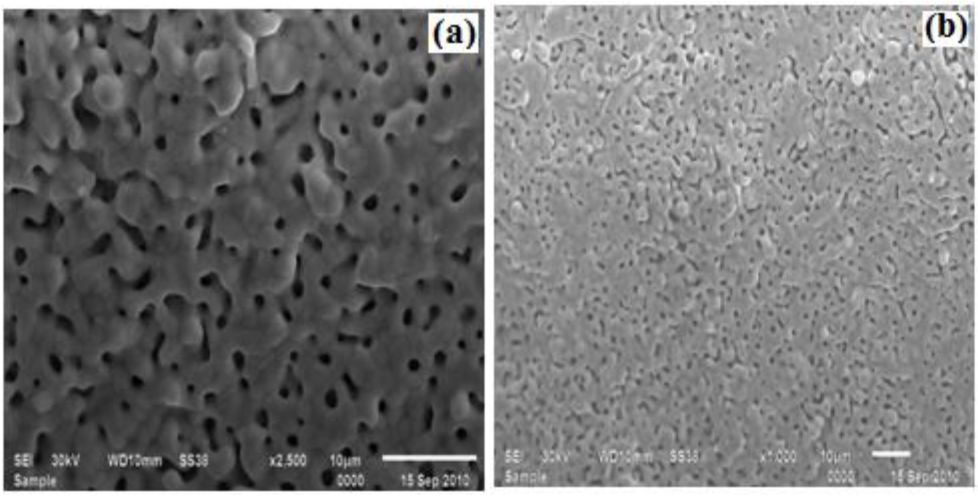

Figure 4.97(a,b): SEM of WC-Co(15%) composite (WP$_3$ series) sintered at 1350 ºC for 3 h.

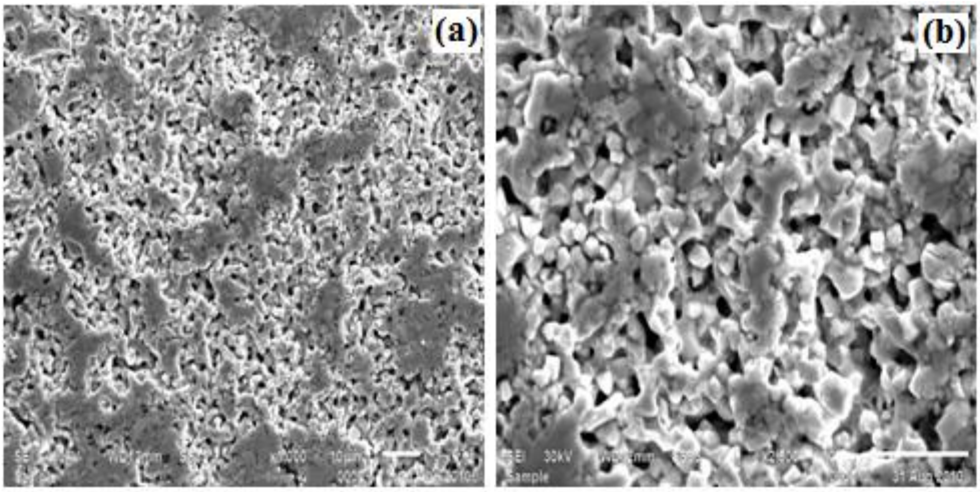

Figure 4.98 (a,b): SEM of WC-Co(15%) composite (WF$_3$ series) sintered at 1350 ºC for 3 h.

In case of wolframite derived composites these cuboids are elongated which is very clear in figure 4.96(a,b) where sharp faceted type features are developed. Moreover, porisity is increasing. This is because of flow of Co binder as its volume fraction got increased. The structural features for high sintering time exhibit good sintering but leads to development of non uniform type of grains in both cases (WP_3 and WF_3 series, figure 4.97 and 4.98). These leads to formation of voids also. Moreover, the product gives complete sintered pellets.

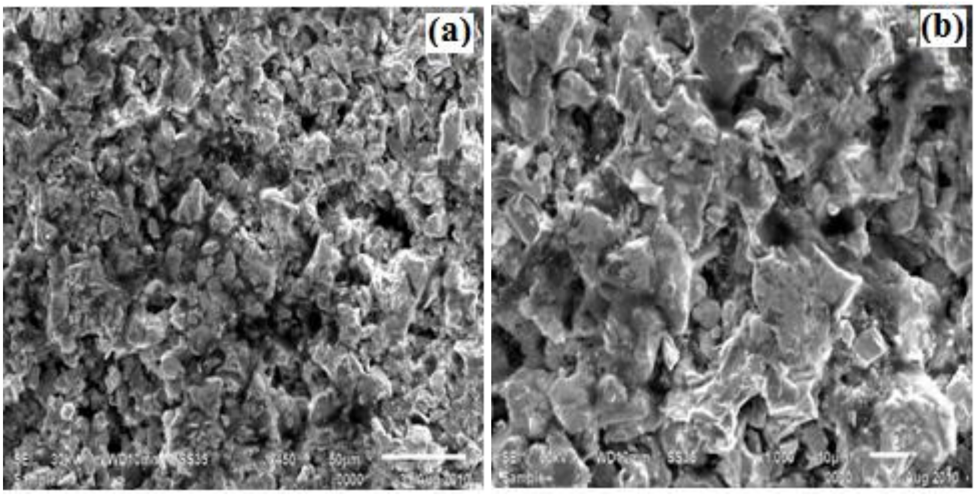

Figure 4.99 (a,b): SEM of WC-Co(15%) composite (WP_3 series) sintered at 1350 ºC for 4 h.

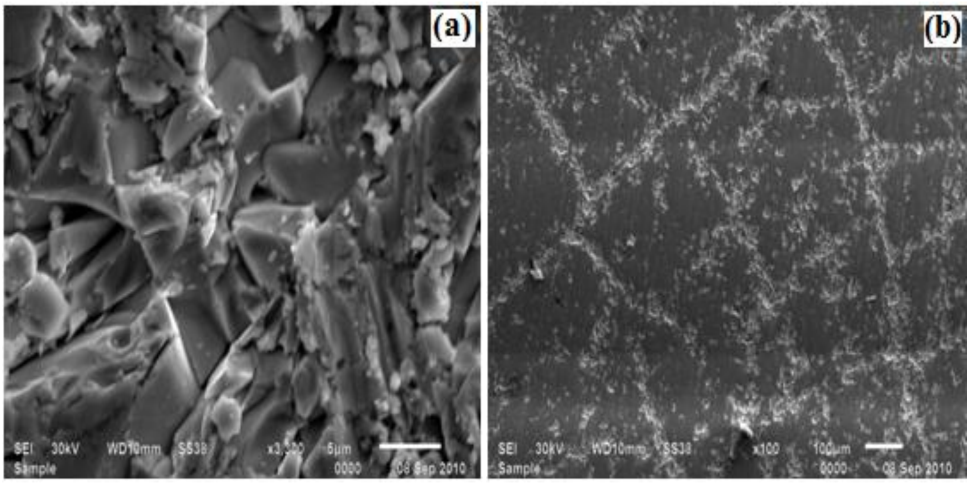

Figure 4.100 (a,b): SEM of WC-Co(15%) composite (WF_3 series) sintered at 1350 ºC for 4 h.

Higher time does not facilitate for obtaining good structure as can be seen in figure 4.99 and 4.100 for WP_3 and WF_3 series, respectively. Flow patterns within the structure are major problem. Moreover, network structure of carbides is also observed (figure 4.100 (b)) which is not desirable.

4.7.7 Effect of Composition variation

In order to see the effect of binder (Co), its composition is varied from 5 to 20 wt% in WC-Co composite, with an increment of 5 wt%. The heating time and temperature is kept constant (1 h and 1350 ºC respectively) as this has shown optimum results.

4.7.7.1 XRD analysis

XRD analysis of the as synthesized composites showed that, in this case also, there is no reacted phase present. WC and cobalt do not react to form complex phases. WC and cobalt remained unreacted indexed with ICDD card No.25-1047 and 88-2325 respectively. Typical XRD patterns are shown in figure 4.101 (a,b,c,d) and figure 4.102 (a,b,c,d).

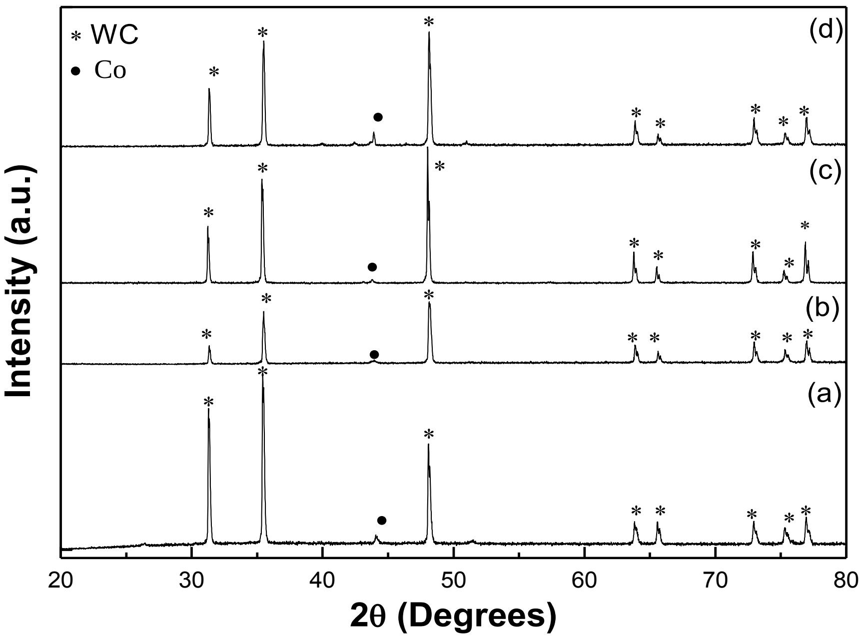

Figure 4.101 (a, b, c & d): XRD of WC-Co (5, 10, 15 and 20 wt%) composite sintered at 1350 °C for 1 h respectively.

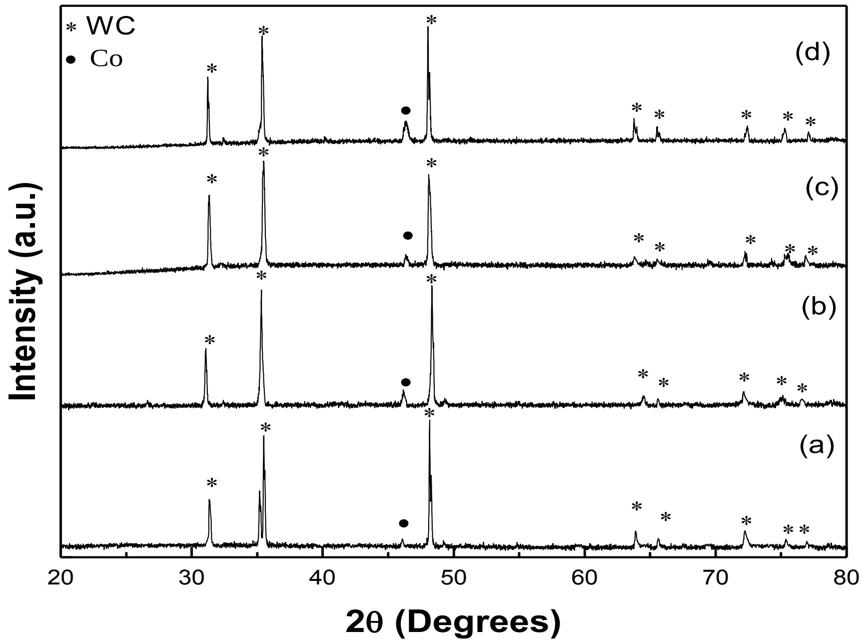

Figure 4.102 (a, b, c & d): XRD of WC-Co (5, 10, 15 and 20 wt%) composite (wolframite) sintered at 1350 °C for 1 h respectively.

In all the samples no free carbon is present and hence no trace of η phase is there. The grain size and internal stress calculated in this case is given in table 4.19. The particle size calculated using XRD showed that there is negligible variation in particle size with composition. The composite is showing non uniform tensile strain. The grain size and lattice strain are derived from the intercept and the slope of the linear plot (table 4.19). The positive slope of βcos(θ) versus sin(θ) indicates the presence of effective non uniform tensile strain in the crystal lattice which is also verified by the shifting of XRD peaks [34-35]. The particle size is almost constant while there is slight variation in density. Higher percentage of binder (Co) leads to less porosity with better compaction.

Table 4.19: Particle size, micro strain and density as a function of binder variation

Cobalt %	**Composite synthesized from WC (WO_3)**			**Composite synthesized from WC (wolframite)**		
	Particle size (nm)	**Micro strain ($*10^{-4}$)**	**Relative Density (%)**	**Particle size (nm)**	**Micro strain ($*10^{-4}$)**	**Relative Density (%)**
5	66.94	1.54	90	65.75	6.67	89
10	66.09	7.86	81	46.45	6.58	79
15	66.66	1.90	92	59.65	8.87	90
20	66.09	1.54	93	73.36	3.35	94

4.7.7.2. Microstructural examination

In order to see the effect of binder (Co), its composition is varied from 5 to 20 wt% in WC-Co composite, with an increment of 5 wt%. The sintering time and temperature is kept constant (1 h and 1350 ºC respectively) as this has shown optimum results (discussed in section 4.7.1.2). In composite with 5 wt% of cobalt, as discussed earlier the grains growth through the process of coalescence of neighboring grains (figure 4.53 (a,b,c,d)) is observed. In composite with 10 wt% of cobalt, microstructure belongs to a two-phase region consisting of WC, and β-Co. Here, the β-Co phase is a cobalt-rich solid solution containing W and C, which is a liquid phase at the sintering temperature (figure 4.63 (a,b) section 4.7.2.2). Composite containing 15 wt% cobalt synthesized from WO_3 is also discussed in section 4.7.3.2 (figure 4.73(a,b,c)).

When the cobalt is increased to 15 wt% and 20 wt%, large WC grains are randomly dispersed in the fine grain matrix. The large grains in these composites exhibit similar morphology. WC grains show the trend of elongated rectangular shape (faceted) features. The majority of WC grains is faceted and accordingly attains the shape of prismatic and basal facets. This means that the WC grains grow preferentially along the [100] crystal direction together with increase in the Co content of WC–Co composite. (figure 4.73 (a,b,c), figure 4.103, and figure 4.70) [18].

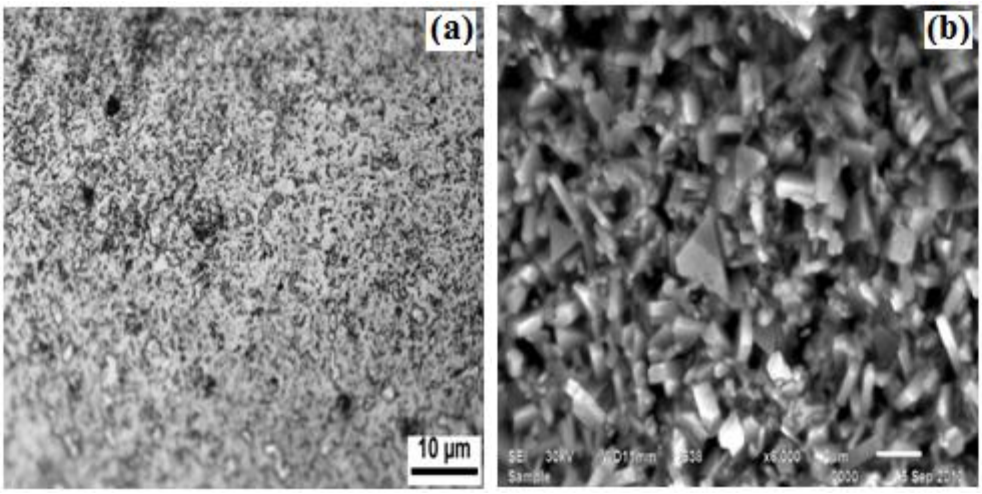

Figure 4.103(a,b): Optical micrograph (left) SEM (right) of WC-Co (20%) composite (WF_4 series) sintered at 1350ºC for 1 h.

Aggregation of individual platelet crystals along certain preferred orientations resulted in such type of morphology. The grain growth is not by coarsening which would yield smooth and continuous surfaces. The particle size calculated using XRD showed that there is negligible variation in particle size with composition variation. The composite are showing non uniform tensile strain (table 4.14). The effect of cobalt is logically related to the solubility of W and C in the cobalt phase. The exact mechanism by which cobalt promotes grain growth, however, is worthy of exploring in light of the need to understand the processes of grain growth. Based on the theories of activated sintering [25], cobalt metal that coats WC grains during milling may serve as a conduit for W and C diffusion which results in densification as well as grain growth.

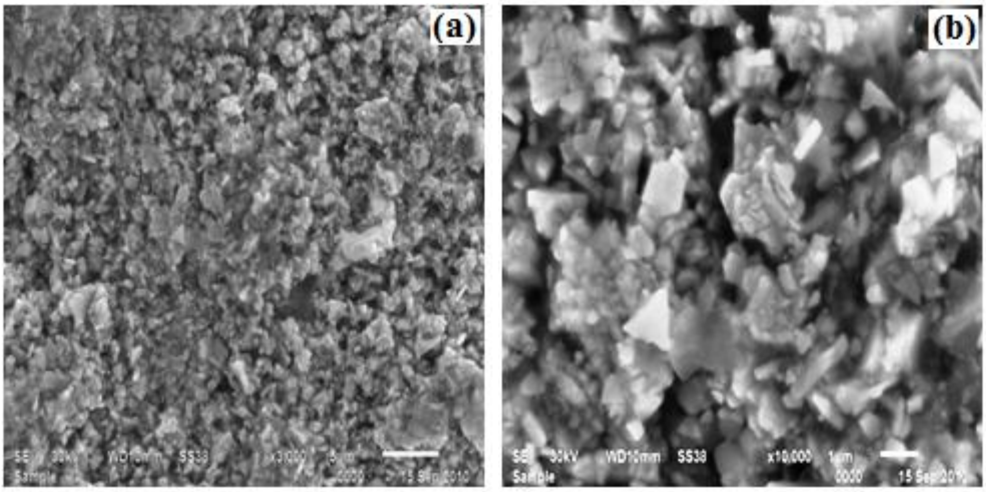

Figure 4.104(a,b): SEM of WC-Co (20%) composite (WF$_4$ series) sintered at 1350 ºC for 1 h.

Similarly composite synthesized from WC (wolframite) containing 5, 10, 15 % cobalt is discussed in section 4.7.1.2 (figure 4.54 (a,b,c), section 4.7.2.2 (figure 4.64 (a,b,c) and section 4.7.3.2 (figure 4.74 (a,b)) respectively. The composites containing 20 wt% binder (figure 4.103(a,b) for WP$_4$ series and figure 4.104 (a,b) for WF$_4$ series respectively) shows similar structural features as for 15% binder composition. The difference is in compactness of pellets, higher the binder higher the density of materials.

4.8 Micro hardness analysis of composites

4.8.1 Effect of temperature

In order to study the effect of sintering temperature of composites containing 5 wt% Co binder microhardness on WC grains were measured. With increase in sintering temperature microhardness of the composites in both cases is observed to increase (WP_1 series and WF_1 series). Similar trends are observed for all the compositions for variable sintering temperature. This increase can also be related to the particle size and density of materials. With increase in temperature the particle size increases. Also as the temperature is increased the phenomenon of liquid phase sintering is more pronounced which leads to increase in density and hence increase in microhardness (figure 4.105(a,b) for WP series and figure 4.105(c,d) for WF series) [37].

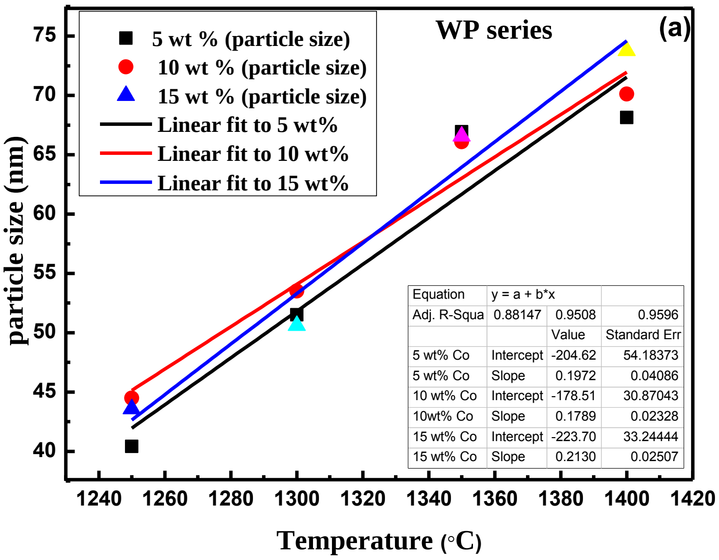

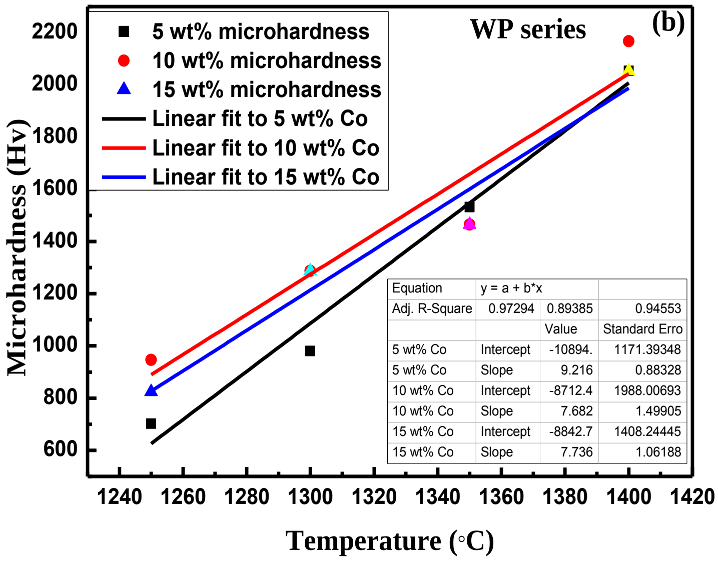

Equation	y = a + b*x		
Adj. R-Square	0.97294	0.89385	0.94553
		Value	Standard Erro
5 wt% Co	Intercept	-10894.	1171.39348
5 wt% Co	Slope	9.216	0.88328
10 wt% Co	Intercept	-8712.4	1988.00693
10 wt% Co	Slope	7.682	1.49905
15 wt% Co	Intercept	-8842.7	1408.24445
15 wt% Co	Slope	7.736	1.06188

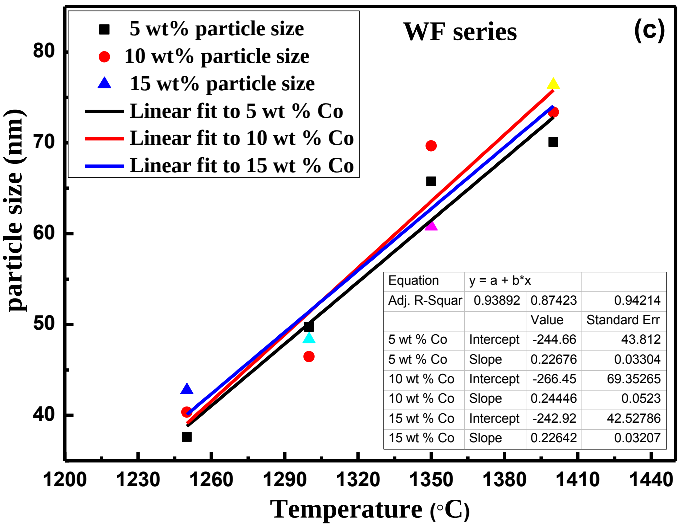

Equation	y = a + b*x		
Adj. R-Squar	0.93892	0.87423	0.94214
		Value	Standard Err
5 wt % Co	Intercept	-244.66	43.812
5 wt % Co	Slope	0.22676	0.03304
10 wt % Co	Intercept	-266.45	69.35265
10 wt % Co	Slope	0.24446	0.0523
15 wt % Co	Intercept	-242.92	42.52786
15 wt % Co	Slope	0.22642	0.03207

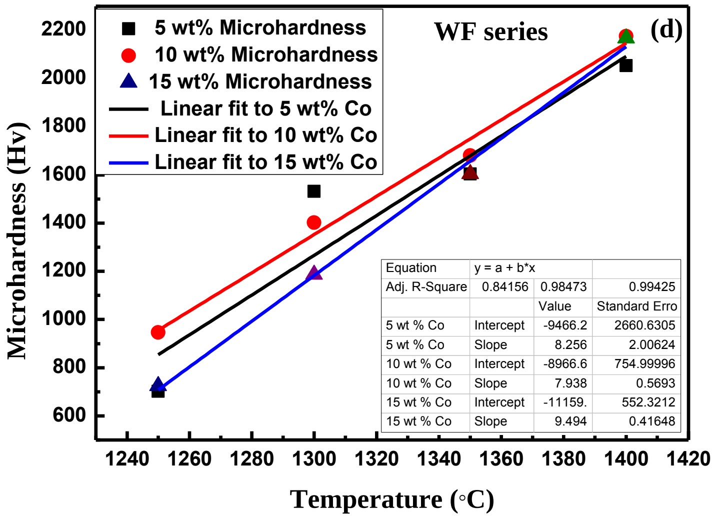

Figure 4.105(a,b,c,d): Particle size and microhardness as a function of sintering temperature.

As compared to modern sintering techniques like spark plasma sintering (SPS), monoaxial vacuum hot pressing (MVHP), pulse plasma assisted sintering technique (PAS), field assessed sintering (FAST) in this traditional liquid phase sintering technique the sintering time is quite large [27]. As compared to MVHP sintering technique the temperature required to achieve density above 90 % is large. In case of MVHP it can be achieved above 1280 °C while in the present case the required temperature is 1350 °C. When 90% density is achieved the microhardness value is higher than the MVHP technique. The distribution of WC particles is also uniform [38]. Similar observation was also seen when compared to PAS technique [39-42].

4.8.2 Effect of sintering time

To study the effect of sintering time composites containing 5% Co binder was sintered at 1350 ºC. The increase in time also leads to increase in micro hardness of the composites in both cases (WP_1 series and WF_1 series). Here also we can relate the hardness with the density of composites. Increased sintering time increases density of composites as discussed in previous sections and hence micro hardness (figure 4.106(a) for WP series and figure 4.106(b) for WF series) [42].

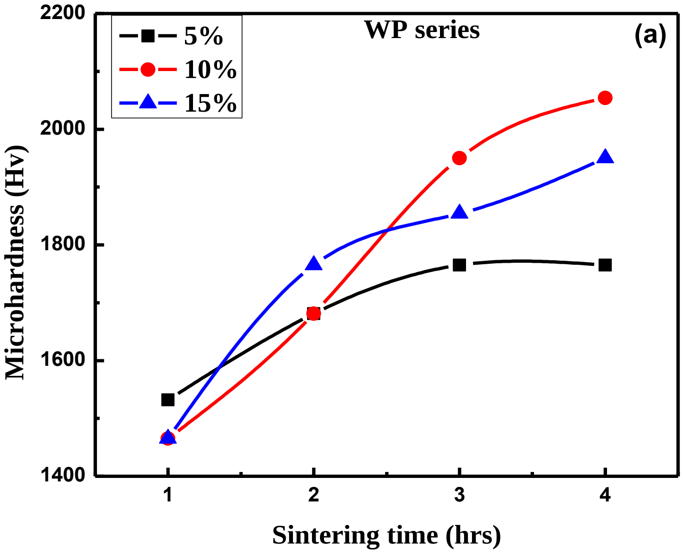

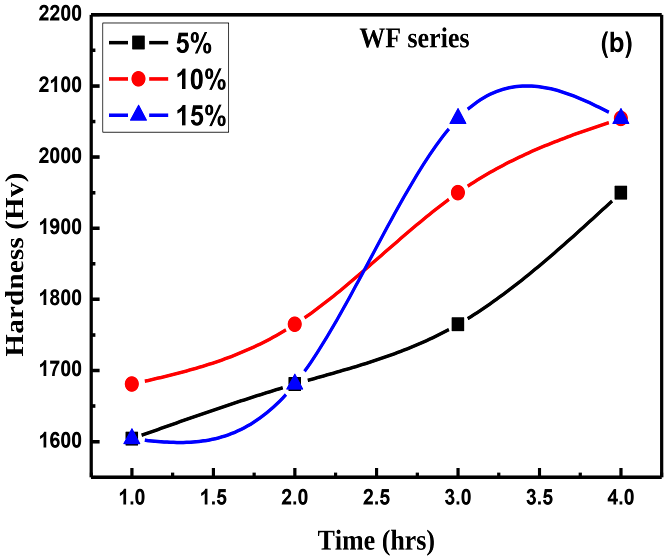

Figure 4.106(a,b): Microhardness as a function of sintering time.

Comparing the results to SPS technique (sintering time 10 min, temperature 1100 °C), the sintering temperature in the present case is 1350 ºC and sintering time is 1 to 4 h to achieve comparable density, but at this comparable density value the Vickers hardness value (Hv) is higher than SPS technique [46]. For SPS the hardness value range is from 1450 to1512 while for present case its range is 1465 to 2054 for WP series and 1681 to 2054 for WF series for similar compositions. While in case of pulse plasma sintering technique the hardness value ranges from 1780 to 2250 with similar densities [42].

4.8.3 Effect of binder composition

In order to study the effect of binder content in composites on sintering behavior of pellets which were sintered at 1350 ºC temperatures for one hour, hardness measurement was done. The increase in binder content did not show a regular pattern but there was exponential increase in hardness in both the cases (figure 4.107 for WP and WF series) when the binder wt% was increased to 20 wt%. This increased hardness value may be related to density of synthesized composites [44-47].

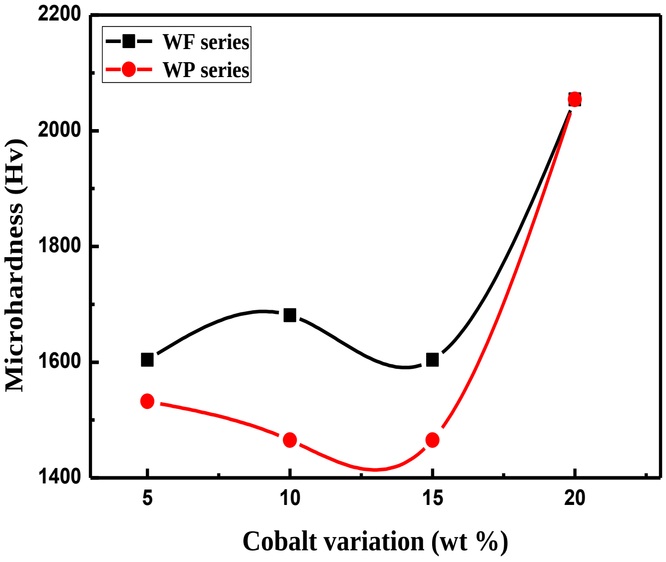

Figure 4.107: Microhardness as a function of binder variation (wt%).

References

[1] C. J. M. Fletcher, Proceedings of the Royal Society of London. Series A, Mathematical and Physical Sciences, 147 (860) (1934) 119-128.

[2] C. Guo, Y Liu, X. Ma, Y. Qian, and L. Xu, Chemistry Letters 35 (11) (2006) 1210-11.

[3] H.Yu, C. Lu, T. Xi, L. Luo, J, Ning and C. Xiang, Journal of thermal analysis and Calorimetry, 82 (2005) 97-101.

[4] G. A. Swift and R. Koc, J of Mat Sci, 35 (2000) 2109-2113.

[5] C. Pham-Huu, K. Nicolas, Vladimir V. Roddatis, G. Mestl, R. Schlogl, and M. J. Ledouxa, J. Phys. Chem. Chem. Phys. 4 (2002) 514-521.

[6] B. Louis, G. Gulino, R. Vieira, J. Amadou, T. Dintzer, S. Galvagno, G. Centi, M.J. Ledoux, C. Pham-Huu, Catalysis Today , 102 (2005) 23-28.

[7] Xiangzhi Cui, Hua Zhang, Xiaoping Dong, Hangrong Chen, Lingxia Zhang, Limin Guo and Jianlin Shi, J. Mater. Chem.18 (2008) 3575-3580.

[8] B. D. Cullity, Elements of x-ray diffraction. Addison-Wesley Publishing London 1977.

[9] J.Mazher, A. K. Shrivastav, R. V.Nandedkar, R. K.Pandey, Nanotechnology 15 (2004) 572-580.

[10] S.B. Qadri, E.F. Skelton, D.Hsu, A.D. Dinsmore, J.Yang, H.F. Gray et al. Phys Rev B 60(13) (1999) 9191-9193.

[11] N. S.Ramgir, Y. K. Hwang, I. S. Mulla, J.S. Chang, Solid State Sci; 8 (2006) 359-362.

[12] A. L. Patterson, Phys Rev 56 (1939) 978-982.

[13] K. Tanioku, T. Maruyama, S. Naritsuka, Diam Relat Mater 17 (2008) 589-593

[14] B.Louis,G.Gulino,R.Vieira,J.Amadou,T.Dintzer,S.Galvagno et al. Catal Today 102-103 (2005) 23-28.

[15] Pengxiang Hou, Chang Liu, Yu Tong, Shitao Xu, Min Liu, and Huiming Chenga, J. Mater. Res., 16(9) (2001) 2526-2529.

[16] Y. Chen, D. Ciuparu, S. Lim, G.L. Haller, L.D. Pfefferle, Carbon 44 (1) (2006) 67–78.

[17] SrinijaRepalle, JiuhuaChen, VadymDrozd,Wonbong Choi, J of Phys Chem of Solids (in press).

[18] Danielle K. Smith, C. Doh Lee, and A. Brian Korgel Chem. Mater. 18 (2006) 3356-3364.

[19] C. Doh Lee, V. Frederic Mikulec, and A. Brian Korgel, J. Am. Chem. Soc. 126 (2004) 4951-4957.

[20] Tao Luo, Luyang Chen, Keyan Bao, Weichao Yu, Yitai Qian, Carbon 44 (2006) 2844–2848.

[21] Jackson K.A. Liquid Melts and solidification. Vol. 174. ASM. 1958.

[22] Jackson K.A. Hunt J.D. Acta Met 13(11) (1965) 1212-15

[23] F.L. Zhang, C.Y. Wang, M. Zhu, Scripta Materialia 49 (2003) 1123–1128

[24] C. S. Barret and T. B. Massalski, Structure Metals Oxford: Pergamon (1980) 204.

[25] C. Pham-Huu, N. Keller, V. V. Roddatis, G. Mestl, R. Schlogl, and M. J. Ledoux, Phys. Chem. Chem. Phys. 4(2002) 514–521.

[26] A. Ludwig and S. Leibbrandt, Mat. Sci. Eng. A 375–377 (2004) 540–546

[27] Z. Zak Fang, Xu Wang, Taegong Ryu, Kyu Sup Hwang, H.Y. Sohn, Int J Refract Metal Hard Mater 27 (2009) 288–299.

[28] Akshay Kumar, K. Singh, O.P. Pandey, Physica E 41 (2009) 677-684.

[29] Akshay Kumar, K. Singh, O.P. Pandey, Physica E 42 (2010) 2477-2483.

[30] G.H. Li, C.A. Ma, J.Y. Tang, Y.F. Zheng, Mater. Lett. 61 (2007) 991-993.

[31] H.J. Zheng, CA. Ma, W. Wang, J.G. Huang, Electrochim. Commun. 8 (2006) 977-981.

[32] S. Kim, S.H. Han, J.K. Park, H.E. Kim, Scripta Mater. 48 (2003) 635–639.

[33] S.B. Qadri, E.F. Skelton, D. Hsu, A.D. Dinsmore, J. Yang, H.F. Gray et al. Phys Rev B 60(13) (1999) 9191-93.

[34] G. K. Williamson, W.H. Hall Acta Metall 1(1953) 22–31.

[35] H. H. Tian, M. Atzmon, Phil Mag A 79(8) (1999) 1769–86.

[36] Xu Wang, Zhigang Zak Fang, Hong Yong Sohn, Int J Refract Metal Hard Mater 26 (2008) 232–241.

[37] A. Michalski, D. Siemiaszko, Int J Refract Metal Hard Mater 25 (2007) 153–158.

[38] Chenguang Lin, Erich Kny, Guansen Yuan, Boro Djuricic, J Alloys Compd 383 (2004) 98–102.

[39] Shixian Zhao, Xiaoyan Song, Jiuxing Zhang, Xuemei Liu, Materials Science and Engineering A 473 (2008) 323–329.

[40] V. Bonache, M.D. Salvador, V.G. Rocha, A. Borrell, Ceram Inter 37 (2011) 1139–1142.

[41] D. Sivaprahasam, S.B. Chandrasekar, R. Sundaresan, Int J Refract Metal Hard Mater 25 (2007) 144–152.

[42] S.G. Huang, L. Li, K. Vanmeensel, O. Van der Biest, J. Vleugels, Int J Refract Metal Hard Mater 25 (2007) 417–422.

Chapter 5

CONCLUSIONS AND FUTURE SCOPE

Overview

The role of different carbon sources, reducing agent and different tungsten sources for obtaining high purity WC nano powders are concluded in this chapter. These nano powders have been further used for fabricating WC-Co composites. The effect of Co binder and sintering temperature in terms of sinterability is also summarized here. The variations in microhardness of the synthesized composites are also described. At the end suggestions for future work in this field is given.

5.1 Conclusions

The aim of present work was to synthesize WC nano particles from WO_3 and wolframite ore. These WC nano particles were subsequently used for making WC-Co composites. WC-Co composites (micro/nano) were synthesized using different wt % of cobalt. The WC nanoparticles were synthesized in a specially designed and fabricated autoclave which can be used at elevated temperatures. Magnesium was used as reducing agent alongwith WO_3 / wolframite to facilitate the reaction. Methanol, ethanol and acetone carbon sources were used as carbon sources. Out of these acetone as carbon source has shown better reduction properties. This (acetone) was further investigated at different processing conditions to obtain quality product and better yield. After that the WC-Co composite was synthesized by using WC and Co nano powders. The effect of sintering temperature, time, and composition of Co binder was also investigated.

From the experimental results it can be concluded that thermo-chemical and mechano-chemical synthesis route can be used to synthesize WC nano powders. In thermo-chemical reaction WO_3 can be reduced to WC nano powders in the presence of a carbon source; ethanol or acetone and reducing agent magnesium. Out of three carbon sources (methanol, ethanol and acetone) only two were able to deliver the required product. Again in case of acetone the yield of WC nano powder was very high and the unreacted carbon was low so it was selected for further experimentation. Acetone was investigated to study the effect of temperature, reaction time and pressure (generated in the sealed autoclave) to find the yield of the product phase (WC) which was maximum in this case. The TEM images indicated a special type of phenomenon occurring at the surface of WO_3 particles. On the basis of data collected from XRD, DTA/TGA and TEM, reaction mechanism for obtaining WC nano powder has been proposed. As given in equation in previous chapters one of the byproduct was hydrogen. The pressure generated by this gas at high temperature played a major role for the conversion of WO_3 to WC nano powder. The reduction of WO_3 has taken place in the atmosphere of hydrogen and ethane. This was confirmed in TEM study as one of the product phases obtained was carbon nanotubes. It seems that the particle size of WC decreases with the increase in amount of carbon source up to certain extent. Reaction time of 20 h and amount of carbon source 36 ml (acetone) gave a maximum yield of WC with the minimum amount of unreacted carbon in an autoclave of 50 ml capacity. Analysis of processing parameters indicated that the yield of nano-WC powder is maximum when the structure is highly textured along (100) plane while the yield is minimum when the structure is highly textured along (001) plane.

In mechano-chemical reaction, it is possible to convert ore of tungsten (wolframite) directly to WC nano particles. In this case also three carbon sources; methanol, ethanol and acetone were tried. Out of the three, acetone was best suited and was used for further investigation. The purity and homogeneity of the synthesized WC nanoparticles was good as compared to WO_3 source. Mechanical activation played a vital role in this synthesis. Increased milling time increases the surface area of reactant and hence the quality of product phases. With increase in milling time, the amount of excess carbon which was a byproduct, decreased. The homogeneity of WC nanoparticles also increased with milling time. Hydrogen generated in the autoclave during the reaction also played a critical role in the synthesis of these particles.

The proposed mechanism indicated that carbon nanotubes were also formed during synthesis, which played very important role in the conversion of tungsten oxides to WC. Additional experiments performed to confirm the formation of CNTs under similar condition in the autoclave when only acetone was heated showed that the diameter of the tubes were 3-14 nm. The shift in G and D band in Raman spectroscopic analysis also confirmed the formation of CNTs.

The analysis of sintering behavior of the composites prepared using WC nano powder synthesized from WO_3 and wolframite ore also showed some exiting results. Traditional liquid phase sintering technique was adopted for the sintering of these composites. Three parameters; temperature, time and binder (Co) composition were varied to find out a suitable sintering combination. The sintering was done in inert (argon) atmosphere. Microstructural examinations were also done for these composites to study the distribution of WC particles in cobalt matrix. The agglomeration of WC nanoparticle in cobalt binder with increase in temperature, time was also studied.

These studies showed that the traditional liquid phase sintering can be used for the sintering of nanocrystalline WC–Co. Sintering of WC-Co composites in argon atmosphere do not show any unwanted phase (η). Sintering temperature (1350 ºC) is critical above which the grain growth increases abruptly. The grain growth through the process of coalescence occurred. The majorities of WC grains are faceted and attains prismatic and basal facets. The effect of composition is negligible when sintered at critical temperature. The time factor also played a vital role. It can be concluded that nano composite required very less sintering time as compared to conventional micro composites. It is very difficult to control the coarsening of WC grains. Nano WC in WC-Co composite after sintering grows to micron level because of higher sintering time and temperature. While low sintering time and temperature does not facilitate to get well sintered product.

Microhardness analyses of the composites were also done. The hardness is directly related with the density of composites. With increase in sintering temperature the density of material increases and hence the microhardness of the sintered composite. Increased sintering time also increased the density of composite with increased microhardness. The increase in binder composition does not show a regular trend up to 15 wt% of binder. Above 15 wt% of binder there in an exponential increase in microhardness of composites. This increase is also related to the density of composite.

5.2 Scope for further work

As synthesizd nano particles can be used as WC-Cu, WC-Ag or with gold in contact materials in electrical circuits. Since the purity of the synthesized material is very high and the size is quite uniform, which is favourable for catalysis so the catalytic activity of these particles can also be tested. WC as catalyst can replace Pt in methanol fuel cell and hence it can reduce the production cost of methanol fuel cell. Role of grain growth inhibitors should be studied to check the grain growth of WC nanoparticles so that it can be used for different metallurgical applications.